THE DOWNSTREAM EXTRATROPICAL FLOW RESPONSE TO RECURVING WESTERN NORTH PACIFIC TROPICAL CYCLONES

by

Heather M. Archambault

A Dissertation
Submitted to the University at Albany, State University of New York
in Partial Fulfillment of
the Requirements for the Degree of
Doctor of Philosophy

College of Arts & Sciences
Department of Atmospheric and Environmental Sciences
2011

ABSTRACT

The factors that govern the downstream flow response to recurving western North Pacific (WNP) tropical cyclones (TCs) are investigated from climatological, composite analysis, case study, and predictability perspectives. A 1979–2009 climatology of WNP TC recurvature indicates that TC recurvature is followed by a four-day period of above-normal North Pacific meridional flow. The relationship between TC recurvature and above-normal North Pacific meridional flow is found to be stronger in late summer through mid-fall than in early summer and early winter, and stronger for TCs that interact strongly with the jet stream than for TCs that interact weakly with the jet stream. This relationship is not affected by the size or intensity of a TC at recurvature, or whether or not a TC reintensifies as an extratropical cyclone.

A 1979–2009 composite analysis of WNP TC recurvature indicates that recurving TCs in fall and late spring favor Rossby wave train (RWT) amplification and dispersion across the North Pacific into North America, whereas recurving TCs in summer do not favor RWT dispersion. The composite analysis also reveals that TCs that interact strongly with the jet stream favor RWT dispersion followed by high-latitude ridge amplification over western North America. In contrast, TCs that interact weakly with the jet stream exhibit a minimal signature of RWT dispersion.

Case studies of two recurving WNP TCs illustrate that recurving TCs can influence the downstream flow pattern in different ways. TC Malakas (September 2010) amplifies a RWT that disperses downstream and leads to high-impact weather over North America, whereas TC Chaba (October 2010) strengthens the North Pacific jet stream, thereby preconditioning the environment for subsequent RWT dispersion that leads to high-impact weather over North America. An examination of predictability associated with TC Malakas finds that poor forecasts of RWT amplification and dispersion lead to large model forecast errors downstream. Thus, individual episodes of TC recurvature may detrimentally impact forecast skill well downstream, despite findings of a 1996–2006 climatological analysis that WNP TC recurvature does not impact overall Northern Hemispheric model forecast skill.

ACKNOWLEDGEMENTS

First and foremost, I'd like to gratefully acknowledge Dan Keyser and Lance Bosart for their advisement and mentorship. Working with Dan and Lance over the past several years has been a true privilege, and I've learned so much from them both. I'm especially appreciative of all the opportunities they've given me to participate in field programs, attend conferences and workshops, give seminars, and work on a variety of research projects during my time at Albany.

I'd also like to thank the rest of my Ph.D. committee: Ryan Torn, Brian Colle (SUNY Stony Brook), and Wayne Higgins (NCEP CPC). All offered me constructive, specific feedback on this dissertation that will be extremely beneficial to me at the paper-writing stage.

My deep thanks go to Chris Davis of NCAR for serving as my host during my three-month visit (May–July 2010) to NCAR as an Advanced Studies Program Graduate Student Visitor. His thoughtful suggestions and comments had a major impact on the direction of my dissertation research. In particular, his suggestion to quantify the downstream flow response to recurving WNP TCs using metrics to represent the North Pacific meridional flow pattern and the TC–jet interaction substantially elevated the quality of the work.

Thanks are due to Anantha Aiyyer (NC State), who contributed many FORTRAN programs that were instrumental to my research. I also want to thank Carl Schreck (CICS-NC) for his help with running NCL scripts on GEMPAK data.

I want to acknowledge fellow Lance Bosart graduate students Jay Cordeira, Nick Metz, Alan Srock, Tom Galarneau (NCAR), and Joe Kravitz – all terrific colleagues and friends who've had a major impact on me, intellectually and otherwise. I was fortunate to have two close friends, Tom and Nick, as officemates, and I can't thank them enough for all the times that they've helped me, work-wise and otherwise. I also want to acknowledge Jay Cordeira, who contributed the most to my research of any graduate student at Albany.

I owe a debt of gratitude to one my closest friends in the department, Ross Lazear, for his friendship, humor, and encouragement. In addition, as someone whose research interests closely align with my own, Ross offered many perceptive comments and suggestions on my research, for which I am grateful.

I want to acknowledge the following "early career" scientists, whom I admire greatly, for their feedback on my research, their career advice, or both: Christian Grams (KIT), Clark Evans (UW–Milwaukee), Russ Schumacher (CSU), Kristen Corbosiero, Olivia Martius (ETH Zurich), Michael Riemer (Johannes Gutenberg University), Ron McTaggart-Cowan (Environment Canada), and Eyad Atallah (McGill University).

My thanks are also due to Sarah Jones (KIT) and Pat Harr (NPS), who were kind enough to meet with me on several occasions to discuss my research, and who helped me to see how my research fit into the "big picture". I am grateful to Morris Weisman (NCAR) for helping me feel so much at home during my three-month stay in Boulder, CO, and for all his professional advice, which has made an indelible mark on me.

I thank my husband and fellow scientist, Scott Runyon, for his love, support, and good humor along the way, and for being so understanding when conferences, field programs, and other career opportunities often took me far from home. I am constantly inspired by his intellectual curiosity. Besides Scott, I owe so much to my wonderful family – my parents Liz and Ray, my brother Seth, my mother-in-law Lillian, my grandparents Harry and Hazel, and all of my aunts, uncles, and cousins – who have cheered me on at every step of the way.

Finally, I thank the entire DAES faculty, especially Chris Thorncroft, John Molinari, Vince Idone, and Arthur Loesch. I am proud to be the graduate of a department in which teaching and mentoring are so highly valued.

TABLE OF CONTENTS

1. Introduction

a. Motivation and purpose

Tropical cyclones (TCs) that recurve into the midlatitudes while undergoing extratropical transition (ET) have long been recognized as hazards due to their capacity to produce high winds, heavy rain, and storm surge (e.g., Pierce 1939; Namias 1963). Perhaps less appreciated is that recurving TCs also may lead to high-impact weather thousands of kilometers downstream. By perturbing the extratropical jet stream, a recurving TC may induce Rossby wave train (RWT) amplification and dispersion (e.g., Riemer et al. 2008; Harr and Dea 2009; Riemer and Jones 2010). Frequent TC recurvatures over the western North Pacific (WNP) are of particular concern to interests in North America because RWT dispersion from the North Pacific has been linked to the onset of large-scale flow anomalies and high-impact weather events over North America (e.g., Archambault et al. 2010).

Individual case studies reveal that the downstream extratropical flow response to recurving TCs varies considerably (e.g., Harr and Dea 2009). The response can range from the excitation or amplification of a high-amplitude RWT, to the intensification and downstream extension of the jet stream, to little discernable flow response. The combination of factors governing this difference in behavior is not well understood, although characteristics of the large-scale flow pattern, the TC itself, and the phasing of the TC with the extratropical flow during ET are believed to be important (e.g., Reynolds et al. 2009; Harr and Dea 2009; Riemer and Jones 2010).

An issue related to the range of possible extratropical flow responses to recurving WNP TCs is that recurving TC episodes are frequently associated with reduced predictability, which is manifested as increased model forecast error and/or increased spread among members of an ensemble prediction system (EPS). For example, large errors in model forecasts of the midtropospheric flow over the North Pacific have been observed during episodes of recurving and transitioning WNP TCs (Jones et al. 2003). The reduced predictability that arises during recurving TC episodes may be due to the high sensitivity of ET to the phasing of the TC with the extratropical flow (e.g., Klein et al. 2000; Jones et al. 2003; Ritchie and Elsberry 2007; Anwender et al. 2010). Reduced predictability may also arise from the upscale growth of error and uncertainty associated with diabatic ridge amplification accompanying ET. In this situation, forecast error and uncertainty may spread well downstream in conjunction with RWT dispersion (e.g., Reynolds et al. 2009; Anwender et al. 2010).

The overarching goal of this dissertation is to understand the factors that modulate the observed downstream extratropical flow response to recurving and transitioning WNP TCs. The following questions will be addressed: (i) How do characteristics of the large-scale flow pattern, the TC itself, and the phasing of the TC with the extratropical flow (e.g., the TC–jet stream interaction) modulate the extratropical flow response to recurving WNP TCs? (ii) What are the important synoptic–dynamic processes accompanying high-amplitude extratropical flow responses and high-impact weather events associated with recurving WNP TCs? (iii) What factors influence the predictability of recurving WNP TC episodes?

b. Organization of dissertation

The dissertation is organized as follows: The remainder of Chapter 1 contains a literature review. A climatology of recurving WNP TCs is presented in Chapter 2, whereas Chapter 3 contains the results of composite analyses constructed using cases identified in the climatology. Chapter 4 contains two case studies of recurving WNP TC episodes associated with strong TC–jet stream interactions, pronounced flow reconfigurations and high-impact weather over North America, and, in the case of one recurving WNP TC episode, reduced predictability. A discussion of the key findings is found in Chapter 5. Finally, Chapter 6 contains a summary and potential future research paths.

c. Literature review

i. General characteristics of TC recurvature

In an otherwise quiescent environment, a westward-moving TC embedded in Northern Hemispheric (NH) tropical easterlies will eventually turn toward the northwest due to beta drift [i.e., steering induced by a beta gyre that forms via planetary vorticity advection induced by the cyclonic circulation of the TC (e.g., Holland 1983, 1984; Carr and Elsberry 1990)]. If the TC is located on the southern edge of a potential vorticity (PV) strip, which is a zonally elongated area of cyclonic PV generated by diabatic heating associated with intertropical convergence zone convection, its turn toward the northwest will tend to be more marked (e.g., Evans et al. 1991; Ferreira and Schubert 1997). In the latter scenario, relative vorticity advection by the TC circulation acts to reinforce planetary vorticity advection by the TC circulation, inducing a more northward

TC motion than would result from beta drift alone. In addition, a westward-moving TC may turn northwestward in response to southerly flow occurring along the western periphery of a subtropical anticyclone (e.g., Camargo et al. 2007) or induced by an equatorially trapped wave such as an equatorial Rossby or mixed Rossby–gravity wave (e.g., Matsuno 1966).

Once a TC tracks northwestward into higher latitudes, it may undergo recurvature (i.e., a further heading change from northwestward to northeastward) as it encounters upper-tropospheric westerlies. During and following recurvature, the structure of the TC typically acquires extratropical characteristics (i.e., the TC undergoes ET) as it becomes embedded in the upper-tropospheric westerlies.

The environmental factors governing TC recurvature are well known. An early study by Riehl and Shafer (1944) documents that TCs tend to recurve in response to upper-tropospheric westerlies associated with the equatorward penetration of an extratropical trough. Subsequent studies establish techniques for forecasting TC track, speed, and acceleration in the event of recurvature or its possibility, all which make use of the concept that TCs tend to be steered by the mid-to-upper-tropospheric flow (e.g., George and Gray 1976, 1977; Chan and Gray 1982; Cheng-Lan and Sadler 1983; Hodanish and Gray 1993).

From a climatological perspective, WNP TC recurvature is favored under certain large-scale flow conditions. During WNP TC recurvature episodes, anomalous mid-tropospheric cyclonic and anticyclonic circulations tend to be present over the extratropical WNP and South China Sea, respectively (e.g., Harr and Elsberry 1991; Camargo et al. 2007). In addition, WNP TC recurvature episodes are more frequent during the warm phase of the El Niño–Southern Oscillation (ENSO; e.g., Bjerknes 1969) and less frequent during the cool phase of ENSO (e.g., Wang and Chan 2002; Elsner and Liu 2003). More frequent WNP TC recurvature episodes during the warm ENSO phase (El Niño) are attributed to enhanced upper-tropospheric southeasterly steering flow around 135°E associated with a deeper-than-normal east Asian upper-tropospheric trough. Conversely, less frequent WNP TC recurvature episodes during the cool ENSO phase (La Niña) are attributed to reduced upper-tropospheric southeasterly steering flow around 135°E associated with a weaker-than-normal time-mean upper-tropospheric trough over eastern Asia (Wang and Chan 2002).

In addition, the tendency for WNP TCs to form farther eastward during El Niño and farther westward during La Niña with respect to climatology (e.g., Chan 1985; Wang and Chan 2002) also is found to impact WNP recurvature frequency. The characteristic eastward shift in the WNP TC genesis region during El Niño is associated with an increased likelihood that a westward tracking WNP TC will encounter an upper-tropospheric trough and recurve (Elsner and Liu 2003). Conversely, the characteristic westward shift in the WNP TC genesis region during La Niña is associated with a decreased likelihood that a westward tracking WNP TC will encounter an upper-tropospheric trough and recurve.

WNP TC recurvature episodes occur primarily between late spring and late fall (i.e., May–December), with a peak in late August and early September (e.g., Jones et al. 2003[1]). A secondary peak in WNP recurvature episodes in the second half of October is

---

[1] Although Jones et al. (2003) specifically examine ET rather than TC recurvature, their ET climatology likely closely corresponds to a TC recurvature climatology since nearly all TC recurvatures are associated with ET, and nearly all ETs are associated with TC recurvatures.

noted in an early study by Burroughs and Brand (Fig. 1.1; Burroughs and Brand 1973). The time of year in which WNP TC recurvature episodes are most frequent corresponds closely to the time of year in which WNP TCs occur most frequently (e.g., Fig. 1.1; Burroughs and Brand 1973; Jones et al. 2003).

Characteristics of recurving WNP TCs are influenced by the relatively large seasonal variability in the extratropical flow pattern over the WNP. An examination of the monthly mean extratropical flow pattern over eastern Asia, the North Pacific, and North America for May–December (Fig. 1.2) reveals that the WNP jet stream and associated baroclinic zone are shifted equatorward and are considerably stronger in late fall and early winter than in summer. The WNP jet stream and baroclinic zone also are shifted equatorward and are slightly stronger in late spring relative to summer (Fig. 1.2). These seasonal changes in the WNP jet stream are consistent with the tendency for WNP TCs to recurve at lower latitudes (e.g., Fig. 1.3; Riehl 1972; Burroughs and Brand 1973), recurve at a higher frequency (e.g., Fig. 1.1), recurve more sharply, and accelerate more rapidly after recurvature in late spring, late fall, and early winter than in summer (e.g., Burroughs and Brand 1973).

A potentially important finding of Burroughs and Brand (1973) that is not necessarily related to the seasonal variability of the WNP extratropical flow pattern is that WNP TCs at recurvature tend to be larger and more intense in the fall (September–November) than in spring or summer. This relationship between the size and intensity of WNP TCs and the season may be relevant to understanding the seasonal variation in the extratropical flow response to recurving WNP TCs. A more general point of interest to be addressed in Chapter 2 is how the Burroughs and Brand (1973) 1945–1969 climatology of recurving WNP TCs would compare to a more modern climatology of recurving WNP TCs.

ii. Extratropical transition

ET is a fundamental aspect of TC recurvature. As TCs moves into the extratropics, they encounter significant environmental changes such as horizontal moisture and sea surface temperature (SST) gradients, lower SSTs, increased westerly flow, increased vertical wind shear (i.e., baroclinicity), and increased planetary vorticity (e.g., Jones et al. 2003). In response to these environmental changes, TCs acquire characteristics of baroclinic, extratropical cyclones (ECs) through a two-stage process of transformation and extratropical reintensification. This two-stage conceptual model for ET is based on studies by Klein et al. (2000, 2002)[2]. Their analysis of 30 WNP ET events occurring from June through October during 1994–1998 reveals that TC structural changes during ET proceed in a relatively similar manner.

During the first step of the transformation stage (Fig. 1.4, left column), the outer circulation of the cyclone begins to interact with an east–west-oriented baroclinic zone (middle and bottom panels) and associated vertical wind shear. On the west side of the cyclone circulation, equatorward advection of cool, dry air (middle and bottom panels) reduces clouds and precipitation (top panel). On the east side of the cyclone circulation, however, poleward advection of warm, moist air (middle and bottom panels) maintains clouds and heavy precipitation (top panel). The cyclone circulation remains

---

[2] Earlier conceptual models of ET are presented in studies by Matano and Sekioka (1971) and Foley and Hanstrum (1994).

approximately axisymmetric (middle and bottom panels) and the inner warm-core circulation associated with the cyclone remains upright (bottom panel).

In the second step of the transformation stage (Fig. 1.4, middle column), the baroclinic zone rotates cyclonically to a southwest–northeast orientation in response to the cyclone circulation (middle and bottom panels). The equatorward advection of cool, dry air (middle and bottom panels) limits clouds and precipitation on the west and south sides of the cyclone circulation (top panel), whereas the poleward advection of warm, moist air (middle and bottom panels) supports heavy precipitation on the east and north sides of the cyclone circulation (top panel). The cyclone circulation becomes asymmetric (middle and bottom panels) and the inner warm core circulation begins to tilt downshear (bottom panel) in response to increasing vertical wind shear.

In the third and final step of the transformation stage (Fig. 1.4, right column), a baroclinic wave develops. Equatorward advection of cool, dry air (middle and bottom panels) continues to limit clouds and precipitation on the west and south sides of the cyclone circulation (top panel), with cloudiness and deep convection on the east and north sides of the cyclone circulation maintained by a low-level jet (middle and bottom panels). The cyclone circulation becomes more asymmetrical (middle and bottom panels) and predominantly cold core, although a weak low-level warm core persists over the surface cyclone center (bottom panel). In this third step of the transformation process, distinct warm and cold frontogenesis is observed to the northeast and southwest of the cyclone center, respectively (e.g., Harr and Elsberry 2000).

The ET transformation stage typically is associated with a substantial weakening of the cyclone. The transformation stage is considered complete when the cyclone center is located on the cold side of a preexisting extratropical baroclinic zone, which corresponds well to the time that operational forecasters consider a cyclone extratropical (Jones et al. 2003).

The transformation stage of ET also can be understood using the cyclone phase space (CPS) paradigm of Hart (2003). Based on an analysis of CPS parameters of North Atlantic ET events, Evans and Hart (2003) define ET onset time to be when the lower-tropospheric thickness field of a transitioning cyclone reaches a certain threshold of asymmetry. Evans and Hart (2003) note that this ET onset time corresponds well with the ET transformation time defined by Klein et al. (2000).

After the transformation stage of ET, a subset of cyclones reintensifies as ECs instead of continuing to weaken. This processes of extratropical reintensification is deemed by Klein et al. (2000, 2002) to be the second stage of ET. During the reintensification stage, fronts form in the presence of high baroclinicity and strong vertical wind shear, with the warm front typically more prominent than the cold front (e.g., Harr and Elsberry 2000). The cloud and precipitation fields become increasingly asymmetric. The cyclone acquires a vertical tilt and typically becomes a deep cold-core system, although a shallow warm core can sometimes be maintained during the reintensification stage (e.g., Browning et al. 1998; Thorncroft and Jones 2000; Jones et al. 2003). Klein et al. (2000, 2002) consider ET complete when reintensification ceases.

Numerous studies have investigated factors that promote extratropical reintensification. Klein et al. (2000, 2002) and others note that the reintensification stage[3] is associated with the phasing of a transitioning TC with an upper-tropospheric disturbance such as an upstream trough (e.g., DiMego and Bosart 1982a,b; Harr and Elsberry 2000; Harr et al. 2000; Sinclair 2004; Ritchie and Elsberry 2007; Kitabatake 2008) or PV anomaly (e.g., Browning et al. 1998, 2000; Thorncroft and Jones 2000; Agustí-Panareda et al. 2004, 2005). The reintensification of a transitioning TC in response to an approaching upper-tropospheric disturbance is described by DiMego and Bosart (1982a,b) and others as similar to type-B EC development (Petterssen and Smebye 1971), whereby differential cyclonic vorticity advection produces surface development along a weak lower-tropospheric baroclinic zone.

A key aspect of the reintensification stage is that a TC may modify its environment such that thermodynamic and dynamic conditions are more favorable for extratropical cyclogenesis. For example, the reduced static stability and preexisting lower-tropospheric PV anomaly accompanying a recurving TC can facilitate a stronger interaction between an approaching upper-tropospheric PV anomaly and the lower-tropospheric PV anomaly of the TC (e.g., Thorncroft and Jones 2000). The stronger interaction promotes stronger enhancement of each PV anomaly by the other and, therefore, more rapid baroclinic development (Hoskins et al. 1985). Additionally, the presence of a recurving TC may enhance surface cyclone development ahead of an approaching upper-tropospheric trough by providing a source of lower-tropospheric cyclonic relative vorticity that subsequently can be enhanced through stretching (e.g., DiMego and Bosart 1982a,b; Bosart and Lackmann 1995). Furthermore, diabatically

---

[3] Jones et al. (2003) expanded the definition of the second stage of ET to include the scenario of further cyclone decay, and thus renamed the second stage the "extratropical stage".

enhanced downstream upper-tropospheric ridge amplification accompanying a recurving TC can enhance quasigeostrophic forcing for ascent over the recurving TC by enhancing differential cyclonic vorticity advection and attendant upper-tropospheric divergence.

Finally, a downstream jet streak induced by the recurving TC can promote extratropical reintensification (e.g., Sinclair 1993, 2004; Harr et al. 2000; Klein et al. 2002; Atallah et al. 2007). A strengthening meridional upper-tropospheric geopotential height gradient [alternatively manifested as a meridional upper-tropospheric PV gradient or potential temperature gradient on the dynamic tropopause (DT)] associated with downstream ridge amplification can produce a jet streak poleward and slightly downstream of the TC, thus placing the TC beneath the ascending branch of the jet entrance secondary circulation. Such a configuration can lead to mutual intensification of the jet streak and TC as long as the TC remains coupled with the jet streak.

iii. Influence of TC recurvature on the downstream extratropical flow pattern

A TC may modulate not only the nearby extratropical flow pattern as it recurves and undergoes ET, but the downstream extratropical flow pattern as well. For example, the lens of negative or low PV residing just below the tropopause associated with a TC may be deformed and advected downstream by the extratropical jet stream as a TC recurves. This process strengthens the upper-tropospheric meridional PV gradient associated with the extratropical jet stream (i.e., waveguide; e.g., Schwierz et al. 2004), resulting in a stronger and more zonally elongated jet stream.

The extratropical flow response to recurving WNP TC Jangmi (2008) provides an example of how a recurving TC may strengthen and zonally elongate the jet stream over the North Pacific. A study by Grams (2010) indicates that diabatic heating along the developing warm front of transitioning and recurving TC Jangmi generates upper-tropospheric outflow that strengthens and elongates the downstream jet stream. Using PV inversion (e.g., Davis and Emanuel 1991) to quantify the impact of the TC on the extratropical flow, Grams (2010) finds that if the TC is removed from the initial conditions of a model simulation, an upper-tropospheric trough develops instead of a zonal jet stream downstream of where the TC would be located. Thus, the upper-tropospheric outflow associated with TC Jangmi apparently acts to prevent upper-tropospheric trough formation downstream of the TC and leads to a strong, zonally elongated jet stream.

Another type of extratropical flow modification by a recurving TC is illustrated by the indirect disruption of the NH extratropical circulation caused by Hurricane Katrina (2005) (McTaggart-Cowan 2007b). Following the recurvature of Katrina, which undergoes ET but does not reintensify as an EC, the upper-tropospheric ridge associated with Katrina acts in conjunction with an extratropical upper-tropospheric trough to produce a corridor of upper-tropospheric southwesterlies over the U.S. The southwesterlies subsequently inject a pool of potentially warm air on the DT into the extratropics that persists for approximately two weeks and nearly circumnavigates the NH. The long-lived impact of Katrina on the NH flow pattern implies that individual episodes of recurving TCs can impact the extratropical circulation on intraseasonal time scales.

In addition to the aforementioned examples of how recurving TCs can modulate the extratropical flow, recurving TCs can perturb the extratropical jet stream/waveguide from its equatorward side such that a RWT is excited or amplified. RWTs occur frequently over the North Pacific in the cool season (e.g., Chang and Yu 1999; Hakim 2003) and are typically excited by DT disturbances or upper-tropospheric troughs originating from Asia that may perturb the WNP jet stream/waveguide from its poleward side (e.g., Orlanski 2005). The high baroclinicity over the WNP established by the warm Kuroshio Current and relatively frequent incursions of cool Asiatic air masses favors frequent cyclogenesis events that can amplify the wave trains (e.g., Hoskins and Valdes 1990; Orlanski 2005). The wave trains then may disperse downstream along the North Pacific jet stream/waveguide, and can be amplified by further cyclogenesis events. Rossby wave train amplification and dispersion is a known precursor to wintertime large-scale flow reconfigurations and attendant downstream high-impact weather events such as heavy precipitation events (e.g., Martius et al. 2008; Archambault et al. 2010). A caveat to considering RWT amplification and dispersion associated with recurving TCs is that the North Pacific baroclinicity and jet stream are considerably weaker in the summer and fall, when most episodes of TC recurvature occur, than in the winter.

Exploration of RWT amplification and dispersion specifically associated with recurving WNP TCs has been conducted via individual case studies. An eddy kinetic energy budget analysis by Harr and Dea (2009) of four recurving and transitioning WNP TCs during 15 July–30 September 2005 reveals that two of the four TC recurvature events are associated with pronounced RWT amplification and dispersion. Considerable variability in the Rossby wave response to the recurving WNP TCs is attributed mainly to differences in phasing between the TC and the extratropical flow. Harr and Dea (2009) further note that a transitioning TC may still induce RWT amplification and dispersion without undergoing reintensification as an EC.

The interaction of a recurving TC with the extratropical flow has been examined via idealized modeling. Riemer et al. (2008) use a full-physics model with an outer domain and a two-way nested inner domain to show that a recurving TC interacting with a straight, extratropical jet stream initiates an upper-tropospheric ridge–trough couplet and jet streak just downstream of the TC (Fig. 1.5a). Extratropical cyclogenesis then occurs in the left-exit region of this downstream jet streak (Fig. 1.5b), which initiates a new ridge–trough couplet downstream, and so on (Figs. 1.5c,d). This sequence of events is consistent with downstream baroclinic development (e.g., Orlanski and Sheldon 1995). In the latter stages of the simulation (Figs. 1.5c,d), cyclonic and anticyclonic wave breaking (CWB and AWB; e.g., McIntyre and Palmer 1983) develops as the upper-tropospheric flow downstream of the recurving TC increasingly deforms.

Numerous case studies of ET (e.g., Hoskins and Berrisford 1988; Bosart and Lackmann 1995; Klein et al. 2000; Colle 2003; Agustí-Panareda et al. 2004; McTaggart-Cowan et al. 2006; Atallah et al. 2007) suggest that along with warm-air advection, diabatic heating associated with heavy precipitation accompanying the transitioning TC can act to amplify a downstream ridge and intensify a jet streak. The idealized modeling studies by Riemer et al. (2008) and Riemer and Jones (2010) demonstrate that the diabatically driven divergent outflow of the TC is essential to initial ridge amplification and jet streak intensification during TC recurvature. As a TC recurves, its diabatically driven divergent outflow builds and "locks in" a downstream upper-tropospheric ridge and jet streak. This interaction induces a downstream ridge–trough pattern. Once the ridge–trough pattern develops, the rotational TC outflow acts with the divergent TC outflow to amplify the downstream ridge by advecting low PV air into the ridge. The diabatic contribution to ridge amplification during TC recurvature implied by the role of divergent outflow in inducing an upper-tropospheric ridge is analogous to the diabatic ridge amplification that can accompany explosively deepening oceanic extratropical cyclones featuring widespread convection in their warm sector [e.g., the 12–14 March 1993 "Superstorm" along the eastern U.S. coast, Bosart et al. (1996); Bosart (1999)].

The importance of diabatically driven outflow in RWT amplification accompanying TC recurvature as indicated in case studies and idealized modeling studies is corroborated by an analysis of ensemble forecast data for recurving WNP TCs Tokage (2004) and Nabi (2005) by Torn (2009). This study finds that downstream ridge amplification accompanying TC recurvature is highly sensitive to the amount of warm-frontal precipitation, lower-tropospheric moisture flux, and upper-tropospheric divergence associated with the TC. That the diabatically driven divergent outflow associated with a recurving TC promotes RWT amplification is also consistent with the concept of negative vorticity advection by the divergent wind as a wave source for low-frequency RWTs emanating from the subtropics (Sardeshmukh and Hoskins 1988). The apparent importance of diabatic heating in RWT amplification during TC recurvature is indicative of a predictability problem because model convective parameterization schemes are notoriously poor at capturing the bulk upscale effect of diabatic heating associated with convection (e.g., Dickinson et al. 1997; Bosart 1999; Langland et al. 2002; Zhang et al. 2003).

The sensitivity of the Rossby wave response to different environmental conditions and TC characteristics during TC recurvature has been tested in idealized model simulations (Riemer et al. 2008; Riemer and Jones 2010). Compared to TCs that recurve into a relatively weak jet stream, TCs that recurve into a relatively strong jet stream are found to be associated with longer-wavelength RWTs that are characterized by more distinct CWB and feature a faster eastward group velocity (Riemer et al. 2008). This finding is consistent with findings that RWT dispersion during recurving WNP TC episodes may be favored when North Pacific lower-tropospheric baroclinicity is relatively strong (e.g., Reynolds et al. 2009).

Riemer et al. (2008) also find that switching off the parameterizations representing moist processes in the outer domain of the simulation results in a lower-amplitude RWT than when the parameterizations representing moist processes are left on. Riemer et al. (2008) attribute the lower-amplitude RWT in the absence of parameterized moist processes in the extratropics to the weaker extratropical cyclogenesis that occurs downstream of the recurving TC in the absence of parameterized diabatic heating. Further, Riemer et al. (2008) find that the initialization of the model simulation with a weaker and somewhat smaller TC than in the original experiment produces a lower-amplitude RWT, which is apparently the result of smaller and weaker upper-tropospheric TC divergent outflow impinging upon the jet stream. Of note is that the wavelength and group velocity of the RWT associated with the recurving TC in the simulations of Riemer et al. (2008) are not affected by either parameterized moist processes in the extratropics or by the size and intensity of the recurving TC.

A modeling study of six cases of Atlantic TCs that undergo recurvature and ET (Davis et al. 2008) indicates that in the presence of strong vertical wind shear, larger TCs are associated with greater vertical mass flux, and by inference, more precipitation, upper-tropospheric divergence, and diabatic heating, than smaller TCs. Davis et al. (2008) hypothesize that larger TCs are more likely to stay coherent as they interact with the jet stream, which enables them to induce higher-amplitude ridges along the extratropical jet stream than smaller TCs with weaker divergent circulations.

In an idealized experiment by Riemer and Jones (2010) in which a TC recurves in the presence of a preexisting extratropical RWT, the evolution of the extratropical flow pattern downstream of the recurving TC is found to be sensitive to the location of the TC relative to the RWT. Specifically, whether the recurving TC acts to enhance or dampen a RWT is found to be highly sensitive to the position of the TC relative to the preexisting trough–ridge pattern along the jet stream (i.e., to the extent of phasing between the TC and trough–ridge pattern). In this study by Riemer et al. (2008), TC recurvature into the leading edge of the RWT is identified as the optimal scenario in which to produce a high-amplitude, long-lived perturbation to the downstream extratropical flow pattern.

iv. Predictability issues associated with TC recurvature

Predicting the behavior of recurving TCs and their downstream impact has long been considered problematic for both human forecasters and numerical models (e.g., Riehl and Shafer 1944; Burroughs and Brand 1973, their Table 1; Chan et al. 1980; Cheng-Lan and Sadler 1983; Dobos and Elsberry 1993; Holland and Wang 1995; Jones et al. 2003). Several studies have found that human and model forecasts of TC track are less skillful for TCs that undergo recurvature than for those that do not (e.g., Riehl and Shafer 1944; Burroughs and Brand 1973; Chan et al. 1980; Dobos and Elsberry 1993). Since the presence of a recurving and transitioning TC in the extratropics can modulate the evolution of the downstream extratropical flow pattern, poor forecasts of TC recurvature and ET may lead to significant reductions in both regional and hemispheric predictability

Due to the complex interaction between recurving TCs undergoing ET and the extratropical flow, it has been hypothesized that the intrinsic predictability of recurving TCs undergoing ET is lower than that of pure TCs or ECs (e.g., Jones et al. 2003). Results of a study by Evans et al. (2006) help support this hypothesis. In their study, they find that model forecasts of cyclone structure verifying during ET tend to be poor relative to forecasts verifying before or after ET. Consistent with the finding of Evans et al. (2006), a study by Torn and Hakim (2009) using an ensemble-based analysis of recurving WNP TCs Tokage (2004) and Nabi (2005) shows high sensitivity of ET to initial condition error associated with the phasing between a recurving TC and an upstream trough.

Episodes of TC recurvature may coincide with skill reductions in model forecasts of the extratropical flow pattern over an entire ocean domain. Jones et al. (2003) note that the skill of 48-h, 72-h, 96-h, and 120-h forecasts of midtropospheric geopotential height for the North Pacific is substantially reduced during three episodes of WNP TC recurvature and ET in August 1996 (Figs. 1.6a–d, respectively). They conclude that the reduced forecast skill is related to model failure to capture the phasing between the TCs and upstream extratropical disturbances. The forecast errors associated with phasing translate to large forecast errors in the TC tracks, which lead to large forecast errors in the placement of synoptic features downstream of the TCs.

Forecast uncertainty associated with a recurving and transitioning TC may grow and spread downstream within the extratropical jet stream. This process can be visualized using a time–longitude plot of the standard deviation of the ensemble member forecasts of a given variable, often 500-hPa geopotential height (Harr et al. 2008; Anwender et al. 2008). Figure 1.7 shows this type of display generated from the ECMWF EPS initialized just prior to the recurvature of TC Tokage in October 2004. The term "plume of uncertainty" is used to describe an increase in magnitude and extent of forecast standard deviation emanating from a point on a time–longitude plot. A plume of uncertainty originating from the time and position of the recurvature of TC Tokage (Fig. 1.7) is apparently reinforced at the time and position of the completion of the ET of TC Tokage. Therefore, Fig. 1.7 indicates that both the recurvature and completion of ET of TC Tokage are associated with increased forecast uncertainty. By examining similar time–longitude plume diagrams for several recurving and transitioning TC episodes, Anwender et al. (2008) determine that forecast uncertainty often increases downstream of recurving and transitioning TCs over the WNP and North Atlantic basins.

Using a combination of principal component analysis and fuzzy clustering (Harr and Elsberry 1995), the range and likelihood of extratropical flow evolution scenarios associated with a given recurving TC episode based on EPS output can be synthesized (Harr et al. 2008; Anwender et al. 2008). This statistical technique groups EPS ensemble members based upon their contribution to the overall ensemble variability. Using this technique, Anwender et al. (2008) determine that forecast uncertainty in the extratropical flow evolution associated with recurving and transitioning TCs generally can be described by uncertainty in the phase, tilt, and amplitude of the extratropical wave pattern.

A sensitivity study of ensemble forecasts for the recurvature and ET of WNP TC Tokage by Anwender et al. (2010) suggests that the uncertainty in the amplitude of the downstream ridge associated with TC recurvature may arise from the high sensitivity of the ridge amplification to lower-tropospheric latent heat release along the developing warm front of the transitioning TC. The study by Anwender et al. (2010), as well as a study by Reynolds et al. (2009), also indicates that small initial condition error associated with TC recurvature and ET may spread downstream and grow with the RWT excited by the TC recurvature. Thus, TC recurvature episodes that excite or amplify a RWT may have a detrimental impact on predictability far downstream.

As discussed in the literature review above, individual case studies (e.g., Harr and Dea 2009; Grams 2010) and idealized modeling studies (i.e., Riemer et al. 2008; Riemer and Jones 2010) have shown that recurving TCs are often accompanied by downstream ridge amplification and jet stream intensification induced by the upper-tropospheric diabatically driven outflow of the TC that may lead to RWT dispersion. However, an investigation of the characteristic downstream extratropical flow response to recurving TCs based on a large number of cases has not yet been performed. By employing a climatology and composite analysis to examine the extratropical flow response to recurving WNP TCs occurring over a 31-year period (1979–2009), this study will assess the synoptic–dynamic factors that modulate the observed downstream extratropical flow response to recurving WNP TCs.

An additional unique aspect of this work is that it will employ multiscale case studies to identify the key synoptic–dynamic processes (e.g., diabatically enhanced ridge amplification and jet streak intensification, CWB and AWB, and extratropical cyclogenesis) that link certain WNP TC recurvature episodes to high-impact weather events over North America. Furthermore, this work will complement previous statistical analyses of the predictability of recurving TCs (e.g., Harr et al. 2008; Anwender et al. 2008; Torn and Hakim 2009; Anwender et al. 2010) by combining conventional statistical assessments of predictability (e.g., EPS member spread) with analyses created from high-resolution gridded datasets in an examination of how synoptic–dynamic processes influence the predictability of the downstream extratropical flow response to recurving WNP TCs.

d. Figures

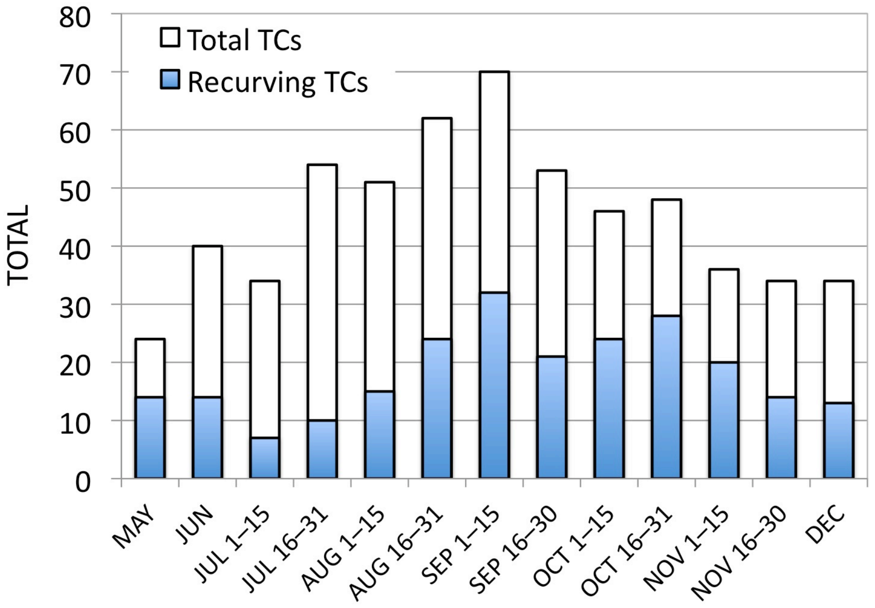

Fig. 1.1. A 1945–1969 climatology of the total WNP TCs and recurving WNP TCs [adapted from Table 2 of Burroughs and Brand (1973)]. TC recurvature is defined as a change in TC heading from generally westward to generally eastward.

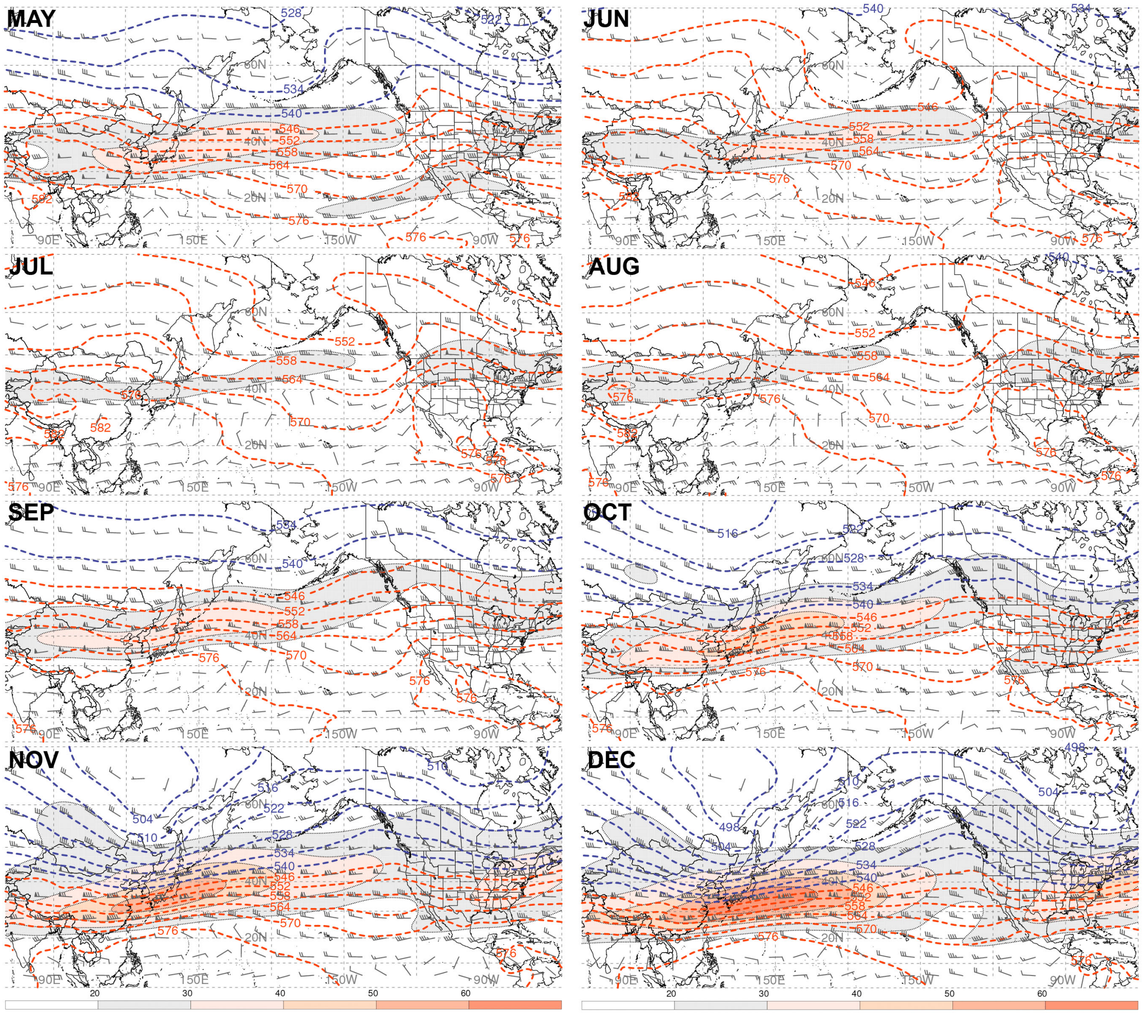

Fig. 1.2. The long-term (1979–2009) monthly mean 250-hPa wind speed (shaded in m s^{-1} according to the color bar), wind (barbs, kt) and 1000–500-hPa thickness (dashed, every 6 dam) over East Asia, the North Pacific, and North America for May–December.

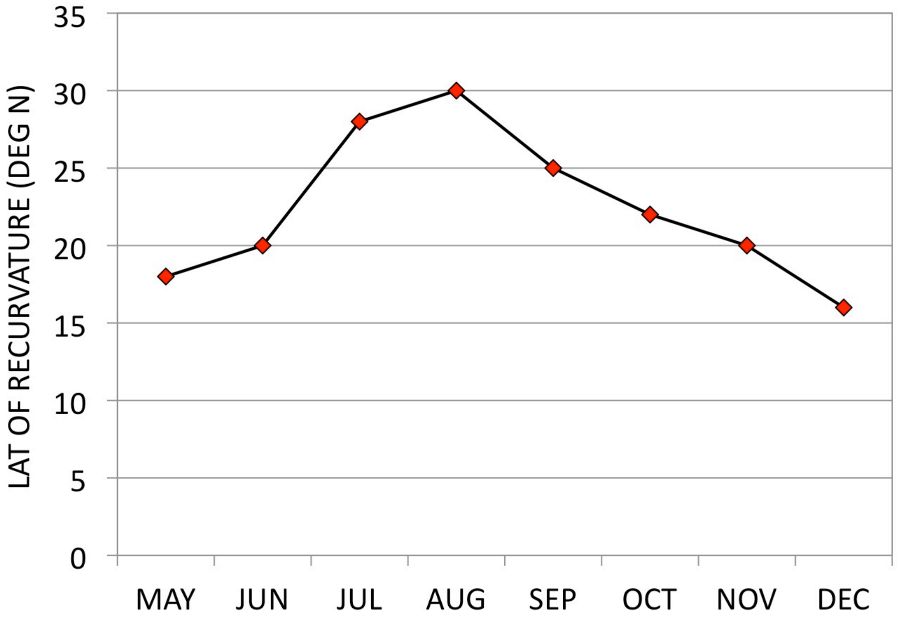

Fig. 1.3. A 1945–1969 climatology of the monthly mean latitude of WNP TC recurvature for May–December [adapted from Fig. 1a of Burroughs and Brand (1973)].

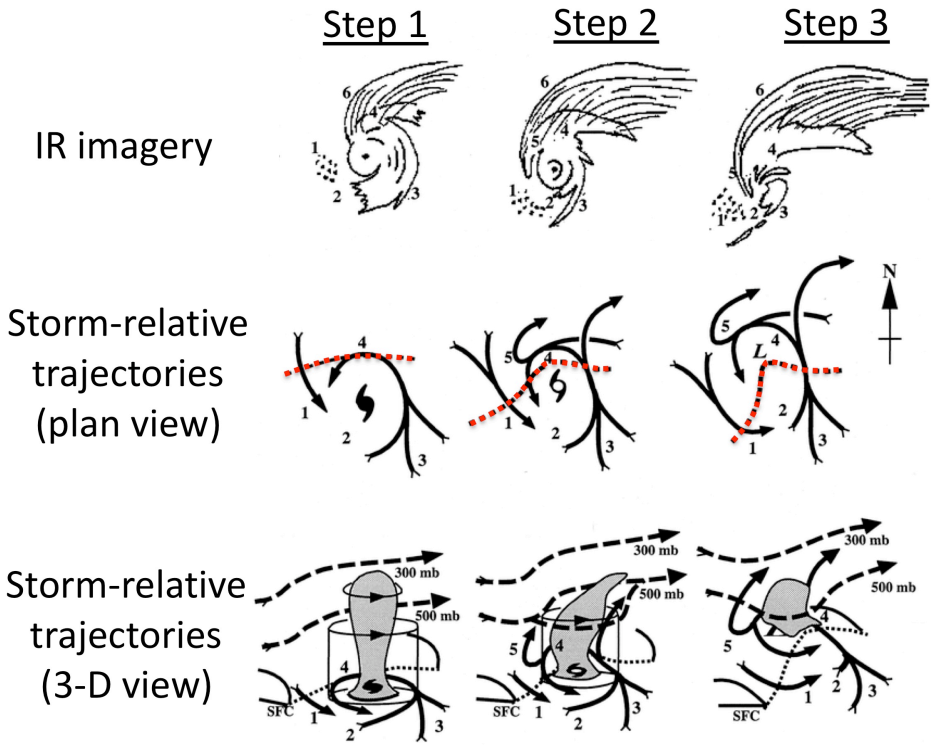

Fig. 1.4. Conceptual model of the transformation stage of ET. Dashed lines represent baroclinic zones, regions of gray shading denote the warm core of the cyclone, dashed arrows indicate polar jet streams, and solid arrows denote trajectories. The small numbers in each panel represent the following processes and features: (1) equatorward advection of cool, dry air; (2) decreased convection on the western side of the cyclone in step 1, which extends to the southern side of the cyclone in steps 2 and 3; (3) poleward advection of warm, moist air that maintains convection on the eastern side of the cyclone; (4) lower-tropospheric ascent of warm, moist air over the baroclinic zone; (5) midtropospheric ascent on the western side of the cyclone in steps 2 and 3; and (6) the cirrus shield. [Adapted from Fig. 5 of Klein et al (2000).]

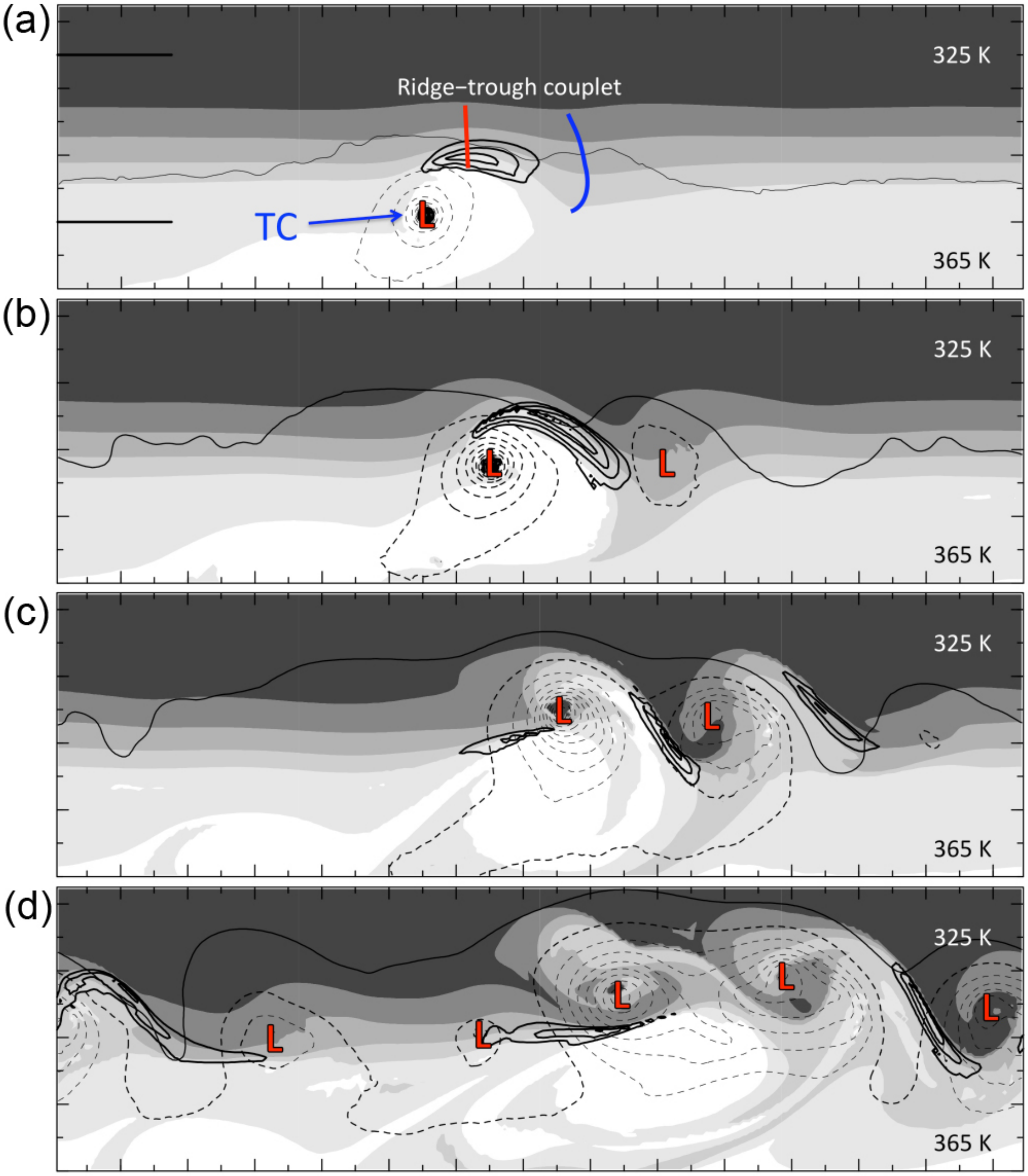

FIG. 1.5. A full-physics numerical model simulation showing the interaction of a recurving TC with an idealized straight jet at (a) 120 h, (b) 156 h, (c) 192 h, and (d) 240 h. Plots show the DT (i.e., 2-PVU surface) potential temperature (shaded every 10 K) and wind speed (thick contours; every 10 m s^{-1} starting at 45 m s^{-1}), and SLP (thin contours, every 5 hPa, values equal to or less than 995 hPa are dashed). The domain extends from 14°N to 65°N, with the jet stream axis at the start of the simulation located at 42°N. The outer model domain is 17 280 km by 8 460 km, and the two-way nested inner domain is 1 200 × 1 200 km. The distance between tick marks is 600 km. [Adapted from Fig. 2 of Riemer et al. (2008).]

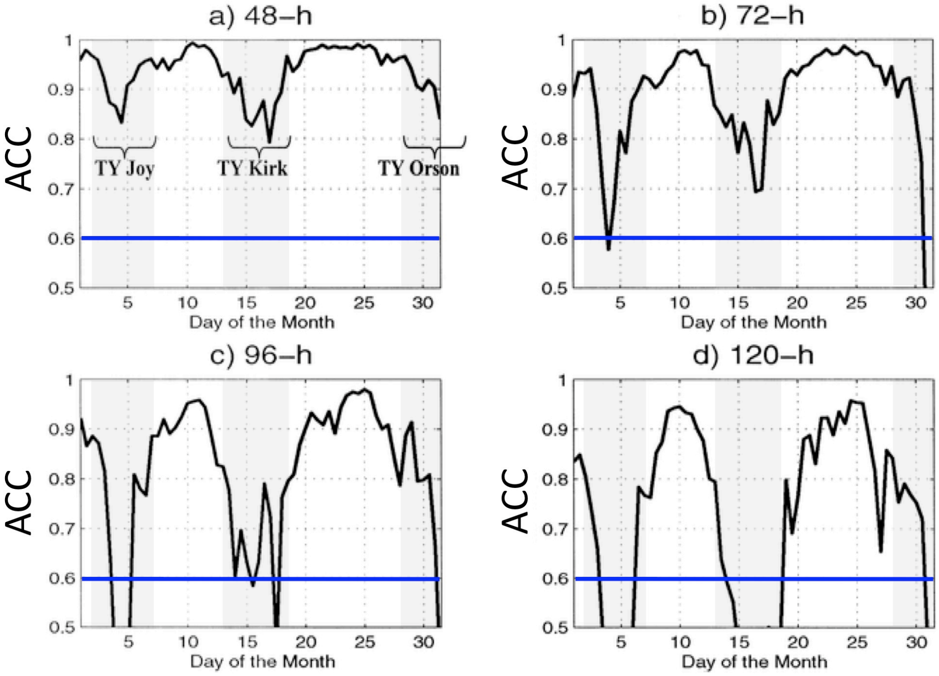

Fig. 1.6. NOGAPS anomaly correlation coefficient (ACC) time series for North Pacific 500-hPa geopotential height forecasts in August 1996. Panels (a) through (d) show 48-h, 72-h, 96-h, and 120-h forecast ACCs, respectively. Three periods of WNP TC recurvature and ET are denoted in (a). Horizontal blue lines delineate the ACC threshold (0.6) above which a forecast is considered skillful. [Adapted from Fig. 8 of Jones et al. (2003).]

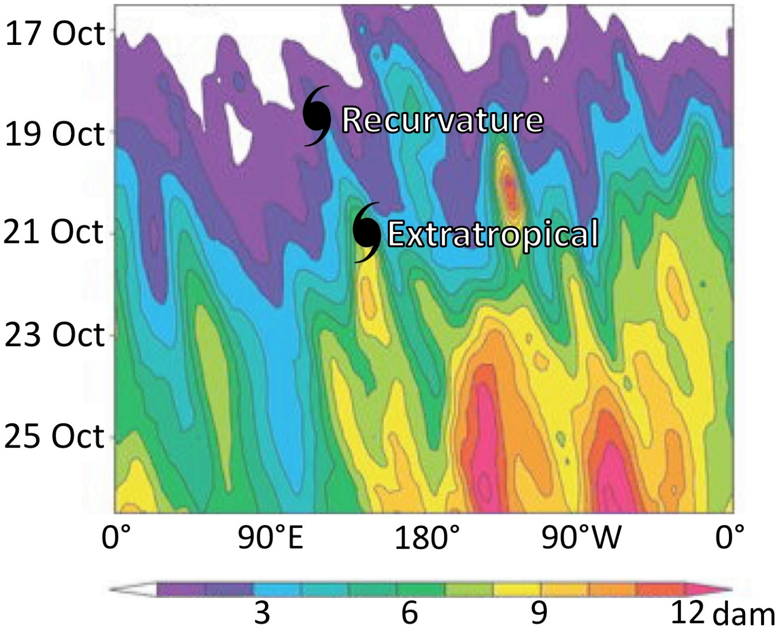

FIG. 1.7. Time–longitude plot showing the 40°–50°N averaged standard deviation of 500-hPa geopotential height forecasts (shaded every 10 m according to the color bar) from the 51-member ECMWF ensemble prediction system initialized at 1200 UTC 16 October 2004. The two typhoon symbols indicate where and when Tokage recurves and becomes extratropical, respectively. [Adapted from Fig. 6e of Anwender et al. (2008).]

2: Climatology of recurving WNP TCs

a. Motivation, purpose, and approach

As discussed in Chapter 1, current understanding of the downstream extratropical flow response to recurving and transitioning TCs is drawn from research conducted using individual case study and idealized modeling approaches. To date, a climatology of the downstream flow response to recurving TCs has not been performed. In this chapter, we present a 31-year (1979–2009) climatology that evaluates how characteristics of (i) the large-scale flow pattern, (ii) the TC itself, and (iii) the phasing of the TC with the extratropical flow influence the downstream flow response to recurving WNP TCs.

In this climatology, the downstream flow response to recurving WNP TCs is evaluated based on the North Pacific meridional flow pattern on the DT. To provide context for the climatology of the downstream flow response to recurving WNP TCs, we also present a comprehensive general climatology of WNP TC recurvature. Finally, we examine the predictability of the large-scale flow pattern during recurving WNP TCs episodes by performing a climatology of the skill of NCEP Global Forecast System (GFS) forecasts of the NH midtropospheric flow pattern verifying in the period surrounding recurving WNP TC episodes.

b. Data and methodology

i. Selection of recurving WNP TC cases

Recurving WNP TCs between 1979 and 2009 are identified using the best-track (post-processed) dataset compiled by the Regional Specialized Meteorological Center Tokyo-Typhoon Center, which is operated by the Japan Meteorological Agency (JMA) under the jurisdiction of the World Meteorological Organization. The JMA best-track dataset includes information on all tropical systems of at least tropical depression (TD) strength occurring within the area of JMA responsibility (the domain bounded by 0°–60°N and 100°E–180°, including the South China Sea) for 1951 through the present.

For a given tropical system, the JMA best-track dataset contains frequent (i.e., every 3 or 6 h) reports of central latitude and longitude, minimum sea level pressure (MSLP), 10-m above ground level (AGL) maximum sustained wind (MSW), storm category [i.e., TD, tropical storm (TS), typhoon (TY), or EC], and orientation and length of the maximum and minimum radii of 30-kt and 50-kt winds at 10 m AGL. Since in-situ observations of WNP TCs using aircraft reconnaissance are infrequently available after 1987 (e.g., Martin and Grey 1993), JMA best-track data are primarily constructed using the Dvorak current intensity technique (e.g., Dvorak 1975, 1984; Velden et al. 2006). This remote sensing technique provides an estimate of TC intensity based on cloud-pattern recognition applied to satellite imagery from which MSLP and MSW are then empirically derived.

An alternate record of WNP TC activity to the JMA best-track dataset is the best-track dataset managed by the Joint Typhoon Warning Center (JTWC). A major difference between the two datasets is that MSW is consistently higher in the JTWC dataset than in the JMA dataset. Nearly all of this difference can be attributed to different time averaging used by the two agencies to obtain MSW (10-min versus 1-min wind averages used by the JMA and JTWC, respectively). The MSW difference between the JTWC and JMA is also attributed to slightly different techniques for obtaining MSW from the Dvorak current intensity technique (e.g., Knapp and Kruk 2010). Despite consistent differences in MSW, neither best-track dataset has been established to be more accurate, and both have been used in TC studies.

The JMA dataset is preferred for this study because it contains detailed information on system characteristics (e.g., length of the maximum radius of 30-kt winds), and includes such information even for systems that have already completed ET (i.e., been designated as ECs), for the entire period of interest (1979–2009)[4]. This information is used to categorize TCs by various system characteristics in order to examine factors that influence the downstream flow response to recurving TCs. While some uncertainty and error are inherently present in the best-track data set, the JMA best-track data are assumed to be sufficiently reliable for the purposes of this study.

In this study, only 6-h (i.e., 0000, 0600, 1200, and 1800 UTC) JMA best-track data are used. TC recurvature is defined as a change in TC heading from westward to eastward while the TC moves poleward. A TC must be a TS (MSW of 33–63 kt) or a TY (MSW of at least 64 kt) at recurvature to be included in the study. The TC recurvature point is defined as the location of the TC at its most westward position. If a recurving TC is at its most westward position for consecutive 6-h intervals (i.e., the TC heading is due north for at least 6 hours), the earliest most westward position is designated as the recurvature point. If a TC undergoes multiple recurvatures, the TC recurvature point is designated as the most westward position of the TC during its last recurvature. For consistency with studies of WNP ET (e.g., Klein et al. 2000, 2002; Jones et al. 2003), TCs that dissipate before becoming extratropical (i.e., fail to complete the transformation

---

[4] The JTWC dataset contains detailed information on tropical system characteristics starting in 2000.

stage of ET) are not included in the study. Of the 801 WNP TCs occurring between 1979 and 2009, 292 are identified as recurving WNP TCs using the above criteria for case selection (36.5% of all WNP TCs).

The tracks and storm categories of the 292 recurving WNP TCs and the composite WNP TC track are shown in Fig. 2.1. This figure indicates that recurving WNP TCs undergo a characteristic life cycle: After genesis, they tend to track northwestward and strengthen to TYs before undergoing recurvature. Once they recurve and track northeastward, the TCs tend to weaken to TSs before becoming ECs. The spaghetti-like appearance of the tracks in Fig. 2.1 indicates that recurving WNP TCs may track nearly anywhere over the WNP basin, including poleward of 60°N (the northern boundary of the area of JMA responsibility). The monthly distribution of recurving WNP TCs displayed in Fig. 2.2 shows that WNP TC recurvature episodes occur mostly between May and December, and most often between August and October. The monthly distribution of recurving WNP TCs is similar to that of all WNP TCs, although the peak in recurving WNP TC activity in September lags the August peak in WNP TC activity. A more detailed presentation of the monthly climatology of recurving WNP TCs follows in section 2c(i).

Similar to Klein et al. (2000, 2002) a recurving WNP TC is considered to undergo reintensification as an EC if the JMA best-track dataset indicates that the system deepens (i.e., MSLP decreases) during any 6-h period following JMA designation of the system as an EC. Using these criteria, 124 out of 292 recurving WNP TCs (42.5%) are identified as undergoing reintensification as ECs.

ii. Climatology categories

To evaluate factors that influence the downstream flow response to recurving WNP TCs, climatologies are constructed and compared for WNP TC recurvature episodes stratified based on characteristics of (i) the large-scale flow pattern, (ii) the TC, and (iii) the phasing of the TC with the extratropical flow. Within the "large-scale flow pattern" category, sets of climatologies are constructed for TC recurvatures grouped by time of year and by recurvature latitude. As discussed in Chapter 1, the strength and latitudinal position of the North Pacific jet stream, which is strongly modulated by the time of year, tends to influence the latitude at which WNP TCs recurve. The relationships between the North Pacific jet stream, latitude of WNP TC recurvature, and time of year are illustrated by plots of TC recurvature points for May through December overlaid on corresponding plots of monthly mean 1000–500-hPa thickness and 250-hPa wind and wind speed computed from the 2.5° NCEP–NCAR reanalysis (Kalnay et al. 1996; Kistler et al. 2001) (Fig. 2.3). Inspection of Fig. 2.3 reveals that relative to July–October WNP TCs, WNP TCs in May, June, November, and December tend to recurve at lower latitudes in conjunction with stronger and equatorward-shifted North Pacific jet streams. Consistent with Fig. 2.3, monthly distributions of WNP TC recurvature episodes grouped by recurvature latitude (Fig. 2.4) show that lower-latitude recurvatures (i.e., equatorward of 25°N) are favored to occur in May, June, November, and December, whereas higher-latitude recurvatures (i.e., poleward of 25°N) are favored to occur in July–October. Based on the aforementioned findings that WNP TC recurvature occurs mainly between May and December (e.g., Fig. 2.2), monthly climatologies of the downstream flow response to recurving WNP TCs are constructed for May–December. Similarly, based on findings that most WNP TCs recurve between 15°N and 35°N (not shown) climatologies of the downstream flow response to recurving WNP TCs are constructed for WNP TCs recurving within 15°–20°N, 20°–25°N, 25°–30°N, and 30°–35°N bands.

For the "TC" category mentioned in the first paragraph of this section, sets of climatologies are constructed for recurving WNP TCs grouped by TC intensity and size at recurvature. Recurving WNP TCs are categorized as strong or weak TCs if they feature an MSLP within the bottom or top quintiles (N = 58), respectively, of all recurving WNP TCs. Table 2.1 indicates that MSLP at recurvature is characterized by almost a perfectly negative correlation with MSW at recurvature ($r = -0.97$). Thus, categorizing TC intensity based on MSLP is essentially equivalent to categorizing TC intensity based on MSW. On average, a TC in the "strong TC" category is a powerful TY with a ~928-hPa MSLP and ~95-kt MSW, whereas the average TC in the "weak TC" category is a minimal TS, featuring a ~994-hPa MSLP and ~41-kt MSW (Table 2.2).

Recurving WNP TCs are categorized as large or small TCs if they feature maximum 30-kt wind radii within the top or bottom quintiles, respectively, of all recurving WNP TCs. Table 2.1 indicates that the maximum 30-kt and 50-kt wind radii for TCs at recurvature are moderately positively correlated ($r = 0.77$). The maximum 30-kt wind radius is used to categorize TC size because the maximum 30-kt wind radius is not as dependent upon TC intensity as the maximum 50-kt wind radius (i.e., the correlation coefficients between the maximum 30-kt wind radius and MSLP and MSW are smaller in magnitude than the correlation coefficients between the maximum 50-kt wind radius and MSLP and MSW; Table 2.1). Table 2.3 shows that an average TC in the "large TC" category features maximum 30-kt and 50-kt wind radii of ~310 nm and 140 nm, respectively. In contrast, an average TC in the “small TC” category features a maximum 30-kt wind radius of only ~110 nm, and no 50-kt winds.

For the “phasing of the TC with the extratropical flow” category, sets of climatologies are constructed for recurving WNP TCs grouped by whether a recurving TC subsequently reintensifies as an EC, and by the strength of the TC–jet stream interaction during TC recurvature. A description of how the strength of the TC–jet stream interaction is computed and used to categorize recurving WNP TCs is found in section 2b(iv).

iii. Evaluation of the downstream flow response to recurving WNP TCs

The downstream flow response to WNP TC recurvature episodes in terms of the waviness of the downstream large-scale flow pattern, which may be indicative of Rossby wave activity, is objectively evaluated using a North Pacific meridional flow index. This index is computed by averaging the absolute value of the meridional wind on the DT (1.5-PVU surface) over 25°–55°N, 140°E–120°W (Fig. 2.5) at 6-h intervals from the 2.5° NCEP–NCAR reanalysis. The North Pacific meridional flow index is found to be insensitive to whether the DT or an upper-tropospheric isobaric surface is used in its computation[5].

To examine whether the North Pacific flow is significantly more or less meridional during recurving WNP TC episodes relative to climatology, the statistical significance of

---

[5] The North Pacific meridional flow index time series computed using 250-hPa meridional wind is found to be strongly correlated with the North Pacific meridional flow index time series computed using DT meridional wind ($r^2 = 95.9$).

North Pacific meridional flow index anomalies surrounding WNP TC recurvature is evaluated using a two-sided Student's *t* test (e.g., Wilks 2006, see section 5.2.1). Table 2.4 shows the climatology used to compute the statistical significance of the North Pacific meridional flow index anomalies for recurving WNP TCs categorized by month. Based on the monthly means shown in Table 2.4, the North Pacific DT flow pattern tends to be more meridional in October–May than in June–September. The monthly standard deviations displayed in Table 2.4 reveal greater variability in the meridional the nature of the North Pacific DT flow pattern tends to be during October–May vs. June–September.

Table 2.5 shows monthly weighted climatologies used to compute the statistical significance of the North Pacific meridional flow index anomalies surrounding WNP TC recurvature for the categories described in section 2b(iii). The monthly weighted climatologies in Table 2.5 are constructed from monthly means and standard deviations (Table 2.4) that are weighted according to the monthly distribution of recurving WNP TCs.

iv. Evaluation of TC–jet stream interaction

As discussed in Chapter 1, section 2c(iii), the impingement of divergent TC outflow upon the jet stream is a critical part of the interaction that takes place between a recurving TC and the jet stream. A schematic of this process (Fig. 2.6) illustrates that negative PV advection by the upper-tropospheric irrotational wind associated with the TC can result in upper-tropospheric ridge amplification and jet streak intensification along a meridional PV gradient (i.e., waveguide/jet stream). With this conceptual picture in mind, negative

PV advection by the upper-tropospheric irrotational wind associated with the TC is used to diagnose the strength of the interaction between recurving TCs and the jet stream.

The TC–jet stream interaction metric is computed as follows: First, the grid point and time of the maximum 250–150-hPa layer-averaged negative PV advection by the irrotational wind for the period surrounding TC recurvature (i.e., T−48 h through T+144 h at 6-h intervals) are identified based upon computations using the 2.5° NCEP–NCAR reanalysis dataset. Geostationary full-disk infrared satellite imagery obtained from the NOAA National Climatic Data Center (NCDC)/Global ISCCP B1 Browse System (GIBBS; http://www.ncdc.noaa.gov/gibbs/) is used to confirm that the identified maximum negative PV advection by the irrotational wind (i.e., the maximum TC–jet stream interaction) is in proximity to the TC cirrus shield, and thus is likely to be directly associated with the TC outflow. As an example, maximum TC–jet stream interaction time for recurving WNP TC Oscar (1995) is shown in Fig. 2.7. Note that the maximum TC–jet stream interaction point is found just poleward of the cirrus shield that extends poleward and eastward of the TC. This configuration of the maximum TC–jet stream interaction point relative to the TC cirrus shield is found to be characteristic of recurving WNP TCs (not shown). For 20 of the 292 recurving TCs, a time and point corresponding to a maximum TC–jet stream interaction cannot be identified (i.e., the negative PV advection by the irrotational wind associated with the recurving TC never exceeds an arbitrarily established threshold of 1×10^{-5} PVU s^{-1}). Accordingly, these 20 cases are designated as null cases (Table 2.6).

Next, a spatial average of 250–150-hPa layer-averaged PV advection by the irrotational wind is computed. The averaging is performed for a 15° × 15° domain centered on the point of the maximum TC–jet stream interaction. The domain used to compute the TC–jet stream interaction metric for recurving WNP TC Oscar is shown in Fig. 2.7.

Finally, a temporal average of domain-averaged 250–150-hPa layer-averaged PV advection by the irrotational wind is computed. The averaging is performed for the 48-h period centered on the time of the maximum TC–jet stream interaction. The outcome of these steps is that a single, negative value representing the strength of the TC–jet stream interaction (the TC–jet stream interaction metric, expressed in PVU day^{-1}) is obtained for each non-null recurving TC. This TC–jet stream interaction metric is weakly correlated with TC intensity and TC size at recurvature (Table 2.1).

Ordering the TC–jet stream interaction metric by largest to smallest magnitude gives a ranking of the strength of the TC–jet stream interaction for each recurving TC. Recurving TCs with a TC–jet stream interaction metric in the top or bottom quintile (based on magnitude) are categorized as strong or weak TC–jet stream interaction cases, respectively (Tables 2.7 and 2.8, respectively). Of note is that of 292 recurving WNP TCs, Oscar (1995) features the second strongest TC–jet stream interaction (Table 2.7).

v. Evaluation of NH model forecast skill

To evaluate NH model forecast skill surrounding WNP TC recurvature episodes, ACCs (e.g., Wilks 2006, see section 7.6.4) of GFS NH 500-hPa geopotential height forecasts at 24-h intervals are used. The ACCs were obtained from Yuejian Zhu at the NCEP Environmental Modeling Center. They are averaged over 20°–80°N and for wavenumbers 1–20, and are provided for 24-h–120-h forecasts for 1 January 1996–20

June 2006, and for 144-h and 168-h forecasts for 1 January 2000–20 June 2006. During these two periods, 105 and 69 episodes of WNP TC recurvature, respectively, are found to occur.

Time series of daily composite ACCs are constructed for all available forecast lead times (24-h–168 h) for WNP TC recurvatures occurring during the two ACC periods of record identified in the previous paragraph. The composite ACCs are compared with monthly weighted ACC climatologies to identify composite ACC anomalies. Tables 2.9–2.15 show the monthly climatologies of the 24-h–168-h ACCs used to compute the monthly-weighted ACC climatologies. Statistical significance of the composite ACC anomalies is evaluated using a two-sided Student's *t* test. In addition to time series of composite ACCs for all recurving WNP TCs, time series of composite ACCs are constructed for recurving WNP TC episodes grouped by month and by TC–jet stream interaction strength.

To illustrate the seasonal variation of GFS 500-hPa geopotential height forecast skill, the monthly mean and standard deviation of the ACCs at all forecast lead times shown in Tables 2.9–2.15 are displayed in graphical form in Figs. 2.8 and 2.9, respectively. Inspection of Fig. 2.8 reveals a clear seasonal signal in the GFS 500-hPa geopotential height forecast skill, with lower mean ACCs in June–September than for other months for all forecast lead times. A seasonal signal is also apparent in the monthly variability of GFS 500-hPa geopotential height forecast skill shown in Fig. 2.9: greater variability in ACCs is seen in June–September compared to other months, particularly for the 24-h–96-h forecast lead times. The lower mean and greater variability of ACCs in June–September relative to other months suggest that the prevalence of NH convection and TC activity during June–September may negatively impact GFS skill overall, as well as lead to occasional periods of reduced GFS skill manifested as dips in the ACC (colloquially termed model forecast “drop outs”).

c. Results

i. General climatology of recurving WNP TCs

A summary of various characteristics of WNP TCs at recurvature is provided in Table 2.16. This table shows that the mean and median points of WNP TC recurvature are 24.9°N, 134.0°E and 24.8°N, 131.4°E, respectively, which imply that recurvature is favored to occur just south of Japan (Fig. 2.1). However, as indicated by Fig. 2.1, TC recurvature occurs over a broad area of the WNP. Specifically, WNP TC recurvature has been noted to occur as far south and north as 9.5°N and 42.3°N, respectively, and as far west and east as 109.8°E and 169.8°E, respectively (Table 2.16).

Typically, a WNP TC is a weak TY at recurvature, with a mean MSLP and MSW of 964.0 hPa and 67.9 kt, respectively (Table 2.16). The median TC intensity at recurvature is similar: the median MSLP and MSW at recurvature are 965.0 hPa and 70.0 kt, respectively. The intensity of a WNP TC at recurvature may range from minimal TS strength[6], with an MSLP and MSW of 1004 hPa and 35 kt, respectively (Forrest 1980), to supertyphoon (STY) strength[7], with an MSLP and MSW of 890 hPa and 120 kt, respectively (Flo 1990).

---

[6] Recall that a TC must be at least TS strength at recurvature to be included in the climatology.

[7] A STY is defined by the JMA as a TC with a MSW of at least 100 kt.

The mean lengths of the maximum 30-kt and 50-kt wind radii of a WNP TC at recurvature are 194.2 nm and 63.8 nm, respectively (Table 2.16). The median size of a WNP TC at recurvature is slightly smaller than the mean: the median lengths of the maximum 30-kt and 50-kt wind radii are 180.0 nm and 60.0 nm, respectively. The size of WNP TCs at recurvature can vary dramatically. The largest TCs at recurvature in terms of maximum 30-kt and 50-kt wind radii, respectively, are Keith (1997) and Holly (1984), which feature a 600-nm maximum 30-kt wind radius and a 200-nm maximum 50-kt wind radius, respectively. In contrast, the smallest TC at recurvature in terms of maximum 30-kt and 50-kt wind radii is Vipa (2001), which exhibits a maximum 30-kt wind radius of 40 nm and contains no 50-kt winds.

As presented in section 2b(i), 292 of the 801 identified WNP TCs are found to undergo recurvature (36.5%). Based on the 292 total recurving WNP TCs in 31 years, ~9.4 WNP TCs are found to undergo recurvature in an average year. Annual totals of recurving WNP TCs (Fig. 2.10a), however, fluctuate considerably, ranging from four in 1983 and 1998 to 15 in 2004. The correlation between the annual totals of all WNP TCs and recurving WNP TCs is relatively small: just 21% of the variance in the annual total of recurving WNP TCs is accounted for by the variance in the annual total of all WNP TCs (Fig. 2.10a). This relatively small correlation is consistent with previous studies (e.g., Harr and Elsberry 1991; Camargo et al. 2007) that indicate that the WNP large-scale flow pattern is more conducive to TC recurvature in some years than in others.

A comparison also can be made between the interannual variability of the number of recurving WNP TCs that reintensify as ECs and that of all recurving WNP TCs (Fig. 2.10b). As mentioned in section 2b(i), of the 292 recurving WNP TCs identified between

1979 and 2009, 124 reintensify as ECs (42.5%). That 124 recurving WNP TCs are found to reintensify as ECs in a 31-year period indicates that four recurving WNP TCs reintensify as ECs in an average year. However, considerable variability in the annual totals of WNP TCs that reintensify as ECs is noted (Fig. 2.10b): In both 1998 and 2008, only one recurving WNP TC is found to reintensify as an EC, whereas, in 1994, eight recurving WNP TCs are noted to reintensify as ECs. The annual totals of recurving WNP TCs and those that reintensify as ECs are better correlated than the two time series compared in the previous paragraph: 39% of the variance in the annual number of recurving WNP TCs that reintensify as ECs is accounted for by the variance in the annual total of recurving WNP TCs.

The extent to which recurving WNP TC activity is modulated by the seasonal cycle is considered in Fig. 2.11. The finding that WNP TC recurvature is most common in August–October is consistent with previous climatologies of WNP TC recurvature (e.g., Jones et al. 2003). August–October is also found to be the preferred time of year for the reintensification of recurving WNP TCs as ECs. September features more recurving WNP TCs and more recurving WNP TCs that reintensify as ECs than any other month. Furthermore, September features a higher percentage of WNP TCs that recurve (53%; Fig. 2.2) and higher percentage that reintensify as ECs after recurvature (54%; Fig. 2.11) than any other month during the typical recurving WNP TC season (i.e., May–December). The aforementioned results suggest that relative to other months, September may feature a higher frequency of midlatitude upper-tropospheric trough passages over the WNP, which would favor both the recurvature of WNP TCs and their subsequent reintensification as ECs.

The period from mid-winter through early spring (January–April) is found to be the most unfavorable time of year for recurving WNP TCs (Fig. 2.11). In general, November–July[8] marks the period with the lowest percentage of recurving WNP TCs that reintensify as ECs (Fig. 2.11). This finding suggests that favorable phasing between WNP TCs that have completed ET and the extratropical flow pattern is less likely to occur in November–July than during the rest of the year.

The seasonal cycle is found to modulate the tracks and recurvature points of recurving WNP TCs, as well as their overall frequency and frequency of reintensification as ECs. Examination of individual and composite recurving WNP TC tracks for May–December (Fig. 2.12) reveals that TCs tend to recurve more sharply in October–May (Figs. 2.12a,f–h) than in June–September (Figs. 2.12b–e). Inspection of WNP TC recurvature latitude by time of year (Fig. 2.13a) reveals that the most poleward WNP TC recurvatures are typically in August when the North Pacific jet stream is relatively weak and displaced poleward relative to its climatological position (Fig. 2.3). Conversely, the most equatorward WNP TC recurvatures typically occur in May and December (Fig. 2.13a) when the North Pacific jet stream is relatively strong and displaced equatorward relative to its climatological position (e.g., Fig. 2.3). However, the seasonal cycle in the position and strength of the WNP jet stream does not entirely explain the observed time-of-year variation in WNP TC recurvature latitude. For example, note that WNP TC recurvature tends to be more poleward in November than in May (e.g., compare Figs. 2.12a and 2.12g; Fig. 2.13a) despite the tendency for stronger and more equatorward

---

[8] The high percentage (67%) of recurving WNP TCs that reintensify as ECs in January likely is an artifact of a small sample size.

displaced upper-tropospheric westerlies in November than in May (Fig. 2.3). The seasonal cycle is not found to have as substantial an influence on the longitude of WNP TC recurvature as on the latitude of WNP TC recurvature (compare Figs. 2.13b and 2.13a). However, the results shown in Fig. 2.13b suggest that WNP TCs may tend to recurve slightly farther west in May–July than in August–December.

Of interest is how the seasonal variability of WNP TC recurvature points relates to the seasonal variability of the WNP large-scale flow pattern beyond the previously discussed position and strength of the WNP jet stream. Specifically, relationships between monthly WNP TC recurvature points and the monthly mean WNP 1000–500-hPa thickness pattern and 250-hPa jet stream structure (e.g., the curvature and entrance region of the jet stream) are discussed using plots shown in Fig. 2.3.

In May and June, TC recurvature tends to occur equatorward of the base of a weak, positively tilted thickness trough near the coast of eastern Asia. This time-mean positively tilted thickness trough may reflect a tendency for PV streamers to form near the eastern Asian coast in association with AWB. In May, TC recurvature points are generally east of the equatorward entrance region of the jet stream, whereas, in June, they appear to be better collocated with the equatorward entrance region of the jet stream, which has shifted eastward to south of Japan. Slight cyclonic curvature to the jet stream is evident poleward of the TC recurvature points in May, whereas the jet stream poleward of TC recurvature points in June is straighter. The WNP meridional thickness gradient and jet stream are slightly weaker in June than in May.

WNP TCs in July tend to recurve upstream of the base of a very weak, positively tilted thickness trough, which, as in May and June, may reflect individual episodes of PV streamer formation associated with AWB. The jet stream and meridional thickness gradient are very weak, and the jet stream exhibits slight cyclonic curvature. In August, WNP TCs are seen to recurve just downshear of a very weak thickness trough over northeastern China and just upshear of a weak thickness ridge over Japan. The jet stream is slightly stronger in August than in July, and features slight anticyclonic curvature in proximity to the TC recurvature points. July and August are marked by the absence of a well-defined jet entrance region in proximity to the TC recurvature points.

In September, WNP TCs tend to recurve east of the base of a slightly positively tilted thickness trough into a low-amplitude trough–ridge thickness pattern extending from northeastern China to just east of Japan. The recurvature points are collocated with an inferred equatorward entrance region of the jet stream, which is anticyclonically curved. The September jet stream and meridional thickness gradient are stronger than in June–August and are of comparable strength to the May jet stream and meridional thickness gradient. The tendency for September TC recurvature points to be downshear of a time-mean thickness trough and collocated with a time-mean equatorward jet entrance region suggests that the large-scale flow pattern over the WNP is more favorable for the phasing of recurving TCs with the extratropical flow in September relative to earlier in the season.

The mean large-scale flow pattern in proximity to TC recurvatures in October is similar to that in September, except that the jet stream and meridional thickness gradient are stronger, and the thickness trough appears to be shifted slightly eastward relative to the TC recurvature points. In addition, the jet stream is not as anticyclonically curved as in September.

In November and December, the jet stream and meridional thickness gradient are substantially stronger over the WNP than in May–October, and the orientation of the jet stream is relatively zonal compared to September and October. Similar to May, TC recurvature points in November and December are generally eastward of the equatorward entrance region of the jet stream. TC recurvature points in November and December tend to be located just east of the base of a slightly positively tilted thickness trough along the eastern Asian coast. This trough is embedded within more cyclonically sheared flow and is considerably broader and less positively tilted than the previously discussed time-mean trough in May and June. The broader, less positively tilted thickness trough in November and December compared to May and June indicates that WNP PV streamers may occur less frequently in November and December than in May and June. A lower frequency of PV streamers in November relative to May may help to explain the previously mentioned finding that WNP TCs tend to recurve at lower latitudes in May than in November (e.g., Fig. 2.13a) despite weaker and more poleward upper-tropospheric westerlies in May than in November (Fig. 2.3). Since PV streamers can extend well equatorward of the time-mean jet stream, the presence of WNP PV streamers favors earlier and more equatorward TC recurvatures than would otherwise occur in the absence of WNP PV streamers.

We now address the influence of time of year on WNP TC characteristics at recurvature. Results suggest that recurving WNP TCs tend to be more intense in September–November than during other months between May and December (Fig. 2.14). Recurving TCs in September–November are found to have a mean MSLP and MSW of 958.7 hPa and 72.1 kt, respectively, whereas recurving TC in June–August have a mean MSLP and MSW of 971.1 hPa and 62.0 kt. The differences in both the mean MSLP and

MSW for recurving TCs in September–November vs. June–August are statistically significant at the 99.9% confidence level[9].

The size of WNP TCs at recurvature, as measured by the length of the maximum radii of 30-kt and 50-kt winds (Figs. 2.15a and 2.15b, respectively), is found to be modulated by time of year in a similar way to intensity: recurving TCs tend to be larger in September–November than during other months between May and December. Recurving TCs in September–November are found to have mean maximum 30-kt and 50-kt wind radii of 218.4 nm and 75.8 nm, respectively, whereas the mean maximum 30-kt and 50-kt wind radii for recurving TCs in June–August are 165.1 nm and 48.2 nm, respectively. These differences between means of the maximum 30-kt and 50-kt wind radii for recurving TCs in September–November vs. June–August are significant at the 99.9% confidence level.

ii. Climatology of the downstream flow response to recurving WNP TCs

As discussed in section 2b(iii), of interest is the extent that the downstream meridional flow pattern over the North Pacific is influenced by WNP TC recurvature episodes. Figure 2.16 reveals that composite mean North Pacific meridional flow index associated with recurving WNP TCs is significantly above normal at the 99% confidence level from T+12 h (12 h after recurvature) through T+108 h, and is significantly above normal at the 95% confidence level at T+114 h. The median and 25th and 75 percentile values of the North Pacific meridional flow index are all elevated during approximately

---

[9] Here and throughout, statistical significance refers to significance determined by a two-sided Student's *t* test.

the same periods. Figure 2.16 thus indicates that the North Pacific flow pattern tends to be more meridional than normal for approximately a four-day period following WNP TC recurvature. To the extent that meridional flow on the DT corresponds to Rossby wave activity, Fig. 2.16 further suggests that, in a climatological sense, WNP TC recurvatures episodes tend to be associated with Rossby wave activity over the North Pacific.

As previously discussed in section 2b(ii), to evaluate factors influencing the downstream flow response to recurving WNP TCs, climatologies are constructed and compared for WNP TC recurvature episodes grouped by characteristics of the large-scale flow pattern, the TC, and the phasing of the TC with the extratropical flow. For the "large-scale flow pattern" category, we consider the downstream flow response to WNP TC recurvatures in terms of the composite North Pacific meridional flow index as a function of TC recurvature month and TC recurvature latitude.

Time series of North Pacific meridional flow index anomaly associated with recurving WNP TC grouped by month (Fig. 2.17) demonstrate that in each month, TC recurvatures are linked to increases in the North Pacific meridional flow index between ~T−24 h and ~T+72 h surrounding TC recurvature. However, the peak in positive North Pacific meridional flow index anomalies following TC recurvature tends to be higher in May and October–December than in June–September, which suggests the possibility of enhanced Rossby wave activity following TC recurvatures in May and October–December compared to June–September. The possibility of enhanced Rossby wave activity following TC recurvatures in May and October–December compared to June–September may be explained by the tendency for a stronger North Pacific Rossby waveguide, manifested as higher baroclinicity and a stronger jet stream, in May and October–December than in June–September (e.g., Fig. 2.3).

Figure 2.17 also indicates that a dip in the North Pacific meridional flow index lasting ~72 h tends to precede WNP TCs that recurve in May, and, to a lesser extent, TCs that recurve in October and November. In addition, WNP TCs that recurve in November and December tend to feature a decrease in the North Pacific meridional flow index to well below-normal levels between ~T+120 h and T+168 h. At issue is whether the recurving TCs play a role in the reduced meridional flow, and why the reduced meridional flow prior to or well after recurvature is only seen in certain months.

We now consider whether WNP TC recurvatures in particular months tend to be associated with anomalous North Pacific meridional flow relative to climatology. Figure 2.18 indicates that the North Pacific meridional flow tends reach significantly above-normal levels for at least a 36-h period following WNP TC recurvatures in six of eight months: May, and July–November. In contrast, no significant anomalies in the North Pacific meridional flow are found to occur in conjunction with TC recurvatures in June or December (with the exception of an above-normal North Pacific meridional flow index at T+36 h in December). Of all the months, August and September feature the most prolonged period (~96 h) of significantly above-normal North Pacific meridional flow following TC recurvature. The onset of significantly above-normal North Pacific meridional flow tends to occur substantially earlier in August–November than in May and July (at ~T+18 vs. T+60 h). The month-to-month differences in the significance, duration, and timing of above-normal North Pacific meridional flow following WNP TC recurvature shown in Figs. 2.17 and 2.18 imply that the typical Rossby wave response to

TC recurvatures may vary substantially by month. This hypothesis will be investigated via composite analysis in Chapter 3.

While the noteworthy finding shown in Fig. 2.18 is that significantly above-normal North Pacific meridional flow following TC recurvatures occurs preferentially in certain months, it is also of note that recurving WNP TCs in certain months tend to be associated with significantly below-normal North Pacific meridional flow. Figure 2.18 indicates significantly below-normal North Pacific meridional flow during T−60 h–T+0 h for May TC recurvatures and during T−30 h–T−24 h for August TC recurvatures. It is speculated that a connection could exist between this significantly below-normal North Pacific meridional flow and the formation of a zonally elongated, relatively straight North Pacific jet stream associated with outflow from the recurving TC. Composite analysis presented in Chapter 3 will be employed to substantiate or refute this speculation. In addition, significantly below-normal North Pacific meridional flow is noted between T+132 and T+192 h during TC recurvature episodes in November, but since this period is more than five days after TC recurvature, a connection to the recurving TC seems less likely.

We now investigate the influence of WNP TC recurvature latitude on the North Pacific meridional flow pattern in the same manner that the influence of WNP TC recurvature month on the North Pacific meridional flow pattern was investigated earlier in this section. Time series of the composite North Pacific meridional flow index anomaly associated with recurving WNP TCs stratified by recurvature latitude are shown in Fig. 2.19, and the statistical significance of these anomalies relative to climatology is presented in Fig. 2.20.

Figure 2.19 shows that WNP TCs recurving within 15°–20°N, 20°–25°N, 25°–30°N, and 30°–35°N latitude bands are all associated with positive composite North Pacific meridional flow index anomalies following TC recurvature. Relative to the other latitude bands, the 20°–25°N latitude band features the largest and the longest-lasting positive North Pacific meridional flow index anomalies following TC recurvature.

A check of Fig. 2.20 reveals that the positive composite North Pacific meridional flow index anomalies following WNP TC recurvature for each of the four latitude bands are statistically significant. The duration of significant positive North Pacific meridional flow index anomalies following TC recurvature within 15°–20°N, 25°–30°N, and 30°–35°N latitude bands is similar (~60 h). In contrast, the significant positive North Pacific meridional flow index anomalies associated with TC recurvature within the 20°–25°N latitude band persist ~48 h longer (108 h) than for the other bands. TCs that recurve in the 15°–20°N band are associated with positive North Pacific meridional flow index anomalies that are mainly significant at the 95% confidence level, whereas TCs that recurve in the other three latitude bands are associated with positive North Pacific meridional flow index anomalies that are significant at the 99% confidence level. This finding suggests that TCs that recurve in the 15°–20°N latitude band may be associated with a less robust impact on the downstream meridional flow pattern than TCs that recurve within the other, higher latitude bands.

As shown in Fig. 2.4, the 15°–20°N recurving TC group contains mainly May and October–December TC recurvature episodes. Of the 15°–20°N, 20°–25°N, 25°–30°N, and 30°–35°N latitude bands, the 15°–20°N recurvature band features the fewest combined August and September TC recurvature episodes (Fig. 2.4), which are associated with long-lasting, significantly above-normal North Pacific meridional flow following TC recurvature (Fig. 2.18). The 15°–20°N recurvature band also features the most December recurving TC episodes (Fig. 2.4), which are associated with minimal significantly above-normal North Pacific meridional flow following recurvature (Fig. 2.18).

The influence of TC characteristics at recurvature on the North Pacific meridional flow pattern is considered by examining the statistical significance of the composite North Pacific meridional flow index anomaly relative to climatology surrounding the recurvature of strong and weak TCs, and large and small TCs (Fig. 2.21). Figure 2.21 shows that strong and weak recurving WNP TCs, as well as large and small recurving WNP TCs, are associated with significant positive anomalies of the North Pacific meridional flow index that persist at least 72 h. Significant positive North Pacific meridional flow index anomalies develop 24 h later after large TCs recurve compared to after small TCs recurve, at T+30 h and T+6 h, respectively.

Finally, the influence of phasing of a recurving WNP TC with the extratropical flow on the North Pacific meridional flow pattern is considered by examining the statistical significance of the composite North Pacific meridional flow index anomaly surrounding recurving WNP TCs that undergo reintensification and no reintensification as ECs, and recurving WNP TCs associated with strong and weak TC–jet stream interactions (Fig. 2.21). Whether or not a recurving TC subsequently reintensifies as an EC does not seem to impact the significance and duration of the positive North Pacific meridional flow index anomalies that occur following TC recurvature. Both reintensifying and nonreintensifying recurving WNP TCs are associated with significant positive anomalies of the North Pacific meridional flow index that persist at least 78 h.

In contrast to the intensity and size of a recurving TC, and whether a TC undergoes reintensification as an EC, the strength of the TC–jet stream interaction associated with recurving WNP TCs does seem to have an influence on the North Pacific meridional flow pattern. Recurving WNP TCs that undergo strong TC–jet stream interactions are found to be associated with significantly positive North Pacific meridional flow index anomalies between T+18 h and T+102 h. In contrast, recurving WNP TCs that undergo weak TC–jet stream interactions are found to be associated with significantly positive North Pacific meridional flow index anomalies for a considerably shorter period, between T+54 h and T+84 h. These anomalies are only significant at the 95% confidence level, whereas almost all the positive North Pacific meridional flow index anomalies associated with strong TC–jet stream interactions are significant at the 99% confidence level. The onset of the significant positive North Pacific meridional flow index anomalies for weak TC–jet stream interactions lags those associated with strong TC–jet stream interactions by 36 h. Finally, a period of significant negative North Pacific meridional flow index anomalies between T−42 h and T−24 h are associated with weak TC–jet stream interactions, whereas no significant negative North Pacific meridional flow index anomalies are associated with strong TC–jet stream interactions.

The foregoing findings suggest that the strength of the TC–jet stream interaction may substantially influence the downstream meridional flow pattern. These findings further suggest that Rossby wave activity over the North Pacific may be preferentially associated with recurving TCs featuring strong rather than weak TC–jet stream interactions. The synoptic evolution of the downstream large-scale flow pattern following recurving TCs that undergo strong vs. weak interactions with the jet stream will be explored using composite analysis in Chapter 3.

Since the strength of the TC–jet stream interaction may play an important role in influencing the downstream flow response to recurving WNP TCs, it is of interest to examine the characteristics of these interactions. Frequency distributions of the timing of the maximum TC–jet stream interaction relative to TC recurvature for strong and weak TC–jet stream interactions (Fig. 2.22) reveal that maximum TC–jet stream interactions for strong interaction cases tend to occur significantly closer to the time of recurvature than do weak interaction cases. The mean time of the maximum TC–jet stream interaction for strong and weak TC–jet stream interaction cases is found to be T+30.5 h and T+56 h, respectively. The difference between the mean times is significant at the 99.9% confidence level.

Recurving WNP TCs associated with strong TC–jet stream interactions are found to occur later in the season relative to the overall climatology of recurving WNP TCs and relative to recurving WNP TCs associated with weak TC–jet stream interactions (Fig. 2.23). Figure 2.23 shows that compared to climatology, strong TC–jet stream interactions occur more frequently in September–December, and less frequently in April–August. The mean WNP TC recurvature date for strong TC–jet stream interactions is found to be 24 September, whereas the overall mean WNP TC recurvature date is 5 September. Additionally, compared to climatology, weak TC–jet stream interactions occur more frequently in May, July, and August, and less frequently in June and September–December. The mean recurvature date for TCs associated with weak TC–jet stream interactions is 18 August, earlier in the season relative to the overall climatology of recurving WNP TCs and to those associated with strong TC–jet stream interactions. The difference in mean WNP TC recurvature dates for strong vs. weak TC–jet stream interactions is found to be statistically significant at the 99.9% confidence level.

Relative to weak TC–jet stream interactions, recurving WNP TCs associated with strong TC–jet stream interactions are found to be significantly more intense at recurvature (Fig. 2.24). The mean MSLP at recurvature for strong TC–jet stream interactions cases is 953.1 hPa, significantly lower at the 99% confidence level than the 968.6-hPa mean MSLP for recurving TCs associated with weak TC–jet stream interactions (Fig. 2.24a). Additionally, the mean MSW at recurvature for strong TC–jet stream interactions cases is 76.4 kt, significantly higher at the 99% confidence level than the 63.7-kt mean MSW for recurving TCs associated with weak TC–jet stream interactions (Fig. 2.24b).

Recurving WNP TCs associated with strong TC–jet stream interactions also tend to be significantly larger at recurvature than those associated with weak TC–jet stream interactions (Fig. 2.25). The mean maximum 30-kt wind radius for strong and weak TC–jet stream interactions cases is 235.5 nm and 184.4 nm, respectively (Fig. 2.25a), and the mean maximum 50-kt wind radius for strong and weak TC–jet stream interactions cases is 87.8 nm and 49.1 nm, respectively (Fig. 2.25b). The differences between the mean maximum 30-kt and 50-kt wind radii for the two TC–jet stream interaction categories are significant at the 99.9% and 99% confidence levels, respectively.

Relative to weak TC–jet stream interactions, strong TC–jet stream interactions tend to occur farther westward (Fig. 2.26). The mean longitude of the maximum TC–jet stream interaction associated with the strong interaction cases is 135.7°E vs. 148.0°E for the weak interaction cases. This difference in longitudes is statistically significant at the 99.9% confidence level. The more westward occurrence of the maximum TC–jet stream interaction associated with strong TC–jet stream interaction cases compared to weak interaction cases is consistent with the aforementioned results that for strong TC–jet stream interaction cases, the maximum TC–jet stream interaction occurs earlier with respect to time of recurvature than for weak interaction cases. Figure 2.26 also shows that maximum TC–jet stream interactions associated with strong TC–jet stream interaction cases tend to occur over a substantially narrower longitudinal range than for the maximum TC–jet stream interactions associated with weak interactions. WNP TCs associated with strong TC–jet stream interactions may also exhibit a tendency to recurve farther westward than those associated with weak TC–jet stream interactions, with a mean recurvature longitude of 132.1°E vs. 136.9°E (Fig. 2.27), but this difference in longitude is found to be significant at only the 85% confidence level.

iii. Climatology of NH model forecast skill surrounding recurving WNP TC episodes

The association between recurving WNP TCs and NH model forecast skill is examined via time series of daily composite GFS ACCs of NH 500-hPa geopotential height forecasts verifying in the period surrounding WNP TC recurvature episodes (Fig. 2.28). The ACC time series displayed in Fig. 2.28 suggest that, in general, WNP TCs recurvature episodes do not have an obvious deleterious effect on NH 500-hPa geopotential height forecasts. In fact, for 24-h–120-h forecast lead times that verify at certain times following TC recurvature (Fig. 2.28), the composite ACC is found to be significantly higher than normal. That forecasts verifying in the days following TC recurvature actually may be more skillful than normal hints at the possibility that recurving WNP TCs may tend to be associated with a more predictable than normal NH flow pattern.

Although, in general, the model forecast skill for various forecast lead times surrounding recurvature either is not significantly different from climatology or is significantly higher than climatology, the composite ACC of the 168-h forecast verifying on Day −2 relative to TC recurvature is found to be significantly lower than normal (Fig. 2.28). Given that this is the only instance of a composite ACC that is significantly below normal surrounding WNP TC recurvature episodes, it is difficult to ascribe much meaning to the finding.

To examine whether TCs recurving in certain months tend to be associated with significant NH model forecast skill anomalies, composite ACC time series for 24-h–120-h NH 500-hPa geopotential height forecasts verifying in the period surrounding WNP TC recurvature episodes are computed for May–December. No statistically significant composite ACC anomalies are found for any verification time surrounding May, November, or December WNP TC recurvatures (not shown). Composite ACCs for June–October recurving WNP TC episodes, on the other hand, are found to be anomalous for particular forecast lead times and forecast verification times (Figs. 2.29–2.33, respectively).

Examination of Figs. 2.29–2.33 indicates that grouping WNP TC recurvature by month generally fails to reveal a systematic tendency for NH model forecast skill to be reduced in association with WNP TC recurvatures at particular times of the year. June is the only month between May and December that is associated with significantly below-normal composite ACCs surrounding WNP TC recurvatures (compare Fig. 2.29 with Figs. 2.30–2.33). The 24-h, 72-h, and 96-h forecasts verifying on Day −2 relative to June recurvatures are associated with significantly below-normal ACCs, as are 24-h and 72-h forecasts verifying on Day +4, 24-h and 48-h forecasts verifying on Day +5, and 24-h forecasts verifying on Day +7. However, since only seven June recurving WNP TCs occur during the available ACC period of record, these findings of significance may result from the undue influence of one or two outlier episodes on the composite ACCs.

In contrast to the findings for June, recurving WNP TCs during July–October are found to be associated with near-normal or above-normal model forecast skill for certain forecast lead times and verification times (Figs. 2.30–2.33). For July recurvatures (Fig. 2.30), 24-h–72-h forecasts are found to feature significantly above-normal NH model forecast skill for most verification times between Day −4 and Day +0 relative to TC recurvature. In addition, two verification times after July recurvatures are found to feature significantly above-normal NH model forecast skill for particular forecast lead times (the 24-h forecast verifying on Day +3, and the 72-h forecast verifying on Day +5).

For August WNP TC recurvatures (Fig. 2.31), significantly above-normal NH model forecast skill is associated with 96-h forecasts verifying on Day +2 and Day +3, 120-h forecasts verifying on Day +3, and 48-h forecasts verifying on Day +8. For WNP TCs recurving in September, NH model forecast skill is found to be below normal for 24-h forecasts verifying on Day +0 and above normal for 24-h forecasts verifying on Day +9 (Fig. 2.32). Finally, for October TC recurvatures (Fig. 2.33), significantly above-normal

NH model forecast skill is noted for 24-h and 48-h forecasts verifying on Day +9, and 48-h and 72-h forecasts verifying on Day +10.

As a final step in the examination of predictability surrounding WNP TC recurvature episodes, we consider whether the strength of the TC–jet stream interaction associated with recurving WNP TCs exerts a discernable influence on NH model forecast skill. Time series of composite ACCs computed for periods surrounding recurving WNP TCs associated with strong and weak TC–jet stream interactions (Fig. 2.34) indicate that NH model forecast skill does not tend to be significantly above or below normal surrounding TC recurvature for either category, with the only possible exception being that, for weak interactions, 24-h forecasts verifying on Day −3–Day −1 tend to be associated with significantly below-normal NH model forecast skill (Fig. 2.34b).

Of interest is that the strong TC–jet stream interaction composite ACC times series for 96-h and 120-h forecasts, while not featuring significantly above- or below-normal ACCs, seem to suggest a general downward trend in NH model forecast skill for verification times between Day −4 and Day +2, after which model forecast skill appears to rebound (Fig. 2.34a). This signature of a downward trend in model forecast skill for 96-h and 120-h forecasts verifying between Day −4 and Day +2 is not seen for weak TC–jet stream interaction cases, which are characterized by a slight rise in NH model forecast skill over the same period (Fig. 2.34b).

The lack of an apparent detrimental impact of WNP TC recurvature episodes on model forecast skill may be in part an artifact of the NH domain used to evaluate model forecast skill in this study, which may serve to mask a relatively localized impact of recurving WNP TCs on model forecast skill. Datasets of ACCs averaged over a regional domain such as the North Pacific, while not readily available for this study, are likely better suited to address whether the recurvature of WNP TCs tends to impact model forecast skill in a climatological sense over regions remote from the TC (i.e., a model forecast skill impact on synoptic-to-planetary scales).

d. Summary

In this chapter, a climatology of WNP TC recurvature is performed based on 292 recurving WNP TC episodes occurring over a 31-year period. This climatology is used to provide context for an examination of how relationships between WNP TC recurvature episodes and the downstream large-scale flow pattern are influenced by characteristics of the large-scale flow pattern, the TC, and the phasing of the TC with the extratropical flow. Relationships between WNP TC recurvature episodes and the downstream large-scale flow pattern are analyzed using a metric that evaluates the waviness of the North Pacific flow pattern. This metric, the North Pacific meridional flow index, is computed by spatially averaging the absolute value of meridional wind on the DT for the North Pacific domain. Above-normal index values imply above-normal meridional flow over the North Pacific, and vice versa. Furthermore, NH model forecast skill surrounding WNP TC recurvature episodes is evaluated using GFS ACCs of NH 500-hPa geopotential height forecasts.

A critical finding of this research is that the North Pacific flow pattern tends to be significantly more meridional than normal between T+12 h and T+114 h relative to WNP TC recurvature. To the extent that meridional flow on the DT corresponds to Rossby wave activity, these findings suggest that WNP TC recurvatures episodes may be associated with above-normal downstream Rossby wave activity.

When recurving WNP TCs are stratified by month, considerable differences emerge in the significance, duration, and timing of the above-normal North Pacific meridional flow that tends to follow recurving WNP TCs. Significantly above-normal North Pacific meridional flow tends to occur for at least a 36-h period following WNP TC recurvatures in May and July–November. In contrast, North Pacific meridional flow tends to remain near normal following TC recurvatures in June and December. Of all the months, August and September feature the most prolonged periods of significantly above-normal North Pacific meridional flow following TC recurvature (~96 h). In August–November, the onset of significantly above-normal North Pacific meridional flow tends to occur ~42 h earlier than in May and July. The month-to-month differences in the significance, duration, and timing of above-normal North Pacific meridional flow following WNP TC recurvature episodes suggest that the Rossby wave response to WNP TC recurvatures may vary substantially by month.

Besides the month of TC recurvature, the strength of the TC–jet stream interaction appears to be a more important factor in influencing the North Pacific meridional flow pattern following WNP TC recurvature than the other factors examined in this study (i.e., latitude of recurvature, TC size, TC intensity, and whether a recurving TC undergoes reintensification as an EC). The strength of the TC–jet stream interaction is evaluated based on the magnitude and duration of negative PV advection by the upper-tropospheric irrotational wind associated with the recurving TC. Strong TC–jet stream interactions are associated with significantly above-normal North Pacific meridional flow for an 84-h period following TC recurvature, whereas weak TC–jet stream interactions are associated with significantly above-normal North Pacific meridional flow that persist for a much shorter period (30 h). In addition, the onset of the significant positive North Pacific meridional flow index anomalies for weak TC–jet stream interactions lags those associated with strong TC–jet stream interactions by 36 h. These findings suggest that recurving TCs associated with strong TC–jet stream interactions may be more likely to be associated with enhanced Rossby wave activity over the North Pacific than recurving TCs associated with weak TC–jet stream interactions.

An evaluation of NH model forecast skill surrounding WNP TC recurvature episodes using GFS ACCs of NH 500-hPa geopotential height forecasts indicates that, somewhat counter to conventional wisdom, episodes of recurving WNP TCs are generally not associated with below-normal NH model forecast skill. In fact, for some forecast lead times verifying at particular times following WNP TC recurvature, model forecast skill is found to be significantly higher than normal. The latter finding suggests the possibility that recurving WNP TCs are associated with periods of enhanced predictability over the NH.

The aforementioned results suggesting that the time of year and the strength of the TC–jet stream interaction may be important in determining the downstream flow response to recurving WNP TCs motivate further exploration of these factors. The influence of time of year and strength of the TC–jet stream interaction on the downstream flow response to recurving WNP TCs will be explored from a synoptic–dynamic perspective via composite analysis in Chapter 3.

e. Tables

TABLE 2.1. Linear correlation between various recurving WNP TC characteristics and between recurving WNP TC characteristics and the TC–jet stream interaction metric.

	MSLP	MSW	Length of maximum 30-kt radius	Length of maximum 50-kt radius	Interaction metric
MSLP	1.00	−0.97	−0.61	-0.84	0.23
MSW	-	1.00	0.59	0.85	−0.23
Length of maximum 30-kt radius	-	-	1.00	0.77	−0.27
Length of maximum 50-kt radius	-	-	-	1.00	−0.28
Interaction metric	-	-	-	-	1.00

TABLE 2.2. Mean MSLP and MSW of recurving WNP TCs categorized as strong and weak.

Category	Mean MSLP (hPa)	Mean MSW (kt)
Strong recurving WNP TCs	928.2	95.3
Weak recurving WNP TCs	993.5	41.1

TABLE 2.3. Mean lengths of maximum 30-kt and 50-kt wind radii of recurving WNP TCs categorized as large and small.

Category	Mean length of maximum 30-kt wind radius (nm)	Mean length of maximum 50-kt wind radius (nm)
Large recurving WNP TCs	311.9	139.0
Small recurving WNP TCs	112.9	–

TABLE 2.4. Long-term (1979–2009) monthly means and standard deviations of the North Pacific meridional flow index used to compute statistical significance of the North Pacific meridional flow index anomalies associated with recurving WNP TCs categorized by month.

Month	Mean ($m\ s^{-1}$)	Standard deviation ($m\ s^{-1}$)
January	12.60	2.52
February	12.53	2.46
March	12.67	2.64
April	12.95	2.45
May	12.21	2.55
June	10.90	2.03
July	9.96	1.78
August	10.30	1.68
September	11.28	2.23
October	12.55	2.90
November	13.11	2.79
December	13.05	2.92

TABLE 2.5. Long-term (1979–2009) monthly weighted means and standard deviations of the North Pacific meridional flow index used to compute statistical significance of the North Pacific meridional flow index anomalies associated with various categories of recurving WNP TCs.

Category	Mean ($\mathrm{m\ s^{-1}}$)	Standard deviation ($\mathrm{m\ s^{-1}}$)
All	11.46	2.28
15°–20°N latitude of recurvature	12.22	2.54
20°–25°N latitude of recurvature	11.75	2.44
25°–30°N latitude of recurvature	11.09	2.15
30°–35°N latitude of recurvature	10.65	1.94
Strong TC at recurvature	11.93	2.50
Weak TC at recurvature	11.10	2.12
Large TC at recurvature	11.88	2.47
Small TC at recurvature	11.15	2.15
Reintensification as an EC	11.34	2.23
No reintensification as an EC	11.55	2.31
Strong TC–jet stream interaction	11.75	2.40
Weak TC–jet stream interaction	11.08	2.14

TABLE 2.6. The 20 null TC–jet stream interaction cases.

TC name (year)	TC name (year)
Abby (1979)	Kinna (1994)
Cecil (1979)	Yanyan (2003)
Dot (1979)	Kulap (2005)
Lola (1979)	Nalgae (2005)
Lex (1980)	Ewiniar (2006)
Marge (1980)	Danas (2007)
Sperry (1980)	Kong-rey (2007)
Tip (1989)	Krosa (2007)
Zola (1990)	Usagi (2007)
Brian (1992)	Dolphin (2008)

TABLE 2.7. The 54 recurving WNP TCs associated with strong TC–jet stream interactions.

Rank	TC name (year)	Interaction metric (PVU day^{-1})	Rank	TC name (year)	Interaction metric (PVU day^{-1})
1	Melor (2009)	−2.58	28	Chaba (2004)	−1.83
2	Oscar (1995)	−2.57	29	Colleen (1989)	−1.82
3	Hunt (1992)	−2.36	30	Mac (1982)	−1.79
4	Haishen (2002)	−2.35	31	Gordon (1982)	−1.78
5	Elsie (1981)	−2.32	32	Megi (2004)	−1.77
6	Orchid (1980)	−2.31	33	Cecil (1993)	−1.76
7	Nanmadol (2004)	−2.18	34	Judy (1982)	−1.76
8	Rammasun (2008)	−2.17	35	Irving (1979)	−1.76
9	Mireille (1991)	−2.15	36	Owen (1979)	−1.75
10	Songda (2004)	−2.13	37	Flo (1990)	−1.75
11	Xangsane (2000)	−2.08	38	Forrest (1986)	−1.75
12	Stella (1998)	−2.08	39	Kinna (1991)	−1.75
13	Choi-wan (2009)	−2.08	40	Irma (1981)	−1.74
14	Vanessa (1984)	−2.06	41	Marge (1983)	−1.73
15	Elsie (1992)	−2.06	42	Gay (1981)	−1.73
16	David (1997)	−2.05	43	Soulik (2006)	−1.73
17	Susan (1988)	−2.01	44	Mamie (1985)	−1.68
18	Dale (1996)	−2.00	45	Phanfone (2002)	−1.67
19	Thelma (1980)	−2.00	46	Agnes (1981)	−1.67
20	Lola (1986)	−1.97	47	Dianmu (2004)	−1.67
21	Polly (1995)	−1.92	48	Ann (1999)	−1.66
22	Dan (1995)	−1.89	49	Podul (2001)	−1.66
23	Nabi (2005)	−1.88	50	Ma-on (2004)	−1.65
24	Dinah (1987)	−1.87	51	Krosa (2001)	−1.63
25	Faxai (2007)	−1.87	52	Winnie (1997)	−1.63
26	Luke (1991)	−1.85	53	Vernon (1980)	−1.62
27	Fern (1996)	−1.85	54	Pat (1985)	−1.62

TABLE 2.8. The 54 recurving WNP TCs associated with weak TC–jet stream interactions.

Rank	TC name (year)	Interaction metric (PVU day^{-1})	Rank	TC name (year)	Interaction metric (PVU day^{-1})
219	Doyle (1981)	−0.69	246	Owen (1989)	−0.53
220	Mindulle (2004)	−0.68	247	Alex (1984)	−0.52
221	Maria (2006)	−0.67	248	Tingting (2004)	−0.52
222	Forrest (1980)	−0.67	249	Ian (1987)	−0.52
223	Tom (1996)	−0.66	250	Mawar (2005)	−0.50
224	Sonamu (2000)	−0.66	251	Cecil (1982)	−0.47
225	Bing (1997)	−0.65	252	Vipa (2001)	−0.46
226	Joan (1997)	−0.63	253	Robyn (1990)	−0.45
227	Wynne (1987)	−0.62	254	Eve (1996)	−0.45
228	Orson (1996)	−0.61	255	Joy (1996)	−0.45
229	Bart (1996)	−0.61	256	Yutu (2007)	−0.44
230	Dan (1999)	−0.60	257	Kirk (1996)	−0.41
231	Parma (2003)	−0.60	258	Hattie (1993)	−0.41
232	Pat (1994)	−0.58	259	Yule (1997)	−0.41
233	Ginger (1997)	−0.58	260	Holly (1987)	−0.41
234	Gay (1992)	−0.57	261	Halong (2002)	−0.40
235	Ken (1979)	−0.57	262	Ivan (1997)	−0.39
236	Kelly (1987)	−0.56	263	Alex (1987)	−0.37
237	Page (1994)	−0.56	264	Lingling (2007)	−0.37
238	Soudelor (2003)	−0.56	265	Caitlin (1991)	−0.37
239	Nancy (1986)	−0.56	266	Isa (1997)	−0.36
240	Percy (1993)	−0.55	267	Abby (1983)	−0.31
241	Tina (1997)	−0.55	268	Doyle (1988)	−0.28
242	Nepartak (2009)	−0.55	269	Etau (2009)	−0.24
243	Chataan (2002)	−0.55	270	Dinah (1984)	−0.21
244	Matsa (2005)	−0.54	271	Ivy (1994)	−0.14
245	Sarah (1986)	−0.54	272	Wilda (1994)	−0.09

TABLE 2.9. Long-term monthly means and standard deviations of ACCs of 24-h NH 500-hPa geopotential height forecasts.

Month	Mean	Standard deviation
January	0.992	0.002
February	0.992	0.003
March	0.993	0.002
April	0.992	0.003
May	0.991	0.003
June	0.990	0.004
July	0.988	0.004
August	0.988	0.005
September	0.990	0.003
October	0.992	0.003
November	0.992	0.003
December	0.992	0.003

TABLE 2.10. As in Table 2.9, except for ACCs of 48-h NH 500-hPa geopotential height forecasts.

Month	Mean	Standard deviation
January	0.974	0.009
February	0.975	0.009
March	0.976	0.009
April	0.973	0.010
May	0.972	0.011
June	0.967	0.014
July	0.963	0.015
August	0.964	0.015
September	0.967	0.014
October	0.972	0.012
November	0.973	0.011
December	0.973	0.012

TABLE 2.11. As in Table 2.9, except for ACCs of 72-h NH 500-hPa geopotential height forecasts.

Month	Mean	Standard deviation
January	0.939	0.023
February	0.941	0.022
March	0.942	0.022
April	0.937	0.024
May	0.933	0.025
June	0.921	0.031
July	0.916	0.033
August	0.918	0.034
September	0.922	0.034
October	0.933	0.030
November	0.936	0.029
December	0.936	0.030

TABLE 2.12. As in Table 2.9, except for ACCs of 96-h NH 500-hPa geopotential height forecasts.

Month	Mean	Standard deviation
January	0.883	0.043
February	0.886	0.045
March	0.885	0.046
April	0.875	0.045
May	0.868	0.051
June	0.849	0.053
July	0.841	0.057
August	0.846	0.060
September	0.846	0.064
October	0.868	0.056
November	0.875	0.056
December	0.878	0.056

TABLE 2.13. As in Table 2.9, except for ACCs of 120-h NH 500-hPa geopotential height forecasts.

Month	Mean	Standard deviation
January	0.808	0.068
February	0.812	0.072
March	0.808	0.073
April	0.790	0.078
May	0.775	0.086
June	0.749	0.078
July	0.740	0.087
August	0.749	0.089
September	0.742	0.096
October	0.780	0.084
November	0.788	0.092
December	0.800	0.085

TABLE 2.14. As in Table 2.9, except for ACCs of 144-h NH 500-hPa geopotential height forecasts.

Month	Mean	Standard deviation
January	0.740	0.091
February	0.728	0.109
March	0.738	0.085
April	0.699	0.108
May	0.694	0.105
June	0.659	0.100
July	0.656	0.102
August	0.679	0.100
September	0.640	0.115
October	0.710	0.102
November	0.727	0.093
December	0.724	0.101

TABLE 2.15. As in Table 2.9, except for ACCs of 168-h NH 500-hPa geopotential height forecasts.

Month	Mean	Standard deviation
January	0.652	0.119
February	0.637	0.132
March	0.647	0.113
April	0.589	0.134
May	0.582	0.130
June	0.540	0.129
July	0.547	0.123
August	0.570	0.124
September	0.527	0.129
October	0.598	0.136
November	0.631	0.113
December	0.627	0.121

TABLE 2.16. Summary of recurving WNP TC characteristics.

WNP TC characteristic at recurvature	Mean	Median	Minimum	Maximum
Latitude (°N)	24.9	24.8	9.5 Kulap (2005)	42.3 Mac (1989)
Longitude (°E)	134.0	131.4	109.8 Russ (1994)	169.8 Lingling (2007)
MSLP (hPa)	964.0	965.0	890 Flo (1990)	1004 Forrest (1980)
MSW (kt)	67.9	70.0	35 (21 TCs)	120 Flo (1990)
Length of maximum 30-kt wind radius (nm)	194.2	180.0	40 Vipa (2001)	600 Keith (1997)
Length of maximum 50-kt wind radius (nm)	63.8	60.0	– (81 TCs)	200 Holly (1984)

f. Figures

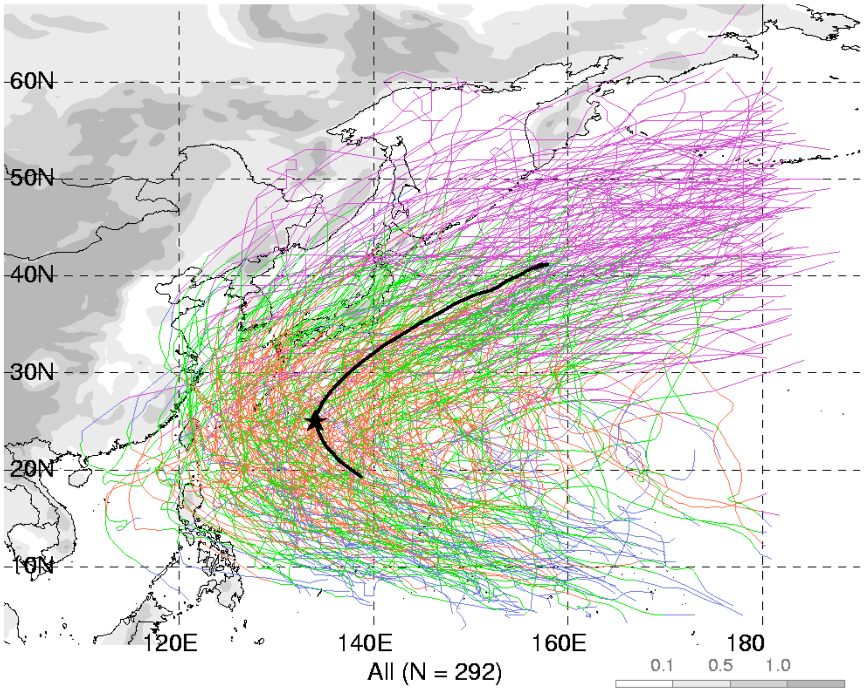

FIG. 2.1. Tracks of 1979–2009 recurving WNP TCs (colored lines) and the composite recurving WNP TC track (black line; T−48 h–T+96 h). The star denotes composite recurvature point (24.9ºN, 134.0ºE). Track color corresponds to TC category (blue to TD, green to TS, red to TY, and purple to EC). Surface elevation is shaded according to the gray scale (km).

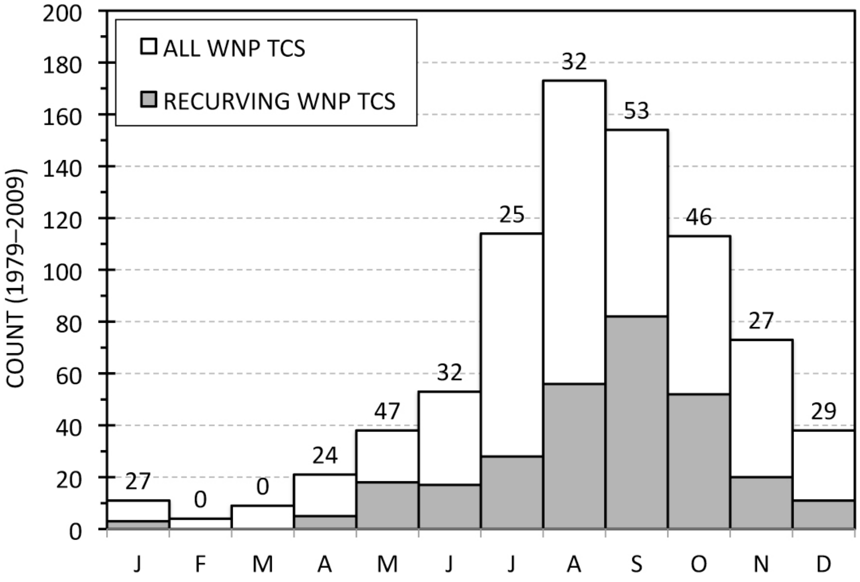

FIG. 2.2. Monthly distributions of all WNP TCs (unshaded) and recurving WNP TCs (light gray shading). Number above each bar indicates percentages of WNP TCs that undergo recurvature in each month.

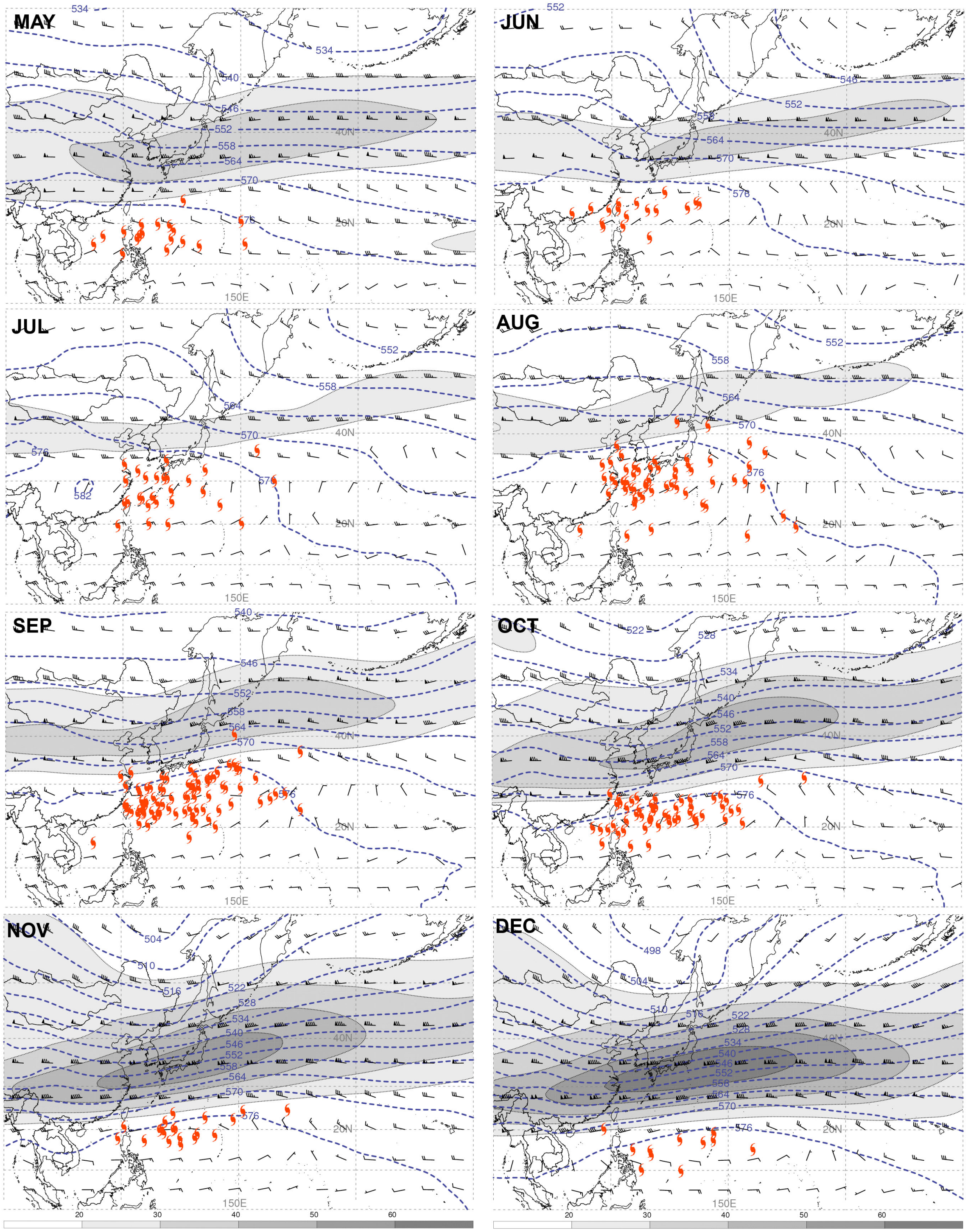

FIG. 2.3. WNP TC recurvature points by month and corresponding long-term (1979–2009) monthly mean 250-hPa wind speed (shaded in m s^{-1} according to the gray scale), wind (barbs, kt) and 1000–500-hPa thickness (dashed, every 6 dam) over eastern Asia and the west–central North Pacific for May–December.

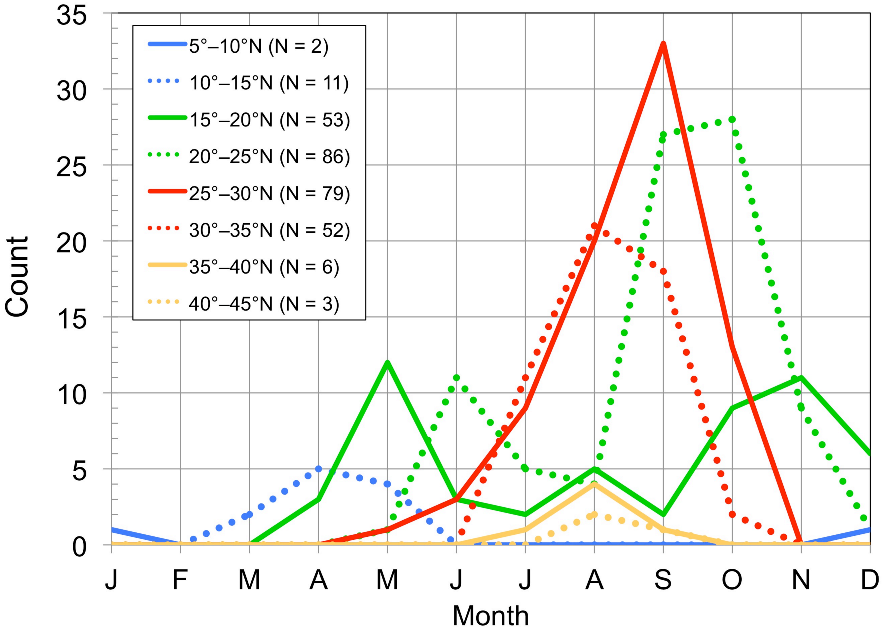

FIG. 2.4. Monthly distributions of WNP TC recurvature stratified by recurvature latitude.

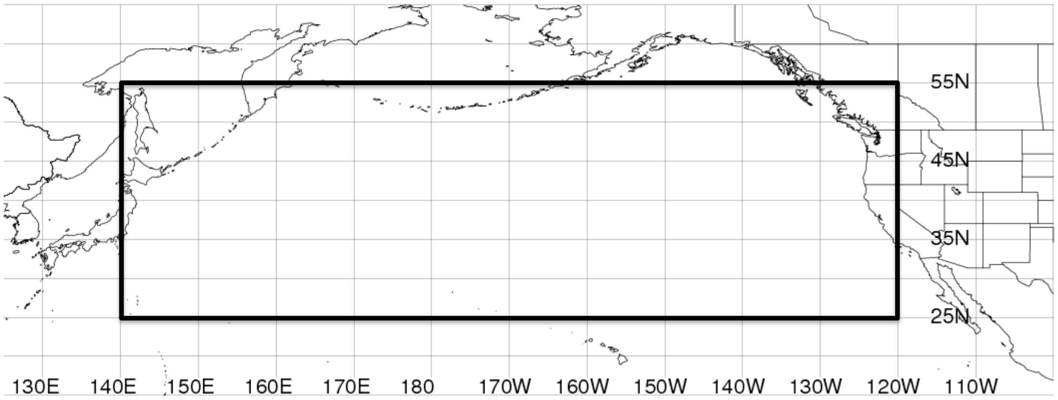

FIG. 2.5. The 25°–55°N, 140°E–120°W domain used to compute the North Pacific meridional flow index.

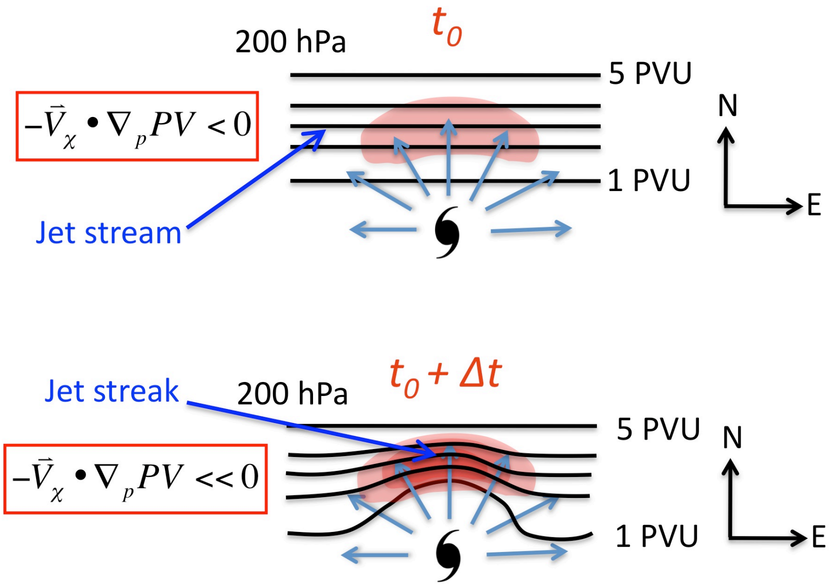

FIG. 2.6. Schematic representation of upper-tropospheric ridge amplification and jet streak intensification associated with divergent TC outflow impinging upon an upper-tropospheric jet stream (i.e., a meridional PV gradient).

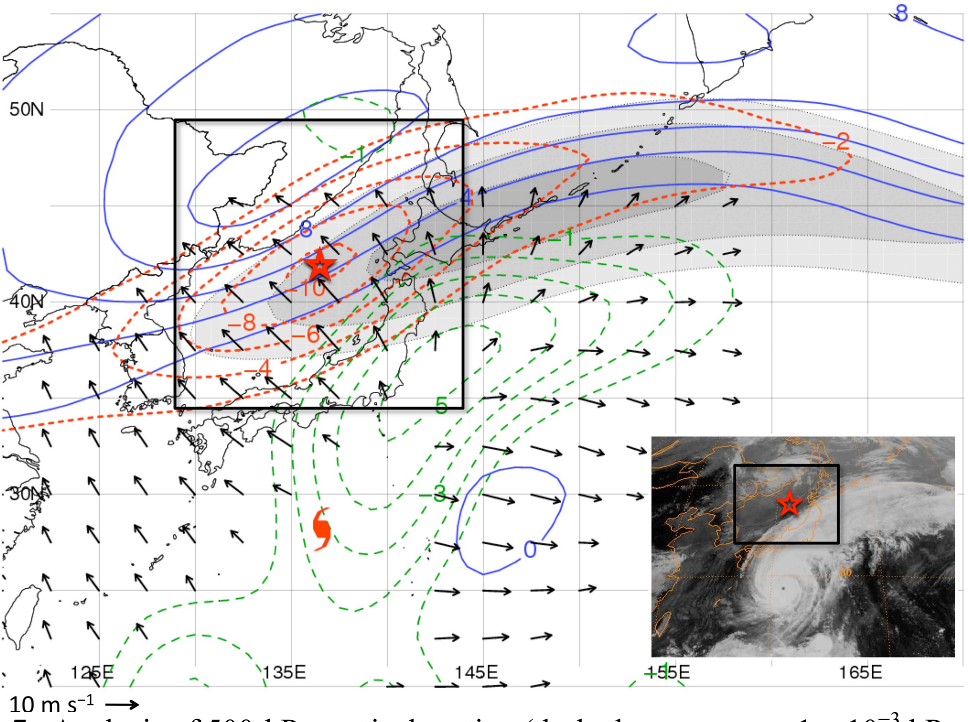

FIG. 2.7. Analysis of 500-hPa vertical motion (dashed green, every 1×10^{-3} hPa s^{-1}, negative values only), and 250–150-hPa layer-averaged wind speed (shaded every 10 m s^{-1} starting at 50 m s^{-1}), PV (solid blue, every 2 PVU), irrotational wind (vectors, >4.0 m s^{-1} only; note reference vector in lower left corner), and PV advection by the irrotational wind (dashed red, every 2 PVU day^{-1}, negative values only) at 0600 UTC 16 September 1995, the maximum TC–jet stream interaction time associated with TC Oscar. The red star denotes the maximum TC–jet stream interaction point, and the black rectangle shows the surrounding 15° × 15° domain used to compute the TC–jet stream interaction metric. The TC symbol denotes the JMA best-track position of TC Oscar. The inset shows an IR image valid at the same time and for approximately the same domain as the main portion of the figure. The star and rectangle in the inset have the same meaning as in the main portion of the figure.

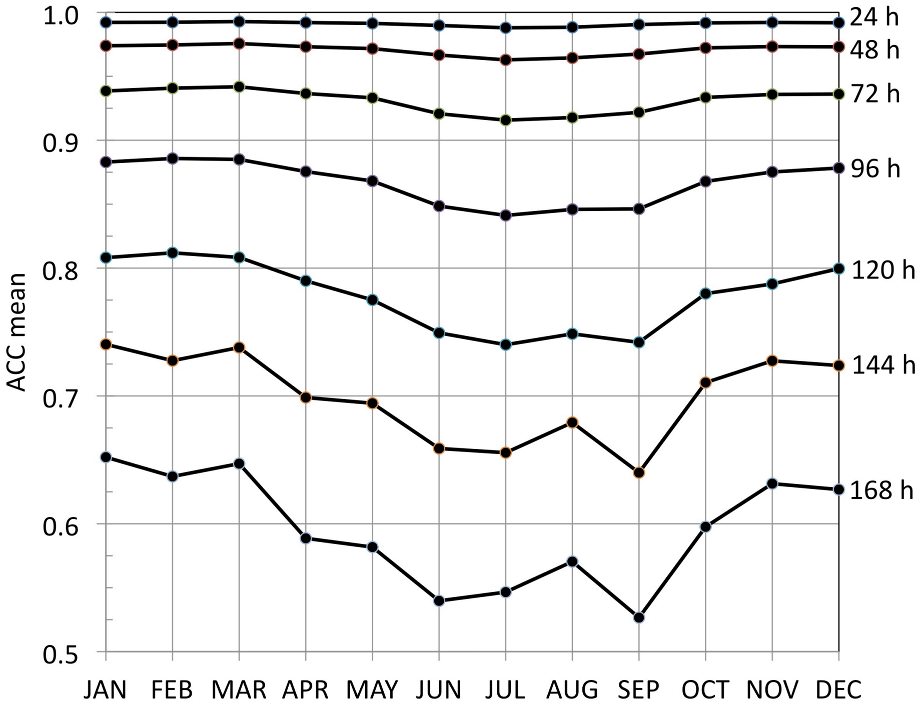

FIG. 2.8. Long-term monthly means of NH GFS ACCs for 24-h–168-h 500-hPa geopotential height forecasts.

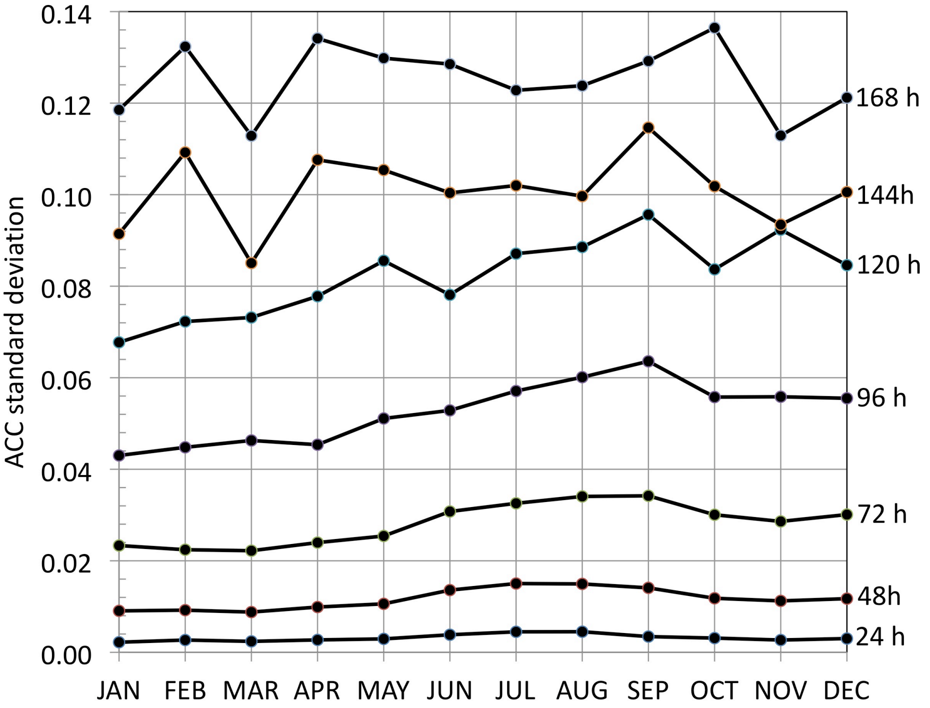

FIG. 2.9. As in Fig. 2.8, except for long-term monthly standard deviations.

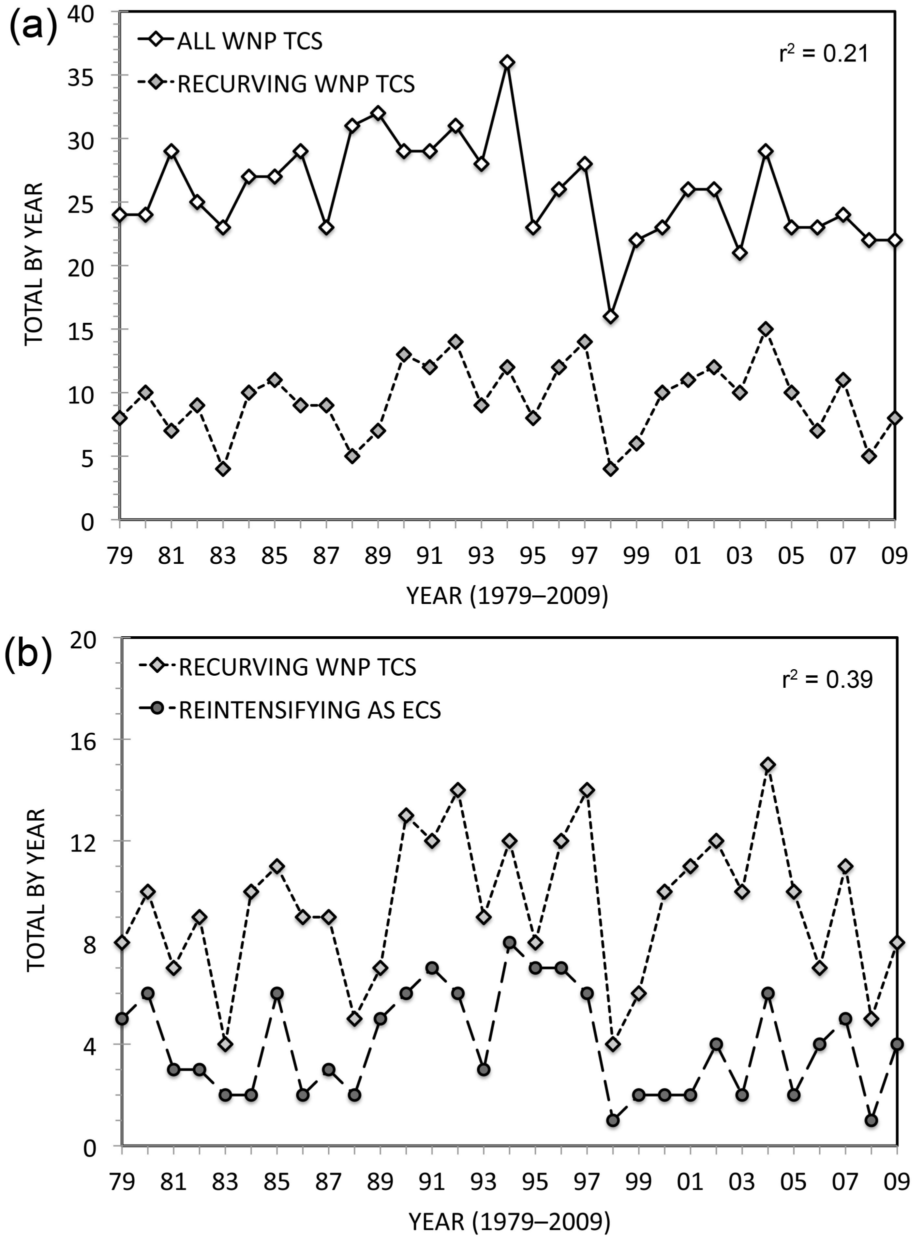

FIG. 2.10. Time series of annual total (a) WNP TCs (open diamonds) and recurving WNP TCs (closed diamonds), and (b) recurving WNP TCs (closed diamonds) and recurving WNP TCs that reintensify as ECs (closed circles) for 1979–2009. The square of the linear correlation between time series (r^2) is given in the top right corner of each panel.

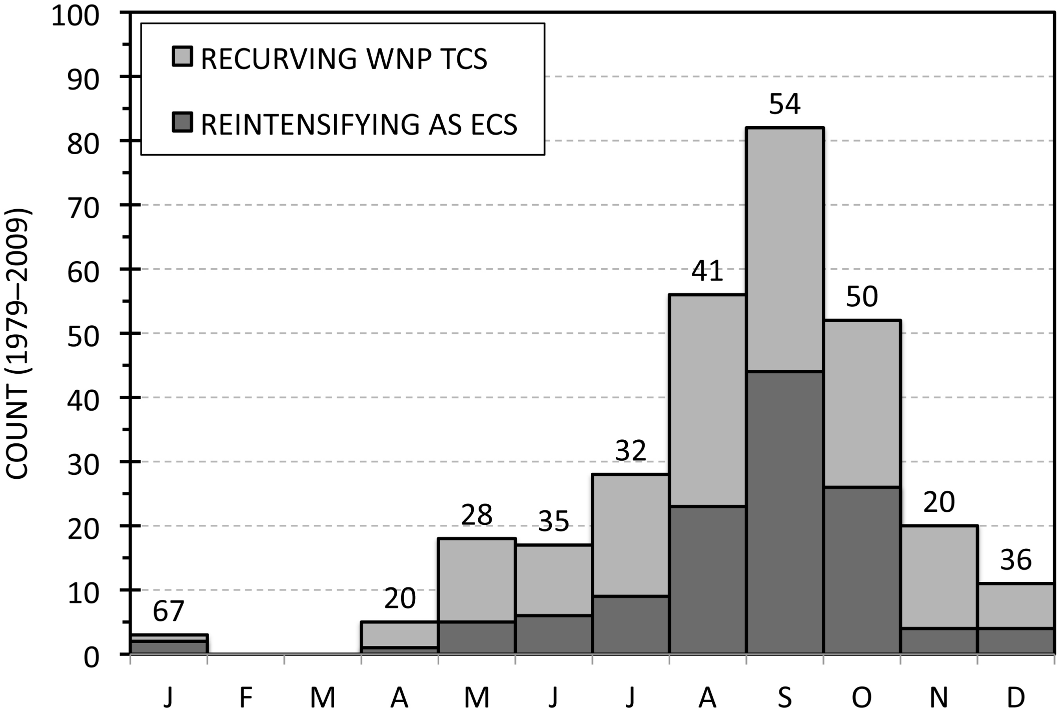

FIG. 2.11. Monthly distributions of recurving WNP TCs (light shading) and recurving WNP TCs that reintensify as ECs (dark shading). Numbers above each bar indicate the percentage of recurving WNP TCs that reintensify as ECs for each month.

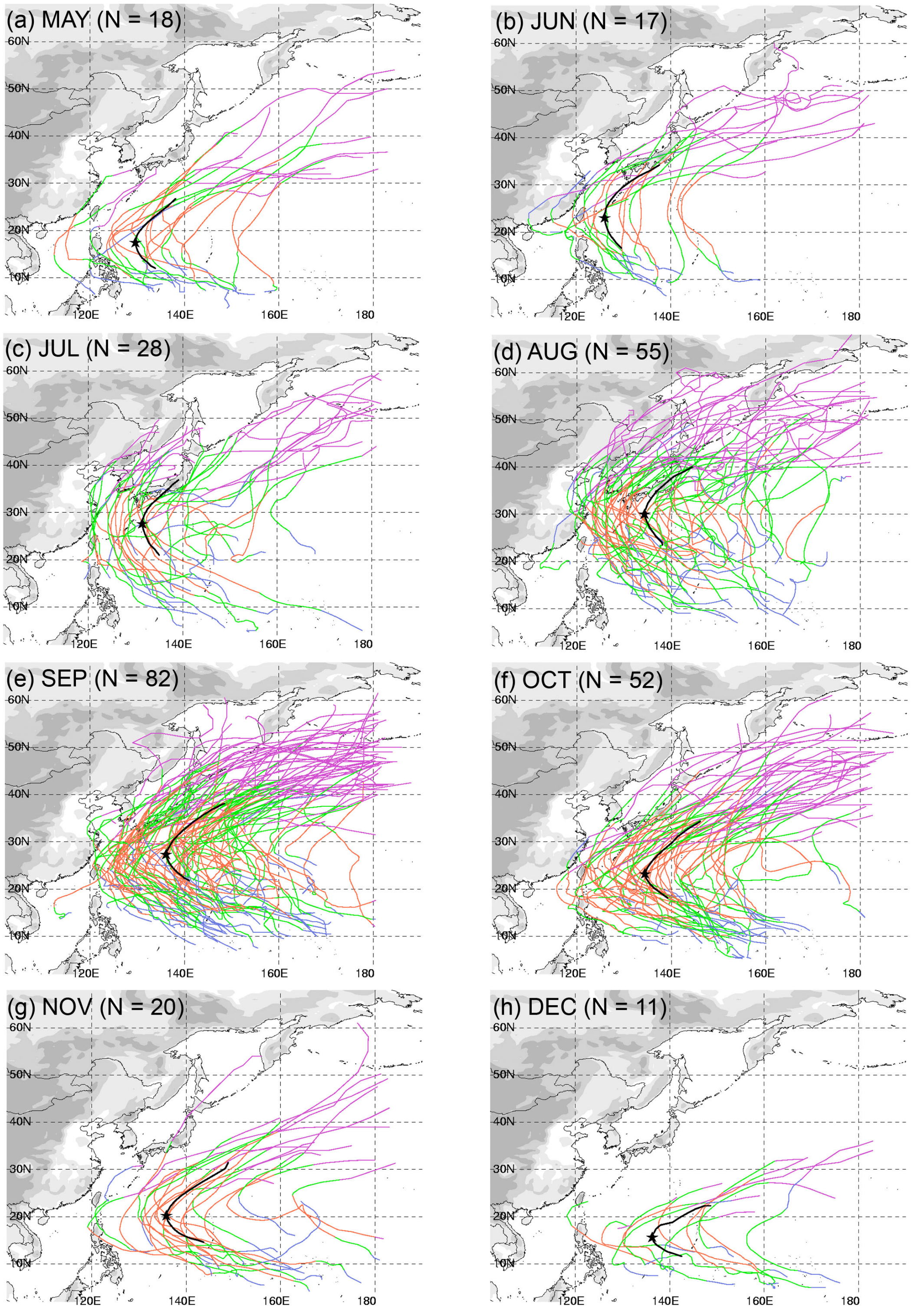

FIG. 2.12. As in Fig. 2.1, except for recurving WNP TC tracks during (a) May, (b) June, (c) July, (d) August, (e) September, (f) October, (g) November, and (h) December. The black line denotes the composite recurving WNP TC track for T−48 h–T+72 h.

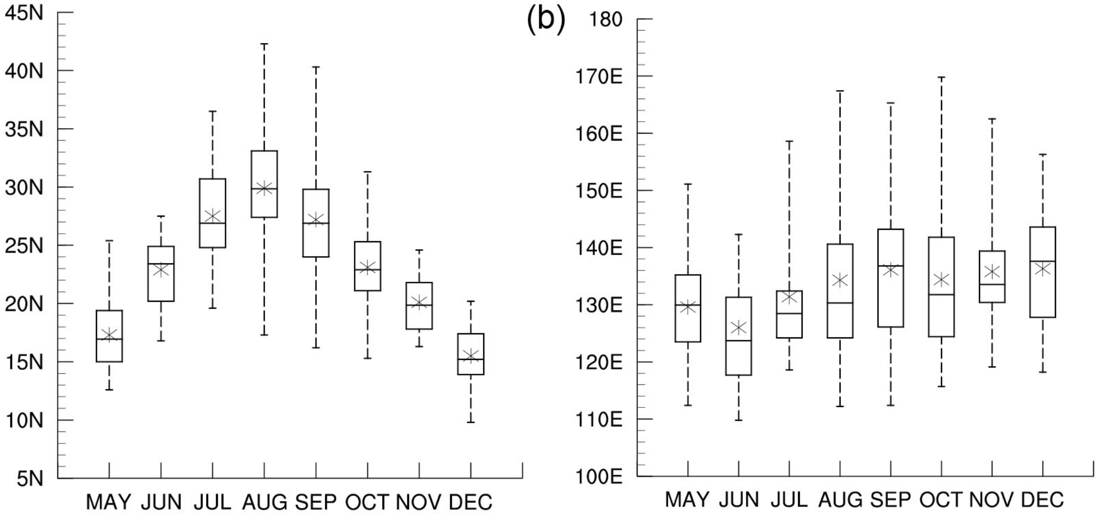

FIG. 2.13. Box plots showing (a) latitudinal and (b) longitudinal distributions of WNP TC recurvature points by month (May–December). The bounds of each box are drawn at the 25th and 75th percentiles, the bar and asterisk inside each box denote the median and mean, respectively, and the whiskers extend from the 75th and 25th percentiles to the maximum and minimum values, respectively.

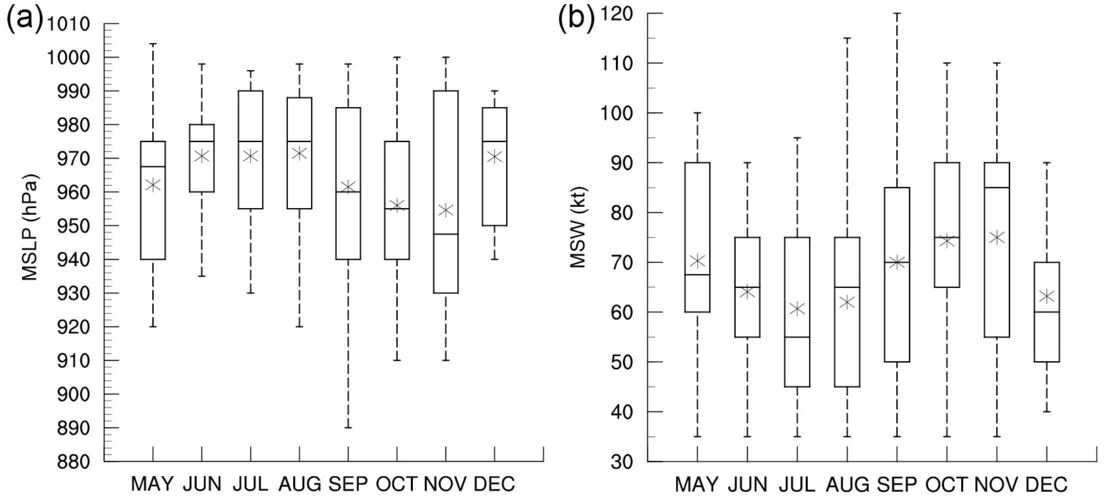

FIG. 2.14. As in Fig. 2.13, except for (a) MSLP (hPa) and (b) MSW (kt) distributions for WNP TCs at recurvature.

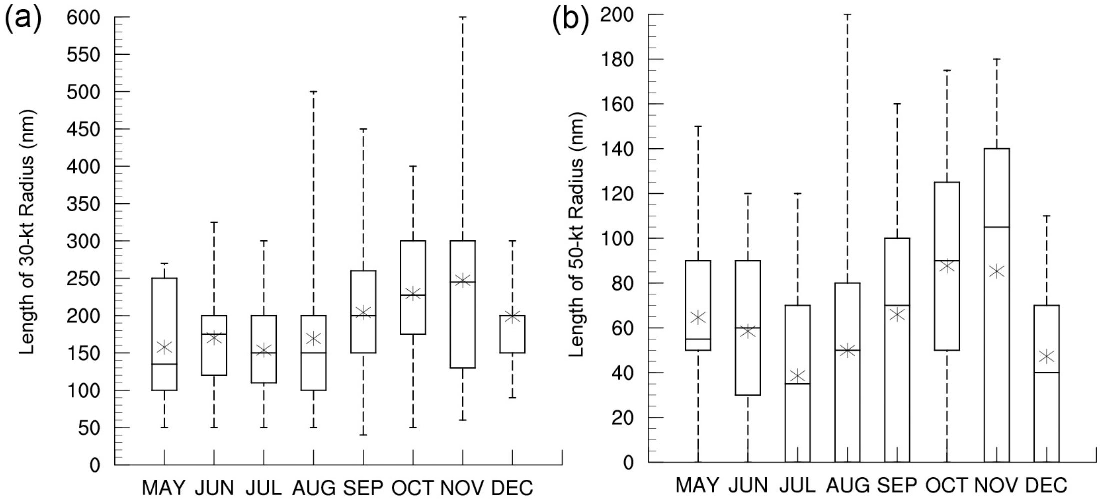

FIG. 2.15. As in Fig. 2.13, except for length of the maximum radius of (a) 30-kt winds (nm) and (b) 50-kt winds (nm) for WNP TCs at recurvature. In (a), the December median and 75th percentile are the same. In (b), the July, August, September, November, and December minimum values and 25th percentiles are the same.

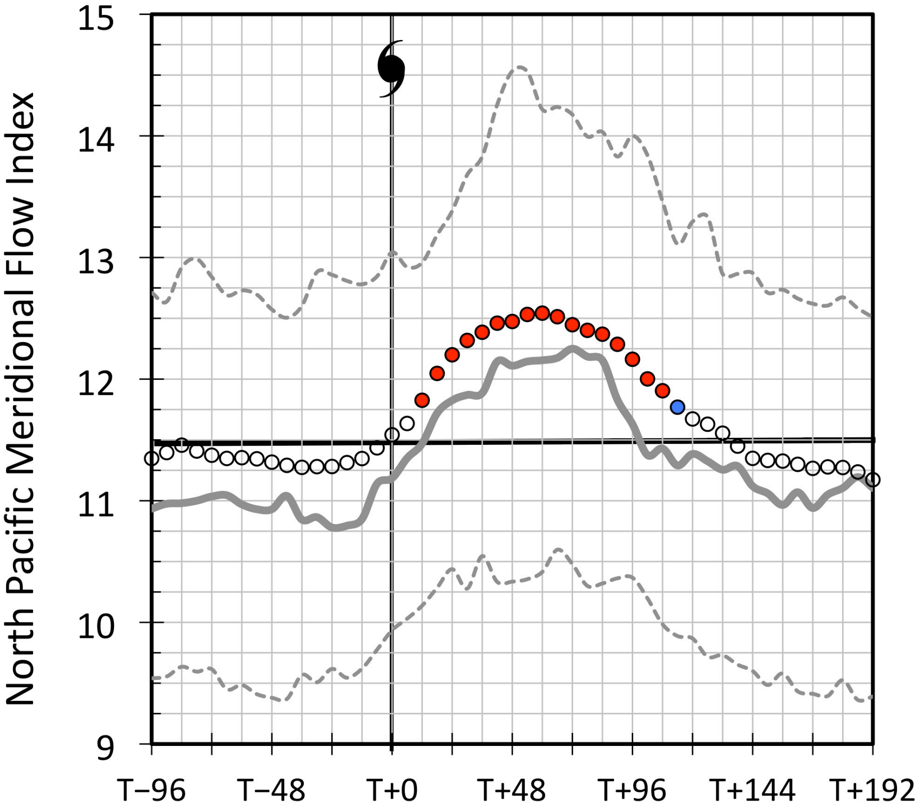

FIG. 2.16. Time series of the 6-hourly composite North Pacific meridional flow index (m s^{-1}) associated with recurving WNP TCs. The vertical line with TC symbol denotes time of TC recurvature (T+0 h). Circles correspond to composite mean values, with statistical significance at the 95% (99%) confidence level shown by the blue (red) dots. The solid gray curve represents the median, and the bounding dashed gray curves denote the 25th and 75th percentiles. The thick horizontal line denotes the monthly weighted mean.

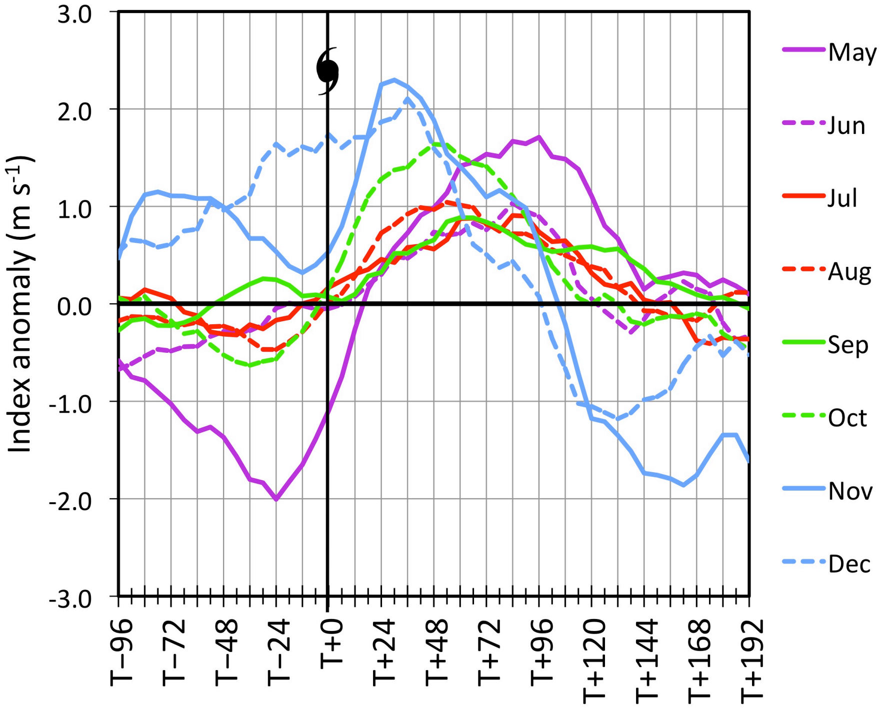

FIG. 2.17. Time series of the 6-hourly composite North Pacific meridional flow index anomaly (m s^{-1}) associated with recurving WNP TCs in May–December.

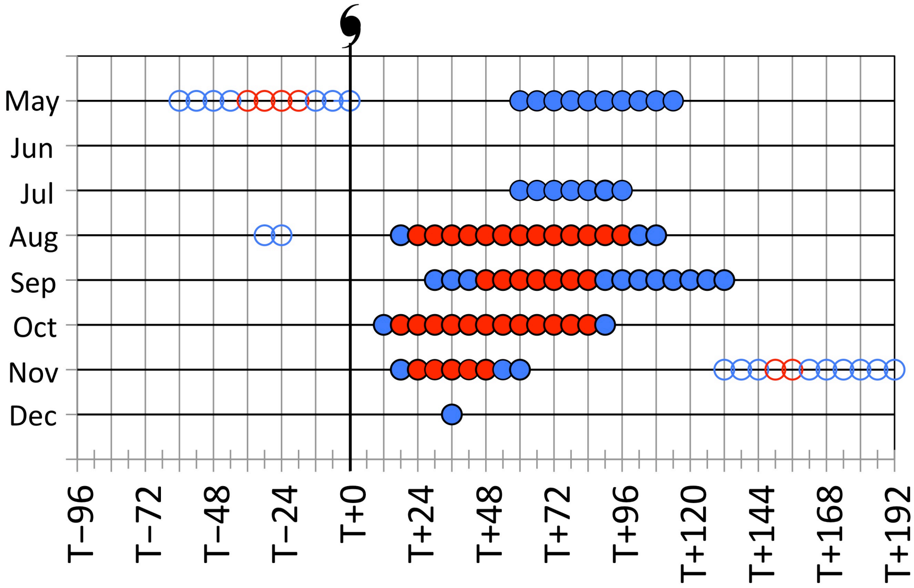

FIG. 2.18. Statistical significance of the 6-hourly composite North Pacific meridional flow index anomaly associated with recurving WNP TCs in May–December. Filled blue (red) circles indicate significantly above-normal values at the 95% (99%) confidence level, whereas open blue (red) circles indicate significantly below-normal values at the 95% (99%) confidence level.

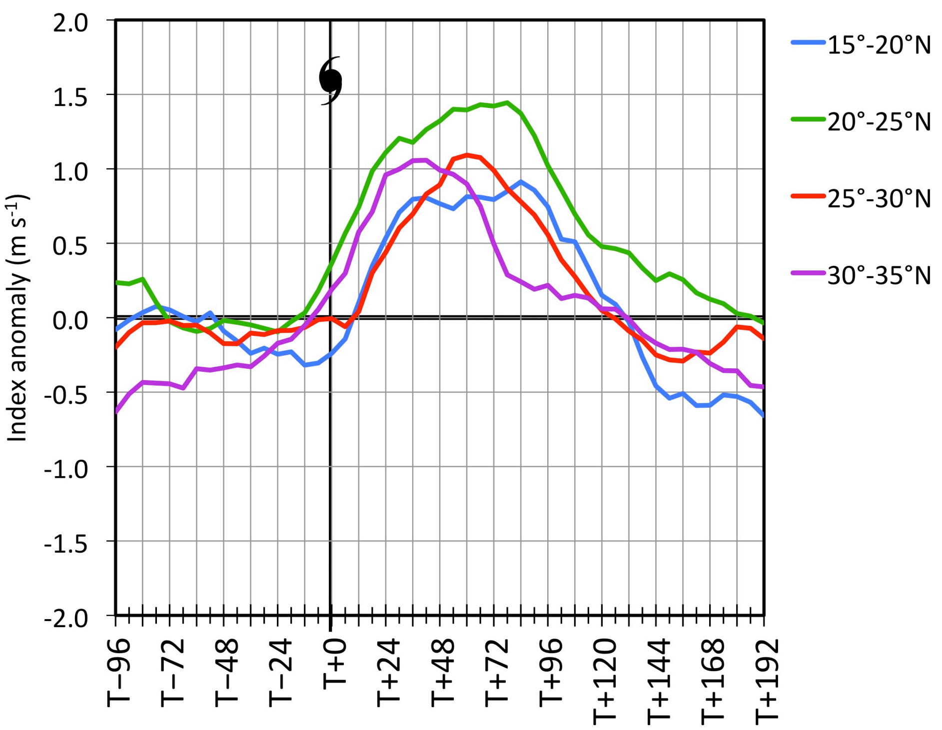

FIG. 2.19. As in Fig. 2.17, except for WNP TCs recurving within 15°–20°N, 20°–25°N, 25°–30°N, and 30°–35°N latitude bands.

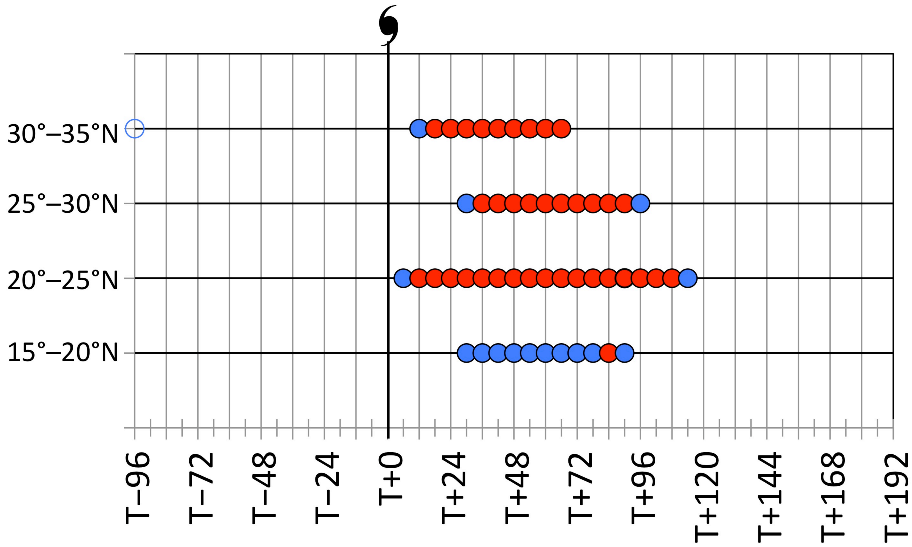

FIG. 2.20. As in Fig. 2.18, except for WNP TCs recurving within 15°–20°N, 20°–25°N, 25°–30°N, and 30°–35°N latitude bands.

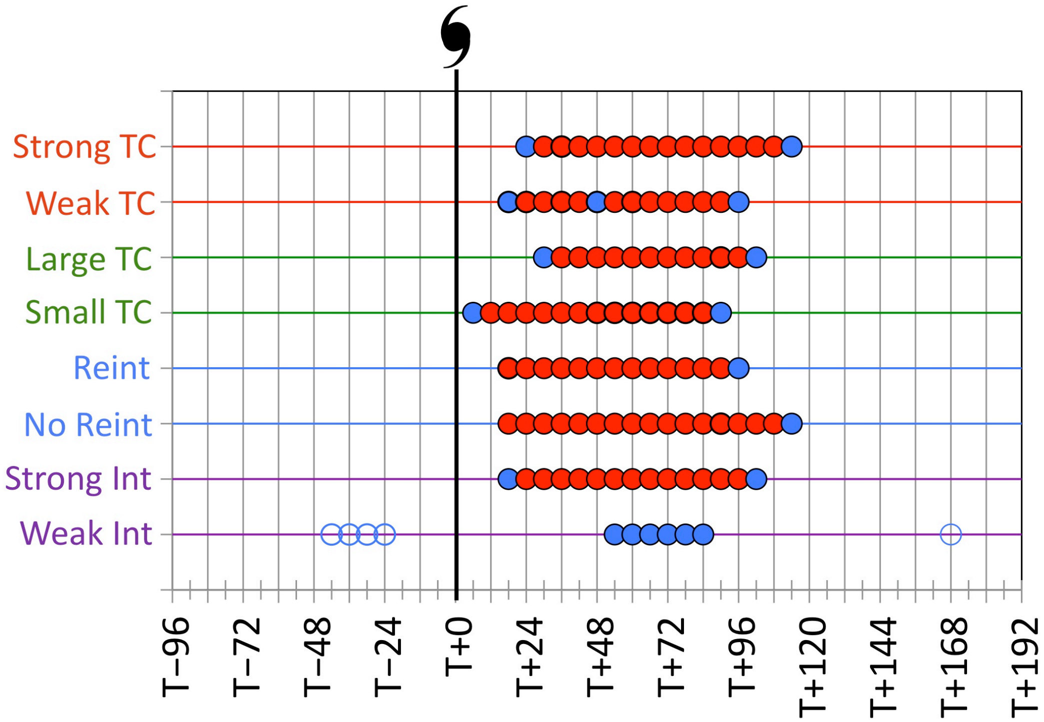

FIG. 2.21. As in Fig. 2.18, except for the following recurving WNP TC categories: strong and weak TCs at recurvature, large and small TCs at recurvature, TCs that undergo reintensification and no reintensification as ECs, and strong and weak TC–jet stream interactions.

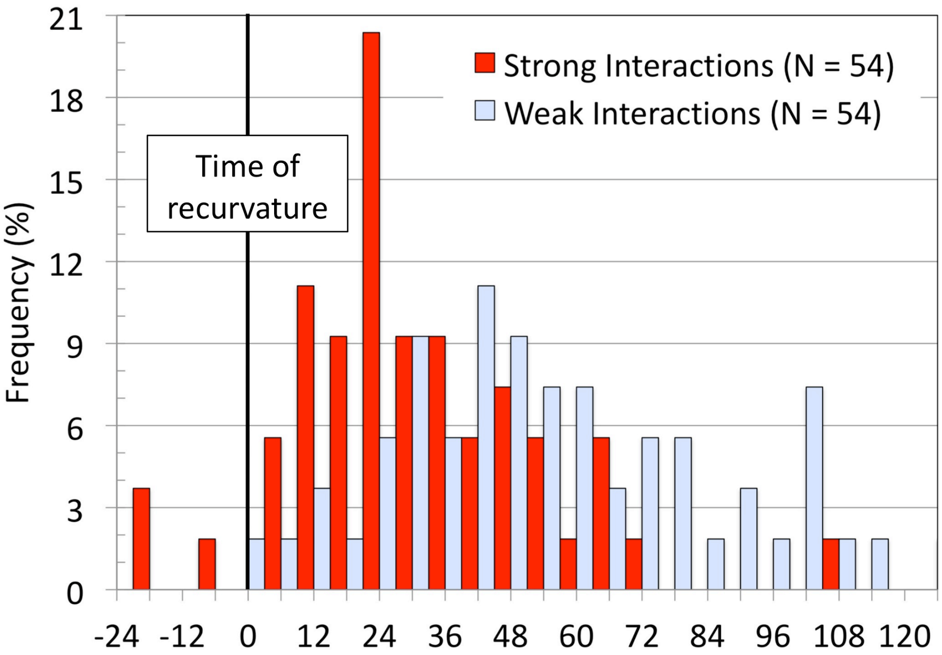

FIG. 2.22. Frequency distribution of the timing of maximum TC–jet stream interaction relative to recurvature for strong and weak TC–jet stream interactions.

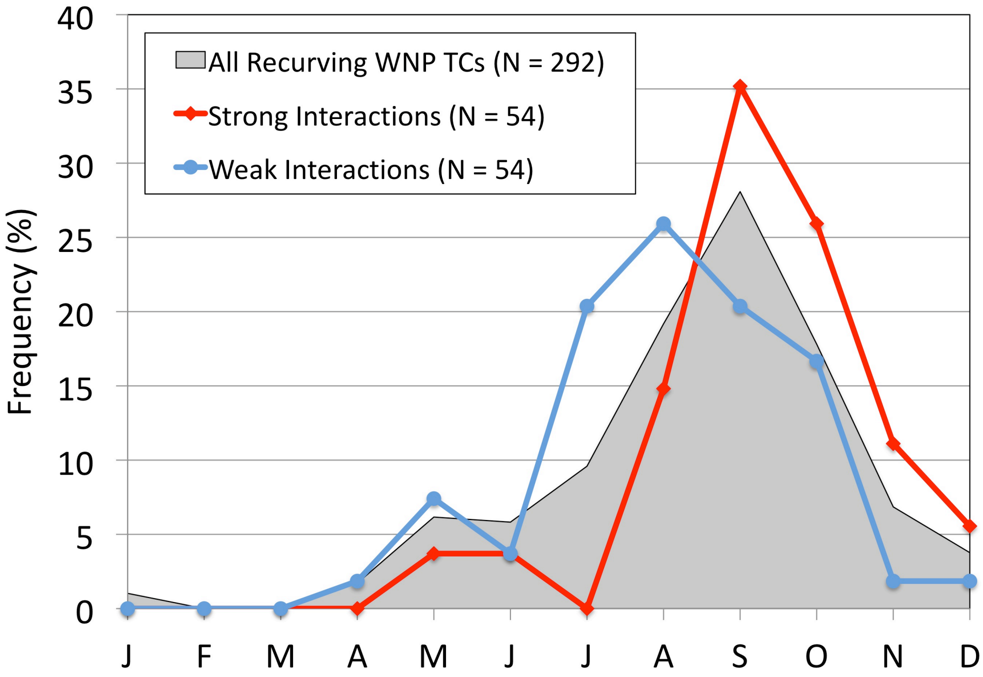

FIG. 2.23. Monthly frequency distribution of all recurving WNP TCs, and of recurving WNP TCs associated with strong and weak TC–jet stream interactions.

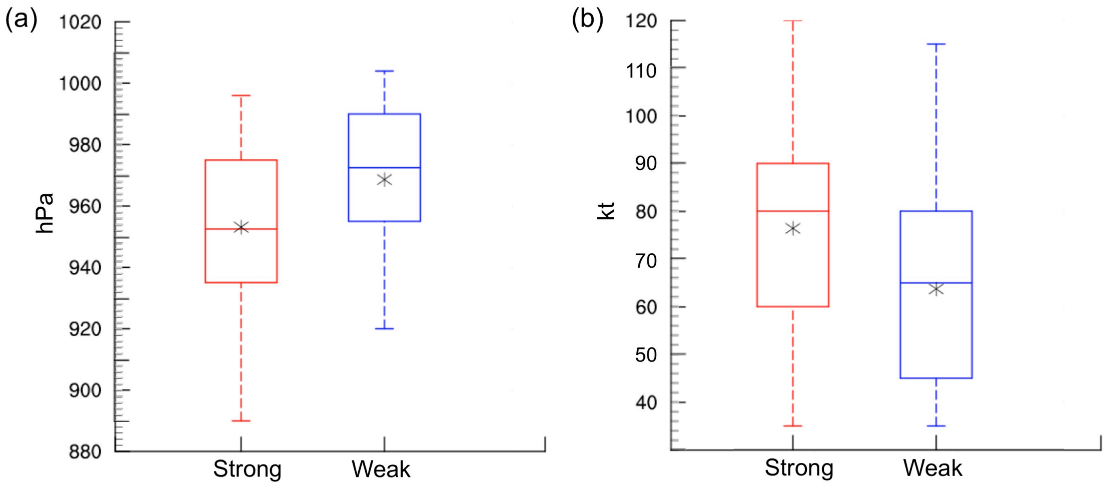

FIG. 2.24. Box plots of (a) MSLP (hPa) and (b) MSW (kt) at recurvature for recurving WNP TCs associated with strong (red) and weak (blue) TC–jet stream interactions. The bounds of each box are drawn at the 25th and 75th percentiles, the bar and asterisk inside each box denote the median and mean, respectively, and the whiskers extend from the 75th and 25th percentiles to the maximum and minimum values, respectively.

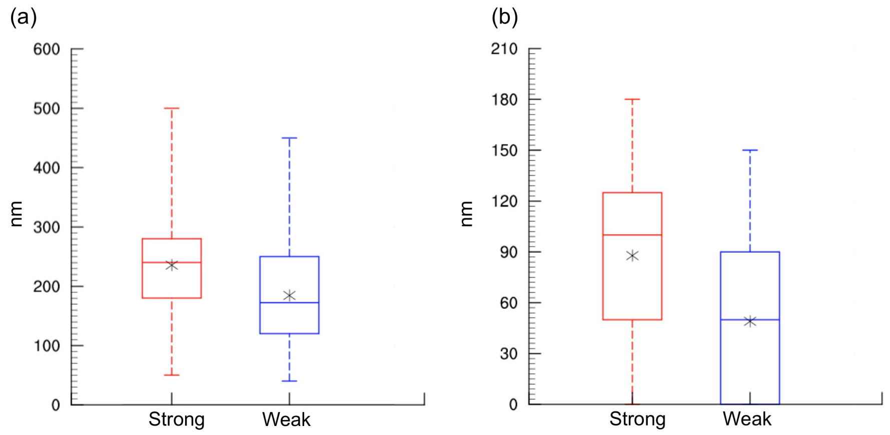

FIG. 2.25. As in Fig. 2.24, except for the maximum radius of (a) 30-kt winds (nm) and (b) 50-kt winds (nm).

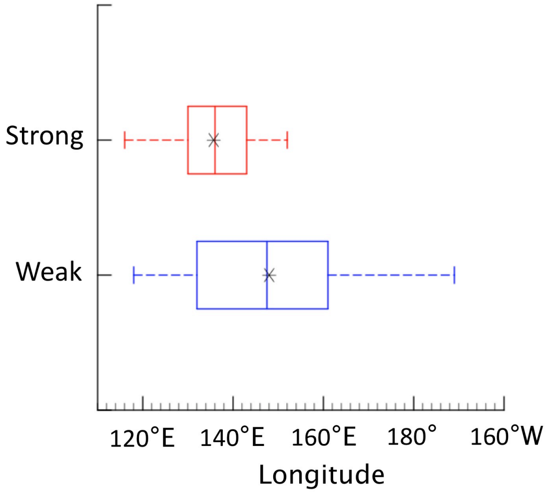

FIG. 2.26. As in Fig. 2.24, except for longitude of maximum TC–jet stream interaction point.

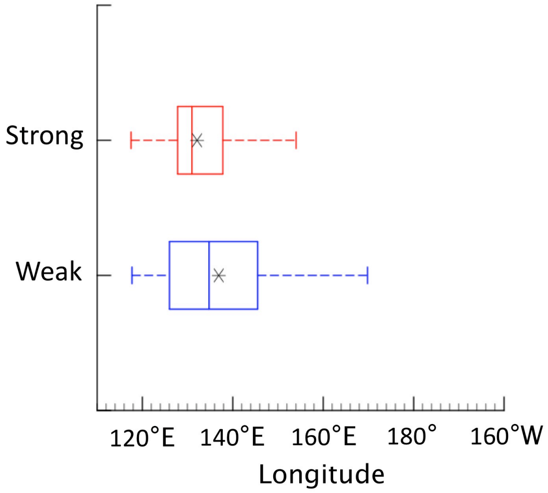

FIG. 2.27. As in Fig. 2.24, except for TC longitude at recurvature.

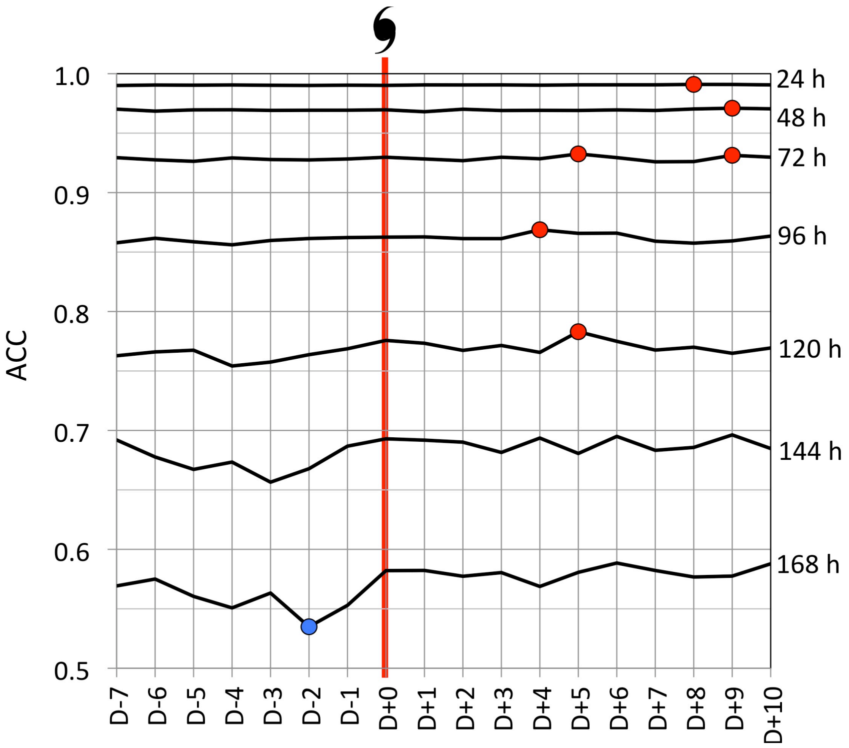

FIG. 2.28. Time series of daily composite ACCs for 24-h–168-h NH 500-hPa geopotential height forecasts verifying in the period surrounding WNP TC recurvature episodes. The red and blue circles denote statistically significant above- and below-normal composite ACCs, respectively, at the 95% confidence level.

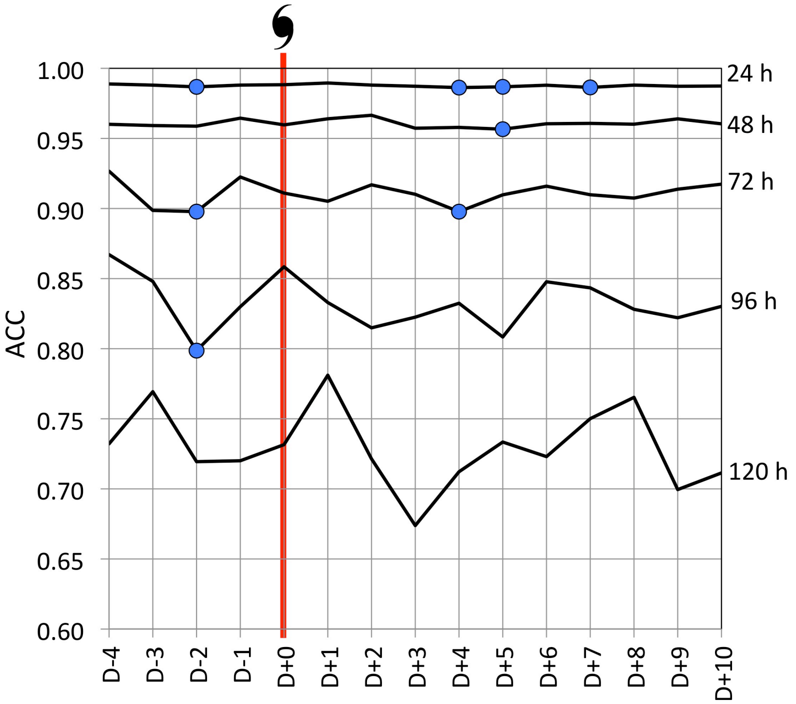

FIG. 2.29. As in Fig. 2.28, except for 24-h–120-h forecasts verifying in the period surrounding June WNP TC recurvature episodes.

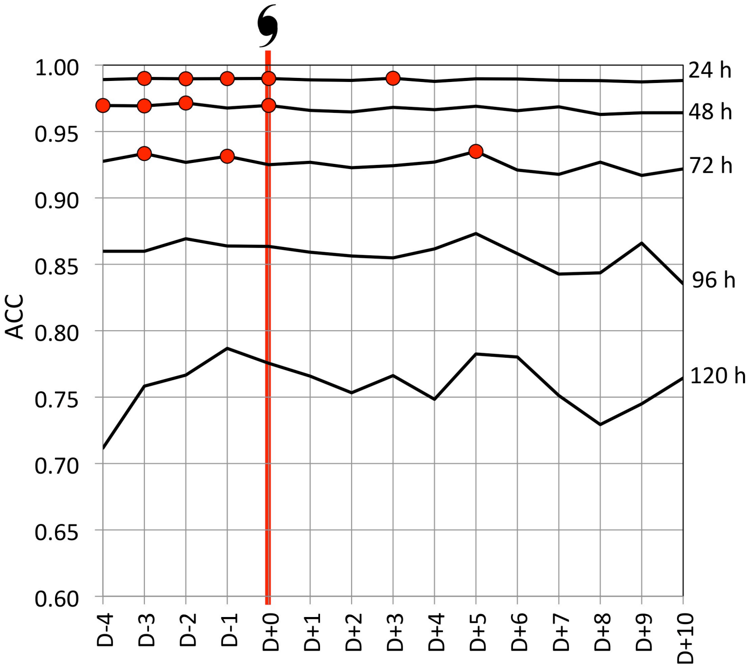

FIG. 2.30. As in Fig. 2.29, except for July WNP TC recurvature episodes.

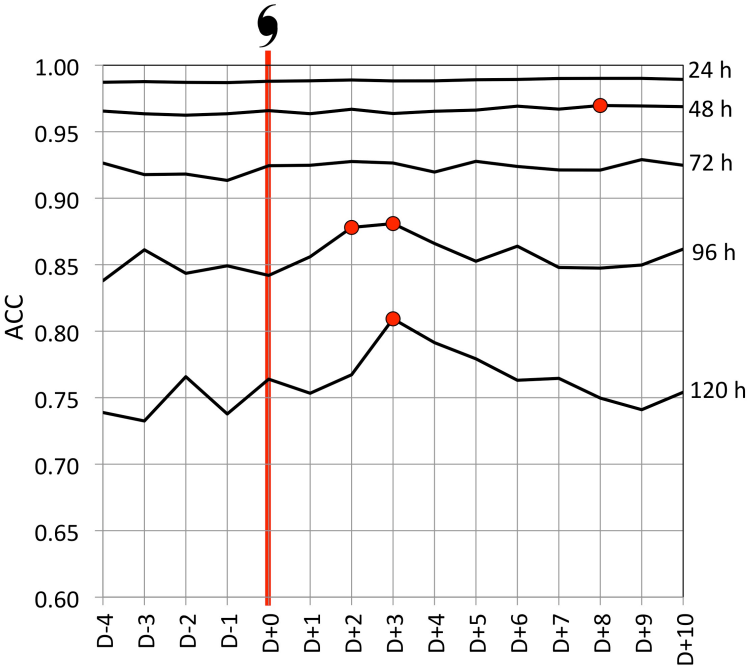

FIG. 2.31. As in Fig. 2.29, except for August WNP TC recurvature episodes.

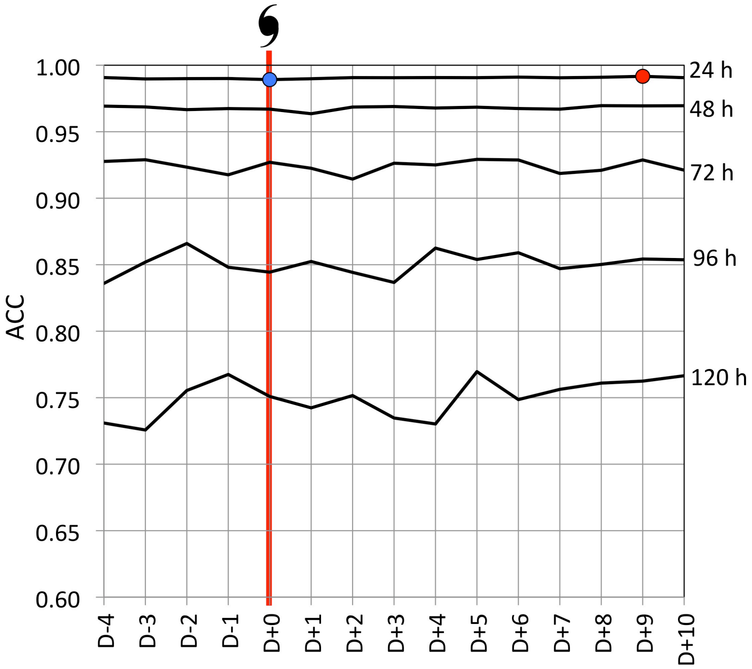

FIG. 2.32. As in Fig. 2.29, except for September WNP TC recurvature episodes.

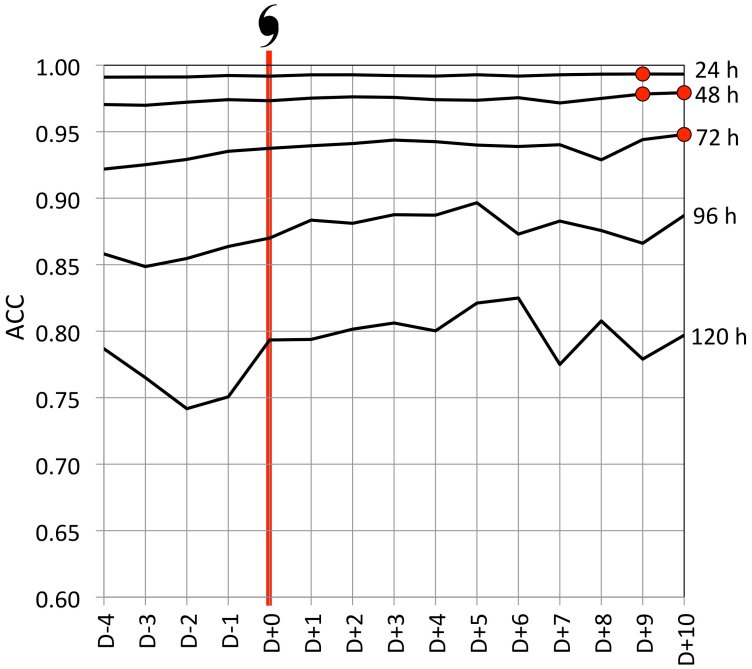

FIG. 2.33. As in Fig. 2.29, except for October WNP TC recurvature episodes.

(a) Strong

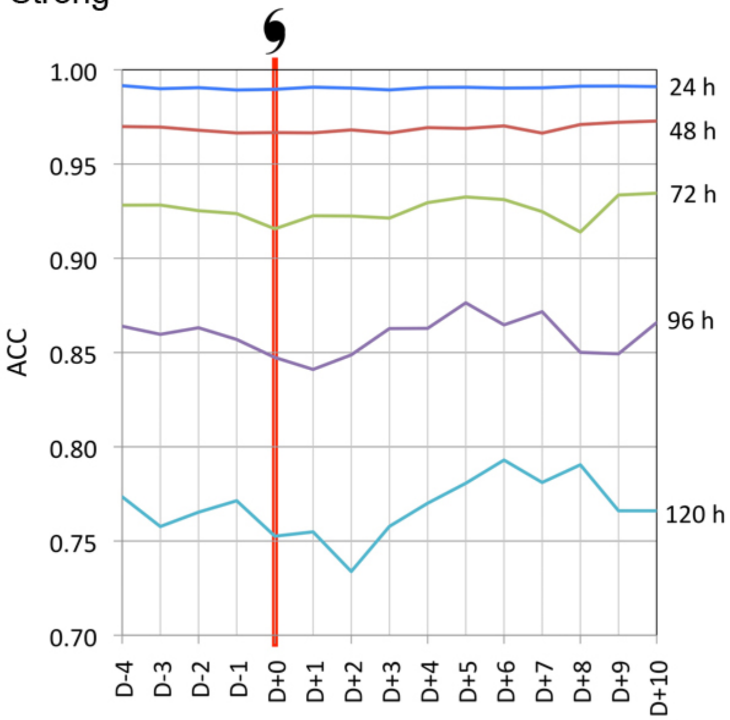

(b) Weak

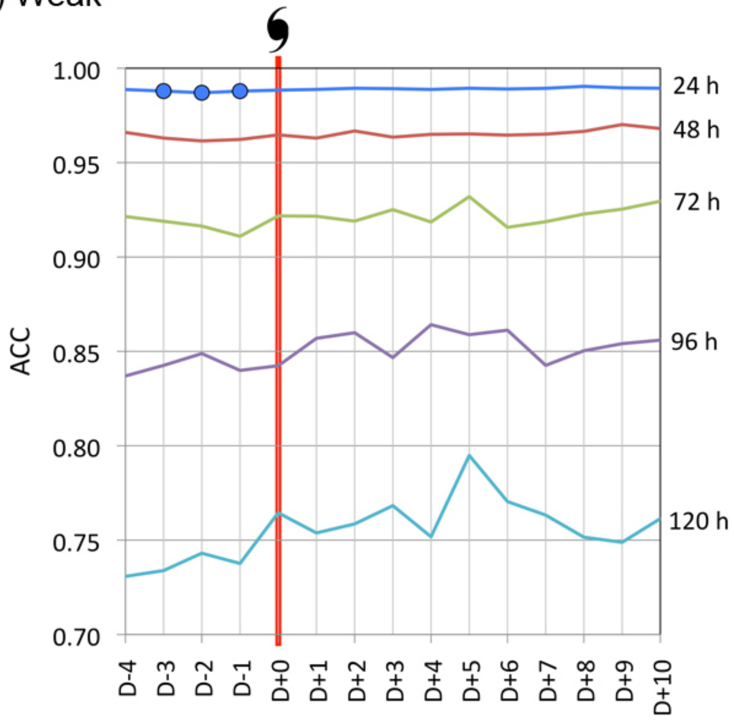

FIG. 2.34. As in Fig. 2.29, except for recurving WNP TCs associated with (a) strong and (b) weak TC–jet stream interactions.

3. Composite analysis of recurving WNP TCs

a. Motivation, purpose, and approach

A climatology of the downstream flow response to recurving WNP TCs presented in Chapter 2 indicates that above-normal meridional flow over the North Pacific is favored to develop following WNP TC recurvature episodes. However, the time of year and the strength of the TC–jet stream interaction substantially modulate the significance, duration, and timing of above-normal North Pacific meridional flow following WNP TC recurvature episodes.

Although the climatology suggests that recurving WNP TCs may induce above-normal meridional flow downstream over the North Pacific, such a causal association cannot be determined from the climatology alone. Accordingly, the goal of this composite analysis study is to examine the impact of recurving WNP TC on the downstream large-scale flow pattern from a synoptic–dynamic perspective. A composite analysis is performed of all recurving WNP TC episodes between 1979 and 2009 to explore the role of recurving WNP TCs in RWT amplification and the characteristic impact of subsequent RWT dispersion on the North American large-scale flow pattern. Composite analysis also is used to examine how time of year and the strength of the TC–jet stream interaction influence the Rossby wave response to recurving WNP TCs.

b. Data and methodology

i. Data

The 6-h (0000, 0600, 1200, and 1800 UTC) 2.5° NCEP–NCAR reanalysis dataset is used to construct all of the composite analyses in this study. Since the focus is on the extratropical flow pattern evolution surrounding WNP TC recurvature episodes rather than on mesoscale features associated with the TCs themselves (e.g., eyewall structure), we consider the NCEP–NCAR reanalysis data to possess sufficient spatial resolution for use in this study. While higher-resolution datasets are available for the period of study (1979–2009), the lower-resolution NCEP–NCAR reanalysis dataset is employed because it allows for the expeditious computation of composites generated from large sets of cases. To complement the composite analyses, case studies in Chapter 4 will employ higher-resolution data sets to examine synoptic and mesoscale details of the flow evolution surrounding recurving WNP TCs that may otherwise be masked by the datasets and compositing procedure used in this chapter.

ii. Compositing methodology

"Recurvature-relative" compositing is performed for all recurving WNP TCs (N = 292) and for recurving WNP TCs in May (N = 18), July (N = 28), September (N = 82), and November (N = 20). This compositing procedure entails shifting the reanalysis grids for each recurving TC case such that the TC recurvature point for each case is collocated with the mean TC recurvature point. This procedure is illustrated by Fig. 3.1, which demonstrates the impact of the recurvature-relative compositing procedure on individual recurving WNP TC tracks. To assess the Rossby wave response to recurving WNP TCs, composite 250-hPa meridional wind anomalies are computed using a recurvature-relative meridional wind climatology constructed from 21-day long-term (1979–2009) means. Unless otherwise indicated, all meridional wind anomalies displayed in this chapter are statistically significant at the 95% or greater confidence level as evaluated using a two-sided Student's *t* test.

Interaction-relative compositing is performed for recurving WNP TCs associated with TC–jet stream interactions that are categorized as strong (N = 54) and weak (N = 54) [see section 2b(iv)]. That is, grids for each recurving TC case are shifted such that the maximum TC–jet stream interaction point, defined as the point of maximum 250–150-hPa layer-averaged negative PV advection by the irrotational wind associated with the TC, for each case is collocated with the mean maximum TC–jet stream interaction point. Composite 250-hPa meridional wind anomalies are computed using an interaction-relative meridional wind climatology constructed from 21-day long-term means.

c. Results

i. Composite analysis of all recurving WNP TCs

As shown in the previous chapter [section 2c(ii)], above-normal meridional flow tends to be present over the North Pacific for several days following WNP TC recurvature episodes, which suggests that recurving WNP TCs may be associated with increased Rossby wave activity over the North Pacific. To identify possible signatures of Rossby wave activity associated with recurving WNP TCs, a recurvature-relative composite Hovmöller diagram of 35°–60°N-averaged 250-hPa meridional wind anomalies is constructed for the period surrounding WNP TC recurvature episodes (Fig. 3.2).

Figure 3.2 shows a marked signature of RWT dispersion across Europe, Asia, and the North Pacific between T−96 h and T+24 h surrounding WNP TC recurvature episodes.

Though RWT dispersion is most evident between T−96 h and T+24 h, statistically significant southerly flow anomalies eventually develop over North America by ~T+84 h in association with RWT dispersion. Considering the first occurrence of statistically significant (at the 99% confidence level) meridional wind anomalies to be the leading edge of the RWT, the zonal group speed of the RWT is estimated to be 42° day^{-1}, or 36.5 m s^{-1}. The estimated zonal group speed is lower (37° day^{-1}, or 32.1 m s^{-1}) when computed based on the peak amplitude of the RWT (i.e., the peak magnitudes of the positive and negative meridional wind anomalies). Based on the northerlies on the eastern flank of the ridge directly downstream of the recurving TC, the zonal phase speed of the RWT is estimated to be 6° day^{-1}, or 5.2 m s^{-1}.

The composite maximum zonal wind speed over the North Pacific between 35°N and 60°N 24-h prior to RWT amplification is ~35 m s^{-1} (not shown), which implies that the zonal group speed of the RWT is ~90–110% of the maximum zonal wind speed. Idealized simulations of a vorticity perturbation within a baroclinically unstable jet stream indicate that the zonal group speed of the resulting RWT is typically 75–100% of the maximum zonal wind speed (e.g., Simmons and Hoskins 1979). In idealized simulations of a recurving TC interacting with a baroclinically unstable jet stream (Riemer et al. 2008), the zonal group speed of the RWT is only 53–60% of the maximum zonal wind speed[10]. Thus, the zonal group speed of the composite RWT is comparable to the typical zonal group speed of a RWT initiated by a vorticity perturbation within the jet stream rather than by a recurving TC equatorward of the jet stream. A possible

---

[10] Riemer et al. (2008) speculate that persistent outflow from the TC hinders the eastward progression of the downstream ridge, thus slowing RWT dispersion.

explanation for the relatively fast composite zonal group speed based on a preliminary examination of individual recurving WNP TC episodes is that a disproportionate contribution to the composite RWT may be from recurving WNP TC cases associated with RWT dispersion along jet streams that contain much stronger zonal wind speeds than the composite maximum zonal wind speed.

Further examination of Fig. 3.2 indicates that the RWT emanating from Europe and Asia amplifies and increases in wavelength between T−24 h and T+24 h. While the RWT is over Europe and Asia, its estimated wavelength[11] is 1800 km, whereas once the RWT is over the North Pacific, its estimated wavelength[12] is 2600 km. This increased wavelength is consistent with the stronger time-mean jet stream over the North Pacific relative to Asia[13] (e.g., Fig. 1.2). After ~T+0 h, the individual meridional flow anomalies constituting the RWT are notably more persistent, lasting ~5 days vs. ~3 days prior to T+0 h.

The composite Hovmöller diagram shown in Fig. 3.2 suggests that recurving WNP TC episodes are associated RWT amplification and dispersion across the North Pacific into North America. To examine the relationship between recurving WNP TCs and RWT amplification and dispersion, recurvature-relative composite plots of 500-hPa ascent, and 250-hPa meridional wind anomalies, PV, and irrotational wind over Asia, the North

---

[11] The wavelength is computed from the separation of the two swaths of southerlies over Europe and Asia.

[12] The wavelength is computed from the separation of the two swaths of southerlies over the North Pacific.

[13] Riemer et al. (2008) find that for WNP TC recurvature episodes, stronger jet streams favor RWTs with longer wavelengths.

Pacific, and North America are displayed for the period surrounding WNP TC recurvature (Fig. 3.3).

The meridional wind anomalies shown in Figure 3.3 indicate that a short-wavelength, low-amplitude RWT migrates along a weak meridional PV gradient (i.e., waveguide) over Europe and Asia at ~55°N between T−96 and T−48 h (Figs. 3.3a–c). By T−48 h (Fig. 3.3c), a positively tilted trough develops over northeastern China. Between T−24 h and T+48 h (Fig. 3.3d–g), ridge amplification occurs over Japan in conjunction with inferred negative PV advection by the irrotational wind. During this period, a clear link is evident between the ridge amplification and the diabatically driven outflow of the recurving TC. The irrotational wind is directed radially outward from ascent coinciding with the recurving TC and into the meridional PV gradient. The irrotational wind also is directed into the upstream flank of the ridge/downstream flank of the positively tilted trough, which helps to anchor the ridge as it amplifies. The strengthening PV gradient along the upstream flank of the ridge between T−24 h and T+24 h (Figs. 3.3d–f) is indicative of jet streak intensification. During the same period, the ascent that is initially coaligned with the TC gradually becomes stretched poleward and eastward, which is consistent with the characteristic poleward and eastward shift in clouds and precipitation observed during the ET transformation stage (e.g., Fig. 1.4).

In conjunction with the implied diabatic ridge amplification and jet streak intensification over the WNP between T−24 h and T+48 h, RWT dispersion is evident across the North Pacific (Figs. 3.3d–g). East of the diabatically amplified ridge, a trough develops over the central North Pacific between T−24 h and T+24 h (Figs. 3.3d–f), and a ridge forms off the western North American coast between T+0 h and T+48 h (Figs.

3.3e–g). Downstream cyclogenesis associated with RWT dispersion is implied by midlevel ascent just downstream of the central North Pacific trough at T+48 h (Fig. 3.3g).

Continued RWT dispersion across the North Pacific into North America between T+72 h and T+144 h is evident in Figs. 3.3h–k. Between T+72 h and T+120 h, ascent is indicated ahead of the aforementioned central North Pacific trough, which has moved eastward from the central North Pacific (Figs. 3.3h–j). At T+96 h, a neutrally tilted high-latitude ridge has become established over western North America, and a positively tilted trough extends southwestward from the northern Plains toward the Four Corners region by T+96 h (Fig. 3.3i). The ridge and trough remain evident in the composite fields through T+144 h, though their amplitudes decrease (Fig. 3.3k). The positive tilt of the trough between T+96 h and T+144 h (Fig. 3.3i–k) are consistent with AWB and southeastward RWT dispersion.

To examine the synoptic flow pattern evolution surrounding WNP TC recurvature episodes, recurvature-relative composite plots of total-column precipitable water (PW), 250-hPa wind speed, 1000–500-hPa thickness, and sea level pressure (SLP) are displayed at 48-h intervals between T−72 h and T+120 h (Fig. 3.4). Figures 3.4a–d shows that as the WNP TC recurves into the midlatitudes between T−72 h and T+24 h, a PW plume associated with the TC surges poleward and eastward, and a thickness ridge and jet streak develop just downstream of the TC. The jet streak formation just downstream of the TC by T+24 h may be associated with Coriolis torquing of prolonged TC divergent outflow between T−24 h and T+24 h (Figs. 3.3d–f) that is collocated with and just upstream of the jet streak (Figs. 3.4b,c). Near the poleward exit region of the jet streak over the Bering Sea, a cyclone becomes evident between T−72 h and T+24 h (Figs. 3.4a–c). East of this cyclone, warm-air advection between T+24 h and T+120 h is implied by the geostrophic surface wind directed toward lower thickness values over Alaska and northwestern Canada (Figs. 3.4c–e). This warm air advection coincides with the amplification of a thickness ridge by T+120 h (Fig. 3.4e) and a PV ridge by T+96 h (Fig. 3.3i).

ii. Composite analysis of recurving WNP TCs grouped by month

To compare the downstream large-scale flow evolution associated with recurving WNP TC episodes at different times of the year, recurvature-relative composite analyses are created for WNP TC recurvature episodes in May, July, September, and November (Figs. 3.5–3.8, respectively). These composite analyses show 500-hPa ascent, and 250-hPa meridional wind anomalies, PV, and irrotational wind over eastern Asia, the North Pacific, and North America at 48-h intervals between T+0 h and T+144 h.

At T+0 h in each month presented, divergent outflow associated with the recurving TC is directed into the eastern flank of an upstream eastern Asian coast trough/western flank of a downstream WNP ridge (3.5a, 3.6a, 3.7a, and 3.8a). In May, September, and November (Figs. 3.5a, 3.7a, and 3.8a), the upstream trough is well defined, positively tilted, and features a relatively strong PV gradient on its eastern flank, whereas in July (Fig. 3.6a), the upstream trough is poorly defined, neutrally tilted, and features a relatively weak PV gradient on its eastern flank. This weak PV gradient at T+0 h in July suggests that PV advection by the irrotational wind associated with the TC is relatively weak. It is hypothesized that the weak PV gradient is a reflection of, and explanation for, the relative absence of downstream ridge amplification and inferred jet streak intensification in July compared to May, September, and November. By T+48 h in May, September, and November, a well-defined and relatively broad ridge with an inferred jet streak along its poleward edge is noted over the WNP (Figs. 3.5b, 3.7b, and 3.8b, respectively). By contrast, the WNP ridge at T+48 h in July is poorly defined, relatively narrow, and lacks a signature of a jet streak along its poleward edge (Fig. 3.6b).

Of interest is a signal of precipitation (i.e., ascent) associated with the recurving WNP TC at T+0 h in each of the four months. At T+0 h in May, July, September, and November, ascent extends northeastward from the recurving TC center (Figs. 3.5a, 3.6a, 3.7a, and 3.8a, respectively), as is typical of a TC undergoing transformation. In May and November, however, an ascent maximum is evident well poleward of the TC center, near southern Japan (Figs. 3.5a and 3.8a, respectively). The position of the ascent within the eastern flank of the upstream trough and inferred equatorward jet entrance region suggests that it is located within a region of synoptic-scale quasigeostrophic (QG) forcing for ascent. This ascent maximum is also collocated with a PW plume extending from the TC, as well as weak lower-tropospheric warm-air advection associated with the intersection of lower-tropospheric southerly flow with a west–east-orientated baroclinic zone (not shown). In May, the ascent maximum associated with the TC is distinct from the poleward ascent maximum associated with QG forcing (Fig. 3.5a), whereas in November, a distinct ascent maximum directly associated with the TC is not discernible within a band of ascent that stretches poleward from the TC (Fig. 3.8a). The more band-like structure of ascent stretching poleward from the recurving TC in November than in May suggests that frontogenetical forcing associated with ET is more dominant for recurving WNP TCs in November than for May at T+0 h.

The absence of pronounced WNP ridge amplification and jet streak intensification in July noted earlier is not conducive to RWT amplification and dispersion (Fig. 3.6). In July, a weak ridge at T+0 h is seen to dissipate by T+48 h, with no new development occurring downstream (Figs. 3.6c,d). In contrast, in May, September, and November, a well-defined RWT, comprised of the upstream trough interacting with the TC, the amplifying downstream ridge, and a new trough farther downstream, is evident at T+48 h (Figs. 3.5b, 3.7b, and 3.8b, respectively).

Although May, September, and November all feature RWT dispersion following WNP TC recurvature episodes, the characteristics of the RWT vary among the months. At T+48 h in November, a RWT extends across the entire North Pacific, with the leading edge of the RWT making landfall along the southwestern U.S coast (Fig. 3.8b). In contrast, at T+48 h in May and September, the leading edge of a RWT has migrated eastward only as far as the central–eastern North Pacific (Figs. 3.5b and 3.7b, respectively). The faster eastward RWT dispersion in November compared to May and September likely reflects the stronger background zonal wind speed present in November compared to May and September (e.g., Fig. 1.2).

At T+48 h, notable month-to-month differences in downstream extratropical cyclogenesis are evident as indicated by coherent ascent maxima located within regions of inferred QG forcing for ascent. In both May and September, an ascent maximum and associated region of divergent outflow are located just downstream of a central North Pacific trough at the leading edge of the RWT (Figs. 3.5b and Figs. 3.7b), although the ascent and outflow are more distinct in May than in September. In November (Fig. 3.8b), two distinct regions of ascent and associated divergent outflow are apparent downstream of the recurving WNP. One region of ascent and divergent outflow is located over the western Aleutian Islands, ahead of a negatively tilted trough and within the inferred poleward exit region of the WNP jet stream. Farther downstream, a second region of ascent and divergent outflow is positioned within the eastern flank of a positively tilted trough over the eastern North Pacific. Recurving WNP TC episodes in July are not associated with any distinct regions of ascent and associated divergent outflow downstream in conjunction with implied QG forcing for ascent at T+48 h (Fig 3.6b).

Between T+96 h and T+144 h, the RWT structure in May, September, and November continues to differ. In May, the RWT is zonally oriented over the eastern North Pacific and western North America at T+96 h (Fig, 3.5c) but migrates southeastward between T+96 h and T+144 h (note the positively tilted ridge along the southwestern Gulf of Mexico coast indicative of AWB at T+144 h in Fig. 3.5d). This southeastward RWT migration is associated with the development of split flow over western North America by T+144 h (Fig. 3.5d)[14].

In September, the RWT is less distinct at T+96 h than at T+48 h (compare Fig. 3.7c with Fig. 3.7b), and is comprised of a neutrally tilted ridge along the western North American coast and a weak positively tilted trough that extends from central Canada to the southwestern U.S. This positively tilted trough is suggestive of AWB and southeastward RWT dispersion similar to May recurving WNP TC episodes. Between T+96 h and T+144, this ridge retrogrades slightly as a trough develops upstream over the

---

[14] The northern and southern branches of this split flow are indicated by the enhanced PV gradient over Canada and the southwestern U.S., respectively (Fig. 3.5d).

central North Pacific.   By T+144 h (Fig. 3.7d) the only part of the RWT that remains is the ridge along the western North American.

Following November WNP TC recurvature episodes, the RWT that extends across the entire North Pacific at T+48 h (Fig. 3.8b) undergoes a structural change by T+96 h (Fig. 3.8c). By this time, a high-latitude ridge amplifies over northwestern North America downstream of a negatively tilted trough near the Aleutian Islands at T+96 h. Combined with the high-latitude ridge amplification over western North America, the negative tilt of the trough near the Aleutian Islands is consistent with northeastward RWT dispersion and is likely a reflection of CWB. The signature of CWB is consistent with the aforementioned negatively tilted trough associated with inferred western Aleutian cyclogenesis seen at T+48 h (Fig. 3.8b).   At the same time, a distinct positively tilted trough has become established downstream over western–central North America, and a positively tilted ridge as suggested by the meridional wind anomaly field has formed over Mexico and the western Gulf of Mexico, downstream of the western–central North American trough (Fig. 3.8c). The positively tilted trough and ridge are indicative of AWB and southeastward RWT dispersion. Thus, both poleward and equatorward RWT dispersion is evident at T+96 in November. By T+144 h (Fig. 3.8d), the RWT is no longer apparent, although a high-latitude ridge remains in place over western North America.

iii. Composite analysis of recurving WNP TCs grouped by TC–jet stream interaction strength

Results of the climatology presented in Chapter 2 indicate that recurving WNP TCs associated with strong TC–jet stream interactions may favor Rossby wave activity over the North Pacific. To examine synoptic differences between recurving WNP TCs associated with strong vs. weak TC–jet stream interactions, interaction-relative composite analyses are constructed and compared for strong and weak TC–jet stream interactions.

Figure 3.9 displays interaction-relative composite analyses of 500-hPa ascent, total-column PW, and 200-hPa PV, negative PV advection by the irrotational wind, wind speed, and irrotational wind over the WNP at the time of maximum TC–jet stream interaction (T+0 h) for strong and weak TC–jet stream interactions[15]. This figure indicates that substantial structurual differences exist between the two categories of recurving WNP TCS.

For strong TC–jet stream interaction cases at T+0 h (Fig. 3.9a), strong ascent is located over and northeast of the recurving TC within a tropical moisture plume (PW values in excess of 55 mm). Just upstream of the recurving TC and its associated strong ascent is a positively tilted trough featuring 200-hPa PV values in excess of 8 PVU. A broad region of strong diabatically driven divergent outflow associated with the TC ascent is impinging upon a strong PV gradient and jet stream. The impingement of the outflow on the PV gradient and jet stream is manifested as strong (greater than 8 PVU

---

[15] Recall from section 2c(ii) that the maximum TC–jet stream interaction for strong and weak TC–jet stream interaction cases tends to occur 30.5 h and 56 h after TC recurvature, respectively.

day^{-1}) negative PV advection by the irrotational wind and a 70 m s^{-1} anticyclonically curved jet streak between the trough to the northwest and a ridge to the southeast. The position of the TC ascent in the equatorward entrance region of the jet streak suggests that the divergent TC outflow acts to reinforce the jet streak, thus maintaining forcing for ascent in the equatorward jet-entrance region that drives the TC outflow.

For weak TC–jet stream interaction cases at T+0 h (Fig. 3.9b), the same synoptic features are present as for strong TC–jet stream interaction cases, but are notably weaker. Relatively weak ascent is located over and northeast of the position of the recurving TC within a diffuse tropical moisture plume featuring 45-mm PW values. The recurving TC and ascent are located near and just downstream of the base of a positively tilted 200-hPa trough that comprises maximum PV values of ~6 PVU. A relatively small region of diabatically driven divergent outflow associated with the TC ascent is impinging upon a relatively weak PV gradient and jet stream. Maximum values of negative PV advection by the irrotational wind of 2 PVU day^{-1} are found just upstream of a 40 m s^{-1} jet streak positioned between the positively tilted trough to the northwest and a relatively flat ridge to the southeast.

A central issue is whether the strength of the TC–jet stream interaction affects the evolution of the downstream large-scale flow pattern following recurving WNP TCs. To address this question, interaction-relative composite analyses of 500-hPa ascent, and 250-hPa meridional wind anomalies, PV, and irrotational wind for eastern Asia, the North Pacific, and North America are compared for strong TC–jet stream interactions for T+0 h–T+72 h (Fig. 3.10) and weak TC–jet stream interactions for T+0 h–T+48 h (Fig. 3.11).

Comparison of Figs. 3.10 and 3.11 readily confirms that the downstream flow response to a recurving WNP TC is substantially different depending on whether the TC undergoes a strong or weak interaction with the jet stream. At T+0 h for strong TC–jet stream interaction cases (Fig. 3.10a), a well-defined RWT stretches from eastern Asia to the central North Pacific. Downstream of the positively tilted WNP trough–ridge couplet noted in Fig. 3.9, a negatively tilted trough is located over the central North Pacific (Fig. 3.10a). The negative tilt of the central North Pacific trough is suggestive of CWB and northeastward RWT dispersion. By T+24 h (Fig. 3.10b), the negatively tilted trough has amplified and a meridionally expansive ridge has developed over the eastern North Pacific. Between T+24 h and T+72 h (Figs. 3.10b–d), a high-latitude ridge is established over western North America. Strong, meridionally extensive northerly flow on the eastern flank of the ridge suggests that cold-air outbreaks over the western U.S. might be favored in this pattern. Downstream of the extensive northerlies, a positively tilted trough stretches from central Canada southward and westward into the Desert Southwest by T+72 h. In summary, Figure 3.10 reveals that strong TC–jet stream interactions favor RWT dispersion across the North Pacific that leads to the onset of a high-latitude ridge over western North America and a trough over central Canada and the southwestern U.S.

In contrast to recurving WNP TCs associated with strong TC–jet stream interactions (Fig. 3.10), Fig. 3.11 indicates that recurving WNP TCs associated with weak TC–jet stream interactions do not favor RWT dispersion across the North Pacific. For weak TC–jet stream interaction cases at T+0 h (Fig. 3.11a), a weak, positively tilted trough is over the central North Pacific downstream of a positively tilted trough–ridge couplet over the WNP associated with the recurving TC. Compared to the downstream trough over the central North Pacific that develops following strong TC–jet stream interactions (Fig. 3.10a), the downstream trough that develops following weak TC–jet stream interactions is considerably weaker and located farther equatorward (Fig. 3.11b). The positive tilt of the troughs and ridges comprising the RWT is suggestive of equatorward RWT dispersion and AWB. Between T+24 h and T+48 h (Fig. 3.11b,c), the weak RWT noted at T+0 h (Fig. 3.11a) dissipates. Recurving WNP TCs associated with weak TC–jet stream interactions thus are found to have little impact on the large-scale flow pattern over the North Pacific and North America.

d. Summary

In Chapter 2, a climatological study revealed that the North Pacific flow pattern tends to become more meridional than normal following WNP TC recurvature. The significance, duration, and timing of the above-normal meridional North Pacific flow pattern was noted to be influenced by the time of year and by the strength of the TC–jet stream interaction. In this chapter, the overall influence of recurving WNP TCs on the downstream large-scale flow pattern is examined from a synoptic–dynamic perspective using recurvature-relative composite analysis. Additionally, recurvature-relative composite analysis is used to examine how time of year influences the downstream large-scale flow pattern evolution following WNP TC recurvature episodes. Finally, interaction-relative composite analysis is employed to examine how TC–jet stream interaction strength influences the downstream large-scale flow response to recurving WNP TCs.

Composite analysis of all recurving WNP TCs for 1979–2009 reveals that recurving WNP TCs are associated with the amplification of a preexisting RWT migrating eastward from Asia that subsequently disperses across the North Pacific and reaches North America within four days of WNP TC recurvature. A key finding is that upper-tropospheric ridge amplification and jet streak intensification over the WNP, which is deemed to be an important antecedent to RWT dispersion across the North Pacific and into North America, appears to occur in direct response to the impingement of diabatically induced upper-tropospheric divergent outflow associated with the recurving TC on the WNP waveguide/jet stream.

Results of the composite analysis of recurving WNP TCs based on time of year reveal that recurvature episodes in certain months favor RWT amplification and dispersion. Recurving WNP TCs in July are not associated with distinct RWT amplification and dispersion, whereas recurving TCs in May, September, and November are associated with RWT amplification and dispersion across the North Pacific into North America. November WNP TC recurvature episodes tend to favor the onset of high-latitude upper-tropospheric ridges over western North America, whereas recurving WNP TCs in May, July, and September do not.

Composite analysis of recurving WNP TCs based on the strength of the TC–jet stream interaction also indicates that strong TC–jet stream interactions are associated with the amplification and dispersion of a RWT that leads to a high-latitude upper-tropospheric ridge over western North America and a trough over the central Canada and the southwestern U.S. In contrast, weak TC–jet stream interactions are associated with a relatively low-amplitude RWT that dissipates within two days of the time of maximum

TC–jet stream interaction. Over the North Pacific, CWB is favored following strong TC–jet stream interactions, whereas AWB is favored following weak TC–jet stream interactions.

Motivated by these composite analysis findings, multiscale case studies will be presented in Chapter 4 that examine the role of recurving WNP TCs in large-scale flow reconfigurations over North America and associated high-impact weather events. In addition, a case study will examine synoptic–dynamic processes that influence the predictability of the downstream extratropical flow response to WNP TC recurvature.

e. Figures

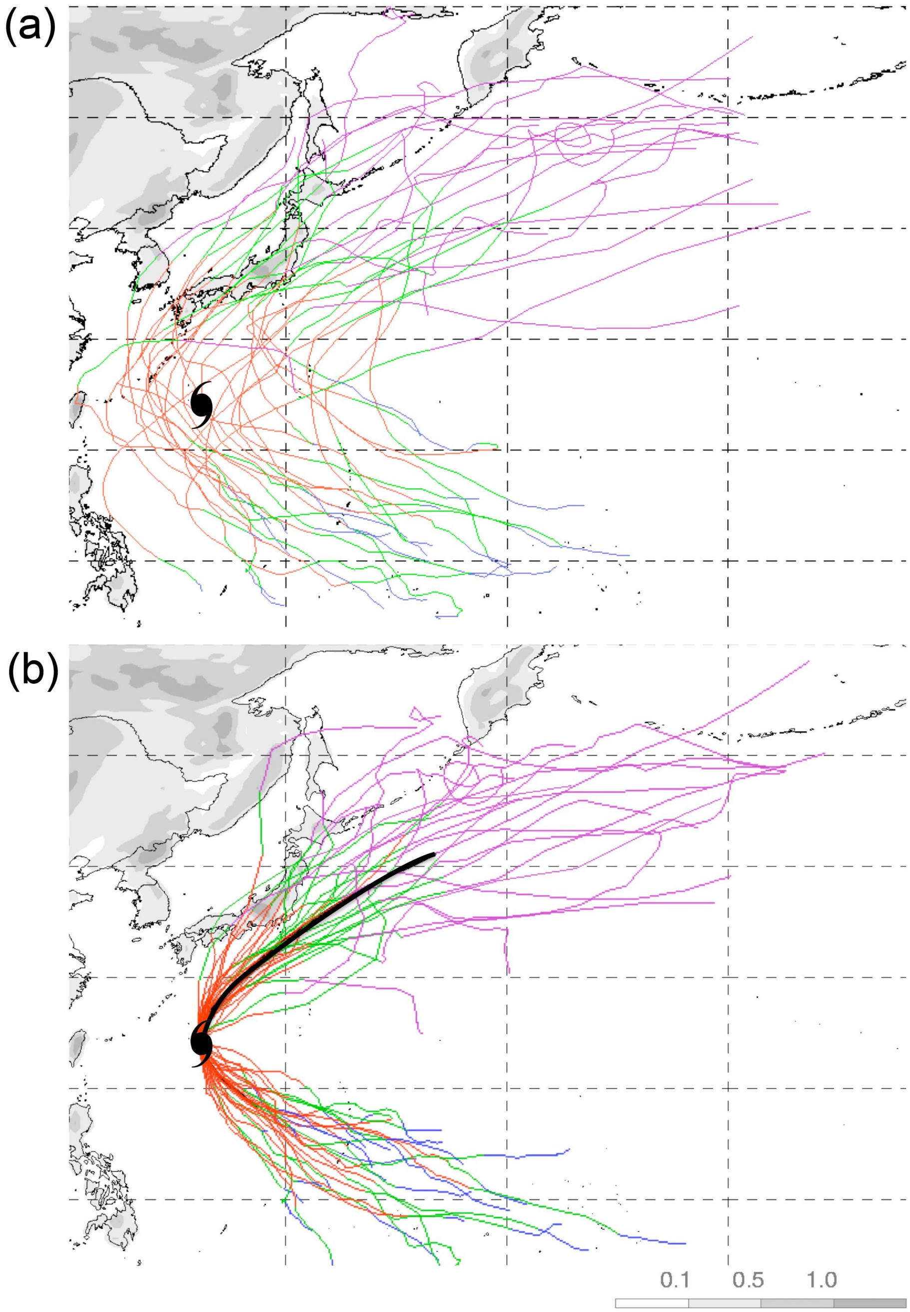

FIG. 3.1. A representative sample of recurving WNP TC tracks (N = 29) plotted in (a) a conventional geography-relative framework and (b) a recurvature-relative framework. The TC symbol denotes the mean TC recurvature point of the sample, and the black curve in (b) denotes the composite TC track of the sample for T+0 h through T+96 h. Track color corresponds to TC category (blue to TD, green to TS, red to TY, and purple to EC). Surface elevation is shaded according to the gray scale (km).

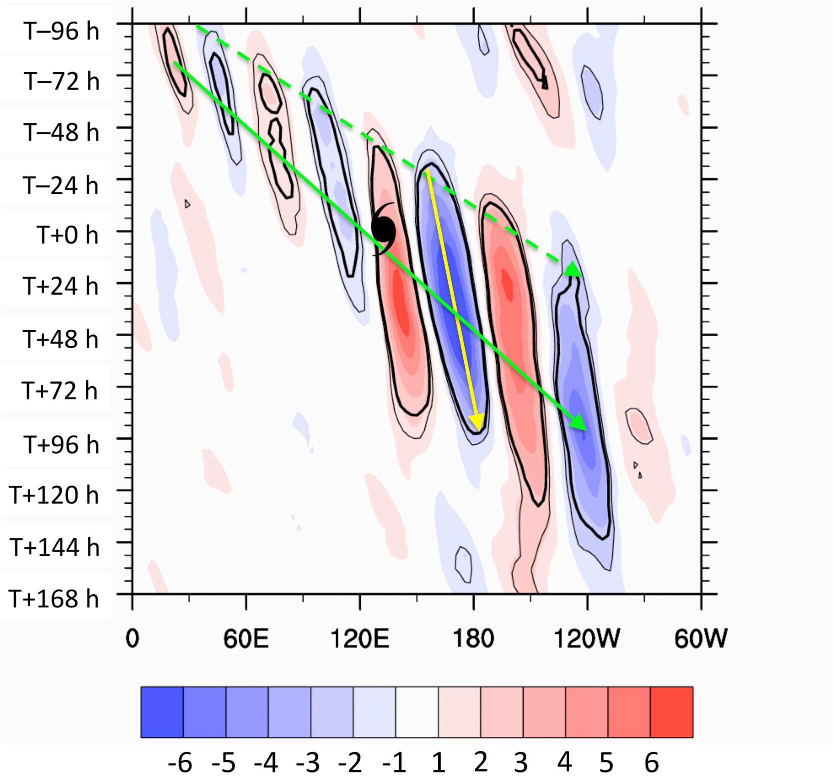

FIG. 3.2. Recurvature-relative composite Hovmöller diagram (0° to 60°W) of the 35°–60°N-averaged 250-hPa meridional wind anomaly (shaded, m s^{-1}) for all recurving WNP TCs (N = 292). Thin (thick) black contours denote statistical significance at the 95% (99%) confidence level. The dashed and solid green arrows indicate estimated zonal group speeds based on the leading edge (c_g = 36.5 m s^{-1}) and peak amplitude (c_g = 32.1 m s^{-1}) of the Rossby wave train, respectively, whereas the yellow arrow indicates the estimated Rossby wave train zonal phase speed (c_p = 5.2 m s^{-1}). The TC symbol denotes the longitude of the composite TC at recurvature.

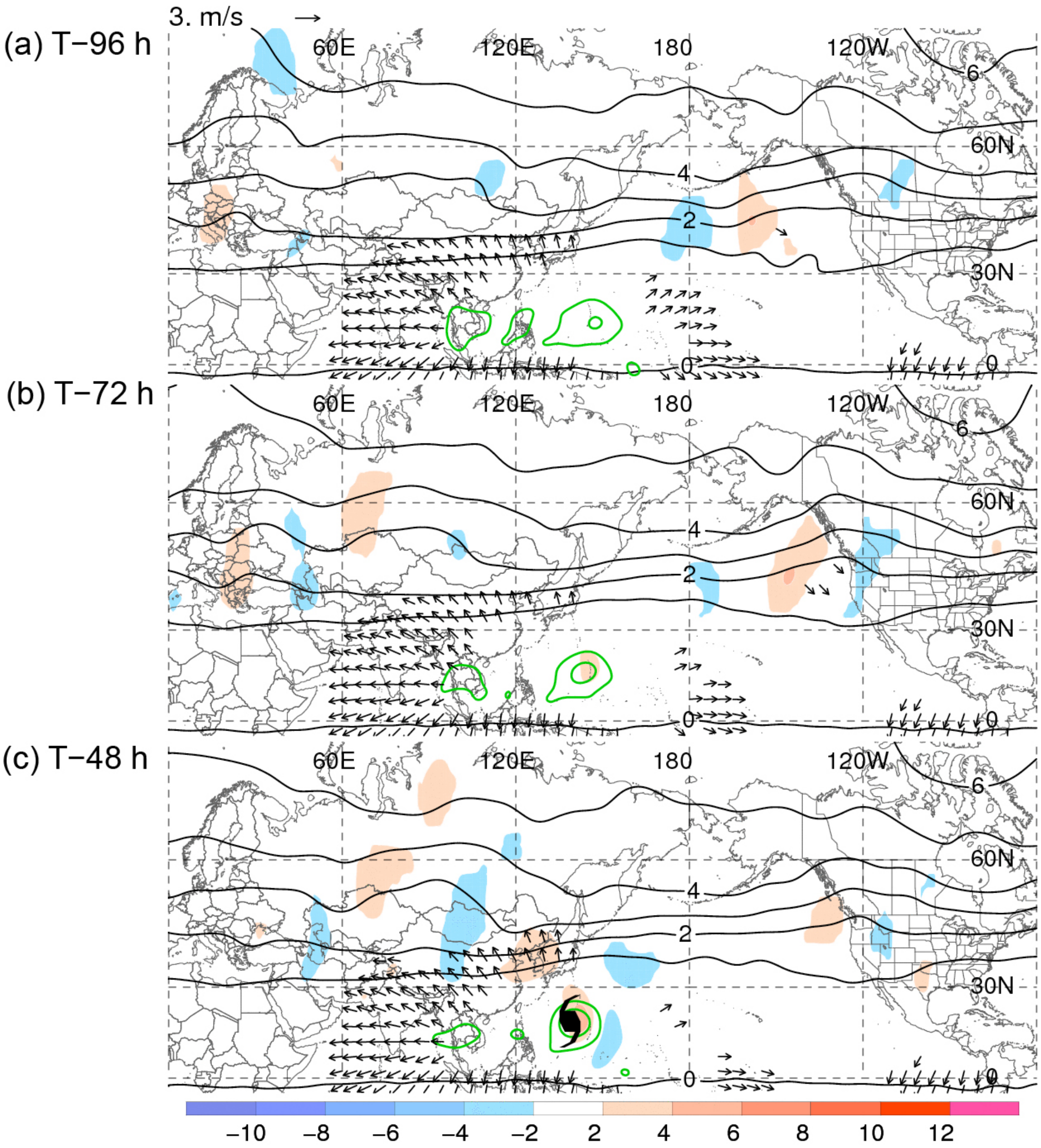

FIG. 3.3. Recurvature-relative composite analyses of all recurving WNP TCs (N = 292) valid at (a) T−96 h, (b) T−72 h, (c) T−48 h, (d) T−24 h, (e) T+0 h, (f) T+24 h, (g) T+48 h, (h) T+72 h, (i) T+96 h, (j) T+120 h, and (k) T+144 h relative to TC recurvature. Analyses show 500-hPa ascent (green, every 0.5×10^{-3} hPa s^{-1}), and 250-hPa meridional wind anomalies (shaded according to the color bar, m s^{-1}), PV (black, every 1 PVU), and irrotational wind (vectors, plotted for speeds exceeding 1.5 m s^{-1}). The TC symbol denotes the composite TC position, which is plotted in (c)–(g) only.

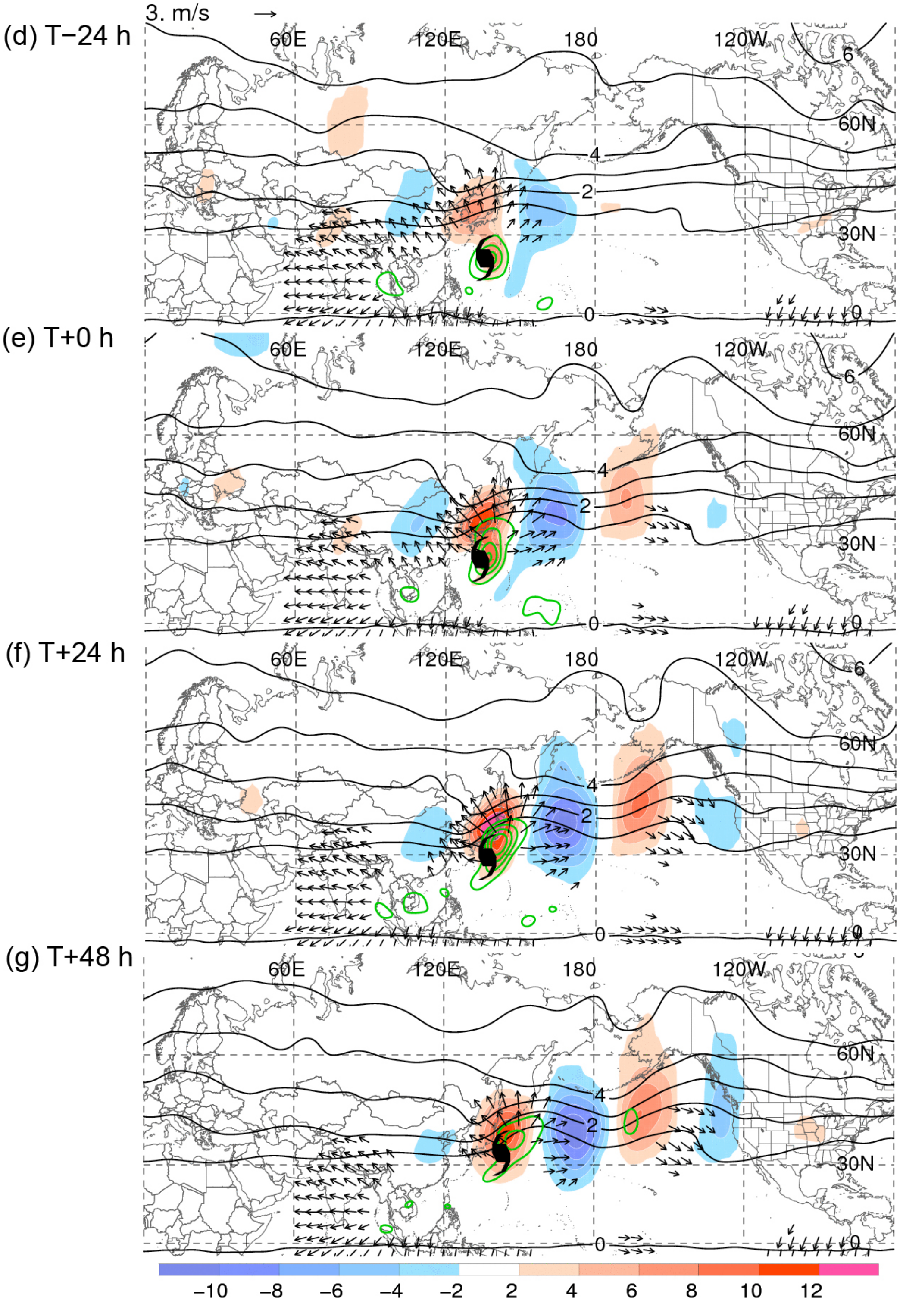

FIG. 3.3 (*Continued*)

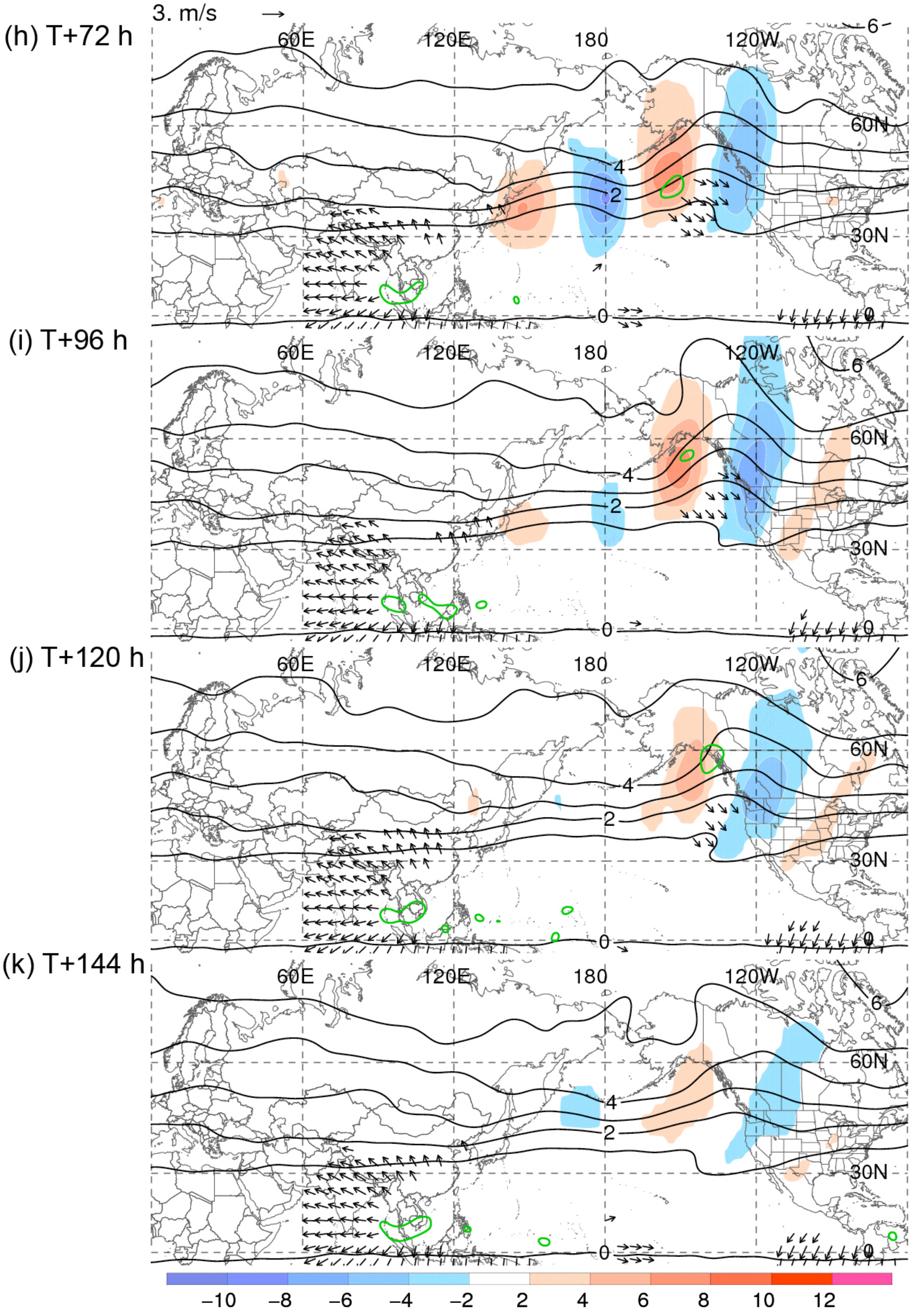

FIG. 3.3 (*Continued*)

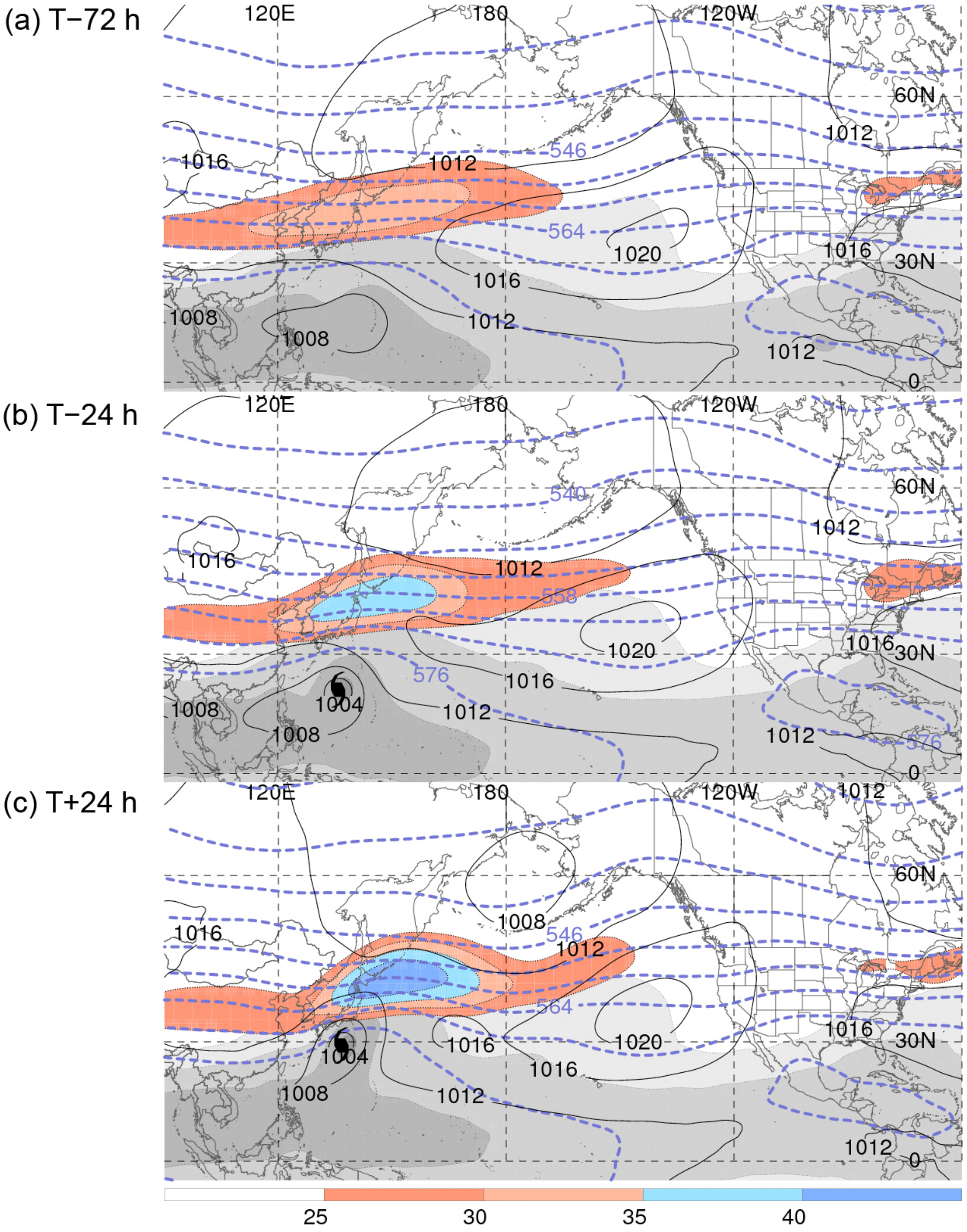

FIG. 3.4. Recurvature-relative composite analyses of all recurving WNP TCs (N = 292) valid at (a) T−72 h, (b) T−24 h, (c) T+24 h, (d) T+72 h, and (e) T+120 h relative to TC recurvature. Analyses show total-column PW (gray shading, every 10 mm starting at 15 mm), 250-hPa wind speed (shaded according to the color bar, m s^{-1}), 1000–500-hPa thickness (dashed blue, every 6 dam), and SLP (solid black, every 4 hPa). The TC symbol denotes the composite TC position, which is plotted in (b)–(d) only.

(d) T+72 h

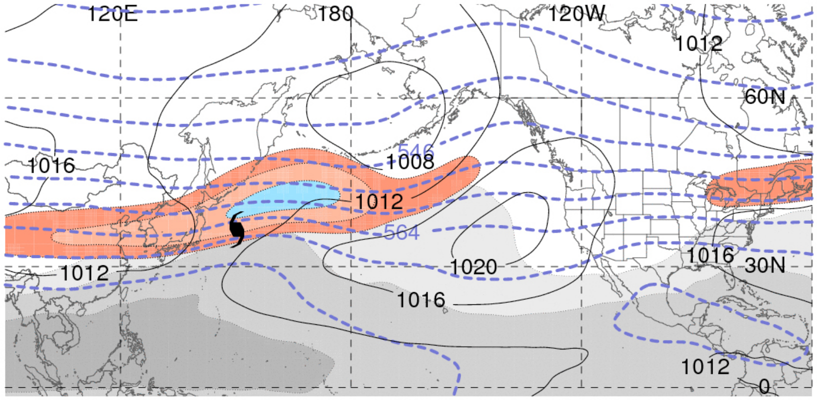

(e) T+120 h

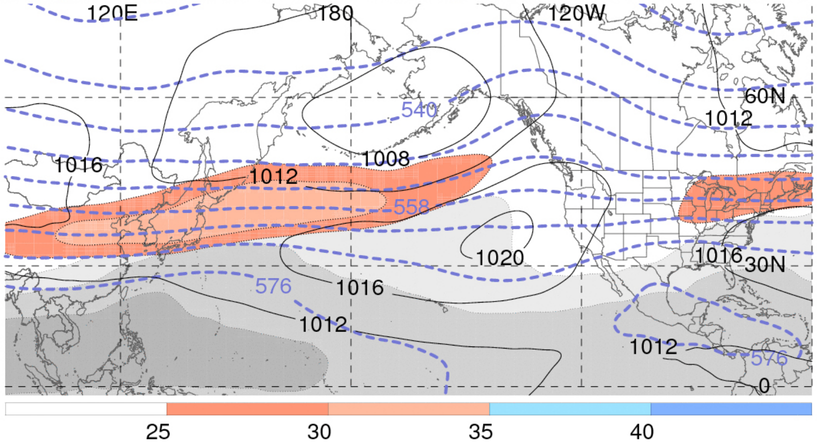

FIG. 3.4 *(Continued)*

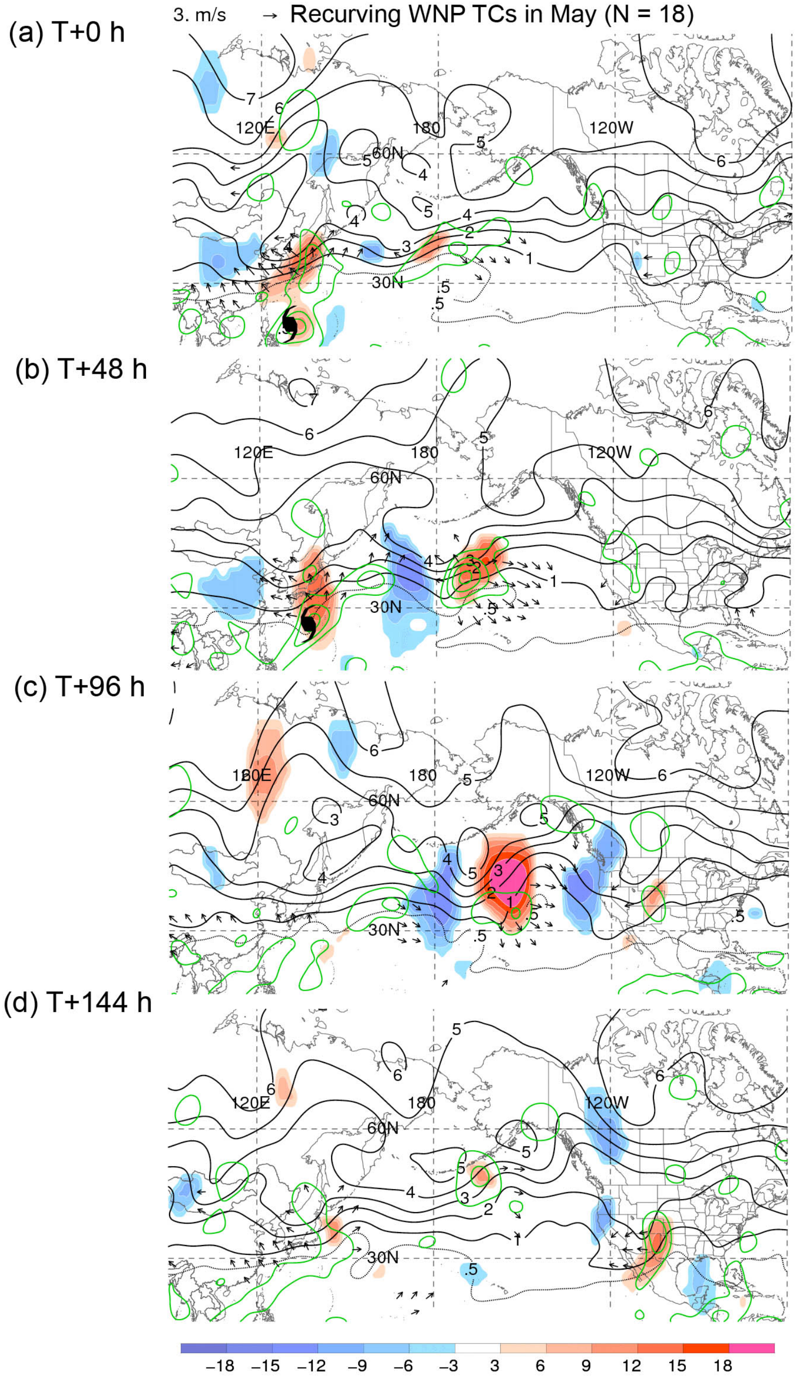

FIG. 3.5. Recurvature-relative composite analyses valid at (a) T+0 h, (b) T+48 h, (c) T+96 h, and (d) T+144 h for recurving WNP TCs in May (N = 18). Analyses show 500-hPa ascent (green, every 0.5×10^{-3} hPa s^{-1}), and 250-hPa meridional wind anomalies (shaded according to the color bar, m s^{-1}), PV (black, every 1 PVU, except gray for the 0.5-PVU contour), and irrotational wind (vectors, plotted for speeds exceeding 2.5 m s^{-1}). The TC symbol denotes the composite TC position, which is plotted in (a) and (b) only.

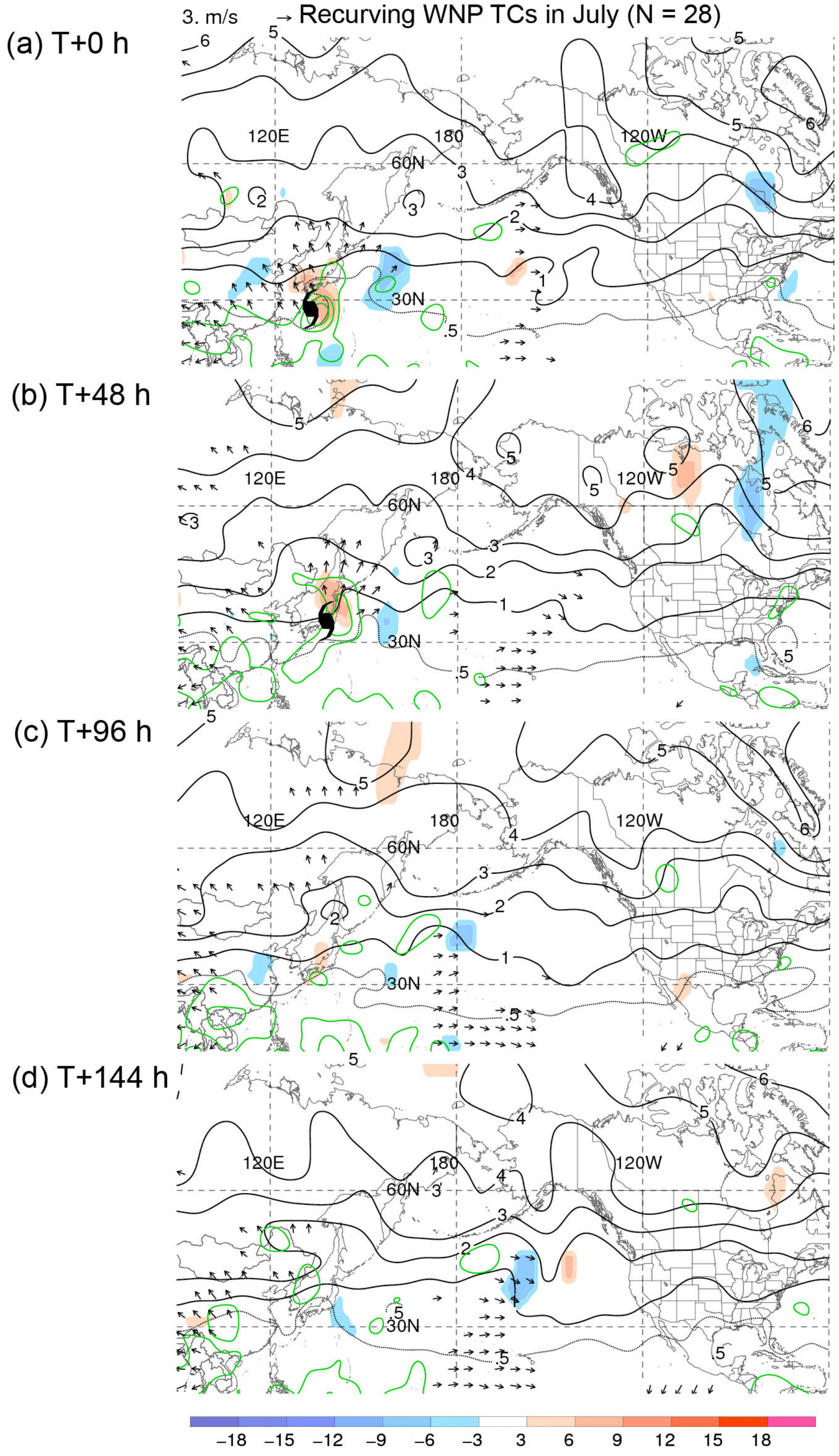

FIG. 3.6. As in Fig. 3.5, except for recurving WNP TCs in July (N = 28).

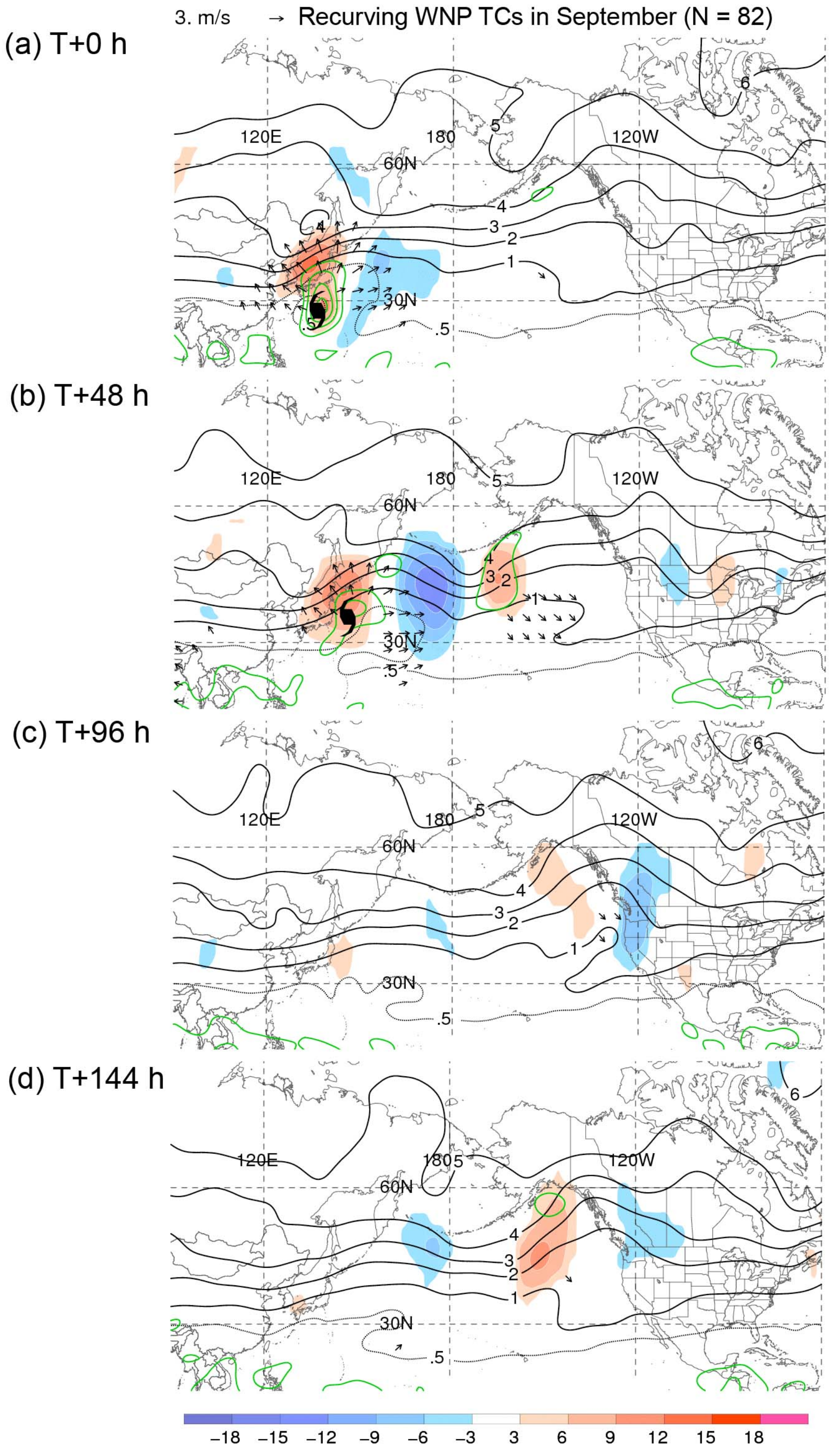

FIG. 3.7. As in Fig. 3.5, except for recurving WNP TCs in September (N = 82).

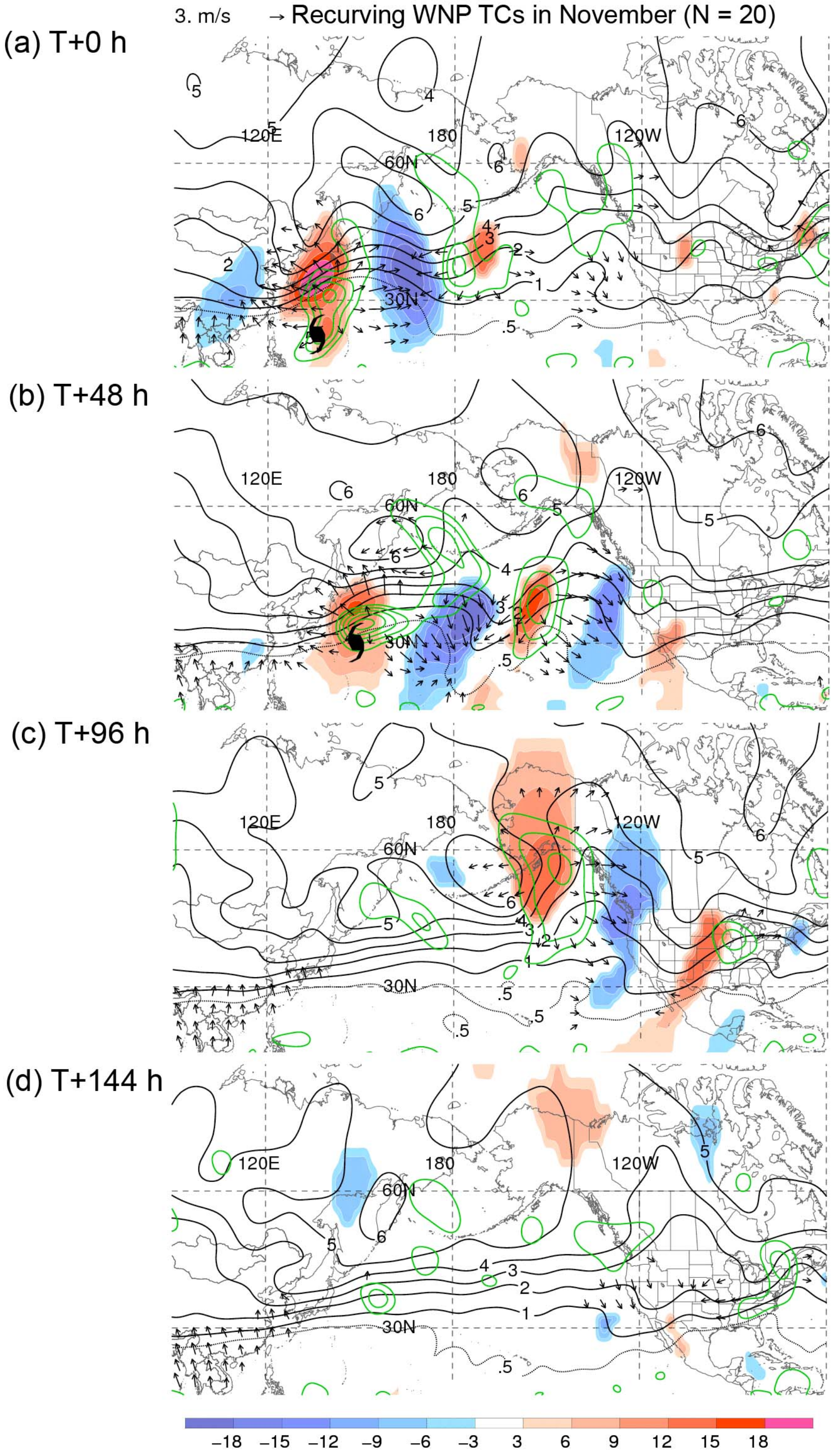

FIG. 3.8. As in Fig. 3.5, except for recurving WNP TCs in November (N = 20).

(a) Strong

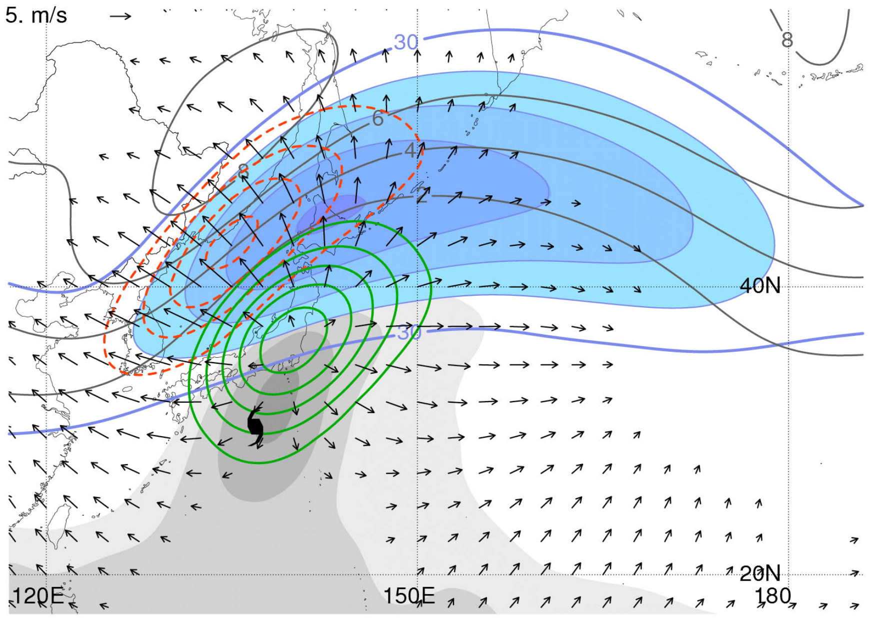

(b) Weak

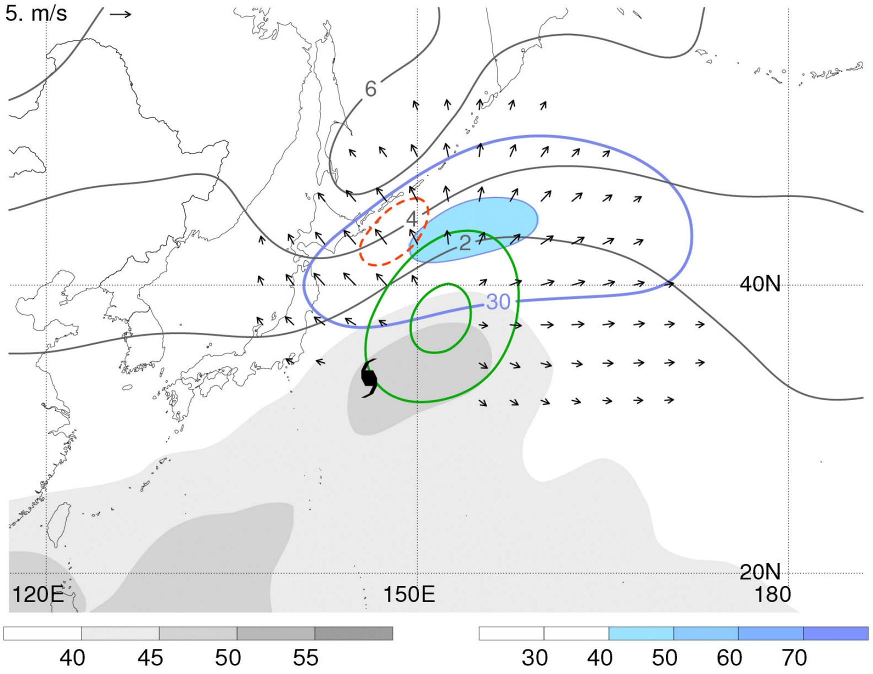

FIG. 3.9. Interaction-relative composite analyses valid at the time of maximum TC–jet stream interaction for recurving WNP TCs associated with (a) strong TC–jet stream interactions (N = 54) and (b) weak TC–jet stream interactions (N = 54). Analyses show 500-hPa ascent (solid green, every 1×10^{-3} hPa s^{-1}), total-column PW (shaded according to the gray scale, mm), and 200-hPa PV (solid gray, every 2 PVU), PV advection by the irrotational wind (dashed red, every 2 PVU day^{-1}, negative values only), wind speed (30-m s^{-1} isotach in solid blue, otherwise shaded according to the color bar), and irrotational wind (vectors, plotted for speeds exceeding 2 m s^{-1}). The TC symbol denotes the composite TC position.

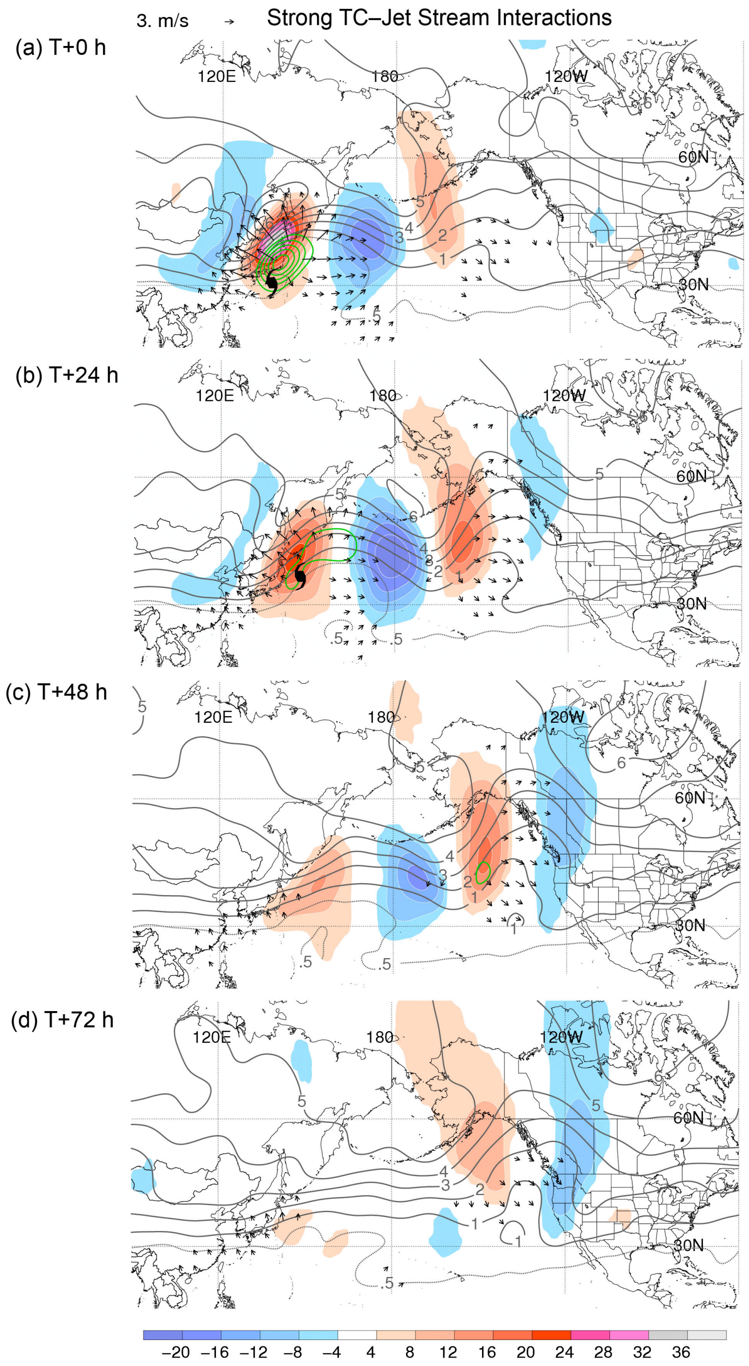

FIG. 3.10. Interaction-relative composite analyses valid at (a) T+0 h (b) T+24 h, (c) T+48 h, and (d) T+72 h relative to the time of maximum TC–jet stream interaction for recurving WNP TCs associated with strong TC–jet stream interactions (N = 54). Analyses show 500-hPa ascent (green, every 1×10^{-3} hPa s^{-1}), and 250-hPa meridional wind anomalies (shaded according to the color bar, m s^{-1}), PV (solid black, every 1 PVU, except dotted black for the 0.5-PVU contour), and irrotational wind (vectors, plotted for speeds exceeding 1.75 m s^{-1}). TC symbol denotes the composite TC position, which is plotted in (a) and (b) only.

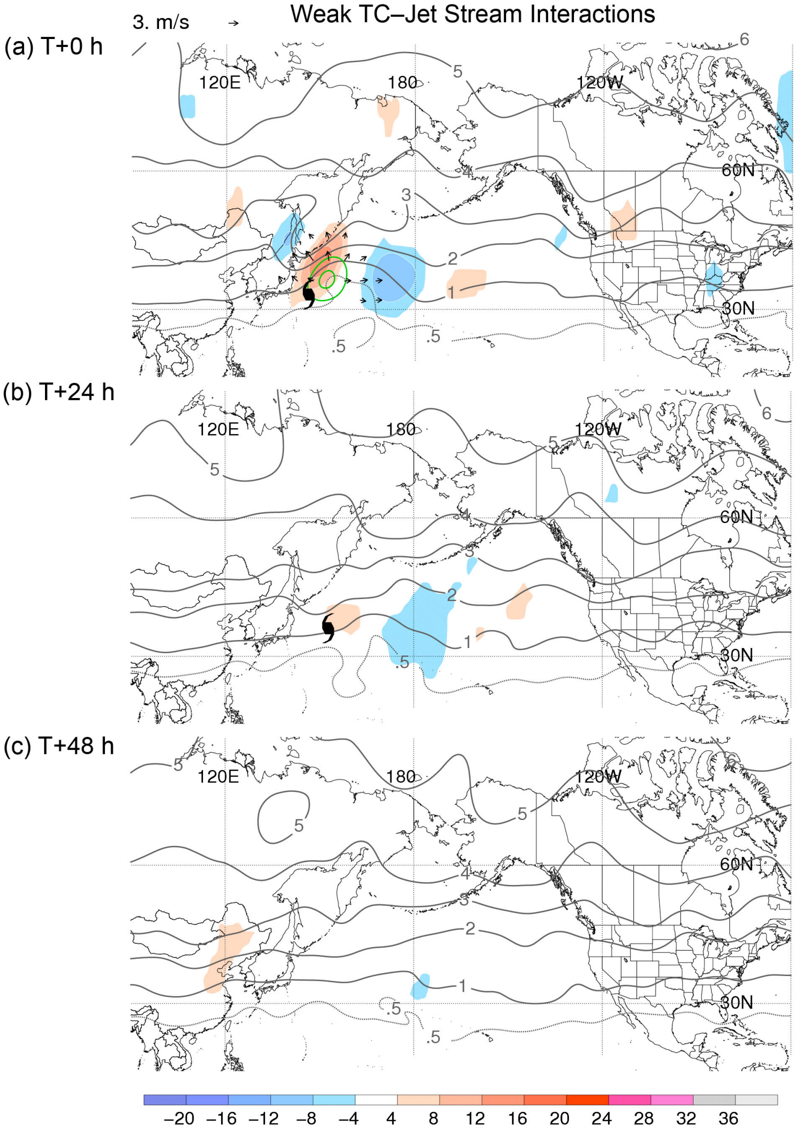

FIG. 3.11. As in Fig. 3.10, except for composite analyses valid at (a) T+0 h, (b) T+24 h, and (c) T+48 h relative to the time of maximum TC–jet stream interaction for recurving WNP TCs associated with weak TC–jet stream interactions (N = 54).

4. Case studies of recurving WNP TCs

a. Motivation, purpose, and approach

In fall 2010, the recurvature of WNP TCs Malakas (September) and Chaba (October) lead to separate episodes of large-scale flow reconfigurations over the North Pacific and North America. Both large-scale flow reconfigurations promote favorable synoptic conditions for extreme warmth over western North America and heavy rain over eastern North America. In addition, the large-scale flow reconfiguration associated with the recurvature of Malakas is associated with reduced predictability (i.e., reduced model forecast skill and increased ensemble model spread) over the North Pacific and North America.

In this study, we use a case study approach to (i) identify the key synoptic-dynamic processes that link TC–jet stream interactions associated with Malakas and Chaba to high-impact weather events over North America, and (ii) relate the TC–jet stream interaction of Malakas to reduced predictability over the North Pacific and North America. The two case studies make use of high-resolution datasets, which allow for a multiscale examination of the extratropical flow response to recurving WNP TCs that supplements the composite analyses of the extratropical flow response to recurving WNP TCs provided in Chapter 3. Conventional assessments of predictability are employed in conjunction with synoptic–dynamic analyses to understand how key dynamic processes influence the predictability of the extratropical flow response to WNP TC recurvature.

b. Data sources

As in previous chapters, all WNP TC data are derived from the JMA best-track dataset. Unless otherwise specified, analyses are plotted using the NCEP GFS analysis, which features ~0.5° horizontal grid spacing and 6-h temporal resolution. Kinematic back trajectories are computed using the Hybrid Single-Particle Lagrangian Integrated Trajectory (HYSPLIT) model available at http://ready.arl.noaa.gov/HYSPLIT.php. A skew T–log$p$ diagram created from rawinsonde data is obtained from the NCAR Research Applications Laboratory website at http://www.ral.ucar.edu/weather/upper/. Geostationary full-disk infrared MTSAT (Multi-functional Transport Satellite) imagery is obtained from NOAA NCDC/GIBBS at http://www.ncdc.noaa.gov/gibbs/.

Daily U.S. temperature and precipitation records are provided by the NOAA Weekly Weather and Crop Bulletin available at http://www.usda.gov/oce/weather/pubs/Weekly/Wwcb/index.htm. Rainfall estimates for the eastern U.S. are obtained from gauge-adjusted radar quantitative precipitation estimates (QPE) provided by the National Mosaic and Multi-Sensor QPE at http://nmq.ou.edu/, whereas rainfall estimates for southeastern Canada are obtained from Environment Canada at http://www.ec.gc.ca/meteo-weather/.

A plot of time series of daily ACCs for 144-h NH 500-hPa geopotential height forecasts verifying during September 2010 for various global models is obtained from the NCEP Environmental Modeling Center at http://www.emc.ncep.noaa.gov/gmb/STATS/STATS.html. Spaghetti plots of 500-hPa geopotential height forecasts produced by various global models are provided by Dr.

Michael Brennan of the NOAA National Hurricane Center (NHC).

c. Case study overview

i. Life cycles of WNP TCs Malakas and Chaba

The life cycles of TCs Malakas and Chaba are illustrated using track maps (Fig. 4.1) and TC intensity time series (Fig. 4.2). Figures 4.1a and 4.2a indicate that after Malakas forms at 0600 UTC 20 September 2010, it quickly intensifies while moving slowly westward, then northward. Malakas reaches TY strength at 0600 UTC 23 September and recurves shortly thereafter at 1800 UTC 23 September at 22.8°N, 140.9°E (Fig. 4.1a). At its time of recurvature, Malakas features a 970-hPa MSLP and 70-kt MSW (Fig. 4.2a) and maximum 30-kt and 50-kt wind radii of 130 nm and 50 nm, respectively (not shown). After recurvature, Malakas intensifies further, attaining an 85-kt MSW and a 945-hPa MSLP at its peak intensity at 1800 UTC 24 September.

The objectively defined maximum TC–jet stream interaction associated with Malakas [section 2b(iv)] occurs at 0000 UTC 25 September, 30 h after recurvature and 6 h after its peak intensity (Fig. 4.2a). The TC–jet stream interaction metric associated with Malakas is calculated to be −1.41 PVU day^{-1}, indicating that if this TC–jet stream interaction had occurred within the 1979–2009 period of study of the climatology and composite analysis, it would rank 88 of 272 TC–jet stream interactions (i.e., within the top third; not shown). Twelve hours later (1200 UTC 25 September), Malakas becomes an EC (Fig. 4.2a). After becoming extratropical, Malakas weakens (Fig. 4.2a) as it tracks rapidly northeastward, then east-northeastward (Fig. 4.1a). At 0000 UTC 28 September, the last time for which best-track data is available, Malakas is an intense EC with an MSLP of 975 hPa (Fig. 4.2a).

Less than a month later, TC Chaba forms at 1800 UTC 23 October (Fig. 4.1b). After genesis, Chaba moves northwestward and intensifies, attaining TY strength by 0000 UTC 26 October (Fig. 4.2b). Thirty-six hours later, Chaba recurves at 20.5°N, 127.9°E at 1800 UTC 26 October (Fig. 4.1a). At recurvature, Chaba is nearly the same intensity as Malakas is at recurvature, featuring a MSLP and MSW of 965 hPa and 70 kt, respectively (Fig. 4.2b). Its maximum 30-kt and 50-kt wind radii are 130 nm and 60 nm, respectively (not shown), indicating that Chaba is approximately the same size as Malakas at recurvature. A comparison with typical WNP TC characteristics at recurvature[16] indicates that Malakas and Chaba are of similar intensity to, but are smaller than, the average WNP TC at recurvature.

Like Malakas, Chaba continues to intensify after recurvature, attaining a 95-kt MSW and a 930-hPa MSLP at its time of peak intensity at 0600 UTC 28 October (Fig. 4.2b). This time coincides with the time of its maximum TC–jet stream interaction. The TC–jet stream interaction metric associated with Chaba is calculated to be -1.64 PVU day^{-1}, which would rank 51 of 272 TC–jet stream interactions (i.e., within the top quintile) and qualify it as a “strong” TC–jet stream interaction had it occurred within the 1979–2009 period of study.

After its maximum TC–jet stream interaction, Chaba weakens rapidly in comparison to Malakas (compare Figs. 4.2b and 4.2a). The system is deemed an EC at 1800 UTC 30

---

[16] The average WNP TC at recurvature features a 964.0-hPa MSLP, 67.9-kt MSW, and maximum 30-kt and 50-kt wind radii of 194.2 nm and 63.8 nm, respectively (Table 2.16).

October (Fig. 4.1b). Thereafter, Chaba slows and continues to weaken (Fig. 4.2b). The system is last tracked by the JMA at 0000 UTC 1 November at 39.9°N, 150.9°E (Fig. 4.1b), after which it dissipates.

ii. Associated Rossby wave trains and high-impact weather events

Following the recurvatures of Malakas and Chaba, separate episodes of extreme warmth over western North America and heavy rain over eastern North America occur in association with RWTs. These associations are depicted in Hovmöller diagrams of the 40–60°N-averaged 250-hPa meridional wind anomaly in Figs. 4.3a,b.

Figures 4.3a,b show that following the recurvatures of both TCs, the onset of extreme warmth over the western U.S. is coincident with upper-tropospheric ridge amplification over western North America associated with RWT dispersion. Furthermore, in both cases, heavy rain along the eastern North American coast develops approximately one day after the extreme warmth over western North America. The heavy rain occurs on the eastern flanks of upper-tropospheric troughs that form in association with RWT dispersion. In the case of Chaba (Fig. 4.3b), the heavy rain along the eastern North American coast persists for several days as the associated trough becomes nearly stationary.

Maps of daily U.S. weather records show that numerous daily high temperature records are set over the western U.S. following both TC recurvature episodes (Figs. 4.4 and 4.5). Coincident with the establishment of the western North American ridge on 27 September (Fig. 4.3a), an all-time record high temperature of 45°C (113°F) is set at Los Angeles International Airport (LAX). Western North American ridge amplification on 4

November (Fig. 4.3b) is associated with a 38°C (100°F) high temperature at San Diego International Airport (SAN), which marks a record high temperature for November.

The maps of daily U.S. weather records for 26 September–2 October (Fig. 4.4) indicate that numerous daily precipitation records are set across the eastern U.S. during the period following the recurvature of Malakas. Maps of 48-h rainfall totals illustrate that a heavy rain event occurs over the southeastern U.S. on 27–28 September (Fig. 4.6a), followed by a heavy rain event along the entire eastern U.S. coast on 30 September–1 October (Fig. 4.6b). More than 25 cm of rain falls over eastern North Carolina during each of the two events (Figs. 4.6a,b). It should be noted that whereas Fig. 4.3a shows that the first heavy rain event is directly linked to a RWT as discussed above, the direct link between the same RWT and the second heavy rain event cannot be shown using this figure. A discussion of the link between the RWT and the second heavy rain event is contained in section 4d(ii).

During the period following the recurvature of Chaba, many daily precipitation records are set over the northeastern U.S. and the Middle Atlantic region (Fig. 4.5). A map of rainfall totals for 4–9 November (Fig. 4.7) reveals that greater than 10 cm of precipitation falls over southeastern New Brunswick and western Nova Scotia during this period, with a 34-cm precipitation maximum occurring in southeastern New Brunswick near the Bay of Fundy. As discussed above, the heavy rain during 4–9 November coincides with the eastern flank of a nearly stationary trough over eastern North America.

d. Large-scale and synoptic flow evolution associated with recurving WNP TC Malakas

i. TC–jet stream interaction

To depict the interaction of the upper-tropospheric divergent outflow of recurving TC Malakas with the jet stream, Figs. 4.8a,b show analyses of 250-hPa wind speed, PV, and relative humidity, 300–200-hPa layer-averaged irrotational wind, and 600–400-hPa layer-averaged ascent displayed at T−18 h and T+0 h (0600 UTC 24 September and 0000 UTC 25 September) relative to the time of maximum TC–jet stream interaction (see Fig. 4.1a). Figure 4.8a shows that at T−18 h, Malakas is situated downstream of a weak upper-tropospheric PV trough, in the equatorward entrance region of the North Pacific jet stream. A signature of diabatically driven divergent outflow associated with the TC is indicated by high values of upper-tropospheric relative humidity (i.e., high cloudiness) and upper-tropospheric irrotational winds directed radially outward from ascent over and downstream of the TC center. Along the eastern flank of the upstream PV trough, the irrotational wind field associated with the TC has a substantial cross-PV contour component, indicative of negative PV advection by the TC divergent outflow.

By T+0 h (Fig. 4.8b), an upper-tropospheric PV ridge has amplified poleward of the recurving TC and just downstream of the PV trough, and a >100-m s^{-1} jet streak has formed along and downstream of the PV ridge crest (Figs. 4.8a,b). The divergent outflow associated with Malakas, which is collocated with the TC cirrus shield (inset in Fig. 4.8b), continues to impinge upon the jet stream. Of note is that the eastern flank of the upstream upper-tropospheric PV trough has remained nearly stationary, suggesting that negative PV advection by the TC divergent outflow may be impeding the eastward translation of the trough.

A vertical cross section taken through the jet stream and Malakas (cross section line indicated in Fig. 4.8b) at T+0 h shows that a band of frontogenesis slants poleward and upward from the surface circulation of the TC, which is represented as an upright PV tower, to the base of the jet stream (Fig. 4.9). Above the PV tower associated with Malakas, regions of low and negative PV reflect the TC outflow layer. The presence of negative PV in the outflow layer is a signature of a diabatic reduction of upper-tropospheric PV associated with latent heat release accompanying clouds and precipitation. A tropopause fold associated with the jet streak is situated on the poleward edge of the TC outflow layer.

An analysis of PW, 250-hPa wind speed, 1000–500-hPa thickness, and SLP over the North Pacific at T+0 h (0000 UTC 25 September; Fig. 4.10a) reveals a signature of warm-air advection poleward and eastward of the TC center where southerly flow associated with the cyclonic circulation of the TC intersects a lower-tropospheric baroclinic zone. A moisture plume (>45-mm PW) is collocated with the southerly flow on the eastern side of Malakas, and is reminiscent of a warm-conveyor belt. Inspection of a plot of 700-hPa Q vectors and Q-vector forcing for vertical motion[17] (Fig. 4.10b) at T+0 h reveals that Q-vector forcing for ascent is situated just eastward of the center of Malakas at 700 hPa. Frontogenesis due to the geostrophic wind is also indicated eastward of the 700-hPa TC center by the orientation of Q vectors toward warm air.

---

[17] Q vector $\vec{Q}$ and Q-vector forcing $-2\vec{\nabla}_p \cdot \vec{Q}$ are defined as in section 5.7.4 in Bluestein [1992, Eqs. (5.7.55) and (5.7.54)].

Based on Figs. 4.8–4.10, the interaction of TC Malakas with the jet stream results in upper-tropospheric ridge amplification and jet streak intensification over the WNP via inferred negative PV advection by the diabatically driven divergent outflow associated with the TC. The divergent circulation of the TC, and thus the TC–jet stream interaction, may be enhanced by ascent tied to lower-tropospheric frontogenesis in a moist environment.

ii. Downstream extratropical flow reconfiguration and high-impact weather

The evolution of the DT (1.5-PVU) flow pattern and lower-tropospheric cyclonic disturbances over the North Pacific and North America following the interaction between Malakas and the jet stream between T+24 h and T+96 h (0000 UTC 26 September–0000 UTC 29 September) is depicted in Figs. 4.11a–d, respectively. Figure 4.11 confirms that the interaction between Malakas and the jet stream leads to RWT dispersion as shown previously in Fig. 4.3a. At T+24 h, an amplified WNP ridge is evident poleward and downstream of Malakas (R1 in Fig. 4.11a). Downstream of this ridge, a developing trough over the central North Pacific (T1) is associated with a strong cyclone as indicated by lower-tropospheric cyclonic relative vorticity.

Twenty-four hours later, at T+48 h (0000 UTC 27 September; Fig. 4.11b), the downstream trough (T1) has amplified sharply, and a ridge is amplifying downstream along the coast of western North America (R2). Downstream of this amplifying ridge, a new trough is developing over Alberta, Canada (T2). To its south, a diffuse filament of low DT potential temperature (i.e., a PV streamer) is evident along the eastern flank of the western North America ridge (R2), indicative of AWB. By T+72 h (0000 UTC 28

September; Fig. 4.11c), the western North American ridge (R2) has amplified further, and the trough previously over Alberta, Canada, at T+48 h (T2 in Fig. 4.11b) has sharpened while moving downstream to the Midwest U.S. The establishment of the ridge (R2) over western North America is concurrent with the extreme warmth on 27 September over the western U.S. (i.e., Fig. 4.3). East and south of the western North American ridge (R2), the aforementioned PV streamer stretches across the southern U.S., with associated easterly flow on the DT extending from New Mexico to southern California.

Figure 4.12a indicates that air parcels reaching San Diego, CA at T+72 h, on the afternoon on the day of extreme warmth over the western U.S. and especially southern California, turn anticyclonically and descend in the prior 72-h period. Their descent and general westward track from the high terrain of the interior West suggests that ridge amplification (R2) and associated AWB provides favorable synoptic conditions for extreme warmth over the western U.S. by promoting subsidence, downslope warming, and the westward transport of warm air from an elevated heat source. These processes are consistent with the 850–650-hPa elevated mixed layer associated with deep easterlies observed at San Diego, CA, at T+72 h (Fig. 4.12b).

By T+96 h (Fig. 4.11d), the western North America ridge (R2) has progressed eastward and deamplified. The trough over the Midwest U.S. 24 h earlier (T2; Fig. 4.11c) has progressed eastward and thinned over the eastern U.S. while coming into close alignment with a separate DT disturbance over the southeastern U.S. (indicated by the star in Fig. 4.11d).[18] The elongated structure of the eastern U.S. trough and its positive tilt are indicative of a PV streamer associated with AWB.

To examine the relationship between the aforementioned PV streamer and the heavy rain over the southeastern U.S. on 27–28 September, a plot of PW, 250-hPa wind speed, 1000–500-hPa thickness, and SLP (Fig. 4.13a), and a plot of 700-hPa Q vectors and Q-vector forcing for vertical motion (Fig. 4.13b) are shown for T+78 h (0600 UTC 28 September). Figure 4.13a indicates that the DT disturbance noted at T+72 h and T+96 in Figs. 4.11c,d, respectively, is manifested in the 1000–500-hPa thickness field as a sharp, negatively tilted trough that extends to the eastern Gulf Coast at T+78 h. On the eastern flank of the thickness trough, a tropical air mass characterized by >45-mm PW values and 570–576-dam thickness values has surged poleward along the eastern U.S. coast in association with southerly surface geostrophic flow that extends from the Caribbean to southeastern Canada. Figure 4.13b illustrates that weak Q-vector forcing for ascent is collocated with the tropical air mass on the eastern flank of the thickness trough shown in Fig. 4.13a. Weak frontogenesis due to the geostrophic wind is also indicated along the southeastern U.S. coast by the orientation of Q vectors toward warm air.

The tropical air mass entrenched along the eastern U.S. coast downstream of a sharp, slow-moving PV streamer, manifested as a thickness trough associated with weak Q-vector forcing for ascent on its eastern flank, are critical ingredients of the observed heavy rain event over the southeastern U.S. on 27–28 September (e.g., Fig. 4.6a). Since RWT dispersion across the North Pacific and North America associated with the

---

[18] This DT disturbance arises from the fracture of a PV streamer associated with AWB over eastern North America between T+24 h and T+72 h (Figs. 4.11a–c).

recurvature of Malakas results in the formation of the PV streamer (Fig. 4.11), the recurvature of Malakas can be viewed as a remote precursor to the heavy rain event of 27–28 September over the southeastern U.S.

As noted in section 4c(ii), a second heavy rain event occurs on 30 September–1 October along the eastern U.S. coast that also can be linked to the RWT associated with the recurvature of Malakas. As will be shown, the eastern U.S. PV streamer associated with the 27–28 September heavy rain event over the southeastern U.S. remains a coherent feature over the southeastern U.S. through 1 October. A DT disturbance associated with this long-lived PV streamer proves instrumental in the heavy rain event over the eastern U.S. on 30 September–1 October by providing QG forcing for ascent and favoring the poleward transport of a tropical air mass along the eastern U.S. coast.

A plot of DT potential temperature and wind and lower-tropospheric cyclonic relative vorticity over the eastern U.S. and western North Atlantic at T+108 h (1200 UTC 29 September; Fig. 4.14a) reveals that the DT disturbance over the southeastern U.S. at T+96 h (Fig. 4.11d) is still present at T+108 h. By T+132 h (1200 UTC 30 September; Fig. 4.14b), the DT disturbance has drifted southeastward and is located on the edge of a region of high (354–378 K) potential temperature air on the DT surging poleward from the eastern Caribbean. Evidence of surface cyclogenesis associated with this DT disturbance is given by a rapid increase in low-level relative vorticity from T+108 h and T+132 (Figs. 4.14a,b) over North Carolina, just east of the DT disturbance.

A plot of total-column PW, 250-hPa wind speed, 1000–500-hPa thickness, and SLP, over the eastern U.S. valid at T+132 h (1200 UTC 30 September; Fig. 4.15a) indicates that the aforementioned DT disturbance within a PV streamer (Fig. 4.14b) is manifested as a closed contour within a 1000–500-hPa thickness trough over the southeastern U.S. A surface low (L1) is positioned within a lower-tropospheric baroclinic zone on the eastern flank of the thickness trough that extends well poleward into the northeastern U.S. A second surface low to the south (L2) is associated with the remnants of a North Atlantic TC (Nicole[19]).

Between T+132 h and T+144 h (Figs. 4.15a,b), L1 tracks poleward and becomes situated on the eastern flank of a thickness trough over the Great Lakes, within the equatorward entrance region of an intensifying jet streak (Fig. 4.15b). Meanwhile, L2 also tracks poleward and becomes positioned on the eastern flank of the southeastern U.S. thickness trough, just east of the closed thickness contour that is a reflection of the aforementioned DT disturbance. A plume of tropical air[20] surges poleward along the eastern North American coast within the warm sectors of L2 and L1 (Figs. 4.15a,b) along the eastern flank of the PV streamer and embedded DT disturbance (not shown). Plots of 700-hPa Q vectors and Q-vector forcing for vertical motion at T+132 h and T+144 h (Figs. 4.15c,d) indicate Q-vector forcing for ascent on the eastern flank of a sharp, deep 700-hPa trough. The PV streamer resulting from AWB following RWT dispersion is therefore shown to be instrumental to the second heavy rain event on 30 September–1 October along the eastern U.S. coast (Fig. 4.6b) by favoring poleward transport of a tropical air mass and QG forcing for ascent along its eastern flank.

---

[19] A detailed summary of the life cycle of TC Nicole is available from the NHC website at http://www.nhc.noaa.gov/2010atlan.shtml.

[20] Note 570–576-dam 1000–500-hPa thickness values and >45-mm PW values.

e. Large-scale and synoptic evolution associated with recurving WNP TC Chaba

i. TC–jet stream interaction

To examine the TC–jet stream interaction associated with Chaba, plots of 250-hPa wind speed, PV, and relative humidity, 300–200-hPa layer-averaged irrotational wind, and 600–400-hPa layer-averaged ascent are displayed at T−18 h and T+6 h (1200 UTC 27 October and 1200 UTC 28 October; Figs. 4.16a and b, respectively) relative to the time of maximum TC–jet stream interaction (Fig. 4.1b). At T−18 h (Fig. 4.16a), Chaba is situated near the equatorward entrance region of the North Pacific jet stream. The jet stream is relatively zonal, with no embedded trough upstream of Chaba as with Malakas (Fig. 4.8a). Similar to Malakas, implied upper-tropospheric diabatically driven divergent outflow is directed radially outward from the region of midtropospheric ascent associated with Chaba (compare Figs. 4.16a and 4.8a).

By T+6 h (Fig. 4.16b), an elongated area of upper-tropospheric divergent outflow associated with midtropospheric ascent over and downstream of Chaba is impinging strongly upon the jet stream. In contrast to T−18 h (Fig. 4.16a), the divergent outflow associated with Chaba is pointed mainly poleward toward the jet stream rather than radially outward in all directions (compare Fig. 4.16b and Fig. 4.8b). This change in the spatial pattern of the divergent outflow of Chaba as a jet streak develops poleward and eastward of Chaba between T−18 h and T+6 h[21] is hypothesized to be a reflection of the increasing role of baroclinic dynamics during the TC–jet stream interaction. Of note is

---

[21] Note the increase in 250-hPa wind speed from ~80 m s^{-1} to ~90 m s^{-1}.

that whereas a pronounced ridge has developed poleward of Malakas by T+0 h (Fig. 4.8b), no ridge amplification has occurred by T+6 h in the case of Chaba.

At T+6 h much of the upper-tropospheric divergent wind field appears to be directed outward from a region of ascent (implied convection) well northeast of Chaba. Infrared satellite imagery at T+6 h (inset in Fig. 4.16b) indicates that an enhanced cirrus shield is associated with this convective feature. At this time, the divergent outflow associated with this convective feature is more prominent than that of the TC, and appears to be impinging more strongly upon the jet stream than is the divergent outflow associated with the TC.

To explore the lower-tropospheric structure of the convective feature and its relationship to Chaba, plots are created of 925-hPa dilatation axes, wind speed, potential temperature, frontogenesis, and ascent at T+0 h and T+12 h (0600 UTC and 1800 UTC 28 October; Figs. 4.17a,b). Figure 4.17a shows that as Chaba is tracking northeastward at T+0 h, a band of lower-tropospheric ascent extends well northeastward from the TC. This band of ascent is coincident with a lower-tropospheric baroclinic zone. At the eastern tip of this ascent band (~33˚N, 140˚E), a small region of vigorous ascent is coincident with maxima in lower-tropospheric frontogenesis, baroclinicity, and wind speed.

By T+12 h (Fig. 4.18b) the convective feature has translated ~800 km downshear during the previous 12 h, which corresponds to an ~18.5 m s^{-1} translation speed. This translation speed is ~3.5 times greater than the ~5.5-m s^{-1} translation speed of Chaba over the same 12-h period. Lower-tropospheric wind speeds (>45-m s^{-1} 925-hPa wind speed) and frontogenesis are noted to have increased substantially with this convective feature between T+0 h and T+12h. The rapid downshear movement of this convective feature in the presence of strong lower-tropospheric baroclinicity and frontogenesis, high PW (values exceeding 55 mm; not shown), and an apparent absence of upper-tropospheric forcing (Fig. 4.16b) suggest that this feature may be a diabatic Rossby vortex (DRV; e.g., Raymond and Jiang 1990; Snyder and Lindzen 1991; Moore and Montgomery 2004, 2005). Over the next 48 h (1800 UTC 28 October–1800 UTC 30 October; not shown), the DRV-like disturbance translates rapidly along the equatorward side of the jet stream, redevelops in the downstream jet streak associated with Chaba, couples with a strong DT disturbance of arctic origin, and undergoes explosive intensification[22] (not shown).

Returning to a consideration of the TC–jet stream interaction, Fig. 4.18a indicates that by T+30 h (1200 UTC 29 October), the 250-hPa jet streak downstream of Chaba has intensified further to over 100 m s^{-1}. The jet streak has become elongated along a strengthening upper-tropospheric PV gradient (Figs. 4.16b and 4.18a). Two notable areas of ascent and upper-tropospheric divergent outflow are evident in proximity to this jet streak. One is a relatively small area associated with Chaba near the right-entrance region of the jet streak, and the other is a somewhat larger, though less coherent, area of ascent within the jet streak exit region. The DRV-like disturbance is nearly indistinguishable at the southern edge of the latter area of ascent. However, in the lower troposphere (925 hPa), it is associated with a distinct band of strong ascent ($<-20 \times 10^{-3}$

---

[22] Its MSLP drops from 988 hPa to 948 hPa between 0600 UTC and 1800 UTC 30 October.

hPa s^{-1}, not shown). Divergent outflow from Chaba, though more localized in comparison to T+6 h (Fig. 4.16b), continues to be directed toward the jet streak.

By T+54 h (1200 UTC 30 October), the jet streak just downstream of weakening Chaba still features 100-m s^{-1} wind speeds at 250 hPa (Fig. 4.18b). The upper-tropospheric divergent outflow associated with the TC continues to impinge upon the jet stream, which may help to anchor the jet streak. The corridor of 70-m s^{-1} wind speeds at 250 hPa within the jet stream has extended eastward. By this time, the former DRV-like disturbance has moved from the equatorward side of the jet stream into the left-exit region of the jet streak and is explosively intensifying (not shown). Upstream of Chaba, an upper-tropospheric PV disturbance is approaching the TC from the west.

At T+78 h (1200 UTC 31 October; Fig. 4.19a), Chaba has become a weak EC featuring a 1010-hPa MSLP (Fig. 4.2b). The upper-tropospheric irrotational wind field in the vicinity of Chaba does not appear to be associated with Chaba, but instead with an upstream region of midtropospheric ascent developing ahead of a sharpening upper-tropospheric PV disturbance (Fig. 4.19a. The 100-m s^{-1} jet streak evident 24 h earlier (Fig. 4.18b) is no longer present, but a strong, relatively straight jet stream now extends all the way across the North Pacific (not shown).[23] This strong, longitudinally extensive jet stream indicates that a strong Rossby waveguide has been established over the North Pacific.

By T+102 h (1200 UTC 1 November; Fig. 4.19b), extratropical cyclogenesis is underway over the WNP. A 996-hPa surface low at T+102 h deepens to a 972-hPa

---

[23] Whereas 80 m-s^{-1} winds extend to 165°W at T+54 h (Fig. 4.18b), they extend eastward to 140°W by T+78 h (not shown).

surface low during the following 24 h (not shown). An upper-tropospheric PV hook has developed upstream of an area of widespread, midtropospheric ascent, which includes disorganized ascent associated with the remnants of Chaba, within a pronounced upper-tropospheric ridge. A broad region of upper-tropospheric divergent outflow is evident emanating from the midtropospheric ascent and a 100-m s^{-1} jet streak has developed in northwesterly flow on the forward flank of the pronounced ridge.

Based on Figs. 4.16–4.19, the interaction of Chaba with the jet stream modifies the flow pattern over the WNP. Rather than directly leading to WNP ridge amplification as in the case of Malakas, the upper-tropospheric divergent outflow emanating from Chaba and a DRV-like disturbance along an associated baroclinic zone appears to elongate and intensify the North Pacific jet stream and thus strengthen the Rossby waveguide.

ii. Downstream extratropical flow reconfiguration and high-impact weather

The evolution of the DT flow pattern and lower-tropospheric cyclonic disturbances over the North Pacific and North America following the recurvature of Chaba is depicted in Fig. 4.20. This depiction confirms the signature of high-amplitude RWT dispersion across the North Pacific into North America for 31 October–5 November shown in Fig. 4.3b. At T+84 h (1800 UTC 31 October; Fig. 4.20a), WNP ridge amplification (R1) is beginning in association with extratropical cyclogenesis induced by an upper-tropospheric PV disturbance as shown in Figs. 4.19a,b. The strong North Pacific meridional potential temperature gradient on the DT at T+84 h is indicative of a strong North Pacific jet stream and Rossby waveguide. The EC that originates as a DRV-like disturbance (e.g., Fig. 4.16b) and then explosively deepens can be seen on the poleward side of the jet stream over the eastern North Pacific. At this time, the EC is a powerful occluded cyclone featuring a 944-hPa MSLP (not shown).

By T+156 h (1800 UTC 3 November; Fig. 4.20b), RWT dispersion is underway across the North Pacific and North America. A sharp negatively tilted trough (T1) associated with CWB has developed over the eastern North Pacific downstream of the WNP ridge (R1). Downstream of the eastern North Pacific trough (T1), a high-amplitude ridge has developed over western North America (R2). This western North American ridge is associated with the extreme warmth that occurs over the western U.S. on 4 November (Fig. 4.3b). On the eastern flank of this ridge (R2), a trough is deepening downstream over the Upper Midwest (T2). By T+204 h (1800 UTC 5 November; Fig. 4.20c), T2 has developed into a well-defined PV streamer over the eastern U.S. in association with AWB. Downstream of T2 and upstream of an amplifying western North Atlantic ridge (R3), a long band of cyclonic relative vorticity stretches from the Bahamas poleward to southeastern Canada. This lower-tropospheric vorticity band is coaligned with a band of vigorous midtropospheric ascent (not shown). Along the eastern flank of T2 and the western flank of R3, which become nearly stationary (not shown), heavy precipitation occurs over southeastern Canada between 4 and 9 November (Fig. 4.3b).

The synoptic features associated with extreme warmth over the western North America and heavy rain over southeastern Canada are presented for T+204 h (1800 UTC 5 November; Fig. 4.21). Figure 4.21a shows that, indicative of a RWT, a high-amplitude thickness ridge–trough–ridge pattern is established over North America and the western North Atlantic. Over western North America, a thickness ridge with maximum thickness values exceeding 564 dam extends poleward of 60°N. East of the thickness ridge, a sharp thickness trough is in place across eastern Canada and the eastern U.S. Between the thickness trough over eastern North America and the thickness ridge over the western North Atlantic, tropospheric-deep southerly flow is implied by southerly surface geostrophic winds, a strong west–east thickness gradient and the implied southerly wind direction of the 60–80 m s^{-1} 250-hPa jet along and off the eastern North American coast. Within the implied tropospheric-deep southerly flow, a moisture plume extends from the Caribbean, where a North Atlantic TC (Tomas[24]) is present, to southeastern Canada.

Figure 4.21b indicates that Q-vector forcing for ascent is present along the eastern flank of the thickness trough and western flank of the thickness ridge shown in Fig. 4.21a. A relative maximum in Q-vector forcing for ascent is seen over southeastern Canada, where strong southerly surface winds interest a lower-tropospheric baroclinic zone (Fig. 4.21a). The presence of QG forcing for ascent, copious moisture (PW values >40 mm), and implied near-unidirectional tropospheric winds over southeastern Canada indicate a favorable synoptic scenario for the heavy rain event over southeastern Canada (Fig. 4.7).

f. Predictability associated with recurving WNP TC Malakas

In this section, we examine the predictability associated with the recurvature of Malakas within the context of the previously discussed TC–jet stream interaction, RWT dispersion, and high-impact weather over North America. Malakas is chosen for an investigation of predictability because its recurvature and interaction with the jet stream

---

[24] A detailed summary of the life cycle of TC Tomas is available from the NHC website at http://www.nhc.noaa.gov/2010atlan.shtml.

coincide with a period of reduced model forecast skill over the NH in late September 2010. To examine NH model forecast skill in September, time series of daily NH ACCs for 144-h 500-hPa geopotential height forecasts are displayed for 1–30 September in Fig. 4.22.

Figure 4.22 reveals that a noticeable dip in model skill among all the global models occurs between approximately 23 and 27 September, surrounding the time of the maximum TC–jet stream interaction associated with Malakas (e.g., 0000 25 September; Fig. 4.1a). During this period, the GFS ACC drops from ~0.8–0.9 to ~0.6–0.7, whereas the ECMWF ACC drops as low as ~0.5 before quickly rebounding. Using an ACC of 0.6 as the threshold for a skillful forecast, GFS and ECMWF forecasts of NH 500-hPa geopotential height verifying near the time that Malakas interacts with the jet stream exhibit little to no skill at a 144-h lead time.

To establish whether this reduction in NH model skill can be linked to forecast error associated with the RWT following Malakas, Hovmöller diagrams are constructed that show the 250-hPa meridional wind error associated with GFS forecasts initialized at 0000 UTC 20 September (Fig. 4.23a,b) and 0000 UTC 21 September (Fig. 4.23c,d). These two GFS initializations are issued 120 h and 96 h prior to the maximum TC–jet stream interaction associated with Malakas (0000 UTC 25 September).

An examination of the 0000 UTC 20 September GFS run (Fig. 4.23a) indicates that the GFS forecast fails to indicate RWT dispersion directly associated with Malakas. This failure of the GFS to forecast RWT dispersion associated with Malakas is highlighted by Fig. 4.23b, which shows the analyzed 250-hPa meridional wind and the difference between the forecast and analysis (model error). This figure shows that substantial errors

($>$24 m s^{-1}) in the magnitude of the 250-hPa meridional wind develop over the North Pacific and extend into western North America where the analyzed 250-hPa meridional wind indicates a RWT. Horizontal plots of 500-hPa and 1000-hPa geopotential height forecasts (not shown) suggest that the 0000 UTC 20 September GFS forecasts the recurvature of Malakas approximately one day earlier than what is observed, when the system is substantially weaker (Fig. 4.2a). In the latter scenario, the interaction of a weaker TC with the North Pacific jet stream fails to produce substantial WNP ridge amplification (not shown).

The GFS forecast of 250-hPa meridional wind made 24 h later, at 0000 UTC 21 September (Fig. 4.23c), 96 h prior to the maximum TC–jet stream interaction associated with Malakas (Fig. 4.1a), is more successful at capturing RWT dispersion associated with Malakas (Figs. 4.23c,d). However, substantial errors are evident with respect to the position and amplitude of the troughs and ridges comprising the RWT over the North Pacific and North America (Fig. 4.23d). Whereas the GFS run from 24 h earlier fails to forecast RWT dispersion with Malakas, the GFS run from 0000 UTC 21 September forecasts the RWT dispersion, but it is too slow (note the differences in the slopes of the arrows in Fig. 4.23d). Based on the relatively large spatial extent and magnitude of the model errors shown in Figs. 4.23b,d, it seems probable that model error related to RWT amplification and dispersion associated with Malakas contributes to the drop in NH GFS ACCs around the time of maximum TC–jet stream interaction in late September (Fig. 4.22).

A comparison of the phase speed of forecast vs. analyzed positive (southerly) meridional flow anomalies near 150°E on 25–26 September (Figs. 4.23c,d; also note black curve in Fig. 4.23c) reveals that the ridge associated with Malakas (e.g., Fig. 4.8b) translates eastward too quickly in the 0000 UTC 21 September GFS forecast. The too-fast eastward translation of the ridge in the forecast suggests that the diabatically driven divergent outflow associated with Malakas, which may help anchor the ridge and prolong ridge amplification, may be underrepresented in the 0000 UTC 21 September GFS run.

To examine the horizontal structure of forecast errors in the 0000 UTC 21 September GFS model run, plots are constructed of 120-h and 144-h forecasts of 500-hPa geopotential height overlaid with the verifying analyses over the North Pacific (Figs. 4.24a,b). Figures 4.24a,b indicate that the 120-h and 144-h forecasts of the position of Malakas and its associated downstream ridge are too far east compared to the analysis. As a result, phase and amplitude error associated with the RWT is seen to grow and develop downstream as the RWT amplifies and disperses downstream (compare Figs. 4.24a,b).

Finally, it is of interest to examine whether model forecasts improve once the maximum TC–jet stream interaction has occurred between Malakas and the jet stream. In Fig. 4.25a, spaghetti plots of the 579-dam 500-hPa geopotential height contour for a variety of 120-h model forecasts made at the time of maximum TC–jet stream interaction (i.e., at 0000 UTC 25 September; top panel) show considerable uncertainty in the amplitude and position of an eastern U.S. trough at 0000 UTC 30 September. As noted in section 4c(ii), this trough (PV streamer) over the eastern U.S. plays a key role in the heavy rain event over eastern North America on 30 September–1 October following the recurvature of Malakas (e.g., Figs. 4.14 and 4.15). Figure 4.25a shows that subsequent forecasts initialized after the time of maximum TC–jet stream interaction (i.e., at 0000

UTC 26 September and 0000 UTC 27 September; middle and bottom panels) come into agreement with regard to the amplitude and position of the eastern U.S. trough.

A plot of the GFS 120-h forecast vs. analyzed 579-dam 500-hPa geopotential height contour highlights the high-impact nature of the forecasts valid at 0000 UTC 30 September (Fig. 4.25b). Whereas the GFS analysis indicates the presence of a high-amplitude trough over the eastern U.S. with substantial moisture transport implied along its eastern flank (as in Figs. 4.15a,b), the 120-h GFS forecast indicates a relatively low-amplitude trough over eastern North America that is not conducive to poleward moisture transport.

g. Summary

During fall 2010, two recurving WNP TCs, Malakas in September and Chaba in October, are associated with downstream large-scale flow reconfigurations that lead to favorable synoptic conditions for extreme warmth over western North America and heavy rain over eastern North America. Following interactions between the TCs and the jet stream, RWT dispersion occurs across the North Pacific into North America, and is followed by AWB and the associated formation of PV streamers over eastern North America that are critical antecedents to heavy rain events.

Whereas the interaction between Malakas and the jet stream leads to RWT dispersion via diabatic ridge amplification, the interaction between Chaba and the jet stream appears to precondition the environment for RWT dispersion by establishing a strong jet stream over the North Pacific. In the case of Chaba, upper-tropospheric divergent outflow associated with a DRV-like feature along a baroclinic zone ahead of the TC appears to be at least as important as the outflow directly associated with the TC in strengthening the North Pacific jet stream.

A key difference between the respective TC–jet stream interactions associated with Malakas and Chaba is that Malakas interacts with an upstream trough, whereas Chaba does not. Although the case study of Chaba indicates that strong TC–jet stream interactions can occur without an upstream trough, that ridge amplification occurs only with Malakas suggests that ridge amplification might be favored when a recurving TC interacts with an upstream trough. Of interest is that both Malakas and Chaba strengthen after they recurve and are at their peak intensity at their times of maximum TC–jet stream interaction (Figs. 4.2a,b). This behavior is suggestive of a synergistic relationship between the TC and the jet stream in which divergent circulation of the TC strengthens the jet streak, thereby strengthening forcing for ascent in the equatorward jet-entrance region that in turn reinforces the divergent circulation of the TC. It is speculated that through this synergistic relationship with the jet streak, a TC may be able to maintain its tropical characteristics in the presence of strong vertical wind shear.

An examination of predictability associated with the recurvature of Malakas finds that uncertainty in the WNP ridge amplification associated with TC–jet stream interaction may contribute to considerable forecast error and uncertainty that develops downstream. The poor forecasts of RWT dispersion associated with the TC–jet stream interaction likely contribute to the observed drop in NH model skill in late September 2010.

h. Figures

(a) Malakas

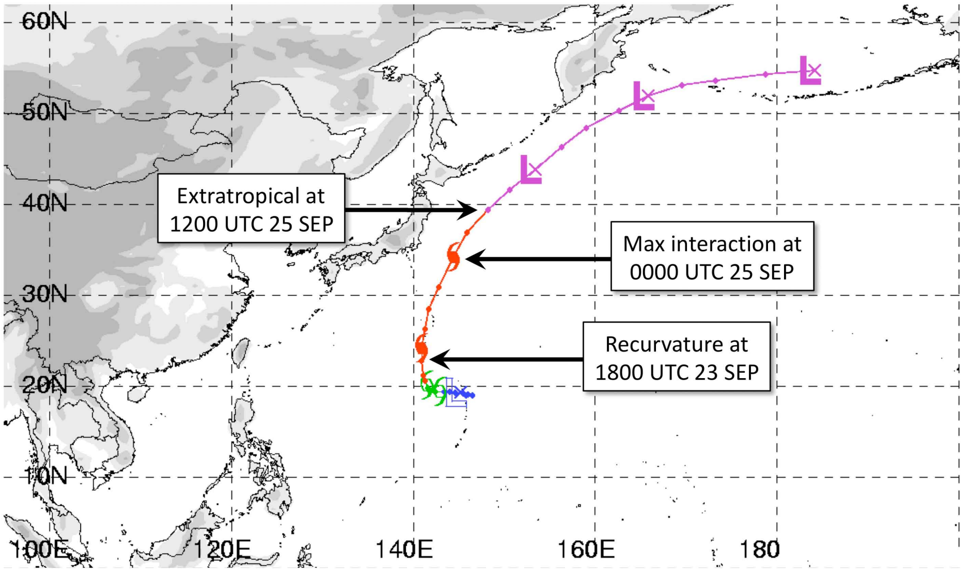

Extratropical at
1200 UTC 25 SEP

Max interaction at
0000 UTC 25 SEP

Recurvature at
1800 UTC 23 SEP

(b) Chaba

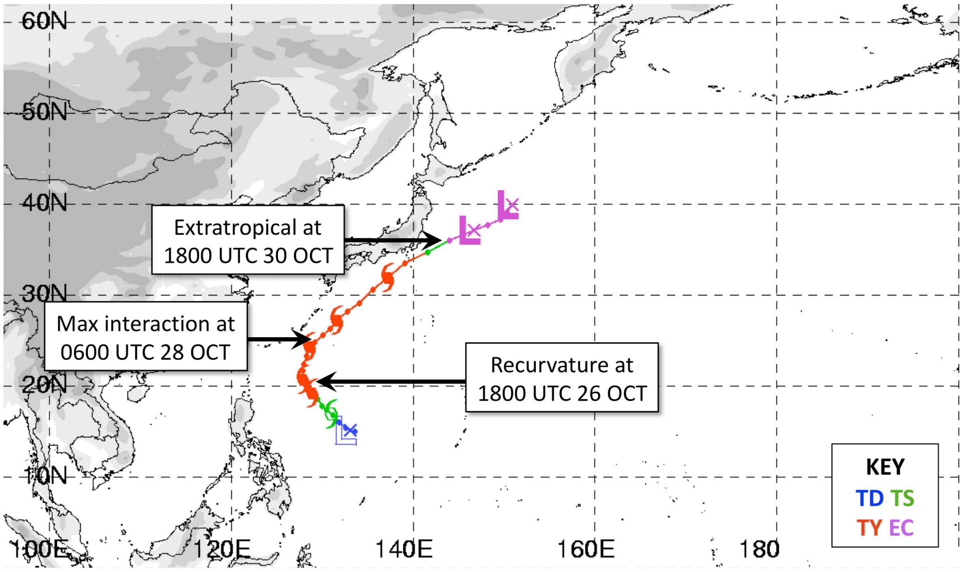

Extratropical at
1800 UTC 30 OCT

Max interaction at
0600 UTC 28 OCT

Recurvature at
1800 UTC 26 OCT

KEY
TD TS
TY EC

FIG. 4.1. JMA tracks of (a) TC Malakas (0600 UTC 20 Sep–0000 UTC 28 Sep 2010) and (b) TC Chaba (1800 UTC 23 Oct–0000 UTC 1 Nov 2010). TC symbols are plotted at 0000 UTC times, whereas dots are plotted at 0600, 1200, and 1800 UTC times. Arrows denote recurvature time, time of maximum TC–jet stream interaction (T+0 h), and time that the system becomes an EC (i.e., completes ET). The color key is provided in the lower-right corner of (b).

(a) Malakas

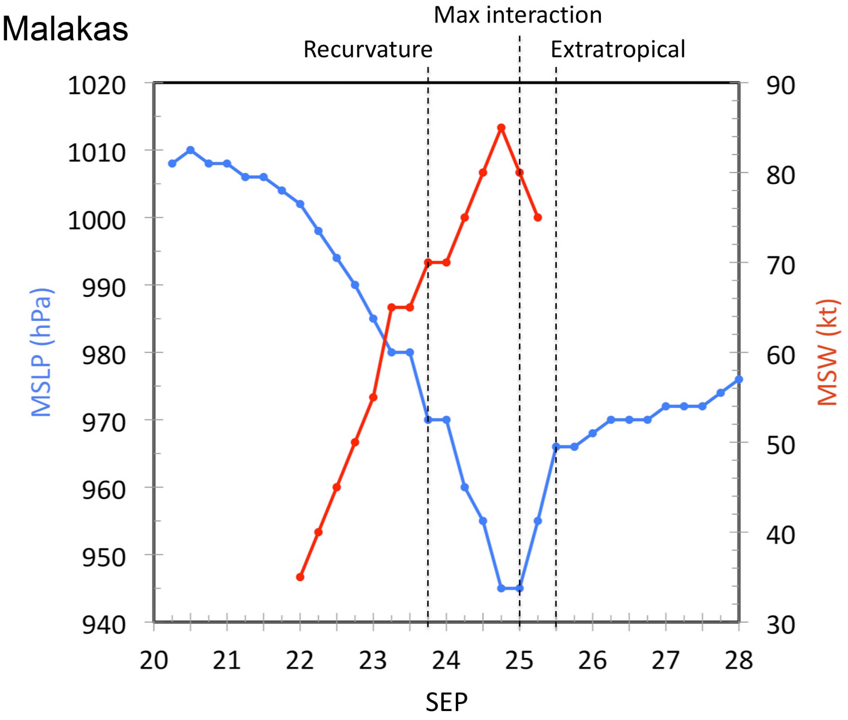

(b) Chaba

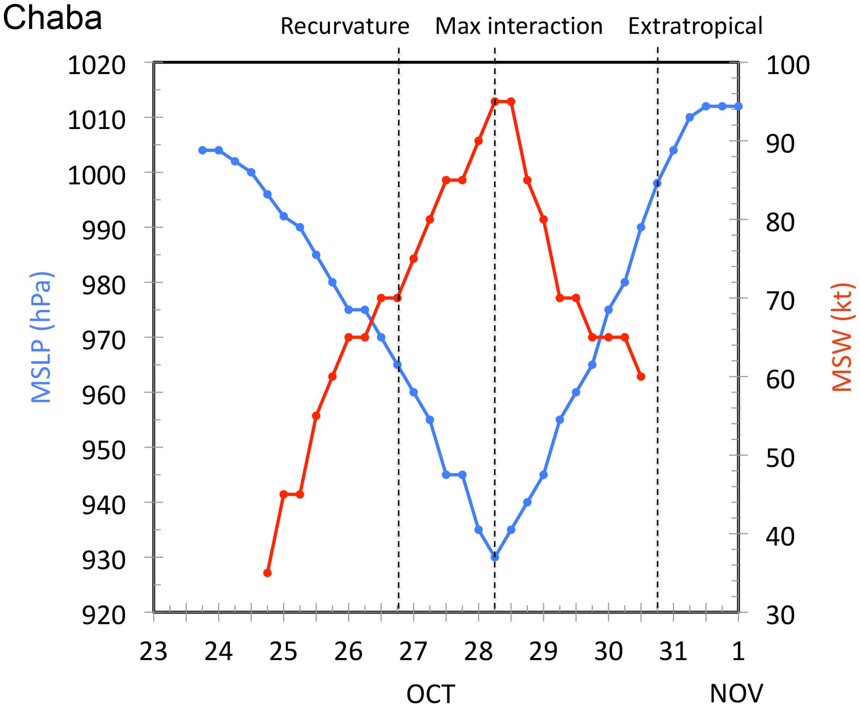

FIG. 4.2. Time series of JMA MSLP (blue, hPa) and MSW (red, kt) for (a) TC Malakas (0600 UTC 20 Sep–0000 UTC 28 Sep 2010) and (b) TC Chaba (1800 UTC 23 Oct–0000 UTC 1 Nov 2010). Dashed vertical lines denote recurvature time, time of maximum TC–jet stream interaction (T+0 h), and time that the system becomes an EC (i.e., completes ET).

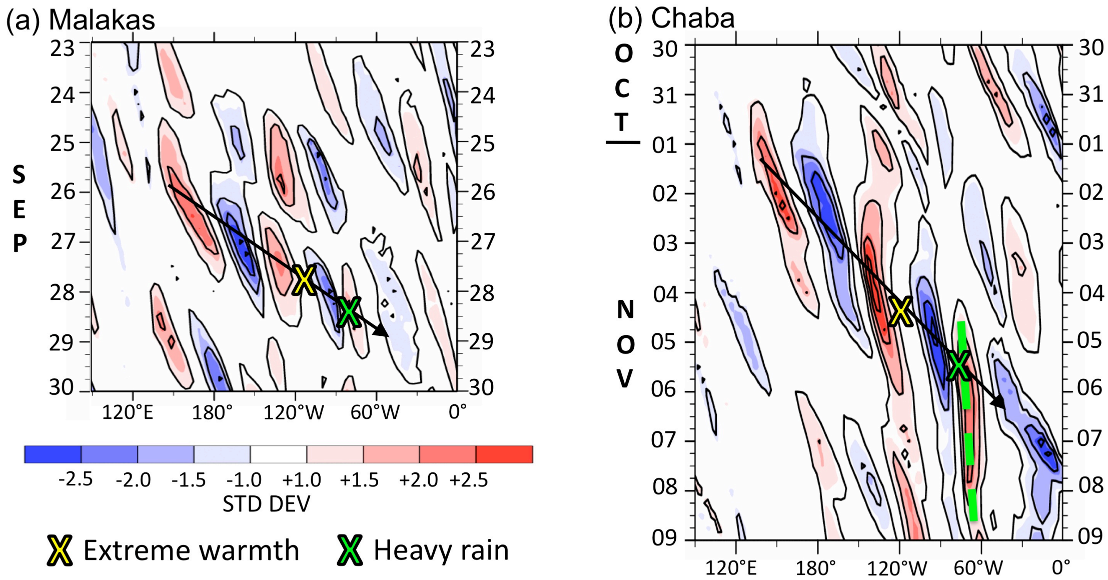

FIG. 4.3. Hovmöller diagram (90°E to 0°) of the 40°–60°N-averaged 250-hPa meridional wind anomaly (shaded according to the color bar, standard deviations) for the period following the recurvature of (a) TC Malakas and (b) TC Chaba. Contours denote absolute difference of meridional wind from climatology (every 15 m s^{-1}, zero line omitted). The "X" symbols indicate approximate time and longitude of high-impact weather events associated with Rossby wave trains. The arrows indicate apparent Rossby wave train dispersion. The dashed green line in (b) indicates the multiday heavy rain event over eastern North America.

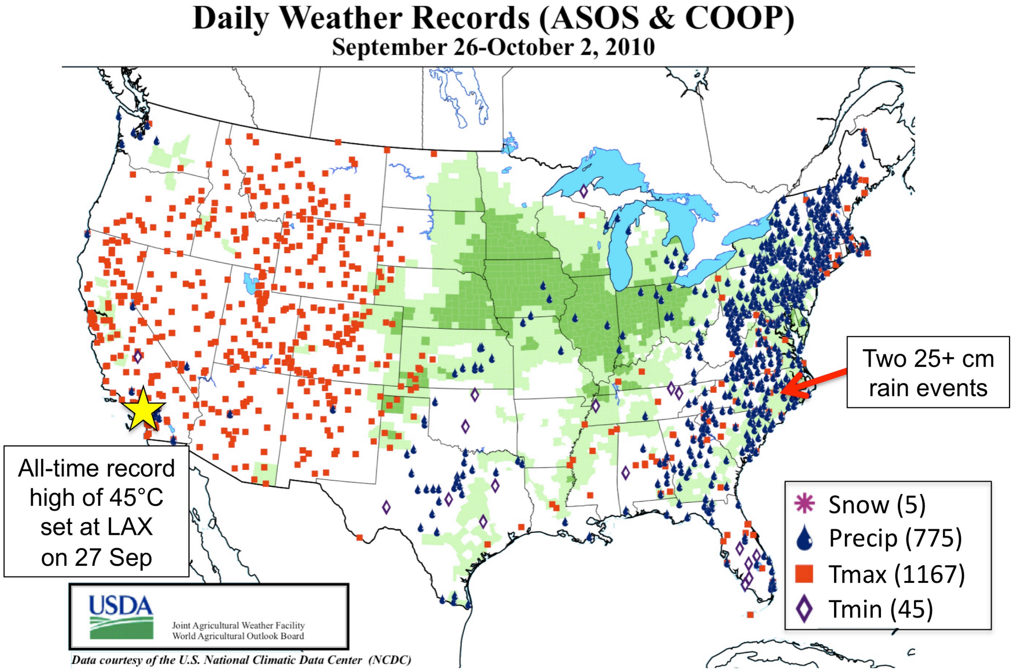

FIG. 4.4. Daily U.S. weather records for 26 Sep–2 Oct 2010. The counts of daily snowfall, precipitation, and maximum and minimum temperature records are indicated in the lower-right corner.

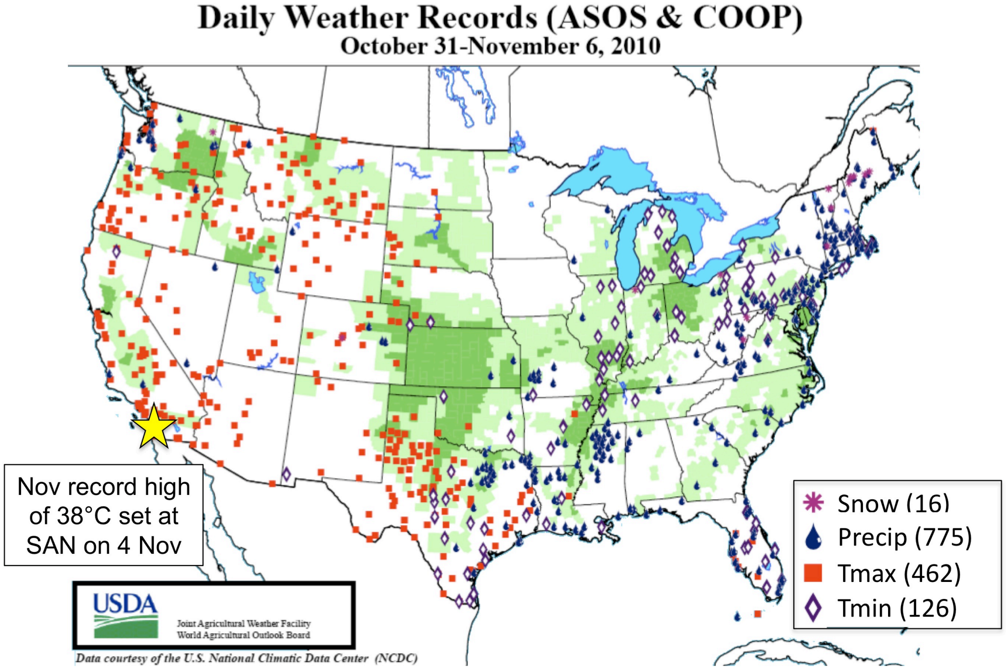

FIG. 4.5. As in Fig. 4.4, except for 31 Oct–6 Nov 2010.

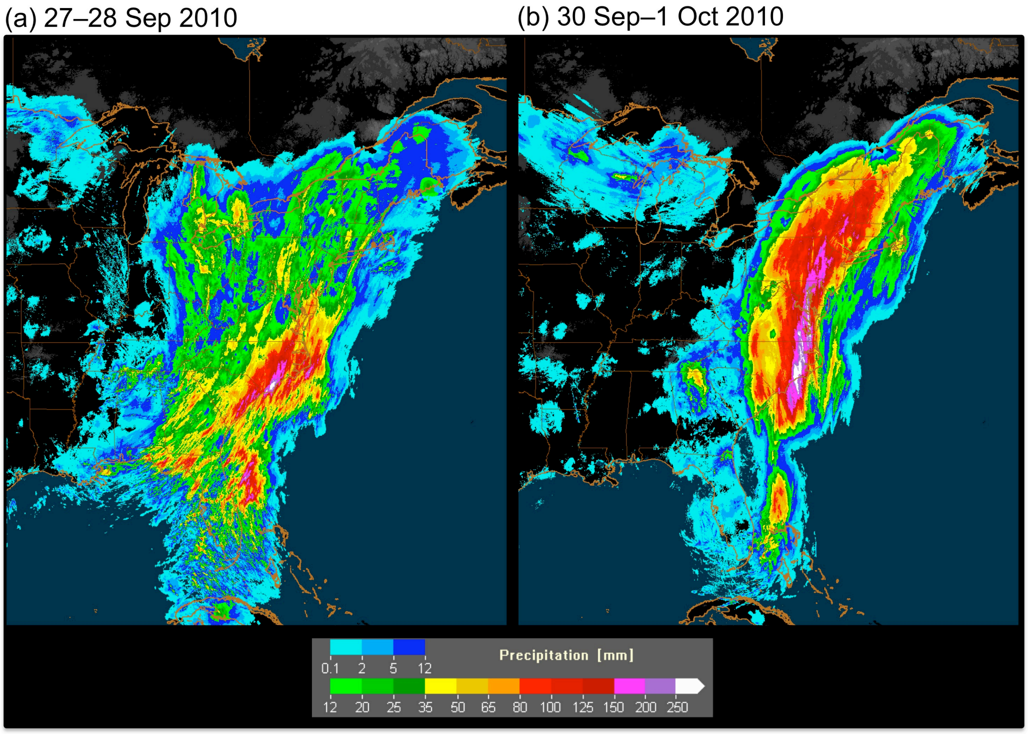

FIG. 4.6. 48-h rainfall totals (shaded according to the color bar, mm) for (a) 0000 UTC 27 Sep–0000 UTC 29 Sep and (b) 0000 UTC 30 Sep–0000 UTC 2 Oct.

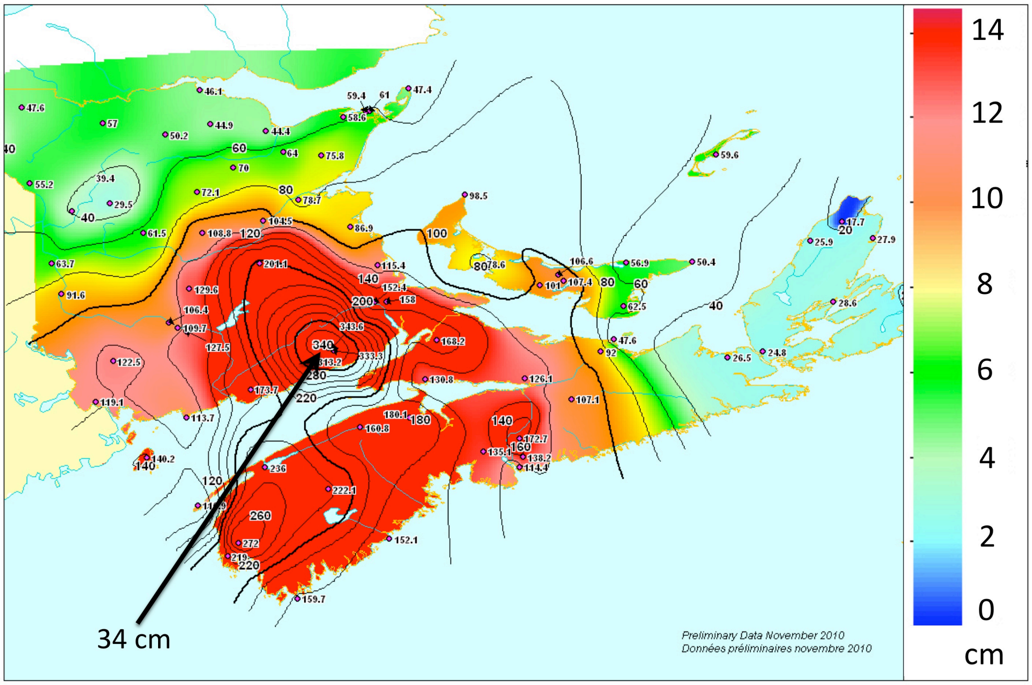

FIG. 4.7. Total accumulated precipitation (shaded according to the color bar, cm) over New Brunswick and Nova Scotia, Canada, for 4–9 Nov 2010.

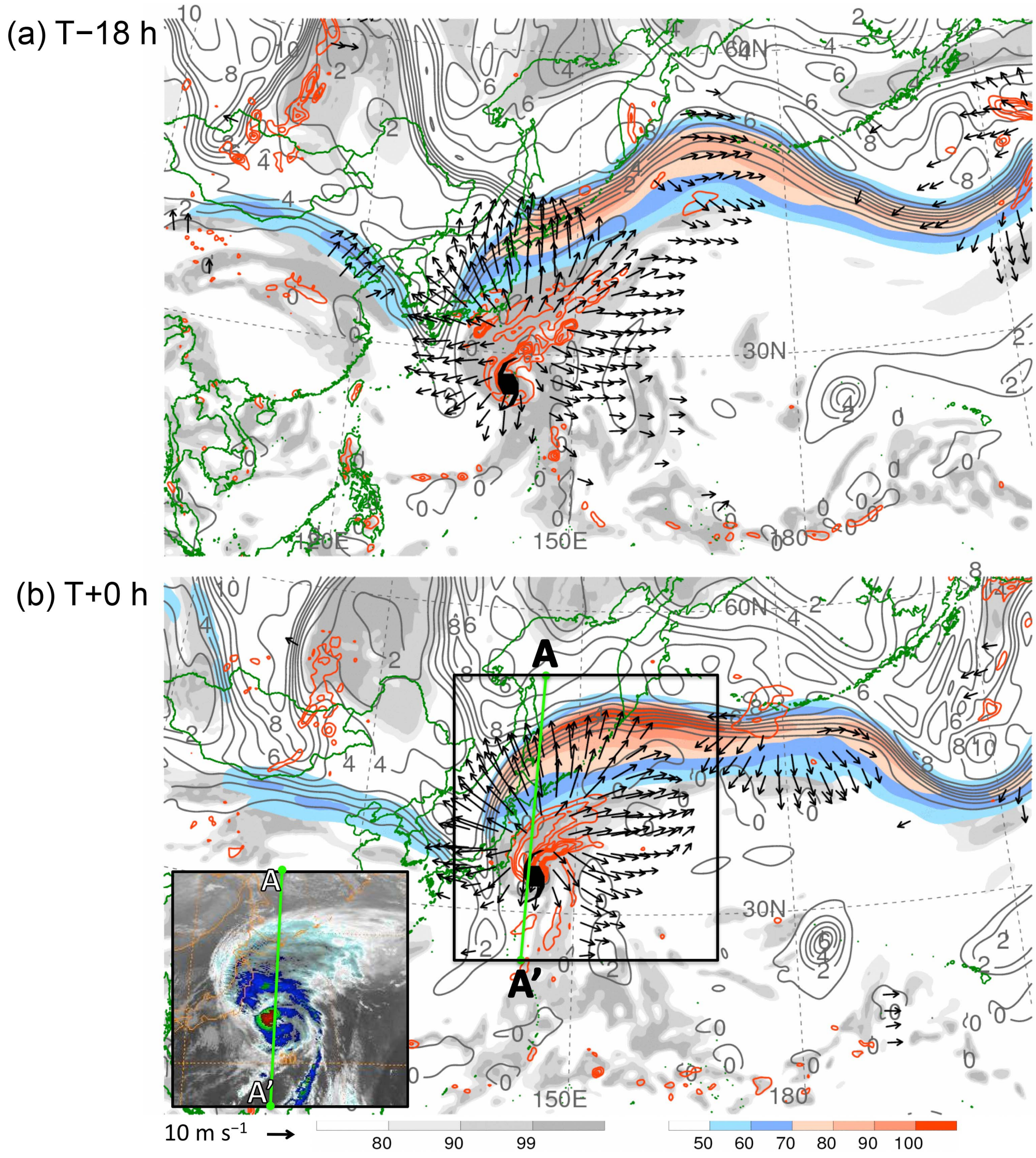

FIG. 4.8. Interaction between recurving WNP TC Malakas and the jet stream at (a) T−18 h (0600 UTC 24 Sep) and (b) T+0 h (0000 UTC 25 Sep). Plots show 250-hPa wind speed (shaded according to the color bar, m s^{-1}), PV (gray, every 1 PVU), and relative humidity (shaded according to the gray scale, %), 300–200-hPa layer-averaged irrotational wind (vectors, speeds greater than 5 m s^{-1}), and 600–400-hPa layer-averaged ascent (red, every 5×10^{-3} hPa s^{-1}). The TC symbols denote the JMA best-track position of TC Malakas. In (b), the box denotes the approximate domain of the inset, which shows the corresponding IR satellite image, and the green line denotes the location of the vertical cross section shown in Fig. 4.9.

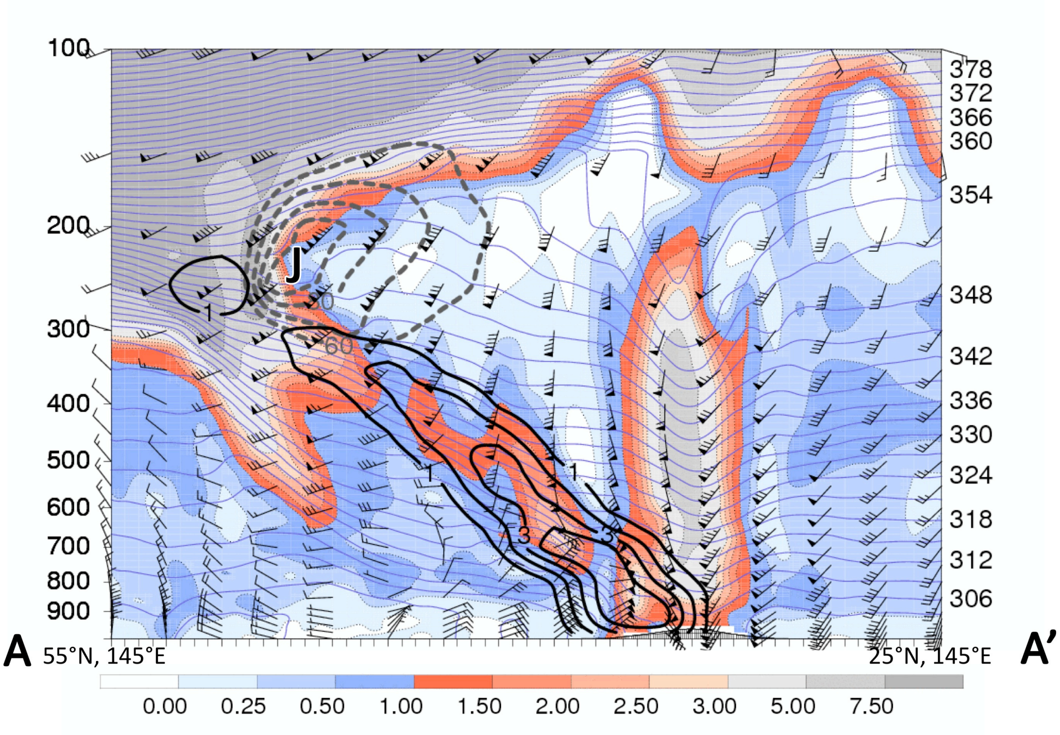

FIG. 4.9. North–south vertical cross section through the jet stream and PV tower associated with TC Malakas at T+0 h (0000 UTC 25 Sep). The location of the cross section is indicated by the green line in Fig. 4.8. Cross section shows Petterssen frontogenesis [thick black, °C (100 km)$^{-1}$ (3 h)$^{-1}$], PV (shaded according to the color bar, PVU), potential temperature (solid blue, K), wind speed (dashed gray, every 10 m s^{-1} starting at 60 m s^{-1}), and wind (barbs, kt). The "J" symbol denotes the jet stream core.

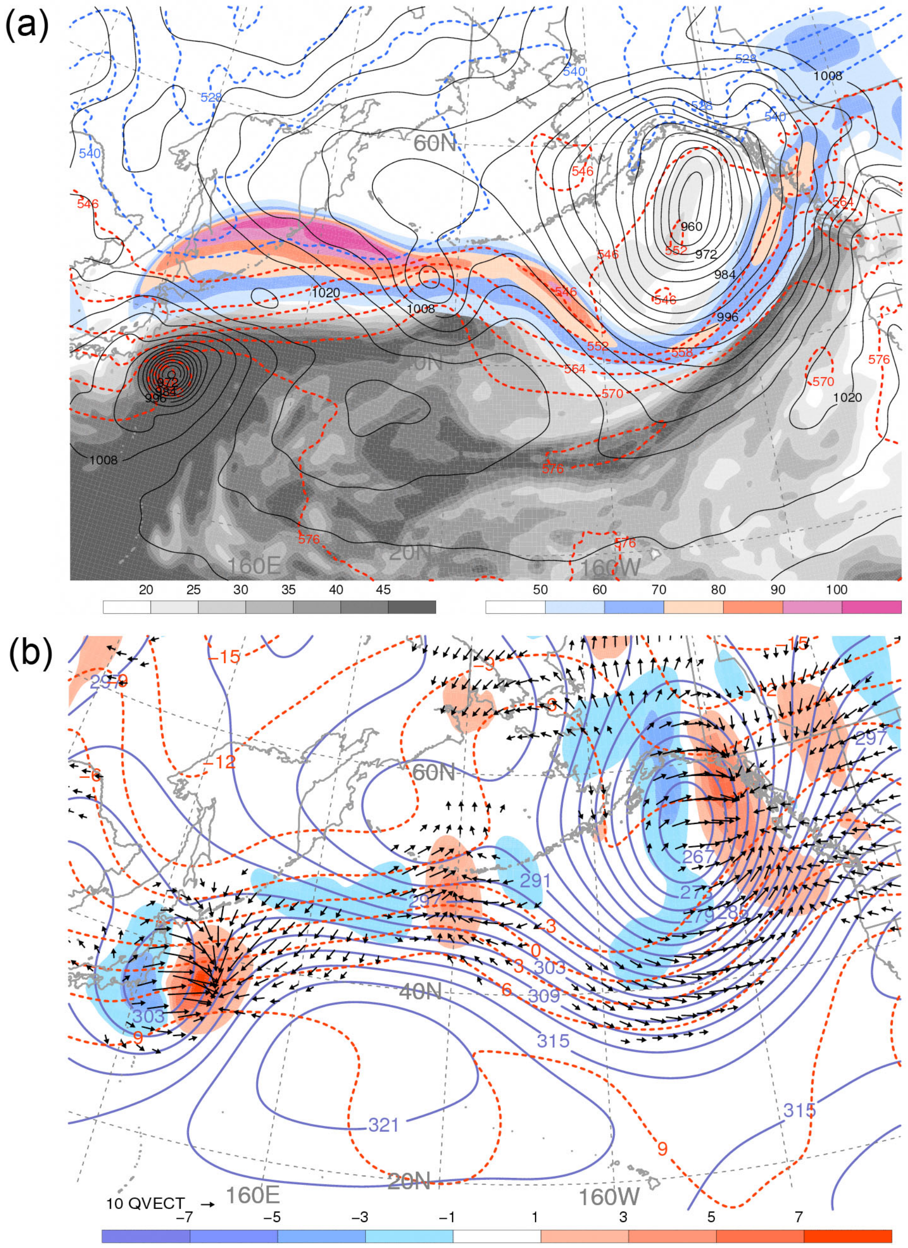

FIG. 4.10. Analyses showing TC Malakas at T+0 h (0000 UTC 25 Sep). Panel (a) shows total-column PW (shaded according to the gray scale, mm), 250-hPa wind speed (shaded according to the color bar, m s^{-1}), 1000–500-hPa thickness (dashed red, except dashed blue for values less than or equal to 540 dam; every 6 dam), and SLP (solid black, every 4 hPa). Panel (b) shows 700-hPa geopotential height (solid blue, every 3 dam), temperature (dashed red, every 3°C), $\vec{Q}$ (vectors, magnitudes greater than 0.5×10^{-7} Pa m^{-1} s^{-1}; the magnitude of the reference vector is 10^{-6} Pa m^{-1} s^{-1}), and $-2\vec{\nabla}_p \cdot \vec{Q}$ [10^{-12} Pa m^{-2} s^{-1}, shaded according to the color bar, with warm (cool) colors denoting forcing for ascent (descent)].

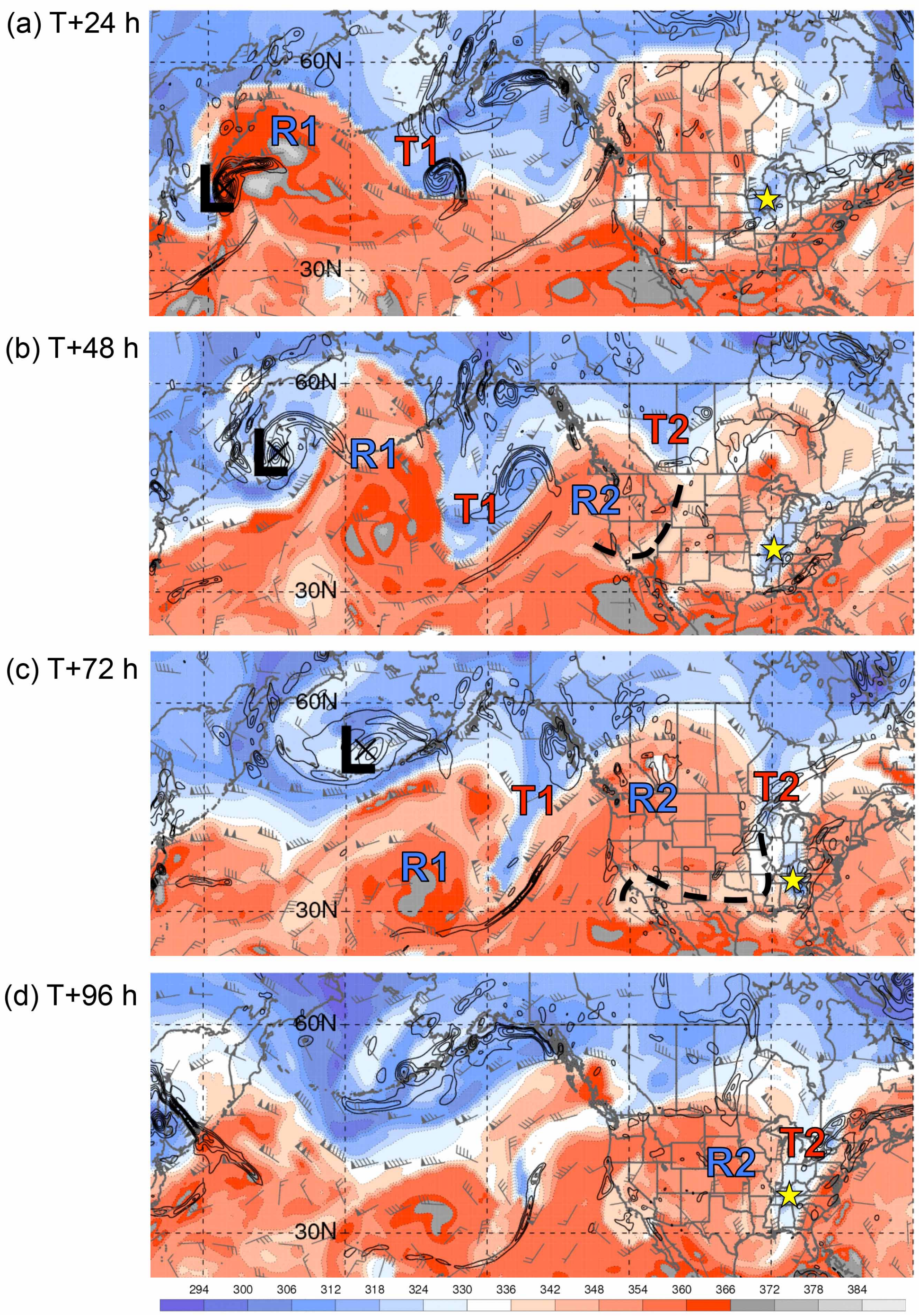

FIG. 4.11. Dynamic tropopause (1.5-PVU) potential temperature (shaded according to the color bar, K) and wind (barbs, kt), and 925–850-hPa layer-averaged cyclonic relative vorticity (solid, every $5 \times 10^{-5}\ \mathrm{s}^{-1}$) for (a) T+24 h (0000 UTC 26 Sep), (b) T+48 h (0000 UTC 27 Sep), (c) T+72 h (0000 UTC 28 Sep), and (d) T+96 h (0000 UTC 29 Sep). The "L" symbol in (a)–(c) denotes the JMA best-track position of Malakas as an EC. Ridges and troughs associated with Rossby wave train dispersion are denoted by the "R" and "T" symbols, respectively. The dashed black curve denotes a PV streamer, and the yellow star indicates a DT disturbance.

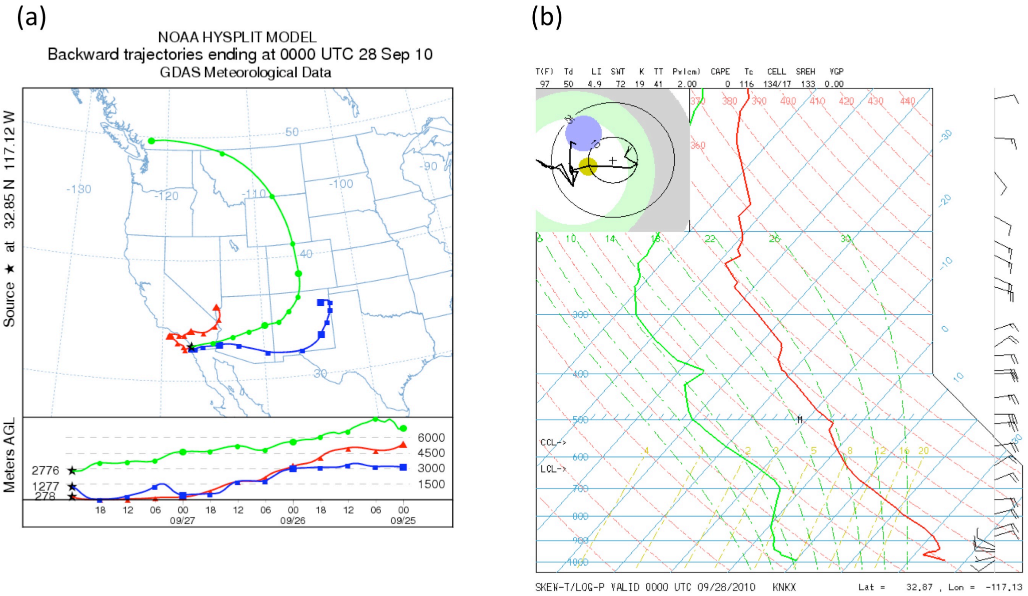

FIG. 4.12. Panel (a) shows paths of three 72-h back trajectories ending at 2776 m (green), 1277 m (blue), and 278 m (red) AGL, respectively, at NKX (San Diego Miramar, CA) at T+72 h (0000 UTC 28 Sep). Lower portion of panel (a) shows 72-h time series of parcel height (every 6 h). Panel (b) shows a skew *T*–log*p* diagram of air temperature (red, °C), dewpoint (green, °C), and wind (barbs, kt) at NKX at T+72 h. Inset in (b) shows the corresponding hodograph.

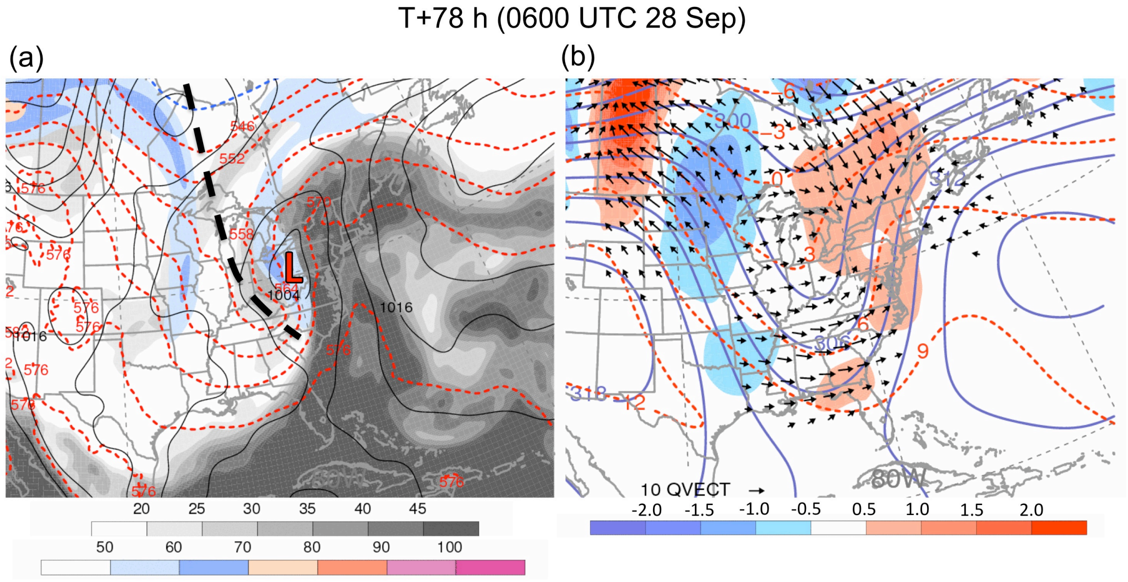

FIG. 4.13. Analyses for T+78 h (0600 UTC 28 Sep). Panel (a) shows total-column PW (shaded according to the gray scale, mm), 250-hPa wind speed (shaded according to the color bar, m s^{-1}), 1000–500-hPa thickness (dashed red, except dashed blue for values less than or equal to 540 dam; every 6 dam), and SLP (solid black, every 4 hPa). The "L" symbol denotes the position of a surface low. The dashed black line denotes the axis of a 1000–500-hPa thickness trough. Panel (b) shows 700-hPa geopotential height (solid blue, every 3 dam), temperature (dashed red, every 3°C), $\vec{Q}$ (vectors, magnitudes greater than 0.3×10^{-7} Pa m^{-1} s^{-1}; the magnitude of the reference vector is 10^{-6} Pa m^{-1} s^{-1}), and $-2\nabla_p \cdot \vec{Q}$ [10^{-12} Pa m^{-2} s^{-1}, shaded according to the color bar, with warm (cool) colors denoting forcing for ascent (descent)].

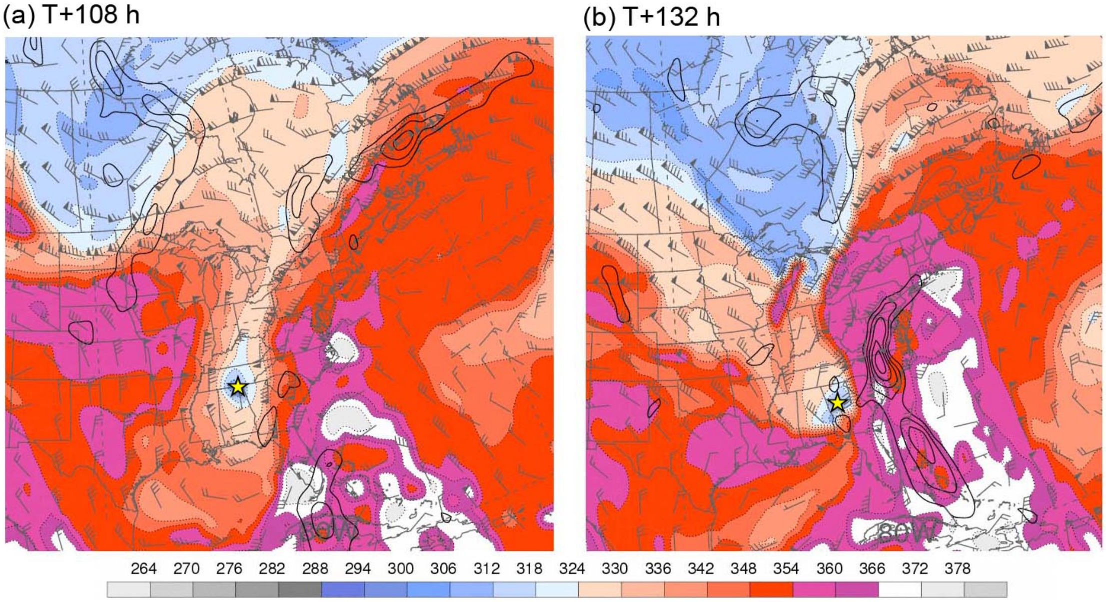

FIG. 4.14. Dynamic tropopause (1.5-PVU) potential temperature (shaded according to the color bar, K) and wind (barbs, kt), and 925–850-hPa layer-averaged cyclonic relative vorticity (solid, every 5×10^{-5} s^{-1}) for (a) T+108 h (1200 UTC 29 Sep) and (b) T+132 h (1200 UTC 30 Sep). The yellow star indicates a DT disturbance.

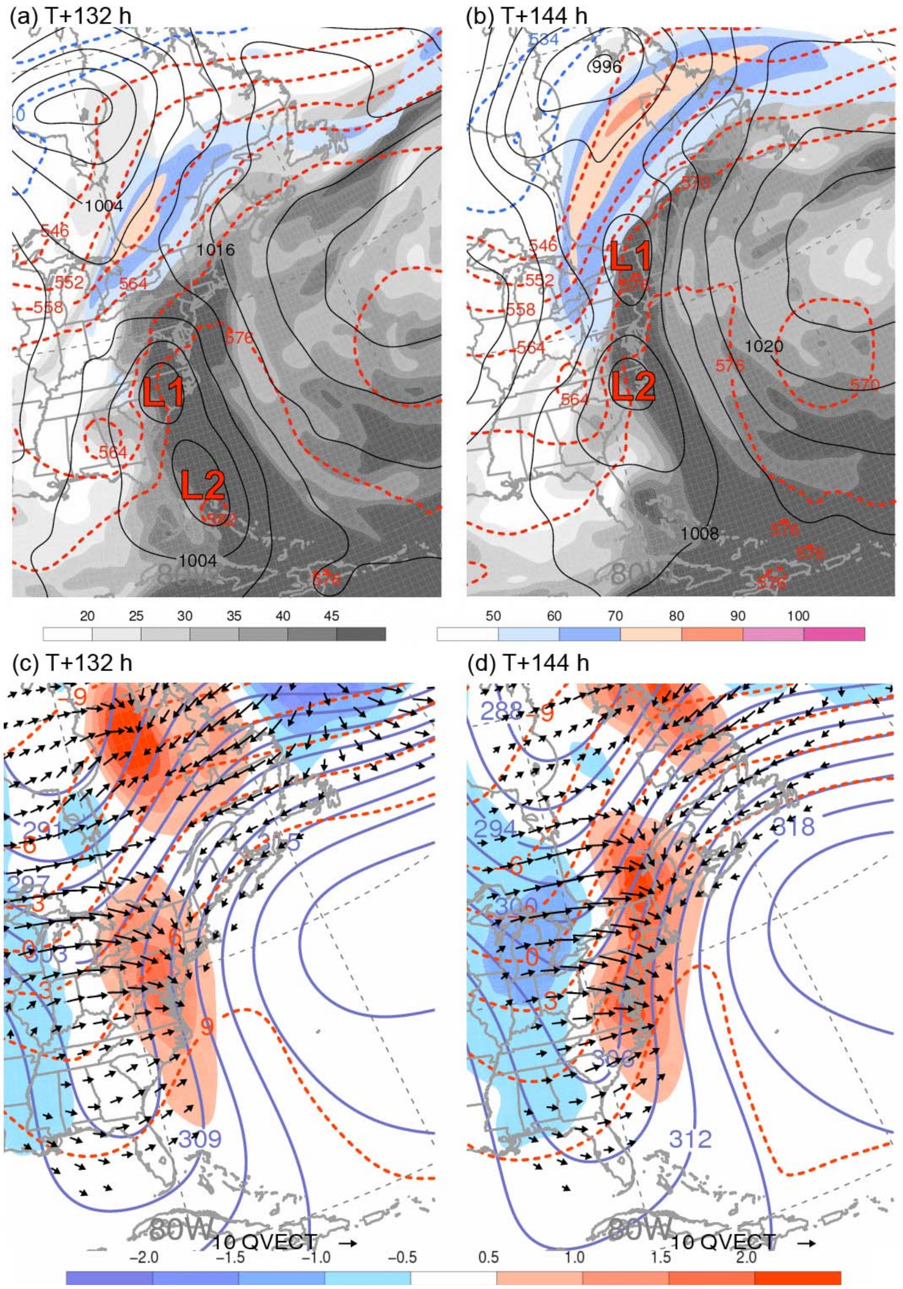

FIG. 4.15. Analyses for (a), (c) T+132 h (1200 UTC 30 Sep) and (b), (d) T+144 h (0000 UTC 1 Oct). Panels (a) and (b) show total-column PW (shaded according to the gray scale, mm), 250-hPa wind speed (shaded according to the color bar, m s^{-1}), 1000–500-hPa thickness (dashed red, except dashed blue for values less than or equal to 540 dam; every 6 dam), and SLP (solid black, every 4 hPa). The "L1" and "L2" symbols denote the positions of surface lows. Panels (c) and (d) show 700-hPa geopotential height (solid blue, every 3 dam), temperature (dashed red, every 3°C), $\vec{Q}$ (vectors, magnitudes greater than 0.3×10^{-7} Pa m^{-1} s^{-1}; the magnitude of the reference vector is 10^{-6} Pa m^{-1} s^{-1}), and $-2\nabla_p \cdot \vec{Q}$ [10^{-12} Pa m^{-2} s^{-1}, shaded according to the color bar, with warm (cool) colors denoting forcing for ascent (descent)].

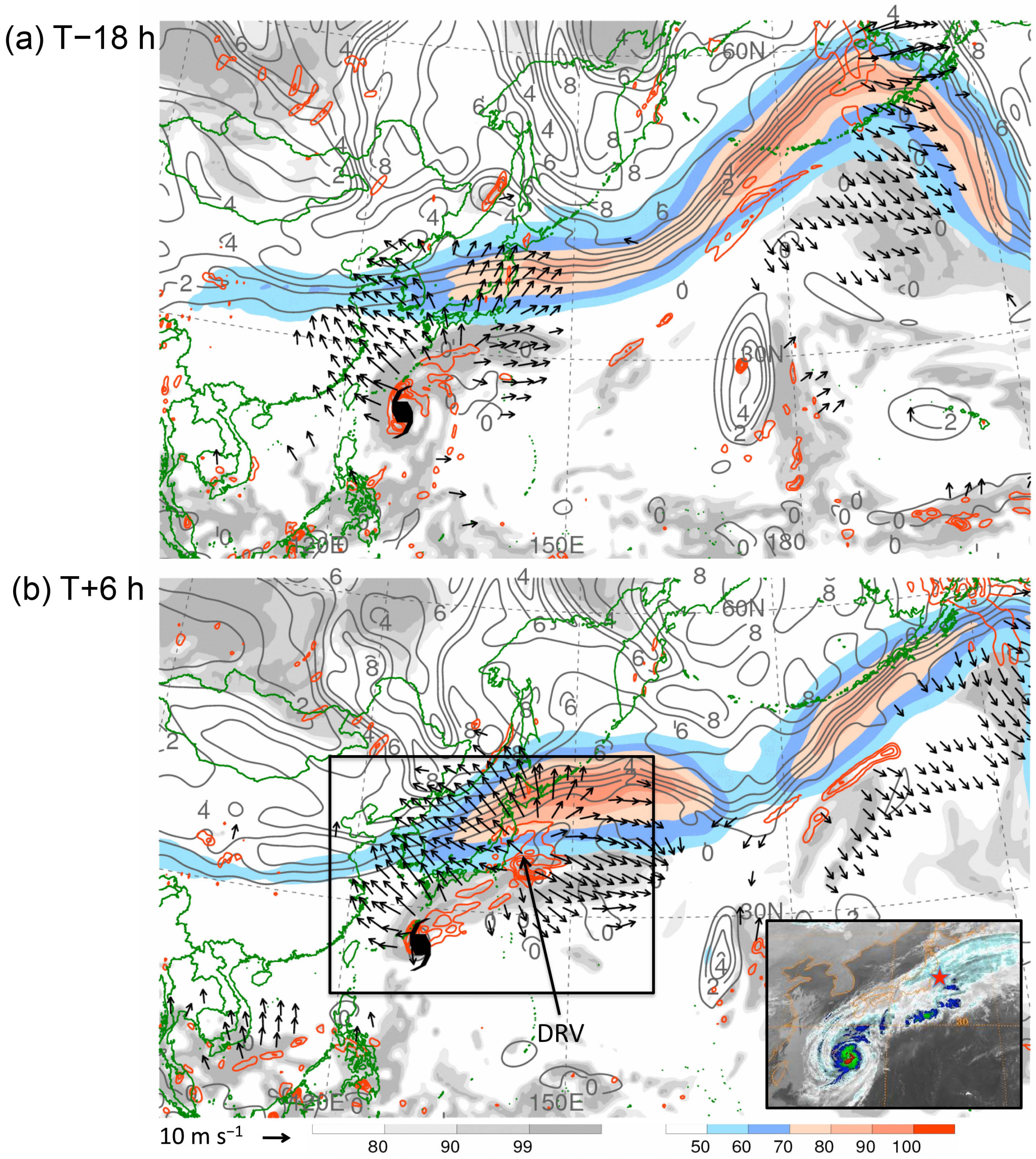

FIG. 4.16. Interaction between recurving WNP TC Chaba and the jet stream at (a) T−18 h (1200 UTC 27 Oct) and (b) T+6 h (1200 UTC 28 Oct). Plots show 250-hPa wind speed (m s^{-1}, shaded according to the color bar), PV (gray, PVU), and relative humidity (%, shaded according to the gray scale), 300–200-hPa layer-averaged irrotational wind (vectors, speeds greater than 5 m s^{-1}), and 600–400-hPa layer-averaged ascent (red, every 5 × 10^{-3} hPa s^{-1}). The TC symbols denote the JMA best-track position of TC Chaba. In (b), the box denotes the approximate domain of the inset, which shows the corresponding IR satellite image. The star in the inset denotes the approximate position of an apparent diabatic Rossby vortex (DRV).

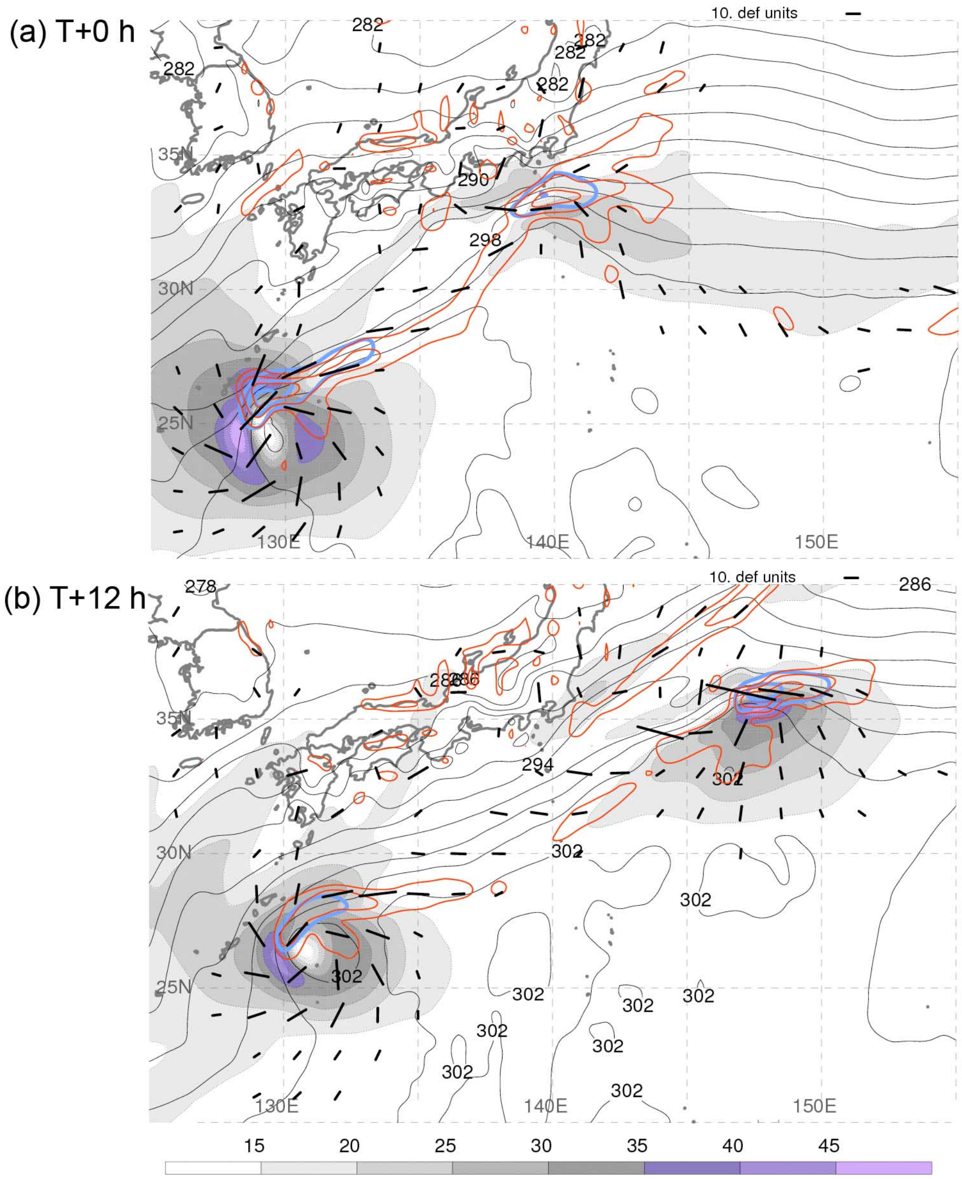

FIG. 4.17. Analysis of 925-hPa dilatation axes (length proportional to magnitude of resultant deformation, plotted for values greater than 5×10^{-5} s^{-1}), wind speed (shaded in m s^{-1} according to the color bar), potential temperature (black, every 5 K), Petterssen frontogenesis [blue, every 10°C (100 km)$^{-1}$ (3 h)$^{-1}$ starting at 5°C (100 km)$^{-1}$ (3 h)$^{-1}$], and ascent (red, every 8×10^{-3} hPa s^{-1} starting at -4×10^{-3} hPa s^{-1}) for (a) T+0 h (0600 UTC 28 Oct) and (b) T+12 h (1800 UTC 28 Oct 2010).

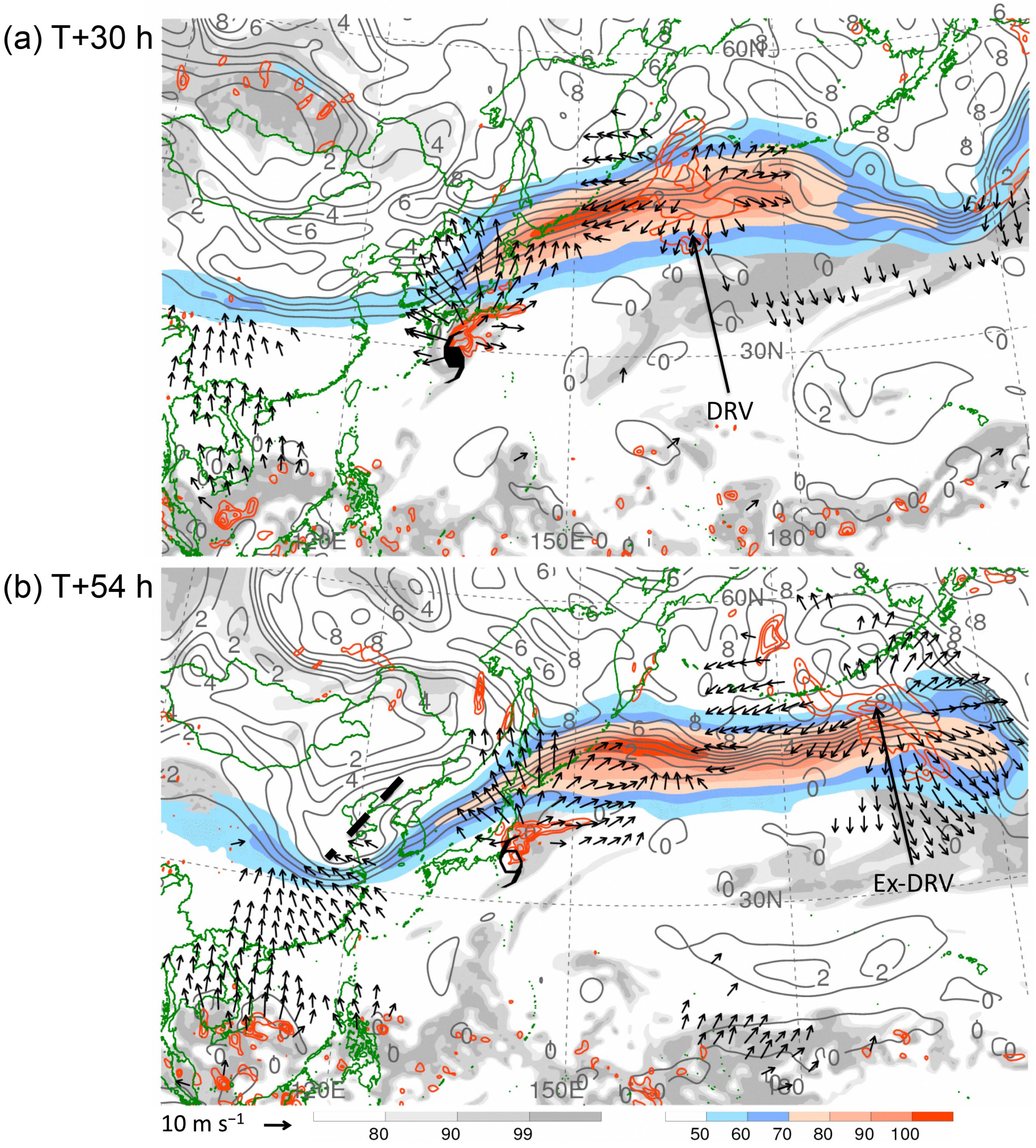

FIG. 4.18. Interaction between recurving WNP TC Chaba and the jet stream at (a) T+30 h (1200 UTC 29 Oct) and (b) T+54 h (1200 UTC 30 Oct). Plots show 250-hPa wind speed (m s^{-1}, shaded according to the color bar), PV (gray, PVU), and relative humidity (%, shaded according to the gray scale), 300–200-hPa layer-averaged irrotational wind (vectors, speeds greater than 5 m s^{-1}), and 600–400-hPa layer-averaged ascent (red, every 5×10^{-3} hPa s^{-1}). The TY symbol in (a) and TS symbol in (b) denote the JMA best-track position of TC Chaba. Dashed line in (b) denotes an upper-tropospheric PV disturbance.

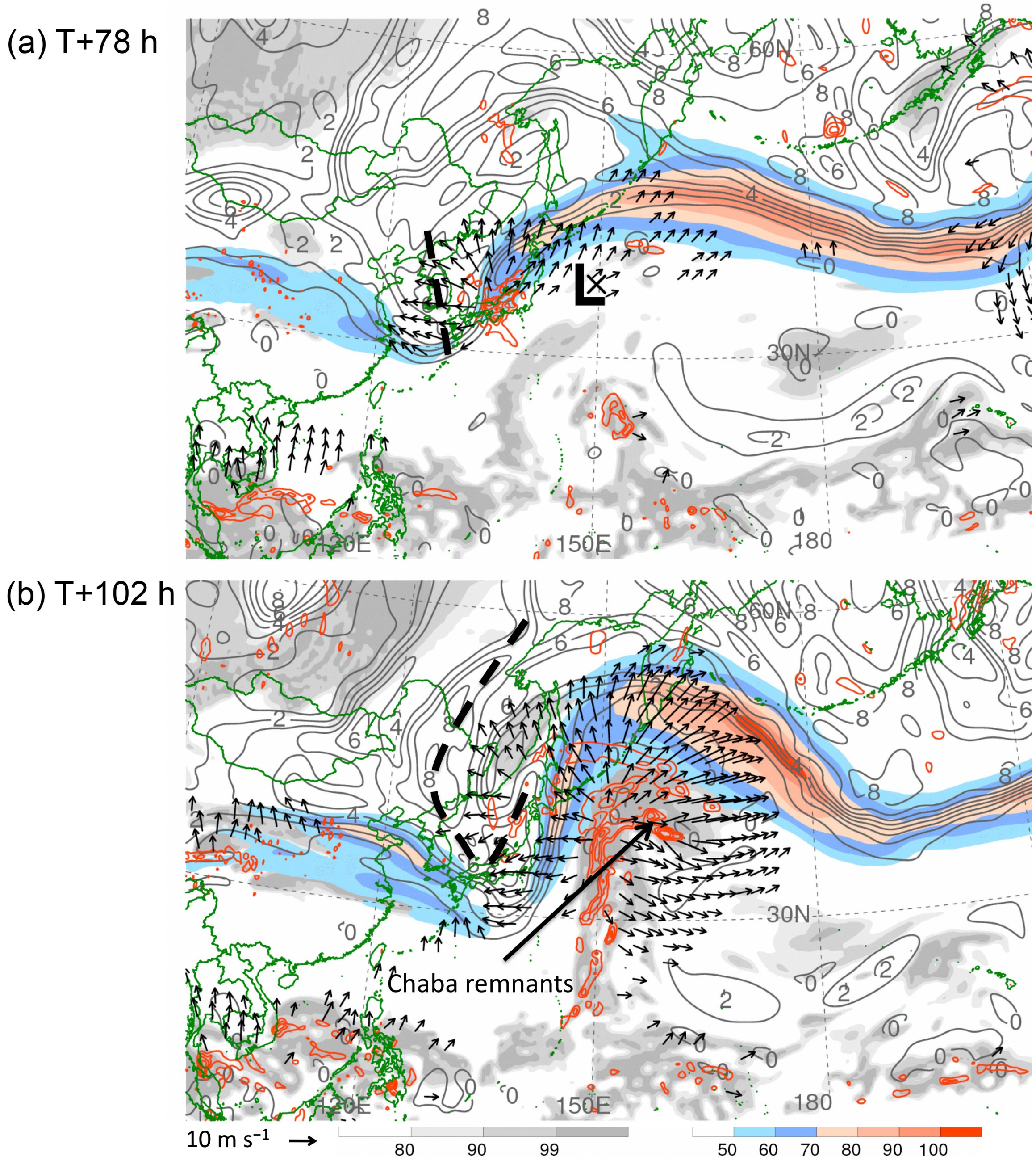

FIG. 4.19. Interaction between recurving WNP TC Chaba and the jet stream at (a) T+78 h (1200 UTC 31 Oct) and (b) T+102 h (1200 UTC 1 Nov). Plots show 250-hPa wind speed (m s^{-1}, shaded according to the color bar), PV (gray, PVU), and relative humidity (%, shaded according to the gray scale), 300–200-hPa layer-averaged irrotational wind (vectors, speeds greater than 5 m s^{-1}), and 600–400-hPa layer-averaged ascent (red, every 5×10^{-3} hPa s^{-1}). Dashed curve denotes upper-tropospheric PV disturbance. The "L" symbol in (a) denotes the JMA best-track position of Chaba.

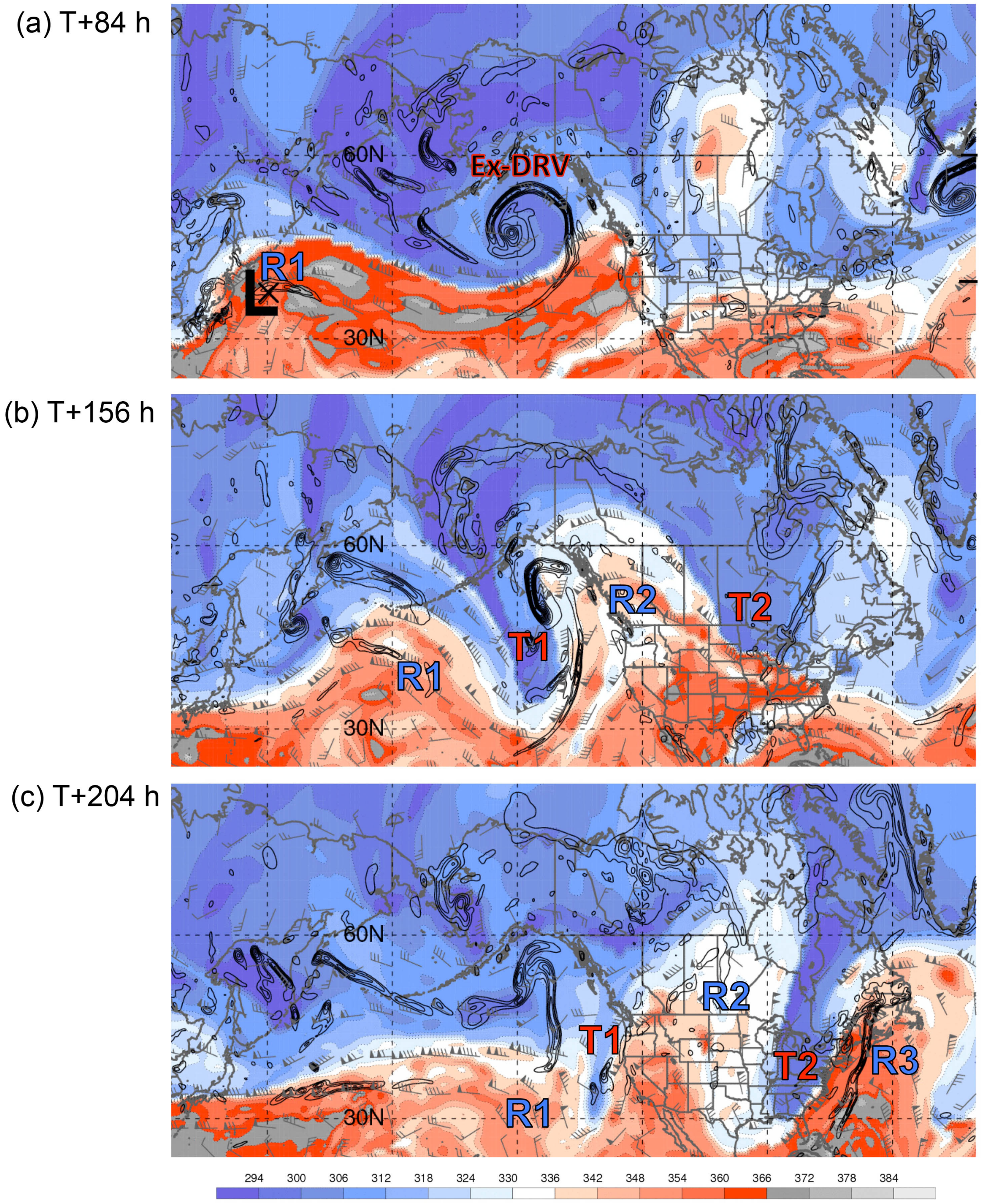

FIG. 4.20. Dynamic tropopause (1.5-PVU) potential temperature (shaded according to the color bar, K) and wind (barbs, kt), and 925–850-hPa layer-averaged cyclonic relative vorticity (solid, every 5×10^{-5} s^{-1}) for (a) T+84 h (1800 UTC 31 Oct), (b) T+156 h (1800 UTC 3 Nov), and (c) T+204 h (1800 UTC 5 Nov). Ridges and troughs associated with Rossby wave train dispersion are denoted by the "R" and "T" symbols, respectively. The "L" symbol in (a) denotes the JMA best-track position of Chaba.

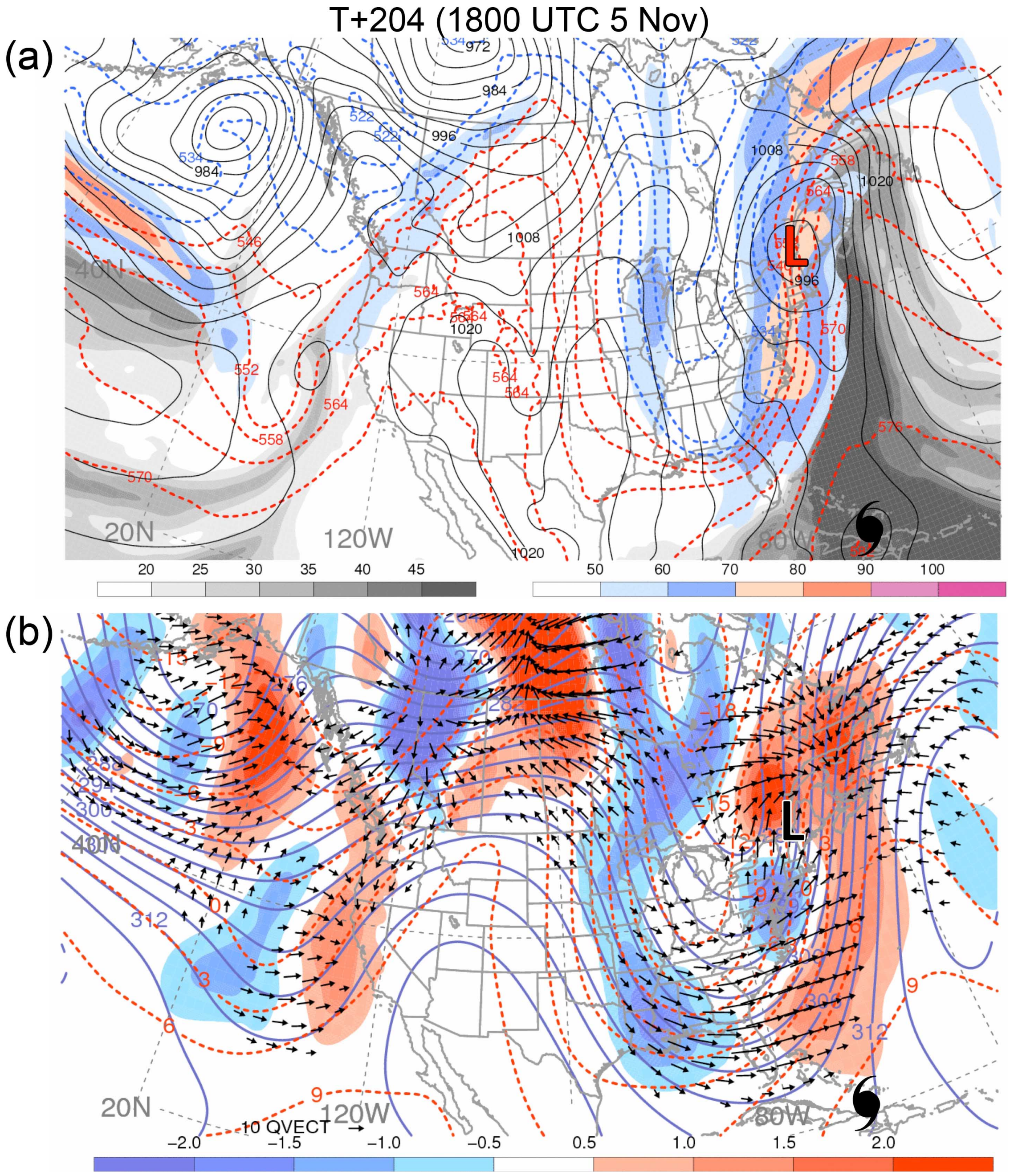

FIG. 4.21. Analyses at T+204 h (1800 UTC 5 Nov). Panel (a) shows total-column PW (shaded according to the gray scale, mm), 250-hPa wind speed (shaded according to the color bar, m s^{-1}), 1000–500-hPa thickness (dashed red, except dashed blue for values less than or equal to 540 dam; every 6 dam), and SLP (solid black, every 4 hPa). Panel (b) shows 700-hPa geopotential height (solid blue, every 3 dam), temperature (dashed red, every 3°C), $\vec{Q}$ (vectors, magnitudes greater than 0.5×10^{-7} Pa m^{-1} s^{-1}; the magnitude of the reference vector is 10^{-6} Pa m^{-1} s^{-1}), and $-2\nabla_p \cdot \vec{Q}$ [10^{-12} Pa m^{-2} s^{-1}, shaded according to the color bar, with warm (cool) colors denoting forcing for ascent (descent)]. The TC symbol denotes the position of TC Tomas, and the “L” symbol denotes a surface low.

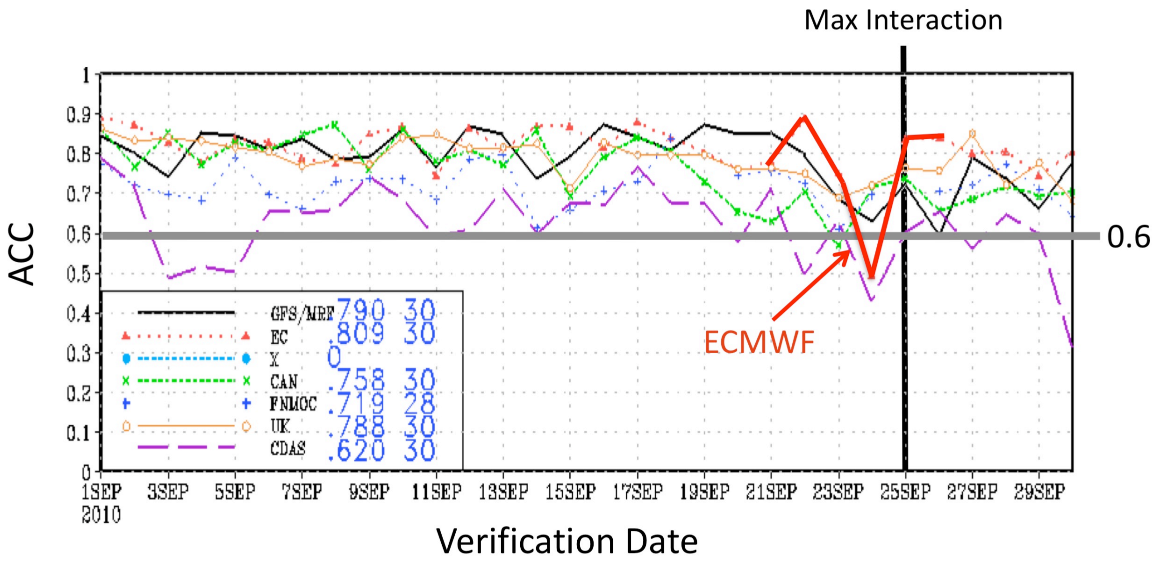

FIG. 4.22. Time series of daily ACCs for 144-h NH 500-hPa geopotential height forecasts verifying 1–30 Sep 2010 for a variety of global models. The black curve indicates the GFS ACC time series, whereas the red dotted curve indicates the ECMWF ACC time series (solid red surrounding the time of interest). The maximum TC–jet stream interaction time (0000 UTC 25 Sep 2010) associated with TC Malakas is given by the black vertical line. The 0.6-ACC threshold, above which forecasts are considered to be skillful, is given by the gray horizontal line.

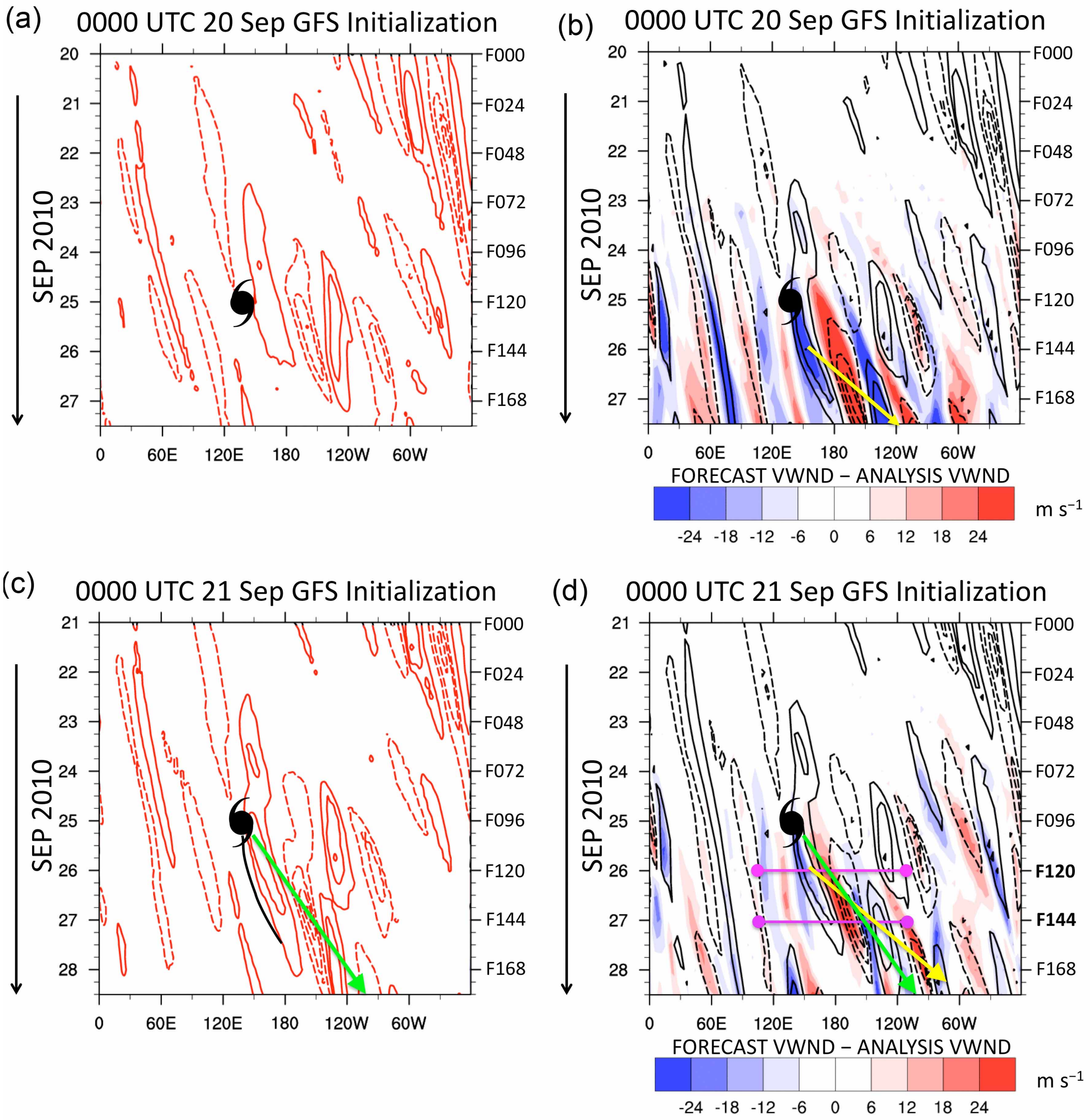

FIG. 4.23. Hovmöller diagrams of 40°–60°N-averaged 250-hPa meridional wind contoured every 15 m s^{-1}, with the zero line omitted. Solid contours denote southerly winds and dashed contours denote northerly winds. The TC symbols denote the time and longitude of TC Malakas at T+0 h (the time of maximum TC–jet stream interaction). Panels (a) and (c) show the GFS forecast, whereas panels (b) and (d) show the GFS analysis, with model error (forecast minus analysis) shaded in m s^{-1} according to the color bar. Forecast data in (a) and (b) are from the 0000 UTC 20 Sep and 21 Sep GFS initializations, respectively. The yellow and green arrows denote Rossby wave train dispersion in the analysis and forecast, respectively. The black curve in (c) shows the analyzed 15-m s^{-1} 250-hPa meridional wind contour displayed in (d). The purple horizontal lines in (d) denote the time and longitudinal extent of the plots in Fig. 4.24.

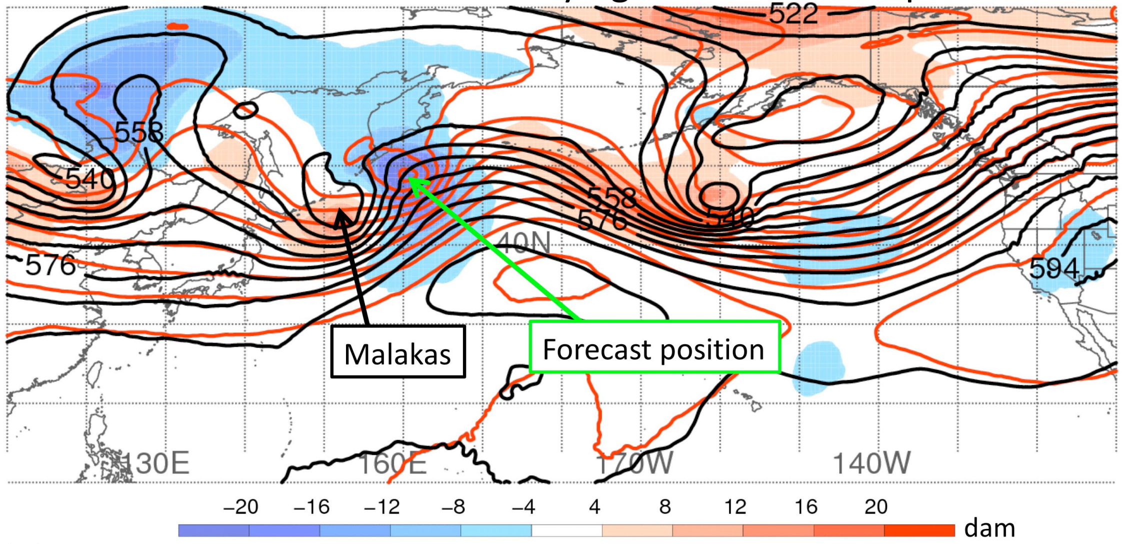
(a) 120-h Forecast Verifying 0000 UTC 26 Sep

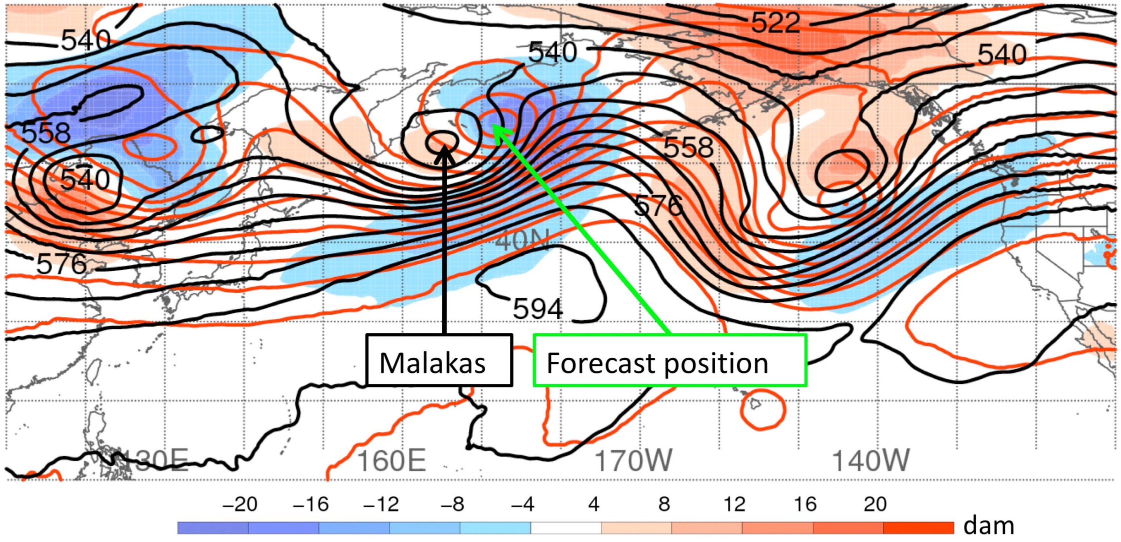
(b) 144-h Forecast Verifying 0000 UTC 27 Sep

FIG. 4.24. Plots showing the 500-hPa geopotential height forecasts from the 0000 UTC 21 Sep GFS initialization (red, dam), the verifying analyses (black, dam), and model error (forecast minus analysis; shaded according to the color bar, dam). In panel (a), the 120-h forecast is shown with the verifying 0000 UTC 26 Sep analysis. In panel (b), the 144-h forecast is shown with the verifying 0000 UTC 27 Sep analysis.

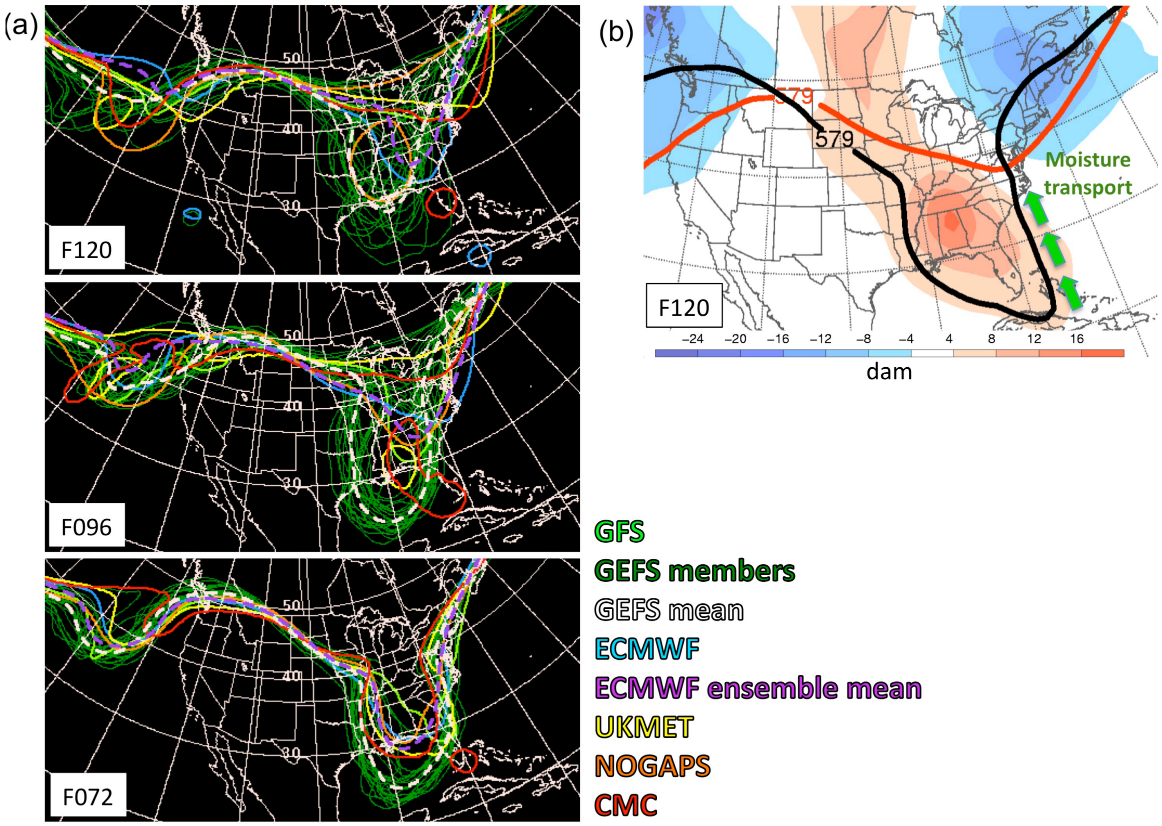

FIG. 4.25. Panel (a) shows spaghetti plots of forecasts of the 579-dam 500-hPa geopotential height contour verifying at 0000 UTC 30 Sep 2010. The top panel shows 120-h forecasts from 0000 UTC 25 Sep model initializations, the middle panel shows 96-h forecasts from 0000 UTC 26 Sep model initializations, and the bottom panel shows 72-h forecasts from 0000 UTC 27 Sep model initializations. Panel (b) shows the 120-h GFS forecast (red) and 0000 UTC 30 Sep 2010 verifying analysis (black) of the 579-dam 500-hPa geopotential height contour, and the 500-hPa geopotential height model error (forecast minus analysis; shaded according to the color bar, dam).

5. Discussion

a. Characteristic downstream flow response to recurving WNP TCs

A climatological analysis reveals that the North Pacific flow pattern becomes significantly more meridional than normal almost immediately following WNP TC recurvature, and remains more meridional than normal for approximately a four-day period (Fig. 2.16). The significantly more meridional flow pattern over the North Pacific that develops following WNP TC recurvature suggests an association between WNP TC recurvature and enhanced RWT activity over the North Pacific. This association is confirmed by a composite analysis, which shows that recurving WNP TCs tend to be associated with the pronounced amplification of a WNP RWT migrating from Asia (Fig. 3.2). As the RWT amplifies, it disperses eastward within the North Pacific jet stream (Fig. 3.4), which serves as a Rossby waveguide (e.g., Schwierz et al. 2004; Martius et al. 2010), between one day before through three days after WNP TC recurvature (Figs. 3.3d–h). The North Pacific RWT dispersion is characterized by ridge amplification and jet streak intensification downstream of the TC and surface cyclogenesis in the poleward exit region of the jet streak (Fig. 3.4). These signatures are consistent with the results from case studies (e.g., Harr and Dea 2009) and idealized modeling studies (e.g., Riemer et al. 2008; Riemer and Jones 2010) that indicate downstream baroclinic development may accompany TC recurvature episodes.

A key finding of the composite analysis is that as a WNP TC recurves, the ridge amplification and jet streak intensification downstream of the TC appear to occur in response to diabatically driven upper-tropospheric divergent outflow associated with the recurving TC impinging on the jet stream (Figs. 3.3d–f). Thus, a dynamical link exists between the divergent outflow associated with the TC and RWT amplification and dispersion. This dynamical link corroborates recent idealized modeling studies of recurving TCs that point to the divergent circulation of the TC as an important aspect of RWT amplification and dispersion associated with TC recurvature (i.e., Riemer et al. 2008; Riemer and Jones 2010; Hodyss and Hendricks 2010).

The composite analysis of all recurving WNP TCs further shows that as the amplified RWT associated with WNP TC recurvature migrates away from the climatologically strong jet stream and waveguide over the North Pacific and toward the climatologically weak jet stream and waveguide over North America (e.g., Fig. 1.2), the RWT evolves into a more anticyclonically arcing configuration. This arcing structure is reminiscent of a Pacific–North America pattern (e.g., Wallace and Gutzler 1981) barotropic RWT forced by anomalous tropical heating that typically evolves on intraseasonal time scales along an approximate great circle path (e.g., Hoskins and Karoly 1981; Sardushmukh and Hoskins 1988; Hoskins and Ambrizzi 1993). Two to three days after WNP TC recurvature, an upper-tropospheric ridge tends to develop over the eastern North Pacific and high-latitude western North America (Figs. 3.3g,h). Four to five days after WNP TC recurvature, a downstream positively tilted trough develops over central Canada and the western U.S. (Figs. 3.3i,j).

b. Factors influencing the downstream flow response to recurving WNP TCs

Climatological and composite analyses of recurving WNP TCs stratified by month indicate that time of year impacts the significance, duration, and timing of the above-normal North Pacific meridional flow that tends to develop following recurving WNP

TCs (Figs. 2.17 and 2.18). This finding implies that RWT activity associated with WNP TC recurvature varies by time of year. Composite analyses indicate that WNP TCs that recurve in fall and late spring feature signatures of RWT amplification and dispersion across the North Pacific into North America (Figs. 3.5, 3.7, and 3.8), whereas WNP TCs that recurve in summer do not favor RWT amplification and dispersion (Fig. 3.6).

The composite analysis for WNP TC recurvature episodes stratified by month further indicates that TCs that recurve in late fall tend to favor CWB and attendant cyclogenesis that leads to downstream amplification of a high-latitude ridge over western North America (Fig. 3.8). A connection between CWB and attendant cyclogenesis, and downstream high-latitude ridge amplification has also been noted in various studies (e.g., Altenhoff et al. 2008; Woollings et al. 2008; Archambault et al. 2010). The finding that high-latitude ridge amplification over western North America tends to follow WNP TC recurvature in late fall suggests that recurving TC episodes could favor the onset of high-latitude blocking (e.g., Woollings et al. 2009) over western North America in late fall, which could subsequently impact the wintertime climate of North America.

The composite analyses indicate that in late spring and late fall, at the time of WNP TC recurvature, precipitation may tend to occur well poleward of the TC near Japan, as suggested by a coherent region of ascent separate from the TC within an equatorward jet-entrance region (Figs. 3.5a and 3.8a, respectively). Further composite analysis (not shown) indicates that this separate region of ascent is collocated with a PW plume extending poleward of the TC in a region of weak warm-air advection. Based on these synoptic signatures identified at the time of recurvature for recurving WNP TCs in May and November, it is speculated that WNP TC recurvature episodes in late spring and late fall may favor the occurrence of predecessor rain events (e.g., Galarneau et al. 2010) that may impact Japan (e.g., Wang et al. 2009).

A climatological analysis of recurving WNP TCs stratified by the latitude of TC recurvature (Figs. 2.19 and 2.20) indicate that TCs that recurve farther equatorward than typical tend to be associated with a less significant impact on the North Pacific meridional flow relative to TCs that recurve at higher latitudes. The low-latitude TC recurvatures tend to occur in late fall–early winter and late spring (Fig. 2.4), when the North Pacific jet stream is strong and displaced equatorward of its climatological position (Fig. 2.3). A cursory examination of WNP TCs recurving into strong, equatorward displaced jet streams (not shown) finds the strong vertical wind shear associated with a strong jet stream often contributes to the rapid decay of recurving TCs, which limits downstream ridge amplification. It is thus speculated that the apparent limited downstream ridge amplification associated with WNP TCs recurving into strong, equatorward jet streams limits the development of statistically significant above-normal meridional flow over the North Pacific.

The findings of the climatological analysis indicate that the tendency for meridional flow to develop over the North Pacific following WNP TC recurvature is not influenced by either TC intensity or TC size at recurvature (Fig. 2.21), or by whether recurving WNP TCs subsequently reintensify as ECs (Fig. 2.21). An implication of the latter finding is that the reintensification of a TC as an EC is not a critical aspect of RWT amplification and dispersion associated with recurving WNP TCs. This implication is borne out by the composite analysis of all recurving WNP TCs, discussed in section 5b, which indicates that RWT amplification and dispersion first becomes evident during a two-day period surrounding TC recurvature (Figs. 3.3d–f and Figs. 3.4b,c), well before the recurving TC becomes an EC.

Unlike TC intensity or TC size at recurvature, or whether a TC reintensifies as an EC, the objectively evaluated TC–jet stream interaction strength appears to be a critical factor in influencing the meridional flow pattern over the North Pacific following WNP TC recurvature. A climatological analysis indicates that relative to weak TC–jet stream interactions, strong TC–jet stream interactions are associated with a more rapid onset of above-normal meridional flow over the North Pacific relative to TC recurvature that persists for a longer period. This finding suggests that strong TC–jet stream interactions may be associated with more enhanced RWT activity over the North Pacific than recurving TCs associated with weak TC–jet stream interactions. Composite analyses of strong and weak TC–jet stream interaction cases confirm that strong TC–jet stream interactions favor enhanced RWT activity. Specifically, the composite analysis reveals that recurving WNP TCs associated with strong TC–jet stream interactions are characterized by the amplification and dispersion of a high-amplitude RWT across the North Pacific into North America (Fig. 3.10). Cyclonic wave breaking occurs over the high-latitude North Pacific upstream of a high-latitude upper-tropospheric ridge that amplifies over western North America one to three days after the time of the maximum TC–jet stream interaction (Figs. 3.10b–d). Between two to three days after the time of maximum TC–jet stream interaction, a positively tilted trough forms over central Canada and the southwestern U.S. (Figs. 3.10c,d). In contrast to recurving WNP TCs featuring strong TC–jet stream interactions, recurving WNP TCs featuring weak TC–jet stream interactions are associated with a relatively low-amplitude RWT that dissipates within two days of the time of maximum TC–jet stream interaction and does not reach North America (Fig. 3.11).

For strong TC–jet stream interaction cases at the time of maximum TC–jet stream interaction (Fig. 3.9a), strong ascent is located over and northeast of the recurving TC within a deep tropical moisture plume. Broad upper-tropospheric divergent outflow directed outward from the ascent impinges upon the jet streak within the eastern flank of a strong, positively tilted trough upstream of the TC. An anticyclonically curved jet streak is situated between the trough and an amplifying ridge downstream. The TC ascent is positioned within the equatorward entrance region of the jet streak. The position of the TC ascent within the equatorward entrance region of the jet stream and the signature of divergent outflow from the ascent impinging upon the jet streak are suggestive of a synergistic relationship between the TC and the jet streak. In such a relationship, the divergent circulation of the TC strengthens the jet streak, thereby strengthening forcing for ascent in the equatorward jet-entrance region that in turn reinforces the divergent circulation of the TC. This signature of a positive feedback between the TC and the jet streak is the same signature that has been noted to occur in association with the reintensification of a TC as an EC (e.g., Sinclair 1993, 2004; Harr et al. 2000; Klein et al. 2002; Atallah et al. 2007).

The composite analysis of weak TC–jet stream interactions at the time of maximum TC–jet stream interaction (Fig. 3.9b) reveals that the same synoptic signatures are present as for strong TC–jet stream interactions, but are noticeably weaker. Relative to strong TC–jet stream interactions, the ascent located over and northeast of the recurving TC is localized and is associated with weak, similarly localized upper-tropospheric divergent outflow. As is the case for strong TC–jet stream interactions, a positively tilted trough is located upstream of the TC, and an anticyclonically curved jet streak is situated between this upstream trough and an amplifying ridge downstream. However, for weak TC–jet stream interactions, the trough, jet streak, and the amplifying ridge downstream are all weaker than for strong TC–jet stream interactions.

A climatological analysis reveals that strong TC–jet stream interactions have different characteristics than weak TC–jet stream interactions (Fig. 2.23). Strong TC–jet stream interactions occur more frequently in fall and early winter and less frequently in summer and late spring in comparison to weak TC–jet stream interactions and recurving WNP TCs in general. Additionally, recurving WNP TCs associated with strong TC–jet stream interactions are significantly more intense (Fig. 2.24) and larger (Fig. 2.25) at recurvature than those associated with weak TC–jet stream interactions.

That strong TC–jet stream interactions, which tend to feature TCs that are relatively large and intense, produce a higher-amplitude, longer-lived RWT compared to weak TC–jet stream interactions is consistent with findings of other studies that large and more intense recurving TCs may be associated with more pronounced downstream ridge amplification. For example, the study by Riemer et al. (2008) indicates that a larger and more intense recurving TC interacting with a straight jet stream in an idealized simulation produces a more amplified ridge and a higher-amplitude RWT due to broader and stronger upper-tropospheric TC divergent outflow impinging upon the jet stream. In addition, the study of Davis et al. (2008) notes that larger TCs with larger divergent circulations are more likely to remain intact as tropical systems as they interact with the jet stream, which could enable them to induce higher-amplitude ridges along the extratropical jet stream than smaller TCs with smaller divergent circulations.

In terms of the life cycle of recurving WNP TCs, the time of maximum TC–jet stream interaction for strong TC–jet stream interaction cases tends to occur significantly closer to the time of TC recurvature than for weak interaction cases (Fig. 2.22). Relative to weak TC–jet stream interactions, strong TC–jet stream interactions tend to occur farther westward (Fig. 2.26), at approximately 136°E, vs. 148°E for the weak interaction cases.

The finding that the TC–jet stream interaction strength (i.e., the strength of the negative PV advection by the upper-tropospheric divergent outflow associated with a recurving TC) influences RWT amplification and dispersion associated with WNP TC recurvature is in line with the findings of an idealized modeling study by Hodyss and Hendricks (2010). In their study, they find that the divergent circulation of a recurving TC can induce baroclinic waves via a Sardeshmukh and Hoskins (1988)-type RWT source term. Based on the findings of the current study, it is proposed that negative PV advection by the upper-tropospheric divergent outflow of the TC is a wave source for baroclinic RWTs in the same way that negative absolute vorticity advection by the divergent outflow associated with tropical heating is a wave source for barotropic RWTs (Sardeshmukh and Hoskins 1988).

c. Contrasting case studies of the downstream flow response to recurving WNP TCs

Although the climatological and composite analyses suggest that RWT amplification and dispersion are a characteristic response to a recurving WNP TC, the two case studies of recurving WNP TCs, Malakas in September 2010 and Chaba in October 2010, illustrate that recurving TCs that strongly interact with the jet stream can yield dramatically different downstream flow responses. In the case of TC Malakas, the interaction between the TC and the jet stream leads to ridge amplification and jet streak intensification (Fig. 4.8) that is associated with RWT dispersion across the North Pacific and North America (Fig. 4.11). The synoptic characteristics of the interaction between Malakas and the jet stream at the time of maximum TC–jet stream interaction (e.g., divergent outflow directed outward from TC ascent impinging upon the eastern flank of an upstream trough; a strong anticyclonically curved jet streak situated between the trough and an amplifying ridge downstream) are noted to be similar to the synoptic characteristics shown in the composite analysis of strong TC–jet stream interactions at the time of maximum TC–jet stream interaction (compare Fig. 4.8b to Fig. 3.9a).

In contrast to the recurvature of TC Malakas, in the case of TC Chaba, the interaction between the TC and jet stream does not directly result in ridge amplification, but instead establishes a strong, zonally extended jet stream and Rossby waveguide (e.g., Fig. 4.18) that precondition the large-scale flow pattern for subsequent RWT dispersion (Fig. 4.20) excited by a trough originating from Asia (Fig. 4.19). Furthermore, in the case of TC Chaba, the upper-tropospheric divergent outflow associated with a DRV-like feature along a baroclinic zone ahead of the TC appears to be impinging upon the jet stream at least as much as is the outflow directly associated with the TC itself (Fig. 4.16b). This case indicates that recurving TC episodes featuring an elongated region of convection along the equatorward side of the jet stream, and thus, an elongated area of diabatically driven divergent outflow directed toward the jet stream, may tend to favor the establishment of a strong, zonally extended jet stream. It is hypothesized that this scenario may be favored when a strong, zonally oriented baroclinic zone is present over the WNP in association with a strong, zonal jet stream, as seen in the case of TC Chaba.

An additional way that recurving TCs can influence the downstream flow evolution is revealed by the explosive intensification of the DRV-like feature that develops east of Chaba along a baroclinic zone (Fig. 4.17). Diabatic Rossby vortices have been identified as precursors to extratropical cyclogenesis (e.g., Wernli et al. 2002; Moore et al. 2008; Cordeira and Bosart 2011), but relatively few studies (e.g., Cordeira and Bosart 2011) have examined the relationship between recurving and transitioning TCs and DRVs. The case of Chaba shows that recurving and transitioning TCs can favor the development of DRVs, which, by serving as precursors to extratropical cyclogenesis, may lead to reconfiguration of the large-scale flow pattern through, for example, the formation of a blocking ridge (e.g., Sanders and Gyakum 1980).

While a RWT is a known precursor to wintertime large-scale flow reconfigurations and attendant high-impact weather events such as heavy precipitation events, case studies contained in the current study establish that RWT dispersion may be associated with large-scale flow reconfigurations and high-impact weather events in the fall when the jet stream and associated waveguide are relatively weaker compared to winter. In both case studies, RWT dispersion that occurs following each recurving WNP TC episode leads to extreme warmth over western North America and heavy rain events over eastern North America. The association of the heavy rain over North America following the recurvatures of TC Malakas and TC Chaba with AWB and PV streamers that develop following RWT dispersion corroborates findings of other studies that AWB and PV streamers that develop following RWT dispersion may serve as antecedents to heavy rain events (e.g., Massacand et al. 2001; Martius et al. 2008).

d. Predictability of the downstream flow response to recurving WNP TCs

As a complement to the investigation of the extratropical flow response to recurving WNP TCs, the predictability associated with recurving WNP TCs is examined from climatological and case study perspectives. A 10.5-year climatology of NH model forecast skill surrounding WNP TC recurvature episodes using composite GFS ACC time series of NH 500-hPa geopotential height forecasts indicates that recurvature episodes do not have an obvious deleterious effect on NH 500-hPa geopotential height forecasts (Fig. 2.38). In fact, for 24-h–120-h forecast lead times that verify at certain times following TC recurvature (Fig. 2.28), the composite ACC is significantly higher than normal. Constructing composite GFS ACC time series based on the time of year (Figs. 2.29–2.33) and the strength of the TC–jet stream interaction (Fig. 2.34) associated with recurving WNP TCs fails to reveal a coherent, statistically significant signal of reduced or enhanced NH model forecast skill associated with WNP TC recurvature.

Whereas the climatological analysis of model forecast skill indicates that recurving WNP TCs are not necessarily associated with reduced model forecast skill, the case study of TC Malakas illustrates that model error in the forecast of RWT amplification and dispersion associated with TC recurvature can lead to the growth and downstream propagation of error that may negatively impact model forecast skill over the North Pacific and North America. This growth and downstream propagation of model error associated with a RWT (e.g., Szunyogh et al. 2002; Zhang et al. 2003; Hakim 2005) has specifically been identified for the case of RWTs associated with recurving and transitioning TCs (e.g., Harr et al. 2008; Anwender et al. 2008; Reynolds et al. 2009; Anwender et al. 2010).

The case study of TC Malakas also highlights that poor model forecasts of the interaction between a TC and the extratropical flow may result in poor model forecasts of high-impact weather events well downstream (e.g., the eastern North American heavy precipitation event of 30 September–1 October 2010; Fig. 4.25). An important point is that a relatively poor forecast of high-impact sensible weather events associated with recurving TCs may not necessarily coincide with reduced hemispheric model forecast skill as evaluated using, for example, ACCs of NH 500 hPa geopotential height forecasts.

A broad implication of the composite analysis and case studies is that latent heat release associated with diabatic processes within the TC core and downstream of the TC along a baroclinic zone in a region of deep tropical moisture and frontogenesis is likely to be critical to the amplification of a RWT during TC recurvature. Thus, this study points to the need for the accurate model representation of diabatic processes associated with a recurving TC in order to attain a successful model forecast of the downstream extratropical flow evolution following TC recurvature.

As discussed above, the strength of the TC–jet stream interaction, defined herein by the strength of the negative PV advection by the upper-tropospheric divergent outflow associated with a recurving TC, has been shown to substantially influence the RWT response to TC recurvature. It is thus proposed that the real-time computation of the forecast TC–jet stream interaction metric for a recurving TC could have utility in an operational setting. Members of an EPS could be grouped based on the TC–jet stream interaction metric to provide forecasters with an understanding of the variation possible in the TC–jet stream interaction, and the impact of that TC–jet stream interaction variation on the downstream large-scale flow evolution.

6. Summary and future research paths

a. Summary

This dissertation describes the results of a three-part investigation of the observed extratropical flow response to WNP TC recurvature that consists of climatological, composite analysis, and case study components. In Chapter 2, a climatology of WNP TC recurvature is performed based on all 292 recurving WNP TC episodes between 1979 and 2009. Relationships between WNP TC recurvature episodes and the downstream large-scale flow pattern are analyzed using a North Pacific meridional flow index, which is computed from the NCEP–NCAR reanalysis by spatially averaging the absolute value of meridional wind on the DT for the North Pacific domain. Higher values of the North Pacific meridional flow index indicate a more wavelike North Pacific flow pattern, and lower values indicate a more zonal North Pacific flow pattern.

A composite time series of the North Pacific meridional flow index constructed for the period surrounding WNP TC recurvature reveals that the North Pacific flow pattern tends to be significantly more meridional than normal, in a statistical sense, between T+12 h and T+114 h relative to WNP TC recurvature. To the extent that meridional flow on the DT corresponds to RWT activity, these findings suggest that WNP TC recurvature episodes may be associated with enhanced RWT activity over the North Pacific.

A climatological examination is performed of how relationships between WNP TC recurvature and the downstream extratropical flow pattern are influenced by characteristics of the large-scale flow pattern, as represented by the time of year and latitude of recurvature. The time of year and latitude of TC recurvature are considered to represent the large-scale flow pattern because they are closely related to the strength and latitudinal position of the North Pacific jet stream. TCs that recurve in late fall–early winter and late spring, when the North Pacific jet stream is strong and displaced equatorward of its climatological position, tend to recurve at lower latitudes. In contrast, TCs that recurve in summer and early fall, when the North Pacific jet stream is weak and displaced poleward of its climatological position, tend to recurve at higher latitudes.

To examine the climatological influence of time of year on the downstream extratropical flow pattern, composite time series of the North Pacific meridional flow index are constructed for recurving WNP TCs stratified by month (i.e., May–December) and by latitude of TC recurvature (i.e., 15°–20°N, 20°–25°N, 25°–30°N, and 30°–35°N). Based on the composite time series of recurving WNP TCs stratified by month, considerable differences in the statistical significance, duration, and timing of the above-normal North Pacific meridional flow that develops following recurving WNP TC episodes are found when TCs are stratified by month. August and September are found to feature the most prolonged periods of significantly above-normal North Pacific meridional flow following TC recurvature (~96 h; Fig. 2.18) compared to other times of the year. Composite time series for recurving WNP TCs stratified by latitude of TC recurvature indicate that TCs that recurve between 15°N and 20°N tend to be associated with a less statistically significant impact on the North Pacific meridional flow relative to TCs that recurve between 20°N and 35°N.

A climatological examination of how relationships between WNP TC recurvature and the downstream extratropical flow pattern are influenced by characteristics of the recurving TC (i.e., TC intensity and size at recurvature) is next conducted. Recurving WNP TCs are categorized as strong or weak if they feature an MSLP within the bottom or top quintiles, respectively, of all recurving WNP TCs at recurvature. Similarly, recurving WNP TCs are categorized as large or small if they feature maximum 30-kt wind radii within the top or bottom quintiles, respectively, of all recurving WNP TCs at recurvature. Composite time series of the North Pacific meridional flow index constructed for strong and weak recurving TCs, and large and small recurving TCs, reveal that that the tendency for significantly above-normal meridional flow to develop over the North Pacific following WNP TC recurvature is not influenced by either TC intensity or TC size at recurvature.

Finally, a climatological examination is performed of how relationships between WNP TC recurvature and the downstream extratropical flow pattern are influenced by characteristics of the phasing of the TC with the extratropical flow pattern (i.e., whether a TC reintensifies as an EC and the TC–jet stream interaction strength). TC–jet stream interaction strength is objectively evaluated based on the magnitude of the negative PV advection by the upper-tropospheric divergent outflow associated with the TC (i.e., the TC–jet stream interaction metric). TC–jet stream interactions are categorized as strong or weak if they feature a TC–jet stream interaction metric within the top or bottom quintiles, respectively, for all recurving WNP TCs associated with a TC–jet stream interaction.

Composite time series of the North Pacific meridional flow index constructed for TCs that reintensify as ECs and for TCs that do not reintensify as ECs indicate that the tendency for significantly above-normal North Pacific meridional flow to develop following WNP TC recurvature is not influenced by whether or not a recurving WNP TC reintensifies as an EC. However, composite time series of the North Pacific meridional flow index constructed for strong and weak TC–jet stream interactions show that the tendency for significantly above-normal North Pacific meridional flow to develop following WNP TC recurvature is influenced by whether a recurving WNP TC is associated with a strong or weak TC–jet stream interaction. Compared to weak TC–jet stream interactions, strong TC–jet stream interactions are associated with more statistically significant above-normal North Pacific meridional flow that persists for a longer period following TC recurvature.

In addition to a climatological examination of how relationships between WNP TC recurvature and the downstream extratropical flow pattern are influenced by characteristics of the large-scale flow pattern, the TC, and the phasing between the TC and the extratropical flow pattern, the NH predictability associated with recurving WNP TCs are examined from a climatological perspective. The evaluation of NH model forecast skill surrounding WNP TC recurvature episodes using GFS ACCs of NH 500-hPa geopotential height forecasts indicates that, somewhat counter to conventional wisdom, episodes of recurving WNP TCs are generally not associated with below-normal NH model forecast skill. In fact, for some forecast lead times verifying at particular times following WNP TC recurvature, model forecast skill is found to be significantly higher than normal. The construction of composite GFS ACC time series for recurving WNP TCs in each month between May and December and for strong and weak TC–jet stream interactions associated with recurving WNP TCs fails to reveal coherent, statistically significant signals of anomalous NH model forecast skill associated with WNP TC recurvature.

In Chapter 3, the overall influence of recurving WNP TCs on the downstream large-scale flow pattern is examined from a synoptic–dynamic perspective using recurvature-relative composite analysis constructed from the NCEP–NCAR reanalysis. Additionally, recurvature-relative composite analysis constructed from the NCEP–NCAR reanalysis is used to examine how time of year influences the downstream large-scale flow pattern evolution following WNP TC recurvature episodes. Finally, interaction-relative composite analysis constructed from the NCEP–NCAR reanalysis is employed to examine how TC–jet stream interaction strength influences the downstream large-scale flow pattern evolution following WNP TC recurvature episodes.

Composite analysis of all recurving WNP TCs for 1979–2009 reveals that recurving WNP TCs are associated with the amplification of a preexisting RWT migrating eastward from Asia that subsequently disperses across the North Pacific and reaches North America within four days of WNP TC recurvature. A key finding is that upper-tropospheric ridge amplification and jet streak intensification over the WNP, which is deemed to be an important antecedent to RWT dispersion across the North Pacific and into North America, appears to occur in direct response to the impingement of diabatically induced upper-tropospheric divergent outflow associated with the recurving TC on the WNP jet stream and waveguide.

Motivated by the findings of the climatological analysis that indicate a seasonal dependence of the relationship between recurving WNP TCs and the downstream extratropical flow pattern, composite analyses are constructed for recurving WNP TCs in May, July, September, and November. The composite analysis reveals that recurving WNP TCs in July are not associated with distinct RWT amplification and dispersion, whereas recurving TCs in May, September, and November are associated with RWT amplification and dispersion across the North Pacific into North America. November

WNP TC recurvature episodes tend to favor the onset of high-latitude upper-tropospheric ridges over western North America, whereas recurving WNP TCs in May, July, and September do not.

To explore the findings of a climatological analysis that TC–jet stream interaction strength influences the downstream extratropical flow pattern during WNP TC recurvature, composite analyses are constructed for recurving WNP TCs featuring strong and weak TC–jet stream interactions. The composite analysis of strong TC–jet stream interactions indicates that strong TC–jet stream interactions are associated with the amplification and dispersion of a RWT that leads to a high-latitude upper-tropospheric ridge over western North America and a trough over the central Canada and the southwestern U.S. In contrast, weak TC–jet stream interactions are associated with a relatively low-amplitude RWT that dissipates within two days of the time of maximum TC–jet stream interaction. Over the North Pacific, CWB is favored following strong TC–jet stream interactions, whereas AWB is favored following weak TC–jet stream interactions.

In Chapter 4, multiscale case studies are presented of two recurving WNP TCs, Malakas (September 2010) and Chaba (October 2010), that are associated with downstream large-scale flow reconfigurations that lead to favorable synoptic conditions for extreme warmth over western North America and heavy rain over eastern North America. Following interactions between the TCs and the jet stream, RWT dispersion occurs across the North Pacific into North America, and is followed by AWB and the associated formation of PV streamers over eastern North America that are critical antecedents to heavy rain events.

Whereas the interaction between TC Malakas and the jet stream directly results in RWT dispersion, the interaction between Chaba and the jet stream appears to precondition the environment for RWT dispersion by establishing a strong, zonally extended jet stream over the North Pacific. In the case of TC Chaba, upper-tropospheric divergent outflow associated with a DRV-like feature along a baroclinic zone ahead of the TC appears to be at least as important as the outflow directly associated with the TC in strengthening and zonally extending the North Pacific jet stream.

A key difference between the respective TC–jet stream interactions associated with TC Malakas and TC Chaba is that Malakas interacts with an upstream trough, whereas Chaba does not. Although the case study of TC Chaba indicates that strong TC–jet stream interactions can occur without an upstream trough, that ridge amplification occurs only with TC Malakas suggests that ridge amplification might be favored when a recurving TC interacts with an upstream trough. The findings that both TC Malakas and TC Chaba continue to strengthen after they recurve and are at their peak intensity at the time of maximum TC–jet stream interaction suggests a synergistic relationship between the TC and the jet stream. In such a relationship, the divergent circulation of the TC strengthens the jet streak, thereby strengthening forcing for ascent in the equatorward jet-entrance region that in turn reinforces the divergent circulation of the TC.

An examination of predictability associated with the recurvature of TC Malakas finds that forecast error in the WNP ridge amplification associated with the TC–jet stream interaction contributes to considerable forecast error and uncertainty downstream due to relatively poor forecasts of RWT dispersion associated with the TC–jet stream interaction. Based on the large magnitude and spatial extent of the model error associated with RWT dispersion, it is suggested that model error associated with the TC–jet stream interaction contributes to an observed drop in NH model forecast skill in late September 2010.

b. Future research paths

This work points to a number of potential research opportunities. A natural extension is to compare the downstream extratropical flow response to recurving TCs in the North Atlantic, which may impact sensible weather over Europe, to the downstream extratropical flow response to recurving TCs in the WNP. The hypothesis to be tested is that the more zonally contracted, weaker jet stream and waveguide typically present over the North Atlantic relative to those over the North Pacific are less conducive to RWT dispersion.

Another extension of this work is to perform composite analysis of recurving WNP TCs stratified by intraseasonal and interannual modes of variability such as the Madden–Julian Oscillation (MJO) and ENSO. Since the MJO and ENSO are associated with tropical heating anomalies that modulate the tropical and extratropical background flow pattern, it is speculated that the signature of RWT dispersion associated with recurving WNP TCs may be substantially influenced by the different background flow patterns associated with different phases of the MJO and ENSO.

Although a climatology of NH ACCs for 500-hPa geopotential height forecasts for wavenumbers 1–20 surrounding WNP TC recurvature episodes does not indicate reduced predictability associated with TC recurvature, this finding should be corroborated using ACCs computed for a more regional domain such as the North Pacific and for all wavenumbers. Also of interest is whether RWTs that amplify in association with recurving WNP TCs are inherently less predictable than those that amplify in association with WNP extratropical cyclogenesis. To address this question, a feature-based tracking algorithm used to identify RWTs (e.g., Souders et al. 2011) could be used to obtain samples of these two types of RWTs. Conventional assessments of model forecast skill and uncertainty could be applied to evaluate whether differences in predictability exist between these two types of RWTs.

The results of the composite analysis and case studies that suggest that the divergent outflow of a recurving TC is critical to the development of a downstream jet streak motivate a kinematic study of the jet streak intensification process during TC recurvature. The relative contributions to jet intensification and PV frontogenesis from the rotational and divergent wind could be examined by partitioning the horizontal wind into irrotational and nondivergent components (e.g., Krishnamurti 1968; Keyser et al. 1989).

Finally, a numerical modeling study of real and idealized cases of recurving and transitioning TCs that specifically examines the influence of diabatic processes on the TC–jet stream interaction could be performed. The roles of latent heat release associated with convection within the TC core vs. poleward and downstream of the TC along a baroclinic zone in ridge amplification and jet streak intensification should be quantified. An exploration of the extent that diabatic processes contribute to reduced predictability associated with recurving and transitioning TCs could be included in such a modeling study.

REFERENCES

Agustí-Panareda, A., C. D. Thorncroft, G. C. Craig, and S. L. Gray, 2004: The extratropical transition of Hurricane Irene (1999): A potential vorticity perspective. *Quart. J. Roy. Meteor. Soc.*, **130,** 1047–1074.

Agustí-Panareda, A., S. L. Gray, G. C. Craig, and C. Thorncroft, 2005: The extratropical transition of Tropical Cyclone Lili (1996) and its crucial contribution to a moderate extratropical development. *Mon. Wea. Rev.*, **133,** 1562–1573.

Altenhoff, A. M., O. Martius, M. Croci-Maspoli, C. Schwierz, and H. C. Davies, 2008: Linkage of atmospheric blocks and synoptic-scale Rossby waves: A climatological analysis. *Tellus,* **60A,** 1053–1063.

Anwender, D., P. A. Harr, and S. C. Jones, 2008: Predictability associated with the downstream impacts of the extratropical transition of tropical cyclones: Case studies. *Mon. Wea. Rev.*, **136,** 3226–3247.

Anwender, D., S. C. Jones, M. Leutbecher, and P. A. Harr, 2010: Sensitivity experiments for ensemble forecasts of the extratropical transition of typhoon Tokage (2004). *Quart. J. Roy. Meteor. Soc.*, **136,** 183–200.

Archambault, H. M., D. Keyser, and L. F. Bosart, 2010: Relationships between large-scale regime transitions and major cool-season precipitation events in the northeastern United States. *Mon. Wea. Rev.,* **138,** 3454–3473.

Atallah, E., L. F. Bosart, and A. R. Aiyyer, 2007: Precipitation distribution associated with landfalling tropical cyclones over the eastern United States. *Mon. Wea. Rev.*, **135,** 2185–2206.

Bjerknes, J., 1969: Atmospheric teleconnections from the equatorial Pacific. *Mon. Wea. Rev.,* **97,** 163–172.

Bluestein, H. B., 1992: *Synoptic–Dynamic Meteorology in Midlatitudes.* Vol. 1*, Principles of Kinematics and Dynamics,* Oxford University Press, 431 pp.

Bosart, L. F., 1999: Observed cyclone life cycles. *The Life Cycles of Extratropical Cyclones,* M. A. Shapiro and S. Grønås, Eds., Amer. Meteor. Soc., 187–213.

Bosart, L. F., and G. M. Lackmann, 1995: Postlandfall tropical cyclone reintensification in a weakly baroclinic environment: A case study of Hurricane David (September 1979). *Mon. Wea. Rev.*, **123,** 3268–3291.

Browning, K. A., G. Vaughan, and P. Panagi, 1998: Analysis of an ex-tropical cyclone after its reintensification as a warm-core extratropical cyclone. *Quart. J. Roy. Meteor. Soc.*, **124,** 2329–2356.

Browning, K. A., A. J. Thorpe, A. Montani, D. Parsons, M. Griffiths, P. Panagi, and E. M. Dicks, 2000: Interactions of tropopause depressions with an ex–tropical cyclone and sensitivity of forecasts to analysis errors. *Mon. Wea. Rev.*, **128,** 2734–2755.

Burroughs, L. D., and S. Brand, 1973: Speed of tropical storms and typhoons after recurvature in the western North Pacific Ocean. *J. Appl. Meteor.*, **12,** 452–458.

Camargo, S. J., A. W. Robertson, S. J. Gaffney, P. Smyth, and M. Ghil, 2007: Cluster analysis of typhoon tracks. Part II: Large-scale circulation and ENSO. *J. Climate*, **20,** 3654–3676.

Chan, J. C. L., 1985: Tropical cyclone activity in the Northwest Pacific in relation to the El Niño/Southern Oscillation phenomenon. *Mon. Wea. Rev.*, **113,** 599–606.

Chan, J. C. L., and W. M. Gray, 1982: Tropical cyclone movement and surrounding flow relationships. *Mon. Wea. Rev.*, **110,** 1354–1374.

Chan, J. C. L., W. M. Gray, and S. Q. Kidder, 1980: Forecasting tropical cyclone turning motion from surrounding wind and temperature fields. *Mon. Wea. Rev.*, **108,** 778–792.

Chang, E. K. M., and D. B. Yu, 1999: Characteristics of wave packets in the upper troposphere. Part I: Northern Hemisphere winter. *J. Atmos. Sci.*, **56,** 1708–1728.

Cheng-Lan, B., and J. C. Sadler, 1983: The speed of recurving typhoons over the Western North Pacific Ocean. *Mon. Wea. Rev.*, **111,** 1280–1292.

Colle, B. A., 2003: Numerical simulations of the extratropical transition of Floyd (1999): Structural evolution and responsible mechanisms for the heavy rainfall over the Northeast United States. *Mon. Wea. Rev.*, **131,** 2905–2926.

Cordeira, J. M., and L. F. Bosart, 2011: Cyclone interactions and evolutions during the "Perfect Storms" of late October and early November 1991. *Mon. Wea. Rev.*, **139,** 1683–1707.

Davis, C. A., and K. A. Emanuel, 1991: Potential vorticity diagnostics of cyclogenesis. *Mon. Wea. Rev.*, **119,** 1929–1953.

Davis, C. A., S. C. Jones, and M. Riemer, 2008: Hurricane vortex dynamics during Atlantic extratropical transition. *J. Atmos. Sci.*, **65,** 714–736.

Dickinson, M. J., L. F. Bosart, W. E. Bracken, G. J. Hakim, D. M. Schultz, M. A. Bedrick, and K. R. Tyle, 1997: The March 1993 Superstorm cyclogenesis: incipient phase synoptic- and convective-scale flow interaction and model performance. *Mon. Wea. Rev.*, **125,** 3041–3072.

DiMego, G. J., and L. F. Bosart, 1982a: The transformation of Tropical Storm Agnes into an extratropical cyclone. Part I: The observed fields and vertical motion computations. *Mon. Wea. Rev.*, **110,** 385–411.

DiMego, G. J., and L. F. Bosart, 1982b: The transformation of Tropical Storm Agnes into an extratropical cyclone. Part II: Moisture, vorticity and kinetic energy budgets. *Mon. Wea. Rev.*, **110,** 412–433.

Dobos, P. H., and R. L. Elsberry, 1993: Forecasting tropical cyclone recurvature. Part I: evaluation of existing methods. *Mon. Wea. Rev.*, **121,** 1273–1278.

Dvorak, V. F., 1975: Tropical cyclone intensity analysis and forecasting from satellite imagery. *Mon. Wea. Rev.*, **103,** 420–430.

Dvorak, V. F., 1984: Tropical cyclone intensity analysis using satellite data. NOAA Tech. Rep. NESDIS 11, 47 pp.

Elsner, J. B., and K.-b. Liu 2003: Examining the ENSO-typhoon hypothesis. *Climate Research*, **25,** 43–54.

Evans, J. L., J. M. Arnott, and F. Chiaromonte, 2006: Evaluation of operational model cyclone structure forecasts during extratropical transition. *Mon. Wea. Rev.*, **134,** 3054–3072.

Feldstein, S. B., 2002: Fundamental mechanisms of the growth and decay of the PNA teleconnection pattern. *Quart. J. Roy. Meteor. Soc.,* **128,** 775–796.

Foley, G. R., and B. N. Hanstrum, 1994: The capture of tropical cyclones by cold fronts off the west coast of Australia. *Wea. Forecasting*, **9,** 577–592.

George, J. E., and W. M. Gray, 1976: Tropical cyclone motion and surrounding parameter relationships. *J. Appl. Meteor.*, **15,** 1252–1264.

George, J. E., and W. M. Gray, 1977: Tropical cyclone recurvature and nonrecurvature as related to surrounding wind-height fields. *J. Appl. Meteor.*, **16,** 34–42.

Grams, C. M., 2010: The interaction between the outflow of Typhoon Jangmi (2008) and the midlatitude jet during T-PARC. Extended abstracts, *29th Conference on Hurricanes and Tropical Meteorology, Tuscon, AZ,* Amer. Meteor. Soc.,9A.7. [Available online at http://ams.confex.com/ams/pdfpapers/168783.pdf]

Hakim, G. J., 2003: Developing wave packets in the North Pacific storm track. *Mon. Wea. Rev.*, **131,** 2824–2837.

Hakim, G. J., 2005: Vertical structure of midlatitude analysis and forecast errors. *Mon. Wea. Rev.*, **133,** 567–578.

Harr, P. A., and R. L. Elsberry, 1991: Tropical cyclone track characteristics as a function of large-scale circulation anomalies. *Mon. Wea. Rev.*, **119,** 1448–1468.

Harr, P. A., and R. L. Elsberry, 1995a: Large-scale circulation variability over the tropical western North Pacific. Part I: Spatial patterns and tropical cyclone characteristics. *Mon. Wea. Rev.*, **123,** 1225–1246.

Harr, P. A., and R. L. Elsberry, 2000: Extratropical transition of tropical cyclones over the western North Pacific. Part I: Evolution of structural characteristics during the transition process. *Mon. Wea. Rev.*, **128**, 2613–2633.

Harr, P. A., and J. M. Dea, 2009: Downstream development associated with the extratropical transition of tropical cyclones over the western North Pacific. *Mon. Wea. Rev.*, **137,** 1295–1319.

Harr, P. A., R. L. Elsberry, and T. F. Hogan, 2000: Extratropical transition of tropical cyclones over the Western North Pacific. Part II: The impact of midlatitude circulation characteristics. *Mon. Wea. Rev.*, **128,** 2634–2653.

Harr, P. A., D. Anwender, and S. C. Jones, 2008: Predictability associated with the downstream impacts of the extratropical transition of tropical cyclones: Methodology and a case study of Typhoon Nabi (2005). *Mon. Wea. Rev.*, **136,** 3205–3225.

Hart, R. E., 2003: A cyclone phase space derived from thermal wind and thermal asymmetry. *Mon. Wea. Rev.*, **131,** 585–616.

Hodanish, S., and W. M. Gray, 1993: An observational analysis of tropical cyclone recurvature. *Mon. Wea. Rev.*, **121,** 2665–2689.

Hodyss, D., and E. Hendricks, 2010: The resonant excitation of baroclinic waves by the divergent circulation of recurving tropical cyclones. *J. Atmos. Sci.*, **67,** 3600–3616.

Holland, G. J., and Y. Wang, 1995: Baroclinic dynamics of simulated tropical cyclone recurvature. *J. Atmos. Sci.*, **52,** 410–426.

Hoskins, B. J., and D. J. Karoly, 1981: The steady linear response of a spherical atmosphere to thermal and orographic forcing. *J. Atmos. Sci.*, **38,** 1179–1196.

Hoskins, B. J., and P. J. Valdes, 1990: On the existence of storm-tracks. *J. Atmos. Sci.*, **47,** 1854–1864.

Hoskins, B. J., and T. Ambrizzi, 1993: Rossby wave propagation on a realistic longitudinally varying flow. *J. Atmos. Sci.*, **50,** 1661–1671.

Hoskins, B. J., M. E. McIntyre, and A. W. Robertson, 1985: On the use and significance of isentropic potential vorticity maps. *Quart. J. Roy. Meteor. Soc.*, **111,** 877–946.

Jones, S. C., P. A. Harr, J. Abraham, L. F. Bosart, P. J. Bowyer, J. L. Evans, D. E. Hanley, B. N. Hanstrum, R. E. Hart, F. Lalaurette, M. R. Sinclair, R. K. Smith, and C. Thorncroft, 2003: The extratropical transition of tropical cyclones: Forecast challenges, current understanding, and future directions. *Wea. Forecasting*, **18,** 1052–1092.

Kalnay, E., and Coauthors, 1996: The NCEP/NCAR 40-Year Reanalysis Project. *Bull. Amer. Meteor. Soc.,* **77,** 437–471.

Keyser, D., B. D. Schmidt, and D. G. Duffy, 1989: A technique for representing three-dimensional vertical circulations in baroclinic disturbances. *Mon. Wea. Rev.*, **117,** 2463–2494.

Kistler, R., and Coauthors, 2001: The NCEP–NCAR 50-Year Reanalysis: Monthly means CD-ROM and documentation. *Bull. Amer. Meteor. Soc.,* **82,** 247–267.

Kitabatake, N., 2008: Extratropical transition of tropical cyclones in the western North Pacific: Their frontal evolution. *Mon. Wea. Rev.*, **136,** 2066–2090.

Klein, P. M., P. A. Harr, and R. L. Elsberry, 2000: Extratropical transition of western North Pacific tropical cyclones: An overview and conceptual model of the transformation stage. *Wea. Forecasting*, **15,** 373–395.

Klein, P. M., P. A. Harr, and R. L. Elsberry, 2002: Extratropical transition of western North Pacific tropical cyclones: Midlatitude and tropical cyclone contributions to reintensification. *Mon. Wea. Rev.*, **130,** 2240–2259.

Krishnamurti, T. N., 1968: A study of a developing wave cyclone. *Mon. Wea. Rev.*, **96**, 208–217.

Langland, R. H., M. A. Shapiro, and R. Gelaro, 2002: Initial condition sensitivity and error growth in forecasts of the 25 January 2000 East Coast snowstorm. *Mon. Wea. Rev.*, **130,** 957–974.

Lu, C., and J. P. Boyd, 2008: Rossby wave ray tracing in a barotropic divergent atmosphere. *J. Atmos. Sci.*, **65,** 1679–1691.

Martin, J. D., and W. M. Gray, 1993: Tropical cyclone observation and forecasting with and without aircraft reconnaissance. *Wea. Forecasting*, **8,** 519–532.

Martius, O., C. Schwierz, and H. C. Davies, 2007: Breaking waves at the tropopause in the wintertime Northern Hemisphere: Climatological analyses of the orientation and the theoretical LC1/2 classification. *J. Atmos. Sci.*, **64**, 2576–2592.

Martius, O., C. Schwierz and H.C. Davies, 2008: Far-upstream Precursors of Precipitation Events on the Alpine South-side. *Quart. J. Roy. Meteor. Soc.*, **134,** 417–428.

Martius, O., C., Schwierz, and H. C. Davies, 2010: Tropopause-level waveguides. *J. Atmos. Sci.*, **67,** 866–879.

Massacand, A. C., H. Wernli, and H. C. Davies, 2001: Influence of upstream diabatic heating upon an Alpine event of heavy precipitation. *Mon. Wea. Rev.,* **129,** 2822–2828.

Matano, H., and M. Sekioka, 1971: On the synoptic structure of typhoon Cora, 1969, as the compound system of tropical and extratropical cyclones. *J. Meteor. Soc. Japan,* **49,** 282–295.

McIntyre, M. E., and T. N. Palmer, 1983: Breaking planetary waves in the stratosphere. *Nature,* **305,** 593–600.

McTaggart-Cowan, R., J. R. Gyakum, and M. K. Yau, 2001: Sensitivity testing of extratropical transitions Using potential vorticity inversions to modify initial conditions: Hurricane Earl case study. *Mon. Wea. Rev.*, **129**, 1617–1636.

McTaggart-Cowan, R., L. F. Bosart, J. R. Gyakum, and E. H. Atallah, 2007a: Hurricane Katrina (2005). Part I: Complex life cycle of an intense tropical cyclone. *Mon. Wea. Rev.*, **135,** 3905–3926.

McTaggart-Cowan, R., L. F. Bosart, J. R. Gyakum, and E. H. Atallah, 2007b: Hurricane Katrina (2005). Part II: Evolution and hemispheric impacts of a diabatically generated warm pool. *Mon. Wea. Rev.*, **135**, 3927–3949.

Moore, R. W., M. T. Montgomery, and H. Davies, 2008: The integral role of a diabatic Rossby vortex in a heavy snowfall event. *Mon. Wea. Rev.,* **123,** 3103–3114.

Namias, J., 1963: Large-scale air-sea interactions over the North Pacific from summer 1962 through the subsequent winter. *J. Geophys. Res*., **68,** 6171–6186.

Orlanski, I., 2005: A new look at the Pacific storm track variability: Sensitivity to tropical SSTs and to upstream seeding. *J. Atmos. Sci.*, **62**, 1367–1390.

Orlanski, I., and E. K. M. Chang, 1993: Ageostrophic geopotential fluxes in downstream and upstream development of baroclinic waves. *J. Atmos. Sci.*, **50,** 212–225.

Orlanski, I., and J. P. Sheldon, 1995: Stages in the energetics of baroclinic systems. *Tellus,* **47,** 605–628.

Petterssen, S., and S. J. Smebye, 1971: On the development of extratropical storms. *Quart. J. Roy. Meteor. Soc.,* **97,** 457–482.

Pierce, C. H., 1939: The meteorological history of the New England hurricane of Sept. 21, 1939. *Mon. Wea. Rev.*, **67,** 237–285.

Reynolds, C. A., M. S. Peng, and J. H. Chen, 2009: Recurving tropical cyclones: Singular vector sensitivity and downstream impacts. *Mon. Wea. Rev.*, **137**, 1320–1337.

Riehl, H., 1972: Intensity of recurved typhoons. *J. Appl. Meteor.*, **11**, 613–615.

Riehl, H., and R. J. Shafer, 1944: The recurvature of tropical storms. *J. Atmos. Sci.*, **1**, 42–54.

Riemer, M., and S. C. Jones, 2010: The downstream impact of tropical cyclones on a developing baroclinic wave in idealized scenarios of extratropical transition. *Quart. J. Roy. Meteor. Soc.*, **136,** 617–637.

Riemer, M., S. C. Jones, and C. A. Davis, 2008: The impact of extratropical transition on the downstream flow: An idealized modeling study with a straight jet. *Quart. J. Roy. Meteor. Soc.*, **134,** 69–91.

Ritchie, E. A., and R. L. Elsberry, 2007: Simulations of the extratropical transition of tropical cyclones: Phasing between the upper-level trough and tropical cyclone. *Mon. Wea. Rev.* 135, 862–876.

Sanders, F., and J. R. Gyakum, 1980: Synoptic-dynamic climatology of the “Bomb”. *Mon. Wea. Rev.*, **108,** 1589–1606.

Sardeshmukh, P. D., and B. J. Hoskins, 1988: The generation of global rotational flow by steady idealized tropical divergence. *J. Atmos. Sci.*, **45,** 1228–1251.

Schwierz, C., S. Dirren, and H. C. Davies, 2004: Forced waves on a zonally aligned jet stream. *J. Atmos. Sci.*, **61,** 73–87.

Shapiro, M., and Coauthors, 1999: A planetary-scale to mesoscale perspective of the life cycles of extratropical cyclones: The bridge between theory and observations. *The Life Cycles of Extratropical Cyclones,* M. A. Shapiro and S. Grönås, Eds., Amer. Meteor. Soc.**,** 39–185.

Sinclair, M. R., 1993: Synoptic-scale diagnosis of the extratropical transition of a southwest Pacific tropical cyclone. *Mon. Wea. Rev.*, **121,** 941–960.

Sinclair, M. R., 2002: Extratropical transition of southwest Pacific tropical cyclones. Part I: Climatology and mean structure changes. *Mon. Wea. Rev.*, **130,** 590–609.

Sinclair, M. R., 2004: Extratropical transition of Southwest Pacific tropical cyclones. Part II: midlatitude circulation characteristics. *Mon. Wea. Rev.*, **132,** 2145–2168.

Souders, B. M., B. A. Colle, and E. K. M. Chang, 2011: Spatial and temporal climatology of atmospheric wave packets. Recorded presentation, *24th Conference on Weather and Forecasting/20th Conference on Numerical Weather Prediction,* Seattle, WA, Amer. Meteor. Soc., 14A.6.
[Available online at
http://ams.confex.com/ams/91Annual/recordingredirect.cgi/id/17195.]

Szunyogh, I., Z. Toth, A. V. Zimin, S. J. Majumdar, and A, Persson, 2002: Propagation of the effect of targeted observations: The 2000 Winter Storm Reconnaissance Program. *Mon. Wea. Rev.*, **130,** 1144–1165.

Thorncroft, C. D., and S. C. Jones, 2000: The extratropical transitions of Hurricanes Felix and Iris in 1995. *Mon. Wea. Rev.*, **128,** 947–972.

Thorncroft, C. D., B. J. Hoskins, and M. E. McIntyre, 1993: Two paradigms of baroclinic-wave life-cycle behavior. *Quart. J. Roy. Meteor. Soc.*, **119,** 17–55.

Torn, R. D., 2010: Diagnosis of the downstream ridging associated with extratropical transition using short-term ensemble forecasts. *J. Atmos. Sci.*, **67,** 817–833.

Torn, R. D., and G. J. Hakim, 2009: Initial condition sensitivity of western Pacific extratropical transitions determined using ensemble-based sensitivity analysis. *Mon. Wea. Rev.,* **137,** 3388–3406.

Velden, C., and Coauthors, 2006: The Dvorak tropical cyclone intensity estimation technique: A satellite-based method that has endured for over 30 years. *Bull. Amer. Meteor. Soc.*, **87,** 1195–1210.

Wallace, J. M., and D. S. Gutzler, 1981: Teleconnections in the geopotential height field during the Northern Hemisphere winter. Mon. Wea. Rev., **109,** 784–812.

Wang, B., and J. C. L. Chan, 2002: How strong ENSO events affect tropical storm activity over the western North Pacific. *J. Climate*, **15,** 1643–1658.

Wang, Y., Y. Wang, and H. Fudeyasu, 2009: The role of Typhoon Songda (2004) in producing distantly located heavy rainfall in Japan. *Mon. Wea. Rev.*, **137,** 3699–3716.

Wernli, H., S. Dirren, M. A. Liniger and M. Zillig, 2002: Dynamical aspects of the life-cycle of the winter storm "Lothar" (24-26 December 1999). *Quart. J. Roy. Meteor. Soc.,* **128,** 405-429.

Wilks, D. S., 2006: *Statistical Methods in the Atmospheric Sciences.* 2nd ed. Academic Press, 627 pp.

Woollings, T., B. Hoskins, M. Blackburn, and P. Berrisford, 2008: A new Rossby wave–breaking interpretation of the North Atlantic Oscillation. *J. Atmos. Sci.,* **65,** 609–626.

Zhang, F., C. Snyder, and R. Rotunno, 2003: Effects of moist convection on mesoscale predictability. *J. Atmos. Sci.*, **60**, 1173–1185.